



UiT The Arctic University of Norway

Faculty of Health Sciences

Institute of Medical Biology

Mechanism and structural requirements for formation of p62 bodies and degradation of p62 by selective autophagy

Anthimi Palara

A dissertation for the degree of Philosophiæ Doctor

September 2021



Mechanism and structural requirements for formation of p62 bodies and degradation of p62
by selective autophagy

By

Anthimi Palara



A dissertation for Degree of Philosophiæ Doctor

UiT-The Arctic University of Norway

Faculty of Health Sciences

Department of Medical Biology

Autophagy Research Group

September 2021

II

“The investigation of the truth is in one way hard, in another easy. An indication of this is found in the fact that no one is able to attain the truth adequately, while, on the other hand, no one fails entirely, but everyone says something true about the nature of things, and while individually they contribute little or nothing to the truth, by the union of all a considerable amount is amassed. Therefore, since the truth seems to be like the proverbial door, which no one can fail to hit, in this way it is easy, but the fact that we can have a whole truth and not the particular part we aim at shows the difficulty of it. Perhaps, as difficulties are of two kinds, the cause of the present difficulty is not in the facts but in us.”

Aristotle-Metaphysics

(384 B.C. - c. 322 B.C.)

Contents

Summary	VI
Acknowledgments	VII
Abbreviations	IX
List of Papers.....	XII
1. Introduction	- 1 -
1.1 Introduction to autophagy	- 1 -
1.2 Autophagosome formation and degradation	- 4 -
1.3 Induction of autophagy.....	- 4 -
1.4 The core autophagy molecular machinery needed for autophagosome formation	- 6 -
1.4.1 ULK complex.....	- 6 -
1.4.2 PI3K Class III complex 1 (PI3KC3-C1)	- 6 -
1.4.3 Transmembrane proteins in mammalian autophagy	- 7 -
1.4.4 Conjugation systems	- 7 -
1.5 ATG8 family proteins and their roles in autophagy.....	- 8 -
1.6 SAR-induced autophagosome formation	- 11 -
1.7 The role of p62/SQSTM1-like receptors (SLRs) in autophagy	- 12 -
1.7.1 PB1 domain of p62 (amino acid residues 3-102).....	- 14 -
1.7.2 ZZ-type domain of p62 (amino acid residues 122-167).....	- 15 -
1.7.3 Conserved LIR-KIR region of p62 (amino acid residues 303-370).....	- 16 -
1.7.4 The UBA domain of p62 (amino acid residues 389-434)	- 19 -
1.7.5 p62 and diseases associated with the UBA domain	- 20 -
1.8 Liquid-liquid phase separation	- 21 -
1.8.1 Phase separation in autophagy	- 23 -
1.8.2 Liquid-liquid phase separation of p62.....	- 24 -
1.8.3 Post- transcriptional modification on p62	- 25 -

2. Aim of the study	- 28 -
3. Summary of the papers.....	- 29 -
3.1 Paper I	- 29 -
3.2 Paper II	- 29 -
3.3 Paper III.....	- 30 -
4. Discussion	- 31 -
4.1 Phase separation of p62 may depend on shortening of the length of p62 filaments	- 31 -
4.2 Phase separation of p62 is regulated by post-translational modification of K420 and K435	- 33 -
4.3 Modification of the K435 residue is crucial for basal autophagy of p62.....	- 37 -
4.4 The complexity of the LIR-KIR region.....	- 38 -
4.5 KEAP1 is degraded by autophagy in response to starvation, and this depends on p62.....	- 40 -
4.6 The p62 filament is evolutionary conserved	- 41 -
5. Methodological consideration.....	- 41 -
5.1 Construction of Stable Cell Lines	- 41 -
5.2 Cell growth and cell culture	- 42 -
5.3 Western blotting assay	- 43 -
5.4 GST pull-down assay	- 44 -
5.5 Ubiquitin-binding assay (Paper III).....	- 44 -
5.6 Transient Transfection.....	- 45 -
6. References	- 46 -

Summary

Selective autophagy is responsible for the lysosomal degradation of damaged and surplus cytoplasmic components, including misfolded proteins and dysfunctional organelles. Selective autophagy is required for protein and organelle quality control basally and upon stress. For the autophagic process to be precise, selective autophagy receptors (SARs) like SQSTM1/p62 are required.

Autophagic substrates are often tagged with ubiquitin. Ubiquitinated substrates can be recognized by p62 and other p62-like SARs. SARs bind to lipidated ATG8 protein family members at the inner phagophore membrane and act as bridges that connect the substrate with the phagophore. Both SARs and their substrates are degraded after the fusion of the autophagosome with one or more lysosomes. Hence, p62 is both a substrate and a receptor for selective autophagy. p62 can polymerize into helical filaments via its N-terminal PB1 domain, bind to ATG8 proteins via its LIR (LC3 interacting region) motif and to the ubiquitin E3 ligase subunit KEAP1 via the adjacent KIR (KEAP1 interacting region) motif. The C-terminal UBA domain of p62 interacts with ubiquitinated substrates. The ability to form helical filaments and to bind to ubiquitin chains endows p62 with the property to form droplets in both the cytoplasm and nucleus of cells by liquid-liquid phase transition. The droplets have been called p62 bodies. They contain p62 and also other SARs like NBR1 and TAXBP as well as KEAP1 and ubiquitinated substrates. By recruiting ATG8 proteins and core autophagy components like FIP200 the droplets are degraded by selective autophagy. The p62 bodies can also function as signalosomes (signal transmitting, multimolecular protein complexes) which can also be degraded by selective autophagy to terminate their signaling.

This thesis presents new studies of the roles of the PB1 domain, the LIR and KIR motifs and the UBA domain in the formation and degradation of p62 bodies. The first paper, a collaborative study led by the research group of Carsten Sachse, demonstrated the importance of the PB1-mediated polymerization of p62 into filaments for the formation of p62 bodies and their degradation by autophagy. In the second paper, we explored if a specific LIR-mediated binding of LC3B is required for autophagic degradation of p62. In our third paper, we focused on the UBA domain of p62 and post-translational modifications that occur and their effects on p62 droplet formation and degradation. It was clear from our findings that K435 plays a crucial role in the degradation of p62 by selective autophagy.

Acknowledgements

First, I would like to thank my main supervisor Professor Terje Johansen, who allowed me to be part of this group 4 years ago and to start my PhD journey. Moreover, I would like to thank him for having his door open, taking time to help, guide and advise me for both things related to my PhD and personal issues.

Furthermore, I would like to thank my co-supervisor Trond Lamark, for being the biggest p62 supporter and the best cloning advisor. He stood by me a lot and his office was also always open to discuss all possible subjects both related to work and not. I appreciate his support and understanding.

Additionally, I want to thank the technicians of our group, boss No1 Aud, boss No2 Gry and boss No3 Hanne, for all the advice and all the help that they provided to me in the lab. But mostly I would like to thank them because when I first came from Greece, and I did not know anyone, they open their hearts and their houses for me and helped me a lot with fixing my house. They have been there for me as colleagues, friends and as a second family. I could and can always count on their help, support, and advice for all matters.

I would like to express my gratitude to all lab members of ARG, former MCRG, both those who are still there and those who left. I would like to thank Mads for all his suggestions during my first years and Mutugi too. I will miss our weekend coffees and the bombing of questions during that time in the pause room. Also, Birendra, who was always smiling, and was willing to help everyone in the lab. I should not forget to mention Pradip and Yakubu, who both have been a great help with lab problems and helped me to improve my technics by sharing with me some of their tips. I would I also like to thank Hallvard, for sharing his knowledge with me, helping me to learn Volocity and his criticism about everything drove me to think deeper and to not take everything for granted but try more, to improve assays and to understand techniques better.

A big thank you to Thanasis, who has been “stalking” me since he entered the same university as me and then did his master in the same place as me. Now, he is at Tromsø in the same group as I! He is the person that I can talk about everything, and he understands me, since we speak the same language! Thank you for all the Saturday mornings that we listen to Greek music together inside the lab.

Last but not least, from the members of the group, I would like to thank all the ladies for being the best co-workers ever. I would like to thank Eva for providing helpful comments and being there for me. Also, Mireia that she pushed me to start writing my thesis and she helped me with things in the lab. In the end, I would like to thank my officemates Juncal and Nikoline, for the nice environment that they created both in the office and in the lab. I also thank Juncal for inspiring me to start running and helping with a lot of matters. Thank you, girls, for being so good friends!

I would also want to thank my fast lege Marit Aasbrenn for her determination to find a solution to my health issues and for her support. Her medical advice definitely improved my daily life.

I don't know if a "thank you" is enough to express my gratitude to my family. Thank you for letting me follow my dream and you were always next to me to support every decision that I make, even though that means that I will be so far away from you. I thank my dad for teaching me how to study and for inspiring me to always look for more than one source to find the information that I wanted and to critically analyze what I read. This advice helped me a lot. Thank you, mom, for always being there to listen to me and support me. I want to thank my little brother Antony, who was the person who pushed me to look for PhD positions in Norway. I also thank him for listening to me, helping me to see clearly when I cannot and for being always there for me to encourage me. I could not have gone through this journey without their encouragement and love.

Finally, I am deeply obligated to my samboer Magnus, who has been next to me for 3 years. I know that the last 1,5 years have been quite difficult for him, because of me and all my work anxiety, but he was the only person who could calm me down. He was always coming home with chocolate when he knew that an experiment did not work as I wanted. I also thank him for listening to me talking and analyzing things related to my work even though it is not his field. Thank you so much for your love and understanding. Finally, I would like to thank his family for supporting me and treating me as an equal member of their family.

Abbreviations

ALS	Amyotrophic lateral sclerosis
AnkB	Ankyrin-2
AnkG	Ankyrin-3
ATG	Autophagy-related genes
ATG6\BECN1	Beclin 1
ATG8-family proteins	the MAP1LC3 (microtubule associated protein 1 light chain 3) and GABARAP (GABA type A receptor-associated protein)
ATG17\FIP200	Focal adhesion kinase family interaction protein of 200kDa
CALCOCO1	Calcium-binding and coiled-coil domain-containing protein 1
CALCOCO2\NDP52	Calcium-binding and coiled-coil domain-containing protein 2 \Nuclear Dot protein 52
CMA	Chaperone-mediated autophagy
ER	Endoplasmatic reticulum
ESCRT	Endosomal sorting complexes required for transport
FIR	FIP200 interaction site
FTLD	Frontotemporal lobar degeneration
FYCO1	FYVE and coiled-coil domain containing 1
GABARAP	Gamma-aminobutyric acid receptor associated protein
GABARAPL1	Gamma-aminobutyric acid receptor associated protein-like 1
GABARAPL2	Gamma-aminobutyric acid receptor associated protein-like 2
HP	Hydrophobic pocket

HSC70	Heat shock-cognate chaperone of 70kDa
IM	Isolation membrane
KEAP1	Kelch-like ECH-associated protein 1
KIR	KEAP1 interaction site
LAMP	Lysosomal membrane protein
LC3	Microtubule-associated protein 1 light chain 3
LDS	LIR docking site
LIR	LC3 interacting region
LLPS	Liquid-liquid phase separation
MG132	Proteasomal inhibitor
MVB	Multivesicular body
mPAS	Mammalian phagophore assembly site
mTOR	Mechanistic target of rapamycin
NBR1	Neighbor of BRCA1 gene 1
NCOA4	Nuclear receptor coactivator 4
OPTN	Optinurin
PAS	Phagophore assembly site
PB1	Phox and Bem 1
PE	Phosphatidylethanolamine
PI3K	Phosphatidylinositol 3 kinase
PI3P	Phosphatidylinositol 3-phosphate

PML	Promyelocytic leukemia
RBP	RNA-binding protein
SAR	Sequestosome -like autophagy receptor
SKICH	Skip carboxyl homology
SLR	Sequestosome1 -like receptor
SNARE	Soluble NSF attachment proteins-Receptor
SQSTM1	Sequestosome 1
TAX1BP1	Tax human T-cell leukemia virus type I binding protein I
TFG	Tumor necrosis factor receptor
TP53INP2	Tumor protein 53-induced nuclear protein 2
TRIM	Tripartite motif containing protein
UBA	Ubiquitin-associated domain
UBL	Ubiquitin -like
ULK	Unc-51-like kinase
VAC	Vacuolar membrane protein (yeast)
VMP1	Vacuole membrane protein 1
WIPI	WD- repeat protein interacting with phosphoinositides
ZZ	ZZ-type zinc finger domain

List of Papers

Paper I

Structural basis of p62/SQSTM1 helical filaments and their role in cellular cargo uptake

Arjen J. Jakobi, Stefan T. Huber, Simon A. Mortensen, Sebastian W. Schultz, Anthimi Palara, Tanja Kuhm, Birendra Kumar Shrestha, Trond Lamark, Wim J. H. Hagen, Matthias Wilmanns, Terje Johansen, Andreas Brech & Carsten Sachse

Nature Communications volume 11, Article number : 440 (2020)

Paper II

Replacement of the LIR of p62 with LIRs from FYCO1 or ULK1 blocks starvation-induced autophagic degradation of p62

Anthimi Palara, Mireia Nager, Hallvard Lauritz Olsvik, Aud Karin Øvervatn, Gry Evjen, Kenneth Bowitz Larsen, Trond Lamark and Terje Johansen

Paper III

The C-terminal Lys435 residue is required for efficient degradation of p62/SQSTM1 by autophagy.

Anthimi Palara, Hallvard Lauritz Olsvik, Mireia Nager, Aud Karin Øvervatn, Gry Evjen, Kenneth Bowitz Larsen, Trond Lamark and Terje Johansen

Papers that have been published during my PhD, that are not part of the thesis.

Regulation of Expression of Autophagy Genes by ATG8a-Interacting Partners Sequoia, YL-1, and Sir2 in Drosophila

Anne-Claire Jacomin, Stavroula Petridi, Marisa Di Monaco, Zambarlal Bhujabal, Ashish Jain, Nitha C. Mulakkal, Anthimi Palara, Emma L. Powell, Bonita Chung, Cleidiane Zampronio, Alexandra Jones, Alexander Cameron, Terje Johansen, Ioannis P. Nezis. Cell Reports, Volume 31, Issue 8, 26 May 2020, 107695

SAMM50 acts with p62 in piecemeal basal- and OXPHOS-induced mitophagy of SAM and MICOS components

Yakubu Princely Abudu, Birendra Kumar Shrestha, Wenxin Zhang, Anthimi Palara, Hanne Britt Brenne, Kenneth Bowitz Larsen, Deanna Lynn Wolfson, Gianina Dumitriu, Cristina Ionica Øie, Balpreet Singh Ahluwalia, Gahl Levy, Christian Behrends, Sharon A. Tooze, Stephane Mouilleron, Trond Lamark, Terje Johansen. J Cell Biol (2021) 220 (8): e20200909

1. Introduction

1.1 Introduction to autophagy

Autophagy (Greek: self-eating) is a term coined by Christian de Duve for processes involving the lysosomal degradation of cytoplasmic components (Klionsky, 2008). Autophagy can be classified into three main pathways: Macroautophagy, microautophagy and chaperone-mediated autophagy (CMA) (Figure 1) of which macroautophagy is the most studied from yeast to man (Ohsumi, 2014).

CMA is a selective lysosomal degradation of single, unfolded, soluble cytosolic proteins that contain a redundant five amino acid motif (KFERQ-like) that is recognized by Hsc70/HSPA8. The HSPA8 complex helps to dock the unfolded protein to the LAMP2A transmembrane receptor for uptake into the lumen of the lysosome (Dice, 1982) (Kaushik and Cuervo, 2016; Kaushik and Cuervo, 2018; Park et al., 2015; Quintavalle et al., 2014) (Figure 1). Some of the main features of this pathway were discovered by the late Fred Dice and further elucidated mechanistically by the group of Ana Maria Cuervo. Similar to proteasomal degradation but distinct from macro- and microautophagy, CMA can only degrade one polypeptide at a time and does not involve membrane dynamics.

Microautophagy is based on the direct engulfment of cytoplasmic substrates by lysosomes or late endosomes (Schuck, 2020). The process has been most studied in yeast and is here in one form mediated by ATP-dependent invaginations of the limiting membrane called autophagic tubes which form constrictions at their neck where scission occurs releasing vesicles into the lumen (Li et al., 2012) (Figure 1). Studies during the last decade have identified many different microautophagy processes both in animals and in plants (Nakamura et al., 2018). The term “microautophagy” is somewhat misleading since rather large structures (micrometer-size) can be targeted such as parts of the nucleus, parts of the ER, lipid droplets and peroxisomes (Schuck, 2020). Because of the diversity in mechanisms, several ways to classify microautophagy have been suggested. One classification involves three types where one is dependent on lysosome membrane protrusions enwrapping parts of the cytoplasm, a second form is mediated via invagination of the lysosomal membrane, and a third by invagination of the endosomal membrane. The latter two are dependent on ESCRT (endosomal sorting complex required for transport) proteins (Oku and Sakai, 2018). The most recent type of classification is from Schuck who distinguishes fission-type and fusion-type microautophagy (Schuck, 2020). Fusion-type

needs ESCRT proteins to seal the invaginating membranes while the fusion type requires the core (macro) autophagy machinery to form a flat double membrane structure (a phagophore as seen in macroautophagy, see later) that helps seal the membrane invaginations.

Interestingly, work by the Cuervo group suggests that a form of endosomal microautophagy may use Hsc70/HSPA8-mediated recognition of proteins with KFERQ-like motifs both to recognize cargo and to bend the limiting membrane to start invaginations and the ESCRT proteins, not core autophagy components, to seal the membrane (Sahu et al., 2011; Tekirdag and Cuervo, 2018). Our group has shown that amino acid starvation triggers the rapid degradation of selective autophagy receptors including SQSTM1/p62, NBR1, TAX1BP1 and NCOA4 by a form of endosomal microautophagy that does not involve Hsc70, only ESCRT III and VPS4, not the other ESCRT complexes. Some of the substrates also need ATG5, ATG7 and lipidated LC3, but not all (Mejlvang et al., 2018).

In macroautophagy (hereafter referred to as autophagy), cytoplasmic components to be degraded are isolated from the rest of the cell within a double-membraned structure known as an autophagosome (Xie and Klionsky, 2007). Autophagosomes can either fuse with a lysosome to create an autolysosome (Figure 1) or with a late endosome to give an amphisome (Sanchez-Wandelmer and Reggiori, 2013) (Seglen et al., 1991). Autophagy can be selective and non-selective (Johansen and Lamark, 2011). Non-selective bulk autophagy is studied most in yeast and is induced during nutrient starvation to provide the cell with nutrients. In basal conditions, there is a need for damaged proteins and organelles to be degraded as important quality control of the cell. This kind of autophagy is cargo-induced selective autophagy (Kirkin and Rogov, 2019; Lamark and Johansen, 2021). Selective autophagy can degrade a variety of cytoplasmic components including dysfunctional and aggregated proteins, lipid droplets, damaged or surplus organelles like mitochondria, ER, peroxisomes, and intracellular pathogens (Lamark and Johansen, 2021; Rogov et al., 2014). Under various stress conditions, both bulk- and selective autophagy pathways may be activated. In the cargo-induced selective autophagy, the cargo to be degraded is often tagged with ubiquitin which is recognized by selective autophagic receptors (SARs) needed for the process (Bjørkøy et al., 2005; Gatica et al., 2018; Grumati and Dikic, 2018; Johansen and Lamark, 2011; Johansen and Lamark, 2020; Thurston et al., 2009). Defects in the autophagic machinery can cause a variety of disease from neurodegenerative diseases, cardiovascular diseases, inflammatory diseases to cancer (Levine and Kroemer, 2019; Mizushima et al., 2008). Recently, deleterious genetic variants of the human core autophagy

gene ATG7 were shown to result in inherited neurodevelopmental disorders in five families analysed (Collier et al., 2021). Studies in worms, flies and mice have clearly shown the importance of autophagy during development, particularly so in stem cell function (Allen and Baehrecke, 2020; Mizushima and Levine, 2010)

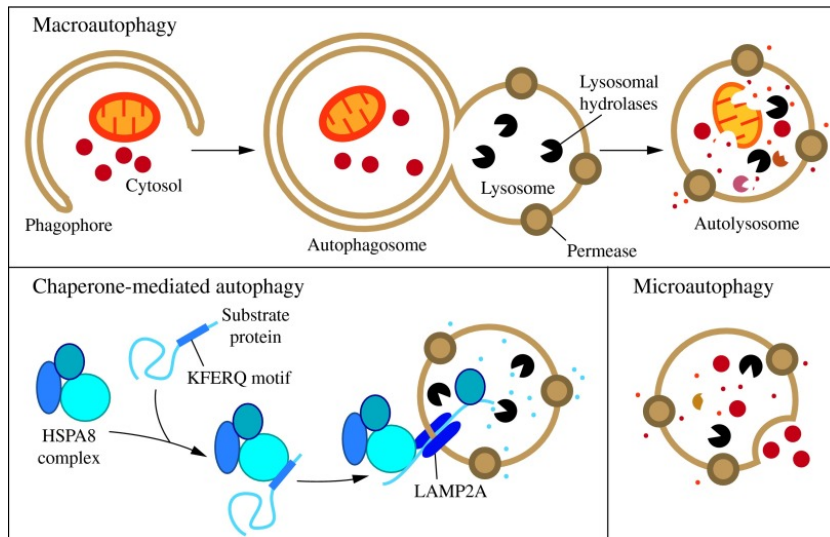


Figure 1. The different types of autophagy in mammalian cells. Macroautophagy is associated with the formation of cytosolic double membraned vesicles called autophagosomes. CMA transports unfolded proteins that carry the KFERQ-like motif recognized by HSPA8/Hsc70 to the LAMP2A receptor which carries the cargo across the lysosomal membrane into the lumen of the lysosome. Microautophagy is associated with the direct uptake of cargo by invagination of the lysosomal membrane. All three pathways lead to the degradation of the cargo by the lysosomes for the cell to reuse the released building blocks (Parzych and Klionsky, 2014).

Autophagy has an essential role in counteracting organismal ageing. Studies in different organisms reported that there is the correlation between ageing and autophagic activity. Compromised autophagy is a hallmark of ageing (Aman et al., 2021). As an organism gets older the autophagic response either in normal conditions or under stress is reduced in parallel with increased risk of cancer and neurodegenerative diseases. On the other hand, studies in worms, flies and mice have shown that increased expression levels of core autophagy proteins like Atg8 and treatment with autophagy inducing agents, like rapamycin, increases lifespan and health span (reviewed in (Aman et al., 2021)). It has also been shown that SQSTM1/p62 improves lifespan and proteostasis both in *C. elegans* and *Drosophila* (Aparicio et al., 2020).

1.2 Autophagosome formation and degradation

Autophagosome formation starts with the formation of a double membrane structure called the isolation membrane, also known as a phagophore. In yeast, the phagophore develops at a single phagophore assembly site (PAS) (Hollenstein and Kraft, 2020) (Figure 2). In mammalian cells, autophagosomes form at multiple sites and the origin of the phagophore has been an important question since the first morphological description of autophagosomes in the early 1960s. There are two suggested models for the origin membrane for autophagosome formation. Based on the first model, the autophagosomal membrane originates from a pre-existing organelle, while based on the second model there is a de novo formation of the isolation membrane by localized lipid synthesis (Simonsen and Tooze, 2009). Various organelles, such as the ER, the Golgi complex, recycling endosomes, and the plasma membrane, have been suggested as phagophore sources (Li et al., 2021; Puri et al., 2018; Tooze and Yoshimori, 2010; Wei et al., 2018). The phagophore membrane expands until the point that it can engulf the target cargo. When the phagophore closes upon itself, the target cargo is isolated inside a double membrane structure called the autophagosome (Glick et al., 2010; Mizushima et al., 2011; Ohsumi, 2014). The autophagosome together with the cargo will mature and undergo fusion with the lysosome(s). A fused autophagosome with a lysosome is called an autolysosome. In the autolysosome, the degradation of autophagosomal contents by lysosomal acid proteases occurs. Lysosomal proteases degrade the contents and transporters export the amino acids or other breakdown-products of degradation back out to the cytoplasm, so the cell can re-use them for other metabolic processes metabolism (Glick et al., 2010; Mizushima et al., 2011).

An evolutionarily conserved set of Atg (autophagy-related) proteins are involved in the different stages of autophagosome formation. The first set of 15 such Atg proteins were initially defined mutagenesis screens in yeast (Tsukada and Ohsumi, 1993), but orthologues have later been described in mammalian cells (Ohsumi, 2014)

1.3 Induction of autophagy

Autophagosome formation can be induced by different cellular stressors such as starvation, organelle damage, or protein aggregation. starvation-induced autophagy serves a survival purpose in case of lack of nutrients. The mechanism is different from cargo-induced selective autophagy and the aim is to recycle macromolecules and energy to the cell. In cargo-selective

degradation, the SARs are essential players, and this process can occur both under basal and stress-induced conditions.

The pathway that is described in the following is the autophagic mechanism is the one most studied due to the pioneering studies in yeast of Ohsumi and colleagues who also moved their studies into mammalian cells. Starvation-induced autophagy in yeast and mammals is the best understood canonical autophagic response (Galluzzi and Green, 2019). Under starvation, the levels of AMP in the cell are increased, which drives the activation of AMPK. Activation of AMPK causes inhibition of the target of rapamycin (TOR) signalling complex. TOR (mTOR in mammals) is working as a hub between different signal stimuli. Growth factors, cytokines and accumulation of nutrient levels can act as a stimulus for mTOR activation (Dunlop and Tee, 2014). In mammals, the result of AMPK-mediated phosphorylation of mTOR is the activation of multiple proteins that are involved in initiation complex like ULK1, ATG13, FIP200 and the class III PI3K complex 1 (Xie et al., 2015) A current model suggests that in multicellular organisms, like mammals, the ULK complex undergoes a liquid-liquid phase transition (LLPS) triggered by dephosphorylation of ATG13. The ULK complex droplet docks onto the ER and initiates the formation of multiple mammalian phagosomes assembly sites (mPAS) (Noda et al., 2020) (Figure 2). The detailed mechanism remains to be revealed.

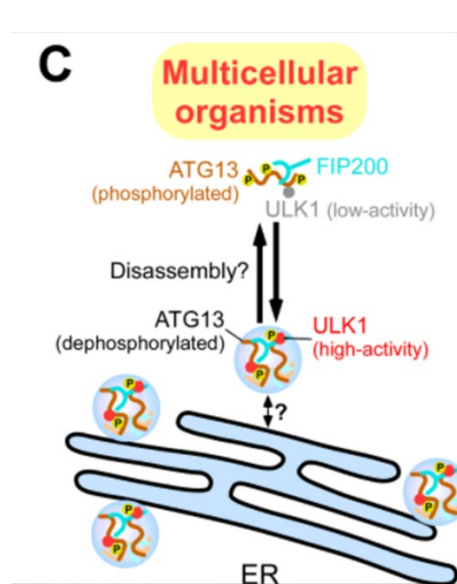


Figure 2 Creation of PAS (phagophore assembly sites) in mammalian cells. The ULK complex with ATG13, FIP200 and ULK1 undergo liquid-liquid phase transition (LLPS) following dephosphorylation of ATG13. The complex moves as a droplet to ER and induces the formation of multiple PAS. Adopted from Noda et al. (Noda et al., 2020).

1.4 The core autophagy molecular machinery needed for autophagosome formation

1.4.1 ULK complex

The yeast Atg1 kinase has an essential role in the induction of autophagy. It works downstream of the target of rapamycin (TOR) complex 1 (TORC1). A family of mammalian Atg1 proteins have been identified; ULK1, ULK 2, ULK3 (Young et al., 2009; Zachari and Ganley, 2017) and ULK4 (Eyers, 2020). In mammalian cells, ULK1 or ULK2 forms part of a complex that includes ATG13, ATG101 and the scaffold protein FIP200/RB1CC1. ATG101 was found to interact with ULK1 in an ATG13-dependent manner and is essential for autophagy (Mercer et al., 2009). The ULK complex is critical for the initiation of phagophore formation. ATG13 interacts with ULK1, ULK2, and FIP200 independent of its phosphorylation state (Hosokawa et al., 2009), and FIP200 binds to ULK1 and ULK2 (Hara et al., 2008). Under starvation, mTORC1 is quickly detached from the ULK1 complex (Hosokawa et al., 2009). Several phosphorylation chain-events follows within this complex, including activating phosphorylations of ATG13 and FIP200 by ULK1 and ULK2 and inactivating phosphorylations of ULK1 and ULK2 by mTORC1 (Hosokawa et al., 2009; Jung et al., 2009). Under starvation conditions, phosphorylation and inactivation of mTORC1 lead to dephosphorylation of ULK1, ULK2, and ATG13. This activates ULK1 and ULK2 to phosphorylate ATG13 and FIP200 (Jung et al., 2009).

1.4.2 PI3K Class III complex 1 (PI3KC3-C1)

The initiation of phagophore formation requires the recruitment of phosphatidylinositol-3 phosphate kinase (PI3K) class III complex 1 (PI3KC3-C1) consisting of the PI3K enzyme VPS34 and scaffold proteins VPS15, Beclin 1 AND ATG14L (Bento et al., 2016; Galluzzi et al., 2017). A fifth member called NRBF2 (Atg38 in yeast) helps form the complex and induce dimerization of PI3KC3-C1 (Nishimura and Tooze, 2020). PI3KC3-C1 associates with the ER membrane and activated ULK1 increases the kinase activity of VPS34 via phosphorylation of VPS34, Beclin1 and ATG14 (Dikic and Elazar, 2018; Russell et al., 2013). AMPK can also directly phosphorylate VPS34 and Beclin 1. PI3KC3-C1 phosphorylates phosphatidylinositol (PI) to produce phosphatidylinositol-3-phosphate (PI3P) which then is bound by WD repeat domain phosphoinositide- interacting proteins (WIPIs 1-4) and the zinc-finger FYVE domain-containing protein 1 (DFCP1). DFCP1 serves as a marker for omegasomes which are PI3P-rich ER membrane areas acting as PAS where autophagosomes are born (Dikic and Elazar, 2018).

In mammals, PI3KC3-C1 is involved in autophagy whereas the second complex PI3KC3-C2 is involved in endocytosis and does not contain ATG4L, but UVRAG (Dikic and Elazar, 2018).

1.4.3 Transmembrane proteins in mammalian autophagy

ATG9A and the vacuole membrane protein 1 (VMP1) and its interacting partner in the ER membrane, TMEM41B, are three multispanning transmembrane proteins that are required for mammalian autophagy (Morita et al., 2018; Nishimura and Tooze, 2020). The ATG9A polypeptide chain crosses the membrane six times with both the N- and C- terminal end located in the cytosol. ATG9A forms a trimeric complex and acts as a lipid scramblase transferring lipids between the outer and inner membrane leaflets to allow expansion of the autophagosomal membrane (Matoba et al., 2020). ATG9A is found in the trans-Golgi network and on late endosomes, but under starvation small 50-60 nm diameter, single membrane ATG9A vesicles are transported to the mPAS where the phagophore expands on the ER and omegasomes form. The mechanism behind the transportation of ATG9A vesicles to mPAS is still unclear (Noda, 2021). In mammals, the recruitment of ATG2 proteins is an essential step for the expansion of the phagophore membrane and the closure of it. ATG2A and ATG2B proteins can bind to the WIPI1 and WIPI4 proteins which are recruited to the PI3P-rich regions where omegasomes develop (Noda, 2021). On the expanding site of the phagophore membrane, ATG9 colocalizes with the ER-localized ATG2. This interaction allows ATG2 to channel phospholipids synthesized in the cytoplasmic leaflet of the ER membrane to the phagophore membrane where ATG9 ensures the localization of the lipids to the inner leaflet (Noda, 2021). ATG2 is also acting as a tether keeping the ER and phagophore membrane together. Hence, ATG2 and ATG9 drive phagophore membrane expansion (Maeda et al., 2019; Nishimura and Tooze, 2020; Noda, 2021; Otomo et al., 2018). At the mPAS WIPI2B recruits ATG16L1 placing the ATG5-ATG12:ATG16L1 E3 ligase complex in position for mediating lipid conjugation of ATG8 proteins (Nishimura and Tooze, 2020).

1.4.4 Conjugation systems

Studies both in yeast and mammals have identified two ubiquitin-like proteins, Atg12/ATG12 and Atg8/ATG8. ATG12 becomes covalently attached to ATG5 dependent on two proteins that function as E1 and E2-like enzymes, ATG7 and ATG10 respectively (Mizushima et al., 2011; Yang and Klionsky, 2010). The ATG12-ATG5 complex interacts with ATG16L, which

oligomerizes to form a larger complex acting as an E3 ligase for the conjugation of ATG8s to phosphatidylethanolamine (PE) enabling firm attachment in the phagophore membrane. Before this conjugation reaction mammalian ATG4A-D family proteases (yeast Atg4) cleave the ATG8s at their C-terminal exposing a Gly residue where the lipid is attached. The cleaved form is called form I, i.e., LC3-I, while the conjugated form is called form II, i.e., LC3-II. The conjugation reaction requires ATG7 and ATG3 proteins as well as the mentioned ATG5-ATG12:ATG16L E3 ligase (Mizushima et al., 2011). The lipidated II forms of ATG8s (i.e., LC3B-II) is located on both faces of the phagophore membrane. Before or during fusion of the autophagosome with the lysosome(s) ATG4 proteases cleave ATG8s off the limiting outer membrane releasing form I ATG8s that can be lipidated and reused (Parzych and Klionsky, 2014). The roles of the four different mammalian ATG4 proteases are not completely clarified. There is evidence that ATG4B is the dominant enzyme in the cleavage of full-length precursor ATG8s to form I while ATG4D has been suggested to be most important for the delipidation reaction (Tamargo-Gómez et al., 2021).

1.5 ATG8 family proteins and their roles in autophagy

Yeast and other fungal species have only a single Atg8 gene while animals, plants and some protists have several (Shpilka et al., 2011). The mammalian ATG8 protein family contains six members distributed into two subfamilies. These are the GABARAPs which includes GABARAP, GABARAPL1 and GABARAPL2 and the LC3s including LC3A, LC3B and LC3C (Shpilka et al., 2011). Studies in HeLa cells where all six ATG8 genes were knocked out showed that lipidated ATG8s are not absolutely required for autophagosome formation but is required for the fusion of the autophagosomes with lysosomes (Nguyen et al., 2016). However, loss of ATG8s hampered the process profoundly as smaller autophagosomes were formed and the rate of their formation was delayed. These observations are also supported from data coming from studies in *C. elegans* which has only two ATG8 homologs. Loss of the LC3 homolog LGG-2 is associated with formation of smaller autophagosomes, while the GABARAB homolog LGG-1 is essential for autophagosome formation and maturation (Wu et al., 2015). ATG8 proteins belong to a group of proteins that share a ubiquitin-like structure or UBL. They follow the same UBL fold (Figure 3). Although, in comparison with ubiquitin, ATG8 proteins' structure have two extra N-terminal α -helices (Johansen and Lamark, 2020).

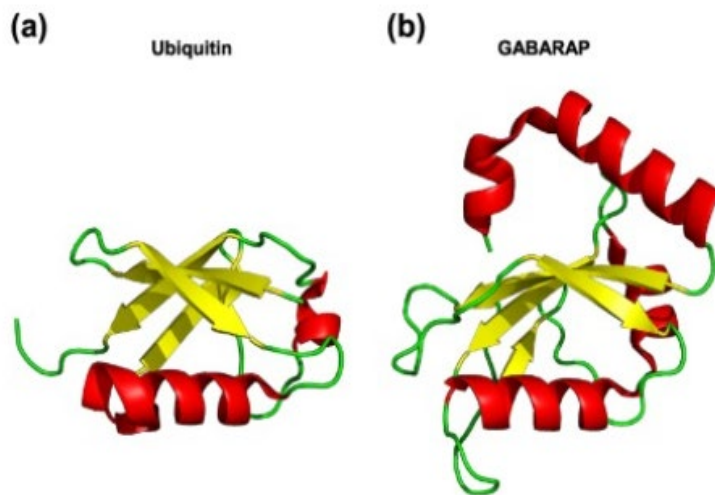


Figure 3 Structural similarities between ubiquitin and GABARAP proteins. Red denotes α -helices, yellow β -sheets and green loops. Adopted from (Johansen and Lamark, 2020).

The degradation of a selected cargo requires the specific interaction between cargo-binding selective autophagy receptors (SARs), such as p62, NBR1 and TAX1BP1, and ATG8 proteins lipidated to the inner membrane of the phagophore. As described below, the interaction with ATG8 proteins is mediated by a LIR motif in the SAR, and this motif is found in all characterized SARs. The ATG8 proteins are this way working as a bridge between the cargo and the inner membrane (Fracchiolla et al., 2017; Johansen and Lamark, 2011). Lipidated ATG8 proteins work as a hook for all LIR-containing proteins located on both sides of the growing phagophore (Birgisdottir Å et al., 2013; Johansen and Lamark, 2020). Particularly GABARAP family members act as platforms on the outer side of the phagophore membrane for LIR-containing proteins that are involved in the initiation complex (ULK1, WIPI-2, ATG13, FIP200)(Alemu et al., 2012), and the PI3KC3 complex 1 (VPS34, Beclin1, ATG14L) (Birgisdottir Å et al., 2019; Johansen and Lamark, 2020; Xie et al., 2015). On the other side, proteins that work as SARs are located at the inner membrane. The role of ATG8 proteins is also extended to tasks related to the closure of phagophore, fusion with lysosomes and transport of autophagosomes (Johansen and Lamark, 2020; Kriegenburg et al., 2018).

In the last years, the number of proteins that can interact with ATG8s has been increased (Marshall et al., 2019). A lot of those are LIR-containing proteins involved in the autophagic

machinery. For example, GAPARAP binds to ULK1 and activates it via a LIR motif (Bento et al., 2016; Johansen and Lamark, 2020). This step is important for the induction of the autophagic machinery. Moreover, FYCO1 interacts with LC3 via a LIR motif. FYCO1 mediates the kinesin-dependent movement from autophagosomes and late endosomes (Johansen and Lamark, 2020; Pankiv et al., 2010). Furthermore, p62/SQSTM1, the first discovered autophagic receptor, binds via LIR to LC3B and delivers the cargo for degradation. Historically, the LIR motif was mapped on p62 (Johansen and Lamark, 2020; Pankiv et al., 2007). The amino acid sequence of the LIR-containing proteins that allows the interaction with ATG8s is quite short, but it constitutes an evolutionary well-conserved motif. Based on more than 100 LIR motifs the core motif is W\F\Y-X-X-L\I\V (Johansen and Lamark, 2020; Marshall et al., 2019) (Figure 4). The aromatic residue (W/F/Y) and hydrophobic residue (L/I/V) interact with the two hydrophobic pockets (HP1 and HP2) in the LIR docking site (LDS) of ATG8s, respectively (Ichimura et al., 2008; Johansen et al., 2017; Noda et al., 2008). This form of LIR is called canonical LIR.

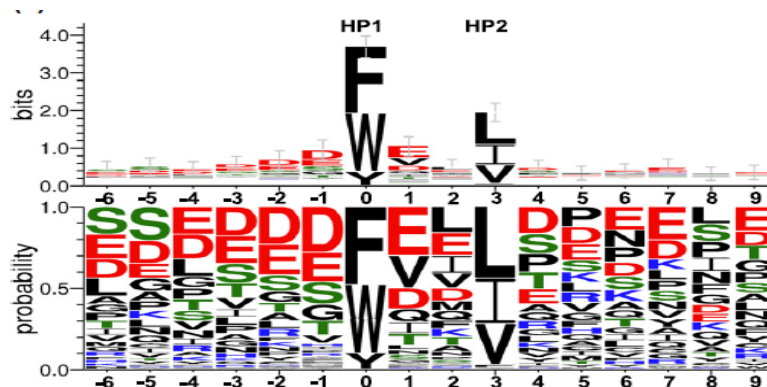


Figure 4 Sequence logos based on 100 different LIR motifs (Johansen and Lamark, 2020). From the 100 that were screened 48 LIRs had F in the first position, 42 had W, and 10 had a Y.

Further structure studies showed that there are more LIR-containing proteins, where their LIR motif does not follow the canonical LIR motif pattern. Some do not even have an aromatic or an aliphatic residue or their LIR binding region is extended. The first protein that was reported to have an atypical/non-canonical LIR was NDP52 (von Muhlinen et al., 2012). Later more proteins have been discovered (Figure 5). Another example of a different type of LIR is found in the giant Ankyrins, AnkB and AnkG. These neuronal proteins form an extremely strong bond

with ATG8s. The bond is based on canonical LIR interaction and an extension of it (Li et al., 2018). The strength of LIR binding interaction between Ankyrins, FAM134B and FYCO1, seems to be organized in two parts, the LIR core and the C-helix extension (Li et al., 2018).



Figure 5 Amino acid sequence of extended non-canonical LIRs. These LIRs containing the LIR core as it has been described above and they are followed by an amphipathic C-helix (Li et al., 2018).

In these canonical-extended LIRs, the presence of the C-helix is needed for the strong binding to ATG8 proteins. Analysis of AnkB, AnkG, FAM134B and FYCO1 LIR motif patterns lead to uncovering a generally extended LIR motif, D/E₂₋₃X₀₋₂ΦXXΨXXXEΨρρΨρρρΨ, where Φ, Ψ, ρ and X stand for aromatic, aliphatic, polar and any residues respectively (Li et al., 2018) (Figure 5).

1.6 SAR-induced autophagosome formation

The evolutionary adaptation of the autophagosome to tackle specific cargos in selective autophagy is an evolutionary survival adaptation that allows the cells both in basal and under stress conditions to selectively degrade targeted cargo. This mechanism can be found from yeast to humans. To target the correct cargo, this process requires the presence of specific scaffold proteins which are called selective autophagy receptors (SARs) (Johansen and Lamark, 2011; Kirkin and Rogov, 2019). The SARs, have the ability to bind both the cargo and lipidated ATG8 proteins (Johansen and Lamark, 2020). The binding to ATG8s occurs through LIR motif (Pankiv et al., 2007). For one protein to be classified as a SAR, it has first to fulfil some basic criteria (Lamark et al., 2017):

- It should contain at least one LIR motif in its sequence, so it can bind to the lipidated form of ATG8
- It should be able to identify the selected cargo and bind directly to it.

- It should be degraded together with the cargo through autophagy.

Other soluble SARs are NBR1, NDP52 (also known as CALCOCO2), Optineurin (OPTN), TAX1BP1, TRIM5 α , NCOA4, STBD1 and NUFIP1 (Dowdle et al., 2014; Jiang et al., 2010; Johansen and Lamark, 2020; Kimura et al., 2015; Kirkin et al., 2009b; Mandell et al., 2014; Newman et al., 2012; Thurston et al., 2009; Wyant et al., 2018). Recently, CALCOCO1 that is evolutionary related to TAX1BP1 and NDP52 (CALCOCO2), was identified by our group as a soluble SAR that mediates both ER-phagy and Golgiphagy (Nthiga et al., 2020; Nthiga et al., 2021)

Common among most of the different soluble SARs is the ability to polymerize or oligomerize together with the ability to identify and bind ubiquitylated cargos. There are also membrane-bound SARs that are involved in mitophagy, ERphagy and pexophagy (Kirkin and Rogov, 2019; Lamark and Johansen, 2021). Most of these act in a ubiquitin-independent manner.

A protein that works as SAR will deliver the cargo to the inner membrane of the phagophore allowing the cargo to be located inside the forming autophagosome (Lamark and Johansen, 2021; Mijaljica et al., 2012).

1.7 The role of p62/SQSTM1-like receptors (SLRs) in autophagy

The most studied SLRs, apart from p62/SQSTM1, are NBR1, TAX1BP1, CALCOCO2\NDP52 and OPTN (Mandell et al., 2014) (Figure 6). The name of this group containing the main autophagic receptors (p62, NBR1, NDP52, TAX1BP1 and OPTN) was given by Vojo Deretic (Deretic, 2012). The main role of SLRs in autophagy is to recognize ubiquitinated cargo and recruit the autophagic machinery for cargo degradation.

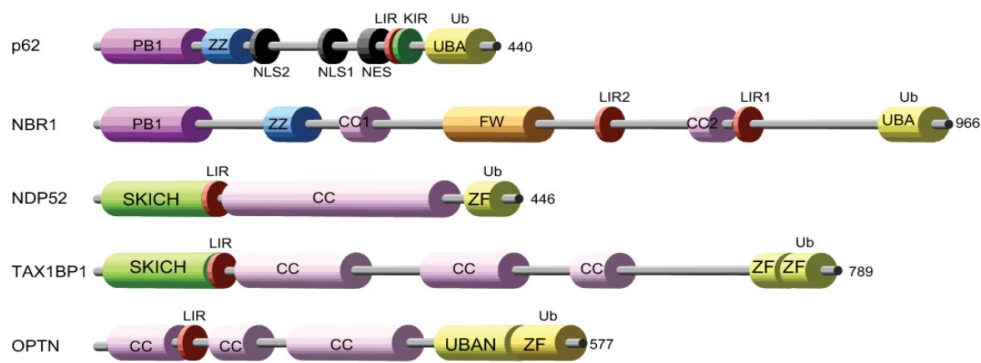


Figure 6 Domain architecture of SLRs. The most well-known and studied SLRs are p62, NBR1, NDP52, TAX1BP and OPTN (optineurin) in mammals. Functional LIR (LC3 interaction region) motifs, oligomerization domains PB1 (phox\Bem1p) and/or ZZ (ZZ-type zinc finger) and ubiquitin-binding domains UBA (Ubiquitin-associated) or ZF (zinc finger) are found in all of them (Birgisdottir Á et al., 2013). NDP52 and TAX1BP1 harbour a skeletal muscle and kidney-enriched inositol phosphatase (SKIP) carboxyl homology domain (SKICH). The linker sequence at the end of the SKICH domain contains a LIR responsible for interaction with the ATG8 family. NBR1 in addition has a domain that contains four tryptophans, FW, which allows NBR1 to interact with MAP1B (Marchbank et al., 2012)

Not all the SLRs work together at the same time or under the same conditions, but how they collaborate in selective autophagy is only partially understood. For example, NBR1 is not dependent on p62 for its degradation and vice versa. Stress stimuli, though, can drive NBR1 to interact with p62 and be a part of the p62 bodies via PB1 domain interactions. These proteins are then degraded together (Kirkin et al., 2009a). NBR1 and p62 have a similar overall domain architecture with an N-terminal PB1 domain followed by a ZZ-type zinc finger domain, a LIR domain and a C-terminal UBA domain (Figure 6). The most well-known autophagy receptor is p62\SQSTM1 (Bjørkøy et al., 2005; Pankiv et al., 2007). p62 is a 440 amino acid long protein, which can act both as a scaffold protein in signalling pathways and as a selective autophagy receptor. NBR1 is conserved both in plants and in animals, while SQSTM1 is found only in animals (Svenning et al., 2011). Both NDP52 and TAX1BP1 contain a SKICH domain and a LIR motif in their N-terminal part, followed by a coiled-coil domain and a zinc finger domain that allows interaction with ubiquitin (Johansen and Lamark, 2020; Tumbarello et al., 2015; Yang et al., 2014) (Figure 6). These two proteins are related by evolution (Yang et al., 2014). OPTN consists of several domains: a LIR motif, multiple coiled-coil motifs, and a ubiquitin-binding domain at the C-terminal, which is a Zinc finger same as NDP52 and TAX1BP1 (Ali et al., 2019) (Figure 6). OPTN interacts with itself to form homo-oligomers (Gao et al., 2014).

These three SLRs are mostly involved in mitophagy and xenophagy processes (Johansen and Lamark, 2020; Thurston et al., 2009; Wild et al., 2011).

1.7.1 PB1 domain of p62 (amino acid residues 3-102)

In general, there are 3 different types of PB1 domains. Type A is acidic and contains OPCA motif (Jakobi et al., 2020; Lamark et al., 2003). Type B is basic, and the third type is a mix of both types called type AB (Jakobi et al., 2020). Plant Nbr1, p62 and TGF PB1 domains are all type AB (Jakobi et al., 2020), while the PB1 in human NBR1 is of type A.

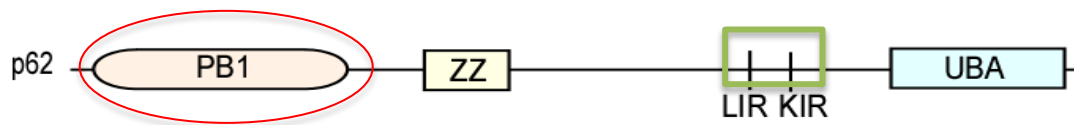


Figure 7 Main structural p62 domains. The N-terminal PB1 domain is responsible for homo- and heterodimerization of p62, followed by a ZZ-type zinc finger domain. The C-terminal UBA domain binds to ubiquitin and is reported to be able to dimerize. The LIR and KIR motifs lie close to each other in a conserved region. The red circle indicates the domain that the text focuses on.

The PB1 domain allows p62 to self-interact and to form polymeric filamentous assemblies (Jakobi et al., 2020; Lamark et al., 2003) (Figure 7). There are residues in the PB1 domain that play an essential role in this process because they play an important role in electrostatic interactions between the PB1 domain and the OPCA motif in another PB1 domain (Lamark et al., 2003). Single mutations of K7, R21 and D69 results in reduced ability or inability of p62 to self-interact (Lamark et al., 2003). The R21A mutant renders p62 monomeric (Jakobi et al., 2020). The K7A mutation also prevents the binding of NBR1 to p62 (Lamark et al., 2003), since the PB1 domain also is responsible for the heterodimerization of p62 together with NBR1 (Lamark et al., 2017). The role of their interaction is still not fully understood. Homologs of NBR1 are found through the whole eukaryotic kingdom while p62 appeared in early metazoans (Svenning et al., 2011).

In mammalian cells, several proteins have PB1 domains with different functions and electrostatic potentials (Figure 8).

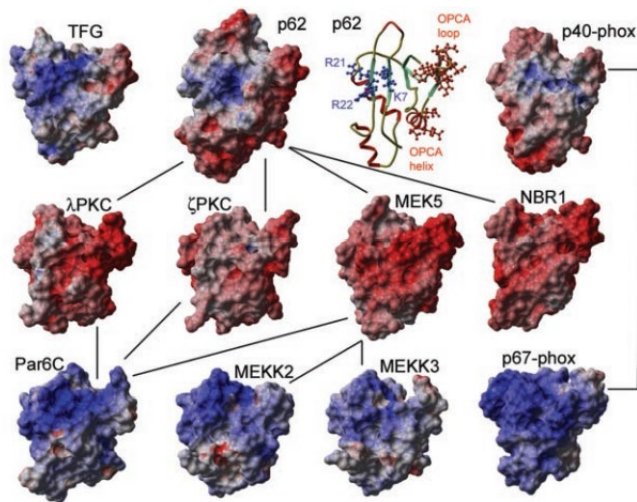


Figure 8 **Electrostatic surface potentials of the mammals PB1 domains** (Lamark et al., 2003). Molecular surfaces and electrostatic potentials were calculated for 11 different proteins. TFG and p62 are quite similar in their electrostatic potentials. Blue are the proteins with the higher electrostatic potential $e > 5$ kcal/electron units and red is with the lowest $e < -5$ kcal/electron units. The calculation method was REBEL.

1.7.2 ZZ-type domain of p62 (amino acid residues 122-167)

The ZZ-type zinc finger domain is a type of protein domain that was named because of its ability to bind two zinc ions (Ponting et al., 1996). These domains contain 4-6 Cys residues that participate in zinc binding (plus additional Ser/His residues), including a Cys-X2-Cys motif found in other zinc finger domains. These zinc fingers are thought to be involved in protein-protein interactions. The structure of the ZZ domain shows that it belongs to the family of cross-brace zinc finger motifs that include the PHD, RING, and FYVE domains (Legge et al., 2004).

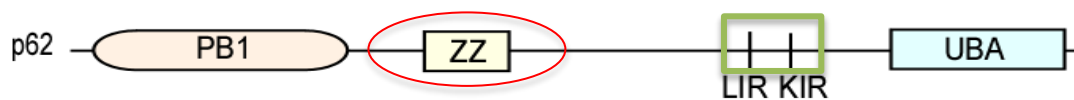


Figure 9 **Main structural p62 domains**. Cartoon of the 4 main domains on the p62 sequence. The red circle indicated where the focus is.

The autophagic function of p62 is strictly dependent on the PB1 domain, the LIR motif and the UBA domain. Interestingly, recent studies showed that the formation and degradation of p62 bodies may be induced by the binding of the ZZ domain with an N-terminal degradation signal, which is called N-degron (Varshavsky, 2011; Zhang et al., 2018). The ZZ-type zinc-finger of p62 is capable of recognizing the N-terminal arginine residue degron (Nt-R) (Zhang et al., 2019)

(Figure 9). The Nt-R signal can be produced either through proteolytic cleavage of the peptide bond or enzymatically added by Arg-tRNA transferases. Despite the significance of p62 for the degradation of arginylated substrates, the exact molecular mechanism underlying its interaction with Nt-R and how that affects autophagy remains uncertain (Zhang et al., 2019). It has been shown that loss of D169, D147 and D149 residue affects the interaction of p62 with N-degrons (Zhang et al., 2018).

1.7.3 Conserved LIR-KIR region of p62 (amino acid residues 303-370)

The FIR, LIR and KIR motifs in p62 are responsible for the interaction with FIP200, ATG8 proteins and KEAP1, respectively. Here, the term conserved region is used to refer to FIR, LIR and KIR motifs together. It has been shown from different studies that the overlap between these motifs precludes p62 from interacting with more than one of these proteins at the time (Jain et al., 2010; Turco et al., 2019). However, p62 is often polymeric which could enable the engagement of several of these interactors on a p62 filament. Different mutations or deletions in the amino acid sequence in the conserved region result in loss of binding between p62 and/or ATG8s, KEAP1 and FIP200 protein (Jain et al., 2010; Omar et al., 2021). Phosphorylation of p62 on residues S349, T350, S365, S366, S370 and T375 leads to the increase of the binding affinity between FIP200 and p62 (Turco et al., 2019). It is also known that phosphorylation of S439 increases the binding of p62 with KEAP1 (Ichimura et al., 2013). In another paper, they showed that L341V mutation of p62 blocks the binding between ATG8s and FIP200 (Omar et al., 2021).

FIP200 is a FAK family-interacting protein of 200 kD (FIP200). It is also called RB1CC1 (Hara et al., 2008). FIP200 is part of the ULK complex together with ULK1\ULK2, ATG13 and ATG101. FIP200 has been found in the nucleus (Chano et al., 2002), the cytoplasm (Ueda et al., 2000) and at the cell periphery (Abbi et al., 2002). The role of FIP200 in autophagy was investigated when it was found that it is colocalized both with ATG16L and ULK1 after starvation (Hara et al., 2008). The role of FIP200 is downstream of the mTORC1 regulation and it is mostly associated with the ULK puncta formation and ULK1 phosphorylation (Hara et al., 2008). It has been shown that the FIP200-p62 interaction is crucial for the organization of the autophagic machinery (Turco E. , 2020). In a previous paper from the same group they propose a model of how the FIP200 Claw domain was binding to p62 and how this interaction between the p62 ubiquitin positive condensates and FIP200 promotes the formation of the

autophagosome (Turco et al., 2019). The FIP200-p62 interaction may be the signal for activation of ATG13 phase separation and localization of ULK1 at ubiquitin-positive condensates to initiate autophagosome formation (Fujioka et al., 2020; Turco et al., 2019). According to their model p62 binds first to the ubiquitinated cargo and creates p62 condensates. The p62- and ubiquitin-positive condensates bind to the autophagy machinery. This interaction is mediated by FIP200. In the next step, the conjugation of LC3B-II with the isolation membrane will cause the switch between a FIP200-p62 interaction to a LC3B-II-p62 interaction. As a result, FIP200 together with the initiation autophagic machinery will be discarded and replaced by the LC3B conjugation system (Turco et al., 2019).

Another important link between FIP200 and p62 involves TBK1. TBK1 is a well-studied kinase and it has been found to phosphorylate many autophagic receptors, such as p62 (Pilli et al., 2012), OPTN (Richter et al., 2016), NDP52 and TAX1BP1 (Fu et al., 2018). Depletion of FIP200 causes a TAX1BP1-dependent accumulation of activated TBK1 (phospho-S172) in aggregates/condensates containing p62 and TAX1BP1. FIP200 regulates the formation of these TBK1-p62 aggregates. However, this regulation occurs independently of the autophagy deficiency caused by knocking out FIP200 (Schlütermann et al., 2021).

The LIR-KIR box is corresponding to the sequence before the LIR motif (336-341 residues) and after the KIR motif (347-352 residues), because it is conserved between different species (Figure 10).

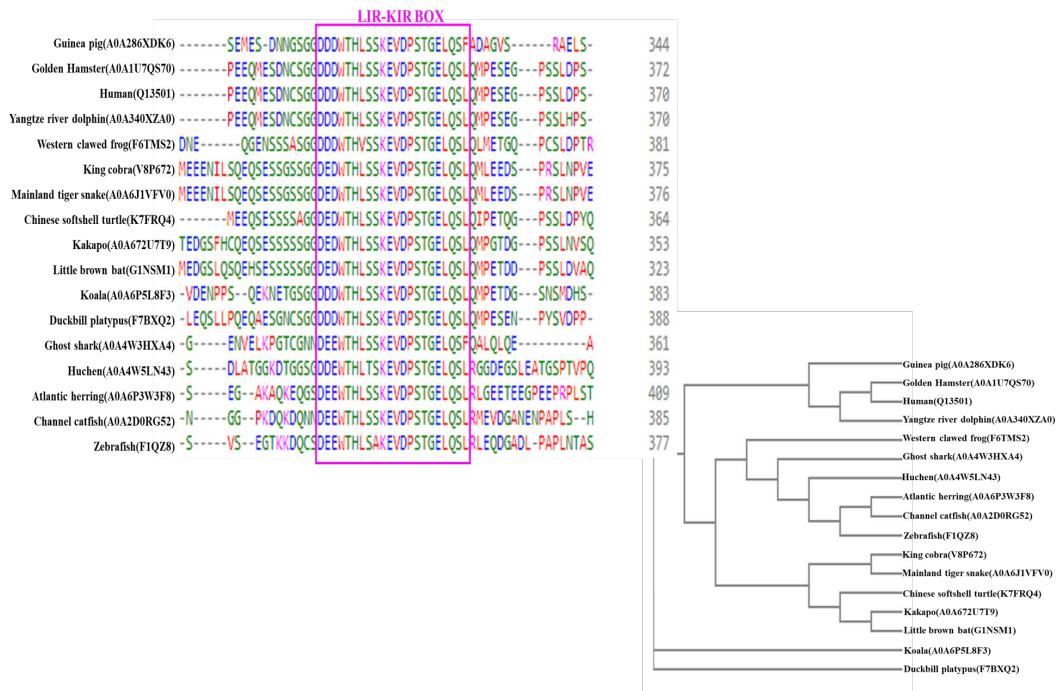


Figure 10 Alignment between different species showing the LIR-KIR box. The alignment is made by using the FASTA format from Uniprot, for each p62 protein. The species are shown with their common names, while the Uniprot code for each of them is in parenthesis. A cladogram shows the evolution of p62 protein sequences between these species.

It is a way to refer to both these two motifs together (Figure 11). The LIR motif on p62 was initially mapped to residues 321-349 (Pankiv et al., 2007). The structures of p62 bound to LC3B and yeast Atg19 bound to Atg8 revealed a common W-x-x-L motif (x=any amino acid) (Ichimura et al., 2008; Noda et al., 2008) and the importance of the acidic residues N-terminal to the core of the DDDWTHL LIR motif of p62 was verified by alanine substitutions (Ichimura et al., 2008; Pankiv et al., 2007). The LIR motif of p62 presents as an extended β -strand that creates a β -sheet with the β 2 strand of LC3B (Birgisdottir \AA et al., 2013). In this LIR docking site, two hydrophobic pockets HP1 and HP2 in the UBL domain of LC3 accommodate the side chains of the W and L residues. The two pockets are located on the opposite side of the hydrophobic patch (L8-I44-V70) of ubiquitin.

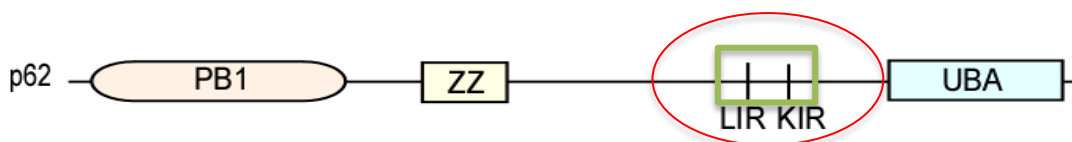


Figure 11 Main structural p62 domains. Cartoon of the 4 main regions on p62 sequence. The red circle is showing which domain the focus is on.

Electrostatic interactions, which involve two of the three aspartic acid residues of the LIR motif and basic residues in the N-terminal arm and UBL domain of LC3 (R10, R11, K49 and K50), are also important for the interaction between p62 and LC3 (Birgisdottir Á et al., 2013; Ichimura et al., 2008).

The KIR motif in p62 is located immediately after the LIR and was mapped to residues 347-352 of p62 (Jain et al., 2010). Inhibition of the interaction between KEAP1 and NRF2 leads to nuclear translocation of NRF2 with the resulting transcription of genes activated by oxidative stress stimuli (Tonelli et al., 2018). KIR is required for p62 to stabilize NRF2, and inhibition of KEAP1 by p62 occurs from a cytoplasmic location within the cell. The LIR and KIR motifs cannot be engaged at the same time by LC3 and KEAP1 since there is an overlap in the p62 sequence between these two motifs. However, p62 is forming polymers enabling different p62 units in the polymer to interact with ATG8s or KEAP1. The interaction between KEAP1 and p62 can lead to accumulation of KEAP1 in p62 bodies, which is followed by autophagic degradation of KEAP1 mediated by p62-LC3B interaction (Jain et al., 2010).

1.7.4 The UBA domain of p62 (amino acid residues 389-434)

In the known mechanism, the UBA domain, at the C-terminal, captures ubiquitinated proteins, and the PB1 domain at the N terminus of p62 induces the formation of p62 bodies through its self-oligomerizing nature (Figure 12). The p62 bodies subsequently recruit core autophagy components for phagophore formation on the ubiquitinated cargo facilitated strongly by the interaction between the LIR of p62 and LC3B at the phagophore membrane ensuring efficient encapsulation of the cargo into an autophagosome (Johansen and Lamark, 2020; Liu et al., 2016).

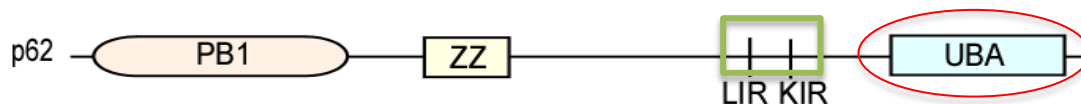


Figure 12 Main structural p62 domains. Cartoon of the main domains on p62 sequence. The red cycle indicates in which domain is the focus on.

Generally, p62 has a low affinity for ubiquitin. p62 UBA differs from other UBA domains because it allows dimerization between UBA domains and it is a unique dimerization mode among the different UBA domains (Isogai et al., 2011; Long et al., 2010). NMR data reveal that the binding mode between the p62 UBA domain and ubiquitin is the same as it was seen in canonical UBA domains (Isogai et al., 2011). However, only the monomeric p62 UBA domain is observed to bind ubiquitin. Dimerization of the p62 UBA domain inhibits the binding to ubiquitin. The C-terminal tail (435-440) is essential for dimer formation but dispensable for ubiquitin-binding (Isogai et al., 2011). It appears that this is a self-regulation mechanism. The affinity for ubiquitin can be changed when post translational modifications occur in the UBA domain, which prevent dimerization. At this point, it should be clear that UBA ubiquitin binding is different from ubiquitination of residues in the UBA domain. Based on the literature there are two Lysines located in and after the p62 UBA domain that can be either ubiquitinated or acetylated and these residues are K420 and K435 (You et al., 2019b). Acetylation of these two residues increases the ability of p62 to bind to ubiquitin (Matsumoto et al., 2011; You et al., 2019b). Moreover, ubiquitination of K420 residue in the UBA domain by KEAP1-Cul3 promotes the formation of p62 condensates (Lee et al., 2017). Furthermore, deubiquitylation of K420 residue by USP8 modulates negatively the autophagic degradation of p62. Deubiquitylation of p62 K420 residue appears to prevent p62 to be degraded by selective autophagy (Peng et al., 2020). Phosphorylation of S403 residue is not increasing the ubiquitin-binding of p62 but also promotes the phase separation but it is appeared to allow p62 to form gel-like structures (Kageyama et al., 2021; Matsumoto et al., 2011). See section 1.8.3 for the description of PTMs affecting the function of the UBA domain of p62.

1.7.5 p62 and diseases associated with the UBA domain

Autophagy is a cellular process associated with the lysosomal degradation of intracellular components and dysfunctional organelles (Dikic and Elazar, 2018). The last two decades have seen increased interest in identifying the roles of autophagy in ageing, neurodegenerative disorders and other pathophysiology's. Autophagy mutants give a poor prognosis for the development of neurodegenerative diseases (Braak et al., 2011) such as Alzheimer's disease, ALS (amyotrophic lateral sclerosis) and Parkinson's disease. Mutations in p62 are linked to hereditary neurodegenerative diseases including frontotemporal lobar degeneration 3 (FTLD3), ALS and Paget's bone disease 3 (PBD3).

Adult-onset Paget's disease of bone (PD) has been reported as the second most widespread metabolic bone condition after osteoporosis. PD of bone has a strong genetic element with family history being noted in 10–20% of cases (Tuck et al., 2017). There is a strong genetic link between the condition and mutations affecting the p62/SQSTM1 gene. Recently SQSTM1 mutations have also been reported in a small number of patients with amyotrophic lateral sclerosis (ALS) and frontotemporal lobar degeneration (FTLD), neurodegenerative disorders. Although several SQSTM1 mutations are common to both ALS/FTLD and PDB, many are ALS/FTLD-specific (Foster et al., 2021). Frontotemporal lobar degeneration (FTLD) is the second most common form of dementia after Alzheimer's disease (Onyike and Diehl-Schmid, 2013). Almost all the mutations that are associated with PDB are located in the UBA domain of p62. FTLD is associated with mutations that are located all over the p62 sequence. Some of them interfere with the ATG8 or KEAP1 binding (Omar et al., 2021). The mutations that occur in both diseases are affecting residues 387, 392 and 425 (Falchetti et al., 2004; Fecto et al., 2011) and the common element between them is that all are located in the UBA domain, and the main effect is loss of ubiquitin-binding.

Total loss of the SQSTM1 gene is associated with a rare, severe childhood- or adolescence-onset neurodegenerative disorder (Haack et al., 2016). In the pioneer study, 9 individuals lacking the SQSTM1 gene with ages between 15 to 35, coming from different families all showed gait abnormalities, ataxia mostly of the upper limbs and dysarthria. Seven out of nine also showed dystonia, vertical gaze palsy and mild cognitive decline. Half of the patients shared cerebellar atrophy, while 25% shared signal abnormalities in basal ganglia with iron accumulation (Haack et al., 2016). Based on the role of SQSTM1/p62 as a crucial player in a variety of vital cellular processes, it was surprising that its loss can be compatible with the survival of people above age 40. However, their functionality and quality of life are dramatically impaired. p62 functions are of particular importance in the brain, where the removal of damaged organelles and misfolded proteins by selective autophagy is crucial for healthy ageing and avoidance of neurodegenerative disease.

1.8 Liquid-liquid phase separation

During the beginning of our studies in biology, we learned that cells are made up of different compartments surrounded by membranes. Later on, we learned about Cajal bodies, stress

granules, P bodies and perhaps promyelocytic leukemia (PML) bodies. All these different kinds of bodies are not membrane-bound (Sun et al., 2018) (Figure 13). These membraneless organelles, bodies, or condensates are created by liquid-liquid phase separation (LLPS) (Dao and Castañeda, 2020).

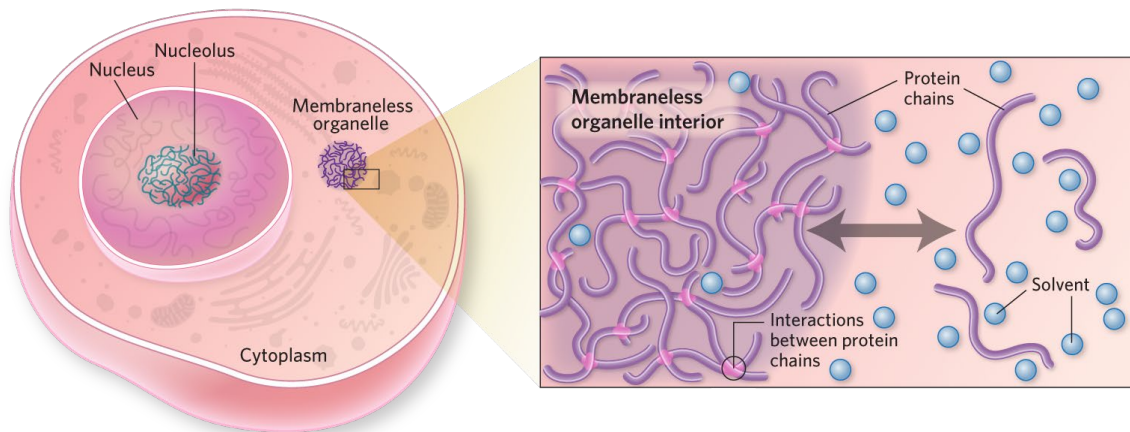


Figure 13 Membraneless organelle formation. Membraneless organelles exist both in the nucleus and the cytosol. Proteins with intrinsically disordered region can form multivalent interactions and at a critical concentration they undergo LLPS. The main protein is in the interior of the membraneless organelles and acts as a platform for protein-protein interactions. The main protein is oligomerized to create the phase separation assembly. There is a selectivity between the protein interactors. Only the proteins from the cytosol that can interact with the proteins in the interior are allowed into the condensates (Crabtree and Nott, 2018).

Membraneless organelles function as a house of reactions. They allow selective entry of enzymes and substrates to carry out various cellular functions such as i) allow cells to compartmentalize and bring compounds together to control reaction rates that would be less efficient or not possible at all in the cytoplasm. It also works as a mechanism to isolate toxic agents. The structures are highly dynamic and range in size from 0.1–3 micrometers in diameter, which is far bigger than ribosomes. They are usually round but can be found in all shapes, even as filaments (Sehgal et al., 2020). For one protein to be able to create membraneless organelles, it has to fulfil some criteria. The phase separation is driven by molecules which work as scaffold proteins (Alberti et al., 2019).

LLPS is triggered by multivalent weak interactions created by intrinsically disordered regions (IDRs). LLPS is often a metastable state. Some proteins can continue further and go through gel-like phase separation and solid-like phase separation (Figure 14). Characteristics of these are the following:

In gel-like phase separation, the components of the complex are held together with strong interactions, but the condensates are still permeable to other proteins. There is limited mobility between the complex and the surrounding environment (Noda et al., 2020). They are formed by prion-like domains, proteins that are prone to nucleation- heterotypic polymerization. Some examples of this category are nuclear pore complex, hnRNPA1 and FUS protein (Noda et al., 2020). Proteins that are in this stage can go back to the LLPS or forward and undergo solid-like phase separation.

In solid-like phase separation, the interacting proteins are held together with very strong interactions and there is almost no interactional mobility with the surrounding environment (Noda et al., 2020). Proteins that are found in this stage can easily be misclassified aggregates.

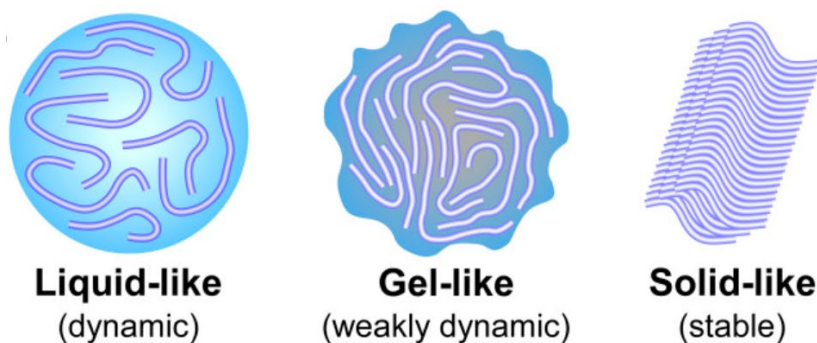


Figure 14 Morphological differences between condensates. Protein condensates formed by liquid-like phase-separation can be very dynamic, more gel-like and less dynamic, like p62 condensates often are, and they can also transition into a more solid-like, aggregated state. The two first categories can reversibly interchange while when a solid-like stable state has occurred this situation is irreversible. The solid-like aggregate may represent a non-degradable structure resulting in a pathological state (Noda et al., 2020).

The term aggregate should be used only for misfolded proteins which aggregates into a dead-end biological process (Wang and Zhang, 2019)

1.8.1 Phase separation in autophagy

As the knowledge about LLPS is increasing, more and more connections are discovered between LLPS and the regulation of autophagy. The connections can be direct and indirect. An example of a direct connection between LLPS and autophagy is the formation of the single PAS in yeast and mPAS in mammalian cells (Noda et al., 2020). In yeast, the TORC1 complex regulates the formation of the PAS. Under normal conditions, the formation of PAS is inhibited by the phosphorylated Atg13. TORC1 is responsible for Atg13 phosphorylation, but under starvation conditions when TORC1 is not anymore active, then Atg13 is dephosphorylated and

it can activate the Atg1 complex (Memisoglu et al., 2019). Dimerization of Atg13 with Atg17 is the initiative signal for phase separation of the Atg1 complex (Fujioka et al., 2020). Interactions between Atg13 and vacuolar membrane protein 8 (Vac8) establish the position where PAS will be created (Fujioka et al., 2020). All yeast Atg proteins downstream of the Atg1 complex are employed to PAS for starting the induction of autophagosome formation (Suzuki et al., 2007).

1.8.2 Liquid-liquid phase separation of p62

Under basal conditions (full media) p62 is located both in the cytosol as a diffusely localized population and in p62 bodies. In physics, the state of materials with the higher entropy (lack of order or predictability) is the gas phase. In the cells, it is not possible to have a gas phase for the proteins, so this “lack of order” phase matches most closely with the diffuse protein fraction (Sehgal et al., 2020). For a diffuse fraction of the protein to undergo LLPS, it requires to reduce entropy (Hyman et al., 2014). So, the protein should be more stabilized. In the case of p62, this state can be achieved by two different procedures (Figure 15). From one side, NBR1 interacts with p62 via the PB1 domain, stabilizing the N-terminal of p62 by regulating the length of the p62 polymeric filaments (Wang and Zhang, 2019). On the other side, p62 binding to ubiquitin via the UBA domain may stabilize the C-terminal of p62. The formation of p62 bodies is promoted by post-translational modification that occurs in the UBA domain, for example, phosphorylation of S403 and S407, and ubiquitination of K420 (Wang and Zhang, 2019). Both these modifications result in increased affinity of the UBA domain towards ubiquitin, thus facilitating efficient cargo recognition.

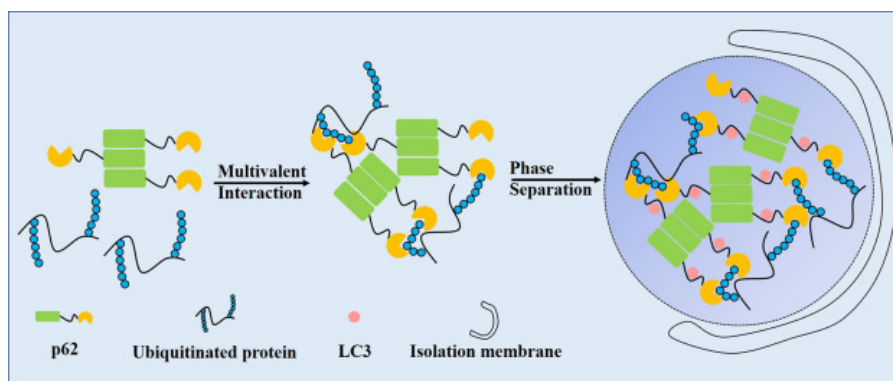


Figure 15 Phase separation of p62. The initiation step for phase separation of p62 to occur is binding to ubiquitin via the UBA domain. This event together with the oligomerization of p62 via the PB1 domain is the main event of the process.

Ubiquitinated proteins act as cargo for degradation and they can be recognized and bound to p62 via the UBA domain. The binding of p62 with the cargo promotes the initiation of the phagophore formation. LC3B helps connect the p62 bodies to the phagophore. Lipidated LC3B works as a bridge. As a result, the phagophore forms on and enwraps p62 bodies allowing p62 bodies to be degraded by selective autophagy (Sun et al., 2020).

The LLPS have separated structures held together with weak interactions and most likely have a rounded shape (p62 bodies) and they perform slow fusion and fission but high rates of exchange with the surrounding environment. They are characterized by high mobility between the interacting proteins (Hyman et al., 2014; Sehgal et al., 2020). After p62 binds to LC3B and the formation of the double autophagic membrane is initiated, then the term p62 bodies cannot be used anymore. After that stage, we refer to them as phagophores or in later steps autophagosomes.

1.8.3 post-translational modifications of p62

Post-translational modifications (PTMs) of proteins tremendously increases the complexity of the proteome making the proteome much more complex than the transcriptome. PTMs are covalent chemical modifications often crucial for the function of the proteins. For example, the activity of most protein kinases is regulated by phosphorylations at the activation loop in their active sites. The subcellular localizations and protein-protein interaction capabilities of proteins may be regulated by PTMs, as well as their interaction with nucleic acids, lipids and cofactors. Proteins can be modified by PTMs anytime during their "life cycle". The most common PTMs are phosphorylations, ubiquitination, hydroxylation, lipidation, SUMOylation, NEDDylation, acetylation, methylation, glycosylation, disulfide bond formation and protein cleavage. Except for the latter, almost all PTMs are reversible. For many types of PTMs we have pairs of "writers" and "erasers" like kinases and phosphatases, acetylases and deacetylases, methylases and de-methylases, ubiquitin E3 ligases and de-ubiquitinases. A single protein may have multiple PTMs, and these may change over time. Many proteins are modified by PTMs following translation to stabilize their folding, to regulate the levels of the protein or to allow the protein to move to distinct cellular compartments (e.g., nucleus, membrane) (Walsh and Roberts, 2006). Other modifications that switch protein status from active to inactive, usually take place after the modifications that regulated the localization and the folding of a protein. Proteins that become tagged with ubiquitin chains are often destined to degradation, either via the proteasome or autophagy. Thus, proteins tagged with K48 ubiquitin chains will preferably be degraded by the proteasome (Grice and Nathan, 2016).

Protein kinases and phosphatases target the specific amino acid residues Y, S or T. So far, researchers have found more than 400 different types of PTMs (Khoury et al., 2011; Ramazi and Zahiri, 2021) affecting a variety of protein functions. According to the dbPTM (Huang et

al., 2019) which is one of the most detailed PTM databases, 24 different PTMs can occur. Moreover, this database has identified the 80 most modified sites. The most common modifications and the most likely modified amino acid residues are shown in Figure 16.

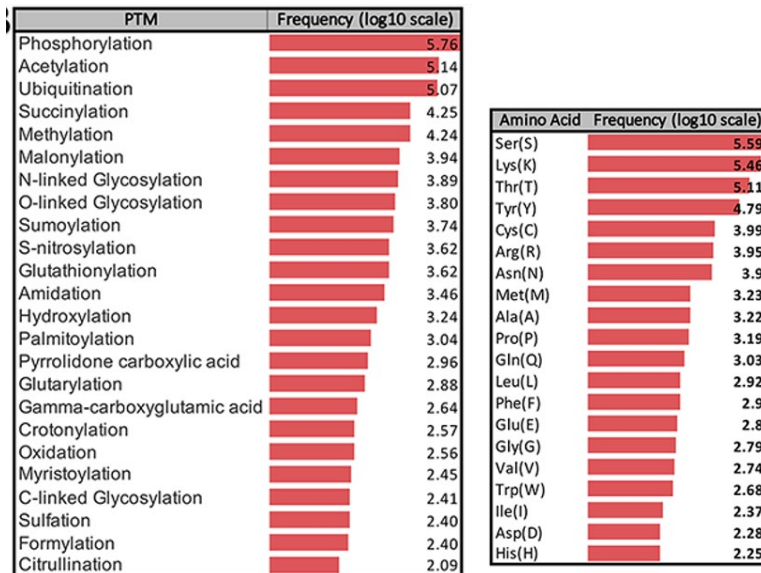


Figure 16 The most common PTMs and the amino acids that are modified based on the dbPTM databank (October 2020). All frequencies are shown on a log scale (Ramazi and Zahiri, 2021).

For p62, phosphorylation, acetylation and ubiquitination have been reported affecting many sites of the protein (PhosphoSitePlus, 2003). Several phosphorylation sites on p62 have already been studied:

- Phosphorylation by CDK1 on S272 and T269 residues controls the timely transit of cells through mitosis and tumor cell proliferation (Linares et al., 2011). The p62 phosphorylation by CDK1 in the stage of mitosis is essential for the stability of the cyclin B levels and maintenance of CDK1 activity during mitosis. Lack of CDK1-mediated phosphorylation of p62 at S272 and T269 make the cells exit faster from mitosis. Upon transformation by Ras cell proliferation and the tumorigenic phenotype is enhanced when p62 is not phosphorylated by CDK1 (Linares et al., 2011).
- Phosphorylation of the S349 residue promotes the binding of p62 to KEAP1 and recruitment of the associated E3 ligase Cullin-3 (Ichimura et al., 2013). This results in the activation of the NRF2 signaling pathway (Jain et al., 2010; Komatsu et al., 2010). This leads to a strong increase in p62 transcription that facilitates the formation of p62 bodies.

- Phosphorylation of S403 by TBK1 strongly increases the binding affinity of p62 for ubiquitin (Matsumoto et al., 2015; Pilli et al., 2012). Phosphorylation of S403 or S407 by ULK1 has a similar effect (Lim et al., 2015; Ro et al., 2014). The phosphorylation of these sites is essential in p62 mediated selective autophagy of ubiquitinated cargos. The phosphorylation of S403 by TBK1 can also work as a link between p62 mediated selective autophagy and immune signaling, where p62 is shown to attenuate signaling by degrading signaling proteins like STING (Prabakaran et al., 2018).

p62 contains 20 different K residues that can be either acetylated or ubiquitinated:

- Ubiquitination of K7 by TRIM21 inhibits p62 oligomerization and thereby the formation of p62 bodies, and it also inhibits the interaction of p62 with NBR1 (Pan et al., 2016).
- Ubiquitination of K91 and K189 by RNF166 catalyzes K29- and K33-linked polyubiquitination of p62 (Heath et al., 2016).
- The UBA domain in p62 can dimerize, and this is shown to ubiquitin binding of p62 (Isogai et al., 2011; Long et al., 2010). Ubiquitination of K420 by recruited E2 ligases UBE2D2 and UBE2D3 (Peng et al., 2017), or by recruited KEAP1-Cullin-3 complexes (Lee et al., 2017) prevents the formation of UBA dimers. This increases ubiquitin-binding and the formation of p62 bodies.
- Acetylation of K420 and K435 by TIP60 similarly inhibits the formation of UBA dimers and promotes the binding of p62 to ubiquitin (You et al., 2019a).

2. Aim of the study

This project aimed to investigate the structure of p62 bodies and the roles of different types of PTMs in regulating their formation and degradation under basal and stress conditions. In our study, we chose to focus on specific domains and motifs and the roles displayed by them in selective autophagy. The aim of the study was to find out if helical filaments formed *in vitro* by the PB1 domain are also formed in cells and to test whether these filamentous structures are essential for the formation of p62 bodies and p62 mediated selective autophagy. The aim of study II was to test if LC3B is required for the degradation of p62 by selective autophagy, or if other ATG8 family proteins can also be used. The aim of study III was to explore the roles of ubiquitination of specific K residues in p62. In particular, we focused on the effects on the interaction of p62 with ubiquitin, and how this is associated with the formation and turnover of p62 bodies. During this work, acetylation of K420 and K435 was reported to play an essential role in promoting ubiquitin-binding via the UBA domain, and we, therefore, extended our study to include acetylation of these two residues.

3. Summary of the papers

3.1 Paper I

In this study, we investigated the role of the PB1 domain of p62 in the formation of filamentous p62 assemblies. Three PB1 containing proteins with the ability to polymerize were analyzed by cryo-electron microscopy, i. e. TFG-1, plant Nbr1 and p62. We found that the formation of filamentous oligomers or polymers of p62 is needed both for the creation of p62 bodies and for the degradation of p62 by selective autophagy. Chimera p62 constructs having the native PB1 domain replaced by that of TFG-1 formed filaments, although these filaments displayed a different helical architecture than those formed by wt p62. The chimera constructs accumulated in bodies when expressed in cells, but the diffuse fraction was higher, and the bodies were smaller in size than seen for wt p62. The chimera constructs were also degraded by selective autophagy, but the p62 cargo KEAP1 was not degraded in cells expressing p62 chimera. KEAP1 was efficiently recruited to p62 bodies formed by either wt p62 or chimera constructs, but only wt p62 delivered KEAP1 for degradation by selective autophagy. This indicates that the native PB1 domain of p62 forms filamentous structures that are functionally adapted to the role p62 has in degrading cargo containing condensates by selective autophagy.

3.2 Paper II

In this study, we investigated the role of the LIR motif of p62. The LIR motif allows p62 to interact with ATG8 family proteins. This interaction is essential for the degradation of p62 or p62-cargo complexes by autophagy, because it is responsible for the docking of p62 to the inner membrane of the phagophore. The main interaction partner of p62 among the six mammalian ATG8 proteins is probably LC3B, but the potential use of other ATG8 proteins instead of LC3B has not been investigated. We created two chimera p62 proteins where the LIR motif of p62 was replaced by the LIR motif from ULK1 or FYCO1, respectively. The LIR motif in ULK1 has a binding preference for the GABARAP subfamily, while the motif in FYCO1 has a binding preference for LC3A and -B. An exchange of the p62 LIR sequence affected dramatically the ability of p62 to bind to KEAP1, even though the KIR motif was conserved in the chimera constructs. The LIR exchange did not prevent the formation of p62 bodies or the degradation of p62 by autophagy under basal conditions. Surprisingly, the only process that was disturbed by the p62 LIR exchange was the autophagic degradation in response to starvation. Chimera constructs were not degraded by starvation induced autophagy. To summarize, our findings

support that the interaction with LC3B is not crucial for p62 phase separation or degradation of p62 under basal conditions. However, our data seems to indicate that the specific interaction of p62 with LC3B may have a key role in starvation-induced autophagy of p62.

3.3 Paper III

In this study, we investigated the role of PTMs in regulating p62, and our main focus was on C-terminal PTMs affecting ubiquitin binding. Ubiquitin binding of p62 is inhibited by the formation of UBA dimers, and acetylation of K420 and K435 or ubiquitination of K420 is previously shown to prevent the formation of UBA dimers. In addition, phosphorylation of S403 or S407 is known to increase the affinity of the UBA domain for ubiquitin. To investigate the importance of PTMs on lysines, we expressed point mutants of p62 where lysine residues were replaced by arginine or glutamate residues. There are 19 lysines in p62. When mutating all these residues except for K7 that is required for PB1 mediated polymerization, p62 was still able to form p62 bodies, strongly indicating that ubiquitination or acetylation of p62 is not essential for the formation of p62 bodies. However, the bodies formed by p62 lacking all lysine residues except for K7 displayed a different and more clustered morphology, suggesting that there is a role of PTMs in regulating the morphology of the structures. The use of K420R or K435R mutated p62 constructs revealed that a modification of only one of these two residues dramatically affects the number and morphology of p62 bodies. There were a reduced number of p62 bodies in cells carrying the K435R mutation and more p62 bodies in cells carrying the K420R mutation. p62 constructs carrying both these mutations were surprisingly similar to wt p62, and this supports the conclusion that there must be some type of crosstalk between modifications affecting these two sites. Different stress conditions induced by TSA or sulforaphane were used to analyze the formation of the p62 bodies. The use of sulforaphane supported the importance of the K420 residue for the formation of p62 bodies upon oxidative stress. Our data also support previous data that acetylation plays an important role in regulating autophagy of p62 and that the acetylation of K435 is important for the degradation of the diffuse fraction of p62.

4. Discussion

The three manuscripts in this thesis focus on three domains that are all important for selective autophagy mediated by p62; II e. the N-terminal PB1 domain (paper I), the conserved region where the LIR, FIR and KIR motifs are located (paper II), and the C-terminal UBA domain (paper III). An important feature of p62 in selective autophagy is its ability to undergo liquid-liquid phase separation. While other domains or motifs in p62 like the ZZ domain (Berkamp et al., 2020; Zhang et al., 2019) or the KIR motif (Omar et al., 2021) may in different ways facilitate phase separation, the only domains that are required for phase separation are the PB1 domain and the UBA domain. Phase separation is triggered by the binding of p62 to ubiquitin (Berkamp et al., 2020; Noda et al., 2020), and the UBA domain is therefore absolutely required. In addition, monomeric p62 is unable to form condensates (paper I). PB1 mediated self-interaction of p62 is therefore also required. The LIR motif is essential for the degradation of p62 droplets or gels by selective autophagy, but there is no evidence that the LIR motif participates in phase separation of p62.

4.1 Phase separation of p62 may depend on shortening of the length of p62 filaments

The focus in the paper I is on the formation of helical filaments by the PB1 domain. The paper is a collaboration with the group of Carsten Sachse that initially discovered and analyzed the helical filaments formed by p62 (Ciuffa et al., 2015). They found that in vitro, p62 spontaneously self-interacts into polymeric chains that fold into two different types of helical structures, one called type T with tubular morphology and another type F with filamentous appearance (Ciuffa et al., 2015).

The PB1 domain is an evolutionarily conserved domain that is found in 13 mammalian proteins (Lamark 2003). However, p62 and TFG are the only mammalian proteins that contain a PB1 domain which allows them to polymerize and create filamentous structures. The filamentous structures of p62 and TFG were analyzed in Paper I, and we also made chimeric constructs where the PB1 domain of p62 was replaced by that of TFG. We observed that the chimeric p62-TFG1 constructs were more diffuse than corresponding p62 constructs, but the readily formed bodies that we propose are condensates. The chimeric constructs were efficiently degraded by selective autophagy. Their efficient degradation by autophagy gave one important conclusion;

p62 does not require its PB1 domain to be degraded, just a PB1 domain that can be polymerized. It is however unclear from our data if it is the diffuse fractions or the condensates that are degraded. It is experimentally challenging to answer this question, and condensates are dynamic structures that exist in equilibrium with diffuse fractions. We found in Paper I that KEAP1 was recruited to condensates formed by the chimera constructs as efficiently as it was recruited to normal p62, but the chimera constructs could not mediate selective autophagy of co-recruited KEAP1. The lack of degradation of KEAP1 is unexpected. It suggests that only the diffuse fractions are efficiently degraded by autophagy and that the condensates have to be solubilized before they can be degraded. Another possibility is that the condensates are degraded, but that overexpressed KEAP1 inhibits the degradation of condensates formed by chimera constructs.

p62 associates into long polymeric chains *in vitro*. In previous *in vitro* experiments, Ciuffa et al., (Ciuffa et al., 2015) found that the binding of p62 to poly-ubiquitin resulted in a shortening of the filaments, and they proposed a model where the interaction of p62 to ubiquitin promotes a transition of the polymeric filaments into shorter oligomeric structures. The presence of oligomeric p62 structures in cells is supported by data in Paper I, where CLEM studies revealed that p62 filaments in p62 bodies are short oligomeric structures with an average size of 50 nm. The length of diffuse p62 filaments is not known, but the transition of p62 filaments into oligomeric structures is probably important for phase separation. since Such a model has later been supported by others (Wang and Zhang, 2019).

The binding of p62 filaments to ubiquitin chains is the key for initiating the phase separation of p62 (Sun et al., 2018; Zaffagnini et al., 2018). As mentioned above, this interaction is involved in regulating the length of p62 filaments. Another interaction that may contribute to the shortening of p62 filaments is the p62-NBR1 interaction. The creation of the filaments depends on the polymerization of the PB1 domain and the K7 and R21-R22 residues in the PB1 domain are required in addition to a functional OPCA motif. The K7 and R21-R22 residues are also important for the binding of p62 to NBR1, resulting in recruitment of NBR1 to p62 bodies (Lamark et al., 2003). This way, NBR1 competes with the self-interaction of p62, and in the paper I, we showed that the presence of NBR1 efficiently reduced the length of p62 filaments *in vitro*. There is strong evidence in the literature that NBR1 facilitates phase separation of p62, both *in vitro* and in cells (Sánchez-Martín et al., 2020; Zaffagnini et al., 2018). As suggested in the discussion of paper I this may be due to a regulation of filament length by NBR1. The

protein level ratio between p62 and NBR1 inside the cells is largely in favor of p62 (Schwanhäusser et al., 2013). This ratio is important for the function of p62. In case that the levels of NBR1 in a cell are decreased that can lead to the creation of more p62 polymeric filaments and reduce the number of the p62 molecules that can undergo phase separation. On the other side increase in the levels of NBR1 can lead to the creation of p62 oligomeric filaments only. So, more p62 molecules will undergo phase separation.

4.2 Phase separation of p62 is regulated by post-translational modification of K420 and K435

There is strong evidence in the literature that phase separation of p62 is regulated by post-translational modifications. Post-translational modifications are required in the UBA domain to inhibit the dimerization of it and allow ubiquitin binding (Long et al., 2010; You et al., 2019b). Among the modifications affecting ubiquitin-binding are phosphorylation of S403 that increases the affinity of the p62-ubiquitin interaction (Matsumoto et al., 2011), ubiquitination of K420 that prevents the inhibitory dimerization of the UBA domain, and acetylation of K420 and K435 that increases the dynamics of the condensates and degradation of p62 (You et al., 2019b). In Paper III, our main focus was on the K420 and K435 residues, and we investigated the morphology of p62 bodies in MEF cells stably expressing selected GFP-tagged mutants of p62.

Condensates formed by p62 are droplets of gel-like structures. p62 bodies induced by the S403 phosphorylation are reported to be gel-like structures (Kageyama et al., 2021). Our data in Paper III also supports this finding. Gel-like condensates contain more dense protein concentrations, and the interchange between the gel structure and the surrounding environment is not as dynamic as in liquid-like condensates (droplets) (Noda et al., 2020). Since gel-like condensates are less dynamic than droplets, their formation may result in a stabilization of p62 in the cytoplasm if their degradation is inhibited or impaired (Kageyama et al., 2021). The morphology of condensates can be tested by FRAP experiments. We performed preliminary FRAP experiments in this study, but these experiments were not included in paper III. Instead, we propose that the presence of small GFP-p62 condensates combined with a high level of diffuse p62 indicates that the condensates are in the form of droplets (Figure 17). Likewise, we

propose that the presence of large condensates combined with an absence or low level of diffuse protein indicates that the condensates are gel-like structures (Figure 17).

One of the mutants, K420R, showed the same phenotype when visualized by confocal microscopy as the S403E mutant. Our conclusion is therefore that the K420R mutation promotes the formation of gel-like p62 condensates (Figure 17). This was unexpected since a post-translational modification of the K420 residue has been shown to inhibit dimerization of the UBA domain, and this increases ubiquitin-binding and p62 condensate formation (Lee et al., 2017) (Peng et al., 2017). Similarly, USP8 is responsible for the deubiquitination of K420, and a knockdown of this enzyme increased the aggregation of p62 in response to proteasomal inhibition (Peng et al., 2020). Together, these data indicate that ubiquitination of K420 may play an essential role in regulating p62 condensation. The K420R mutation was therefore expected to have a negative effect on p62 condensate formation.

One of the E3 ligases that are believed to ubiquitinate the K420 residue, and this way regulate p62 condensate formation is the KEAP1-Cullin3 ligase complex. The role of p62 in regulating the KEAP1-NRF2 pathway was initially demonstrated in several separate studies published in 2010 (Fan et al., 2010; Komatsu et al., 2010; Lau et al., 2010; Zhang, 2010). Only one of these early studies focused on the effect KEAP1 has on p62 bodies (Fan et al., 2010). Later studies have confirmed that KEAP1 affects both the morphology and the degradation of p62 bodies (Omar et al., 2021). Our data in Paper I demonstrated that an increased level of KEAP1 increases both the number and the size of p62 bodies, and this correlates with the ability of KEAP1 to facilitate the transition of p62 droplets into gels (Kageyama et al., 2021; Lee et al., 2017).

The data of Lee et al. (Lee et al., 2017) indicated that gel formation is induced by ubiquitination of the UBA domain in p62 by the KEAP1-Cullin3 E3 ligase complex. In their model, it is K420 that is ubiquitinated, and this has a negative effect on UBA domain dimerization leading to increased binding of p62 to ubiquitin (Lee et al., 2017). Contrary to our results in Paper I, they found that p62 K420R makes p62 bodies that are more dynamic than those formed by WT p62. Both studies were performed with MEF cells. Our study was performed with stably transfected cells while Lee et al. (Lee et al., 2017) analyzed transiently transfected cells. They based their

conclusion that only K420 is ubiquitinated by the KEAP1-Cullin 3 E3 ligase complex on a lack of ubiquitination of K420R as found by immunoprecipitation experiments. However, our experience in Paper III is that immunoprecipitation of p62 K420R can be very difficult because of the aggregated morphology of p62 bodies formed by this mutant construct. Perhaps in the absence of K420, another K can compensate for the lack of K420 and become ubiquitinated in a KEAP1-dependent manner. In Paper III, we found that the wild-type K420 residue is needed for sulforaphane-induced condensate formation of p62. More studies are clearly needed to fully understand the role of KEAP1-Cullin 3 in regulating the ubiquitination of p62.

Also, other ubiquitin ligases than KEAP1-Cullin3 may regulate p62 condensation. One example is the reported ubiquitination of K420 by the E2 ligases UBE2D2 and UBE2D3 (Peng et al., 2017). In this study, also other K residues in p62 were ubiquitinated, and their focus on the K420 residue was partially based on the assumption that there is a need to modify the K420 residue to inhibit the reported UBA dimerization. A more recent study performed in our research group showed that the E3 ligase TRIM32 may play an important role in regulating p62 condensation. TRIM32 was shown to ubiquitinate multiple K residues in p62 (Overå et al., 2019). Future studies need to find out if the main role of ubiquitination is to inhibit UBA domain dimerization, or if the main role is instead to facilitate cross-linking of p62 filaments in the condensates. In the latter case, the modification of other K residues than K420 and K435 may perhaps be equally efficient.

In Paper II we also tested the effect of the K435R mutation which appeared to be opposite to that of the K420R mutation. The K435R mutant inhibited p62 condensation, indicating that the modification of this residue has a positive effect on p62 condensation. Cells expressing the K435R mutant accumulated a high level of diffuse p62, and there were few and small p62 bodies. Moreover, immunoprecipitation experiments indicated that this construct had a strongly reduced affinity for ubiquitin, although it could still interact with ubiquitin *in vitro*.

The opposite phenotypes of the K420R and K435R mutants of p62 were interesting, suggesting that there may be a fine-tuned crosstalk between these two residues in regulating p62 condensation. Another observation that made us believe that there is a regulatory balance between these two Ks came from the results with K420R and K435R double mutants. A general finding throughout Paper III was that p62 mutant constructs carrying both the K420R and the K435R mutations displayed a phenotype closer to wild type p62 than mutant constructs carrying

one of these mutations. Our data also indicated that the K435 residue may be more prone to acetylation than the K420 residue.

The complexity of the phenotypes seen in Paper III clearly tells us that the UBA domain of p62 is prone to regulation in several different ways. We, therefore, need to be aware that the effect of specific post-translational modifications may be context dependent. Hence, we should be careful not to make too many conclusions only based on the behavior of the K420R and K435R mutants. We also tested the effect of the NRF2 activator sulforaphane (SFN) on cellular condensation of p62, a compound that is known to induce the condensation of p62 (Darvekar et al., 2014). In this specific case, we found that the wild type K420 residue was required for the induction of p62 condensation by SFN, and our data support that the residue may be ubiquitinated.

To simplify thing, we may argue that there are two different kinds of effects mediated by PTMs regulating the UBA domain of p62, the one that stabilizes p62, which we can observe in K420R and S403E mutants and the one that promotes degradation of p62 by selective autophagy, as is seen with the K420Q/K435Q construct (Figure 17). Acetylation increases the affinity of the UBA domain for ubiquitin (You et al., 2019b), while the modifications that occur on S403 and K435 may increase the ubiquitination of p62 itself. Unfortunately, we were unable to distinguish between these possibilities in the present study.

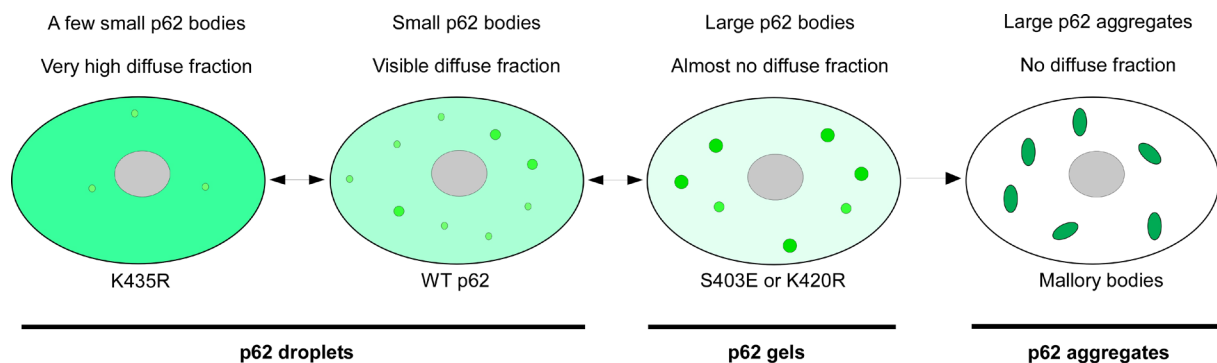


Figure 17 Proposed model illustrating how the p62 localization pattern (size of bodies and amount of diffuse protein) can be used to distinguish between the formation of p62 droplets and p62 gels. Mallory bodies are keratin positive p62 aggregates induced in liver diseases (Lahiri et al., 2016).

4.3 Modification of the K435 residue is crucial for basal autophagy of p62

The data in paper III clearly show that the K435R mutation prevents the degradation of p62 by selective autophagy under basal conditions. The K435R mutated p62 construct was efficiently degraded in response to starvation, meaning that the impaired autophagy of this construct was only seen under basal conditions. The impaired degradation is not easily explained since the mutation is in the UBA domain of p62. A p62 construct with the UBA domain deleted is efficiently degraded by autophagy (Pankiv et al., 2007). We have no evidence that the UBA domain is needed for the degradation of full-length p62. The only elements known to be needed are the PB1 domain and the LIR motif.

How can the UBA domain with a K435R mutation inhibit the degradation of p62? One possibility is that a UBA domain that is not modified on K435 forms an intramolecular interaction inhibiting the PB1 domain or the LIR motif. Another possibility is that the effect is more indirect and caused by structural changes in the UBA domain. The rather dramatic phenotypes seen for p62 constructs containing single K420R or K435R mutations suggest that the K435R mutation may have a significant effect on the structure of the UBA domain. This may potentially inhibit autophagy either by increasing UBA dimer formation, or it may affect PB1 mediated polymerization or the binding of p62 to the phagophore. Another assumption would be that the K435R mutation affects the droplet dynamics of p62, but since the K435R construct is mainly diffuse and since degradation of diffuse p62 does not depend on p62 condensation into droplets or gels, we consider this explanation as unlikely.

Intriguingly, we found that a K420R/K435R double mutation rescued the autophagic degradation of p62 under basal conditions. This correlates with the idea that the lack of one of the critical K residues in the UBA domain may affect the structure of the UBA domain in ways that are not seen if both residues are mutated. Our interpretation is therefore that the defective degradation is the result of a post-translational modification of the K420 residue, that in the absence of a balancing modification of the K435 residue has this type of effect. Our data in Paper III supports that the acetylation of K435 residue specifically increases the selective degradation of the diffuse p62 fraction, but our data gives no mechanistic explanation to the observed inhibition of basal autophagy seen for the K435R construct. In the paper by You et al. (You et al. 2019) only double mutants of K420 and K435 were studied. However, their results clearly implicate that acetylation of these residues increases the dynamics of p62 body

formation and selective degradation of p62. This is consistent with our interpretation based on the K435R mutant.

4.4 The complexity of the LIR-KIR region.

In Paper II, we made p62 chimeras with the native LIR motif replaced by a LIR motif with a different specificity. When expressed in cells, these chimeras were efficiently degraded by selective autophagy under basal conditions, suggesting that the specificity of the LIR motif is not essential for the degradation of p62 by autophagy. However, the chimeras were not degraded like wild type p62 in response to starvation.

The explanation may in part be due to the fact that there are mechanistic differences in how p62 is degraded under basal conditions and in response to starvation. The degradation of p62 upon starvation occurs via two different degradation pathways, i. e. macroautophagy and endosomal microautophagy (Mejlvang et al., 2018). The endosomal microautophagy pathway is poorly understood mechanistically, but this pathway may be more dependent on the LC3B interaction than the macroautophagy pathway. In paper III, we observed a related type of discrepancy when analyzing the autophagy of the K435R mutated p62 construct. This construct was not degraded under basal conditions but was efficiently degraded in response to starvation. This supports our conclusion that there may be mechanistic differences in how p62 is degraded under basal and starvation conditions. Perhaps the K435R mutated p62 construct is degraded via the endosomal microautophagy pathway (Mejlvang et al., 2018).

Alternatively, or in addition, the defective autophagy under starvation may be because our p62 LIR substituted constructs also are affected in their interactions with KEAP1 or FIP200. There is evidence that the binding of p62 to KEAP1 facilitates the degradation of p62 bodies (Fan et al., 2010), and a lack of interaction with FIP200 is also likely to affect the degradation of p62 (Turco et al., 2019). It is nevertheless intriguing that basal autophagy is not inhibited by the substitutions. Our initial plan when making these constructs was to avoid destruction of the KIR motif, but our substitutions had a strong and unexpected effect on the affinity of p62 to bind to KEAP1. We tried to avoid this by keeping the core KIR motif (STGE) intact. However, despite the presence of an intact core KIR motif, p62-LIR(FYCO1) displayed a significantly reduced ability to bind to KEAP1 while p62-LIR(ULK1) was unable to bind. This means that

residues N-terminal to the KIR motif and extending into the LIR motif are critical for the binding of p62 to KEAP1. The LIR, KIR and FIR motifs overlap, and this entire region is conserved in the evolution of p62 suggesting a coregulation here that we have not yet elucidated. Our knowledge of residues critical for the ATG8 and KEAP1 interactions is incomplete. Further studies are required to identify all residues involved.

In Paper III, immunostaining of p62 bodies with LC3B and KEAP1 antibodies showed that endogenous KEAP1 and LC3B co-localize in p62 bodies under basal conditions. Because of the sequence overlap between the LIR, KIR and FIR motifs, p62 cannot simultaneously bind to LC3B and KEAP1 (Jain et al., 2010), or LC3B and FIP200 (Turco et al., 2019). In a proposed model of selective autophagy mediated by p62 (Turco et al., 2019)(Figure 18), the binding of FIP200 is necessary to induce phagophore formation. However, the binding to FIP200 is inhibited by docking of p62 to ATG8 proteins on the phagophore. This way, FIP200 is excluded from being degraded by autophagy along with p62. In a similar model, we propose that KEAP1 will be excluded from binding to p62 on the surface of a p62 condensate (Figure 18). Unlike FIP200 and many other interaction partners of p62, KEAP1 is also localized in the interior of p62 condensates. This is seen very clearly in our confocal images of co-localized p62 and KEAP1 in Paper I and III. Internal p62 is free to interact with KEAP1, and KEAP1 is therefore degraded by autophagy as a constituent of the p62 condensates. However, we propose that the diffuse filaments of p62 may not similarly interact with KEAP1, since they have no interior and the interaction with LC3B will in this case exclude KEAP1 from being degraded together with diffuse p62 (Figure 18). This may explain why the LIR and KIR motifs are localized together on the p62 molecule, since then KEAP1 can only be degraded as a part of p62 condensates, and the degradation of KEAP1 is then a specific response to the accumulation of p62 condensates.

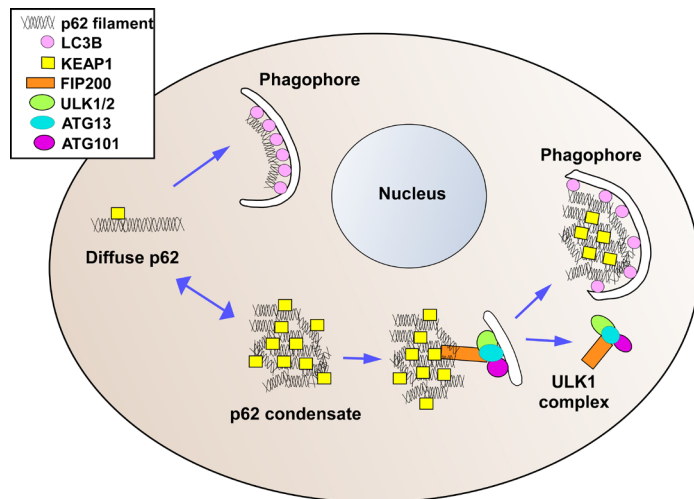


Figure 18 Model of p62 phase separation.

P62 can interact with FIP200, ATG8s and KEAP1 by binding to them via the corresponding interaction regions. P62 can bind one protein at the time. LC3B and FIP200 will be always located at the outside part of the condensates. Keap1 is located inside. P62-LC3B interaction is responsible for the degradation of diffused p62 fraction. When

condensate is formed KEAP1 will be always found together with p62. For the degradation of condensate, the initiation complex needs to bind to p62 via FIP200 mediated interaction so the formation of mPAS will start. At the elongation step, the initiation complex is not needed anymore so there is a switch in binding to p62 from FIP200 back to LC3B. When the isolation membrane is closed the autophagosome is formed.

A pre-print paper was shown that K344E mutation increases the affinity of p62 to bind to KEAP1 because it promotes the phosphorylation of S349 residue of p62 (Omar et al., 2021). Perhaps the preference of p62 for ATG8s or KEAP1 is regulated by the K344, which is located between the LIR and the KIR sequence. It is possible that a modification on K344 residue or another residue of this region could regulate the binding preference for KEAP1 or ATG8s. In the abovementioned paper (Omar et al., 2021), several different point mutants were tested, some belonging to the LIR region including D336N or L341V and some belonging to the KIR region, like P348L or G351A. In both cases, there were variations in binding affinity between ATG8s and/or KEAP1. This supports the notion that these two motifs actually work as a co-regulated domain.

4.5 KEAP1 is degraded by autophagy in response to starvation, and this depends on p62

Previous studies have shown that KEAP1 is degraded by selective autophagy and that this strongly depends on p62 and its ability to bind to KEAP1 via its KIR motif (Jain et al., 2010). In paper III, we observed that endogenous KEAP1 is efficiently degraded by selective autophagy under starvation, and this was only seen in cells expressing p62. We hypothesise that p62 droplets or gels are degraded by macroautophagy and that KEAP1 is degraded as a part of these structures. We further propose that the diffuse fractions of p62 may perhaps be

more efficiently degraded by endosomal microautophagy, and that KEAP1 is not degraded via this pathway. However, this hypothesis remains to be rigorously tested.

4.6 The p62 filament is evolutionary conserved

p62 and NBR1 are evolutionarily related, and the current proteins resulted from a gene duplication that occurred early in the metazoan development (Svenning et al., 2011). It seems that NBR1 lost its ability to polymerize shortly after this duplication event, while the polymeric PB1 domain was kept in p62. The p62/Nbr1 orthologue is evolutionary conserved and found in all eukaryotic species except for fungi (Svenning et al., 2011). Based on higher sequence similarity to metazoan Nbr1 than to metazoan p62, non-metazoan p62/Nbr1 orthologues have been named Nbr1, but they contain features from both the two metazoan proteins. The first non-metazoan orthologue to be studied was the protein from the plant *Arabidopsis thaliana* (AtNbr1), and this protein contained several features characteristic for p62, including a polymeric PB1 domain, a LIR motif, and C-terminal UBA domains with a low intrinsic affinity for ubiquitin (Svenning et al., 2011) It also formed ubiquitin-positive condensates when expressed in cells and was degraded by LIR dependent selective autophagy. In Paper I, we confirmed that the PB1 domain of AtNbr1 formed filaments that resemble those formed by mammalian p62. Our conclusion is therefore that p62/Nbr1 is responsible for the formation of a distinct type of condensate that is crucial in selective autophagy and conserved in all eukaryotic species except for fungi. When analyzing p62/Nbr1 genes in different species, a surprising finding was that virtually all species contained only a single p62/Nbr1 gene, suggesting a selective pressure against the presence of two different polymeric variants.

5. Methodological consideration

5.1 Construction of Stable Cell Lines

We used a retroviral terminal repeat (LTR) promoter fused to EGFP to reconstitute MEF (mouse embryonic fibroblasts) p62 KO cells. MEF cells are ideal for microscopy and the expression level of p62 is not as high as in HeLa cells. HeLa cells have different p62 body

formation and create more p62 bodies. HeLa cells allows p62 to aggregate a lot, so some of the p62 variant cell lines from paper III would probably cluster even more. We avoided HEK293 cells mostly because of technical reasons. We used a lot of different cell lines and HEK cells are more sensitive, detached easily and not ideal for confocal microscopy. Also, they tend to form fewer p62 dots than HeLa or MEF cells.

Unfortunately, we cannot be sure that the expression levels that we observed are similar to the endogenous.

One of the biggest challenges that this project had to overcome was the limited available market for reliable antibodies generated for MEF cells. Many of the antibodies that we have validated and used in the lab are mouse anti-human antibodies. A lot of experiments were not presented in the thesis and a lot we had to avoid, because of the antibody limitation.

5.2 Cell growth and cell culture

For this study, we used 10 different cell lines. Taking care of so many cell lines can be challenging especially if they have very dissimilar growth rates and show different sensitivity to environmental parameters. One problem, that appeared quite early, was the sensitivity of the cell lines. We had to transfer the cells to an incubator, separate from the rest of the research group. Temperature changes promoted the detachment of the cells and cell death. Though, not all the cell lines were affected. The second problem was that all the cell lines did not have the same growth rate. K420R\K435R, K420Q\K435Q, (K\R), (K\R) R7K\R420K\R435K and (K\R) R7K\R420Q\R435Q cell lines were growing at a slow rate, and it was easy to lose the cell line if the cells were split too thin. For that reason, we could not split them more than 1:4. On the other hand, the K420R and K435R cell lines were growing extremely fast, but again if you split them too thin, it was possible to lose the cell line. The third problem was focused on the K420R\K435R cell line. This cell line had a slow growth rate and had to be kept in Blasticidin all the time to avoid losing the expression of the GFP-p62 construct. For some of the GST-p62 constructs, treatments with TSA and sulforaphane were very difficult to perform because the cells would either die or stop growing. Last but not least, the (K\R) R7K\R420K\R435K cell line had a high death rate, which created problems for comparative analyses where different cell lines were compared.

5.3 Western blotting assay

Western blotting is a well-established method for measuring protein levels, and it is really sensitive when the protein or proteins of interest are in low concentrations. In this technique, a mixture of proteins is separated based on molecular weight, through SDS PAGE gel electrophoresis. The separated proteins are transferred to a membrane and the membrane is incubated with antibodies specific to the protein of interest (Mahmood and Yang, 2012). In order to be able to compare different samples, the loading of the samples needs to be equal. Proteins that are constitutively expressed are commonly used as loading controls. Examples are actin, tubulin, GAPDH (glyceraldehyde 3-phosphate dehydrogenase). However, often we cannot be completely sure about their actual levels since these proteins exist in high levels inside the cells, and it may be difficult to detect differences due to potential overexposure. Another issue is the quantification of the results. Western blotting is a semi-quantitative method since it provides a relative comparison of protein levels, not an absolute measure of quantity. The quantification problem is most challenging when using the chemiluminescence system to develop the membranes since the linear range is very limited and hard to control. We used this method when we wanted to detect a pattern of increase or decrease or binding or not. When there was a need for more accurate quantifications, we used the LICOR near-infrared (NIR) detection system to develop our membranes. In this method the primary antibodies used are linked to fluorescence residues. Moreover, instead of using a housekeeper protein as a loading control, the LICOR system gives the option to measure the total amount of the proteins from the lysate (Revert™ Total protein stain). In more simplified words, it allows you to measure the total amount of proteins similarly as done when using a Ponceau S staining of the membrane.

In our studies in Paper III, we compared p62 levels in 10 different cell lines. Among those, some created very largely, gel-like p62 bodies like K420R, some clusters of bodies like (K\R) R7K and (K\R) R7K\R420K. Solubilization of the different aggregates poses difficulties not easily resolved. Normally we use 1-2% boiling SDS buffer to solubilize proteins. This was not sufficiently effectively extracting the most aggregated p62 constructs. At the end, we concluded that the best lysis buffer to harvest the cells was containing 5% SDS, but that should be followed with 10-sec sonication of the lysates after boiling them first.

5.4 GST pull-down assay

GST pull-down assay is an *in vitro* assay, which allows us to detect direct interactions between proteins. As all assays, it has its limitations. Since proteins are *in vitro* translated, post-translational modifications are only partially present. This may lead to false-negative results; in case a specific modification is required for the interaction between the *in vitro* translated protein and the one that is fused to the GST beads. On the other hand, usage of phosphomimic or acetyl-mimic mutants can partly overcome this problem and give reliable results, if the missing modifications are specific phosphorylations or acetylations. However, mimicry is still an artificial approximation. Furthermore, during this assay we create an artificial environment as inside the cells the two proteins being studied are not colocalized and do not meet. Also, there is a possibility that during the *in vitro* translation the protein may misfold and as a result one may experience loss or gain of binding. Despite the mentioned putative issues, GST-pull down assay is a very useful assay that usually can be trusted keeping in mind the importance of always using the proper controls, both negative and positive for binding with the GST-fused protein. Moreover, always our observations made using an *in vitro* assay should be compared with observations made by assays that are conducted in cells.

5.5 Ubiquitin-binding assay (Paper III)

In order to test the ubiquitin-binding of the different p62 constructs in cells, we performed a GST-pull down assay using lysates from the p62 mutant stable cell lines. An obstacle here was the buffer used for this assay. Normally, in a pulldown from cell lysates, the protocols use RIPA buffer in order to harvest the cells. As we already discuss in the western blotting part, some of our cell lines express p62 variants that are clustered, which is making them difficult to dissolve. Moreover, we could not use sonication to dissolve the lysate. For that reason, we used two different buffers to lyse the cells, one containing 1M UREA and one with 8M UREA. 1M UREA buffer is a medium-strength buffer, harsher than RIPA, which was perfect for p62 wt and constructs that have diffused background like K435R or K420R\K435R. Unfortunately, it was not strong enough for the ones that cluster, like (K\R) R7K and (K\R) R420K. So, we used 8M UREA buffer for lysing the cells. The next problem was that the 8M UREA buffer denatures p62 and unfolds the protein. For p62 to bind and the UBA domain to be functional, p62 needs to be folded. We solved this problem by diluting the 8M UREA lysates into 1M UREA before adding them to the GST-beads. 8M UREA will also inhibit the binding to the beads so this

dilution had a double positive effect. In a normal pull-down from cell lysates, 2 hours are enough for incubating the lysate together with the beads. In this case, we did it overnight in order to ensure that p62 will be able to fold back and then bind to ubiquitin. Fortunately, after all these optimizations of the protocol, we created a new trustworthy assay for pull-down of p62 from cell lysates.

5.6 Transient Transfection

Transient transfection of plasmids including the protein of interest usually fused to a fluorescent tag is a common fast and quite informative method to investigate if proteins are colocalized or where proteins are located. In this study, we used this method extensively, especially when we needed to overcome the problem of lacking good antibodies for staining of MEF cells. Most of the times though, we used it to perform the double-tag assay. Double-tag assay allows us to separate p62 protein which is located in the cytosol in p62 bodies from p62 protein that has been delivered to autolysosomes for degradation. Same applies if we want to detect an autophagic substrate, such as KEAP1. The assay is based on the stability of fluorescent proteins. In a double-tag system, there are two tags fused together with the protein of interest an mCherry and an EYFP tag. mCherry (red color) is stable in an acidic environment like an autolysosome, while the EYFP tag (green color) is not. So, when we observe red puncta under the confocal microscope, we know that they are autolysosomes, while the yellow puncta are p62 bodies or condensates that are located in the cytosol. The ratio between red and yellow puncta can be a significantly useful marker to measure the ability of different protein variants to be degraded by autophagy by quantifying red and yellow dots.

Unfortunately, using transient transfections is connected with overexpression of the proteins. Moreover, tags can interfere with the protein function and mobility in comparison to endogenous one and can lead to protein aggregation. Another issue is that transfection of extracellular DNA itself is a stress stimulus for the cells, which again can cause accumulation and disturbance of the proteins inside the cell-that can lead again to unwanted aggregation. In order to solve this problem, we observed the cells 48h after transfection, so the cells can be adjusted.

6. References

- Abbi, S., H. Ueda, C. Zheng, L.A. Cooper, J. Zhao, R. Christopher, and J.L. Guan. 2002. Regulation of focal adhesion kinase by a novel protein inhibitor FIP200. *Mol Biol Cell*. 13:3178-3191.
- Alberti, S., A. Gladfelter, and T. Mittag. 2019. Considerations and Challenges in Studying Liquid-Liquid Phase Separation and Biomolecular Condensates. *Cell*. 176:419-434.
- Alemu, E.A., T. Lamark, K.M. Torgersen, A.B. Birgisdottir, K.B. Larsen, A. Jain, H. Olsvik, A. Øvervatn, V. Kirkin, and T. Johansen. 2012. ATG8 family proteins act as scaffolds for assembly of the ULK complex: sequence requirements for LC3-interacting region (LIR) motifs. *J Biol Chem*. 287:39275-39290.
- Ali, D.M., S.S. Ansari, M. Zepp, M. Knapp-Mohammady, and M.R. Berger. 2019. Optineurin downregulation induces endoplasmic reticulum stress, chaperone-mediated autophagy, and apoptosis in pancreatic cancer cells. *Cell Death Discov*. 5:128.
- Allen, E.A., and E.H. Baehrecke. 2020. Autophagy in animal development. *Cell Death Differ*. 27:903-918.
- Aman, Y., T. Schmauck-Medina, M. Hansen, R.I. Morimoto, A.K. Simon, I. Bjedov, K. Palikaras, A. Simonsen, T. Johansen, N. Tavernarakis, D.C. Rubinsztein, L. Partridge, G. Kroemer, J. Labbadia, and E.F. Fang. 2021. Autophagy in healthy aging and disease. *Nature Aging*. 1:634-650.
- Aparicio, R., M. Hansen, D.W. Walker, and C. Kumsta. 2020. The selective autophagy receptor SQSTM1/p62 improves lifespan and proteostasis in an evolutionarily conserved manner. *Autophagy*. 16:772-774.
- Bento, C.F., M. Renna, G. Ghislat, C. Puri, A. Ashkenazi, M. Vicinanza, F.M. Menzies, and D.C. Rubinsztein. 2016. Mammalian Autophagy: How Does It Work? *Annu Rev Biochem*. 85:685-713.
- Berkamp, S., S. Mostafavi, and C. Sachse. 2020. Structure and function of p62/SQSTM1 in the emerging framework of phase separation. *Febs j*.
- Birgisdottir Å, B., T. Lamark, and T. Johansen. 2013. The LIR motif - crucial for selective autophagy. *J Cell Sci*. 126:3237-3247.
- Birgisdottir Å, B., S. Mouilleron, Z. Bhujabal, M. Wirth, E. Sjøttem, G. Evjen, W. Zhang, R. Lee, N. O'Reilly, S.A. Tooze, T. Lamark, and T. Johansen. 2019. Members of the autophagy class III phosphatidylinositol 3-kinase complex I interact with GABARAP and GABARAPL1 via LIR motifs. *Autophagy*. 15:1333-1355.
- Bjørkøy, G., T. Lamark, A. Brech, H. Outzen, M. Perander, A. Overvatn, H. Stenmark, and T. Johansen. 2005. p62/SQSTM1 forms protein aggregates degraded by autophagy and has a protective effect on huntingtin-induced cell death. *J Cell Biol*. 171:603-614.
- Braak, H., D.R. Thal, and K. Del Tredici. 2011. Nerve cells immunoreactive for p62 in select hypothalamic and brainstem nuclei of controls and Parkinson's disease cases. *J Neural Transm (Vienna)*. 118:809-819.
- Chano, T., K. Kontani, K. Teramoto, H. Okabe, and S. Ikegawa. 2002. Truncating mutations of RB1CC1 in human breast cancer. *Nat Genet*. 31:285-288.
- Ciuffa, R., T. Lamark, A.K. Tarafder, A. Guesdon, S. Rybina, W.J. Hagen, T. Johansen, and C. Sachse. 2015. The selective autophagy receptor p62 forms a flexible filamentous helical scaffold. *Cell Rep*. 11:748-758.

- Collier, J.J., C. Guissart, M. Oláhová, S. Sasorith, F. Piron-Prunier, F. Suomi, D. Zhang, N. Martinez-Lopez, N. Leboucq, A. Bahr, S. Azzarello-Burri, S. Reich, L. Schöls, T.M. Polvikoski, P. Meyer, L. Larrieu, A.M. Schaefer, H.S. Alsaif, S. Alyamani, S. Zuchner, I.A. Barbosa, C. Deshpande, A. Pyle, A. Rauch, M. Synofzik, F.S. Alkuraya, F. Rivier, M. Ryten, R. McFarland, A. Delahodde, T.G. McWilliams, M. Koenig, and R.W. Taylor. 2021. Developmental Consequences of Defective ATG7-Mediated Autophagy in Humans. *N Engl J Med.* 384:2406-2417.
- Crabtree, M., and T. Nott. 2018. These Organelles Have No Membranes. *In The Scientist, The Scientist.*
- Dao, T.P., and C.A. Castañeda. 2020. Ubiquitin-Modulated Phase Separation of Shuttle Proteins: Does Condensate Formation Promote Protein Degradation? *Bioessays*:e2000036.
- Darvekar, S.R., J. Elvenes, H.B. Brenne, T. Johansen, and E. Sjøttem. 2014. SPBP is a sulforaphane induced transcriptional coactivator of NRF2 regulating expression of the autophagy receptor p62/SQSTM1. *PLoS One.* 9:e85262.
- Dice, J.F. 1982. Altered degradation of proteins microinjected into senescent human fibroblasts. *J Biol Chem.* 257:14624-14627.
- Dikic, I., and Z. Elazar. 2018. Mechanism and medical implications of mammalian autophagy. *Nat Rev Mol Cell Biol.* 19:349-364.
- Dowdle, W.E., B. Nyfeler, J. Nagel, R.A. Elling, S. Liu, E. Triantafellow, S. Menon, Z. Wang, A. Honda, G. Pardee, J. Cantwell, C. Luu, I. Cornella-Taracido, E. Harrington, P. Fekkes, H. Lei, Q. Fang, M.E. Digan, D. Burdick, A.F. Powers, S.B. Helliwell, S. D'Aquin, J. Bastien, H. Wang, D. Wiederschain, J. Kuerth, P. Bergman, D. Schwalb, J. Thomas, S. Ugwonal, F. Harbinski, J. Tallarico, C.J. Wilson, V.E. Myer, J.A. Porter, D.E. Bussiere, P.M. Finan, M.A. Labow, X. Mao, L.G. Hamann, B.D. Manning, R.A. Valdez, T. Nicholson, M. Schirle, M.S. Knapp, E.P. Keaney, and L.O. Murphy. 2014. Selective VPS34 inhibitor blocks autophagy and uncovers a role for NCOA4 in ferritin degradation and iron homeostasis in vivo. *Nat Cell Biol.* 16:1069-1079.
- Dunlop, E.A., and A.R. Tee. 2014. mTOR and autophagy: A dynamic relationship governed by nutrients and energy. *Seminars in Cell & Developmental Biology.* 36:121-129.
- Eyers, P.A. 2020. Marveling at the Incredible ULK4. *Structure.* 28:1181-1183.
- Falchetti, A., M. Di Stefano, F. Marini, F. Del Monte, C. Mavilia, D. Strigoli, M.L. De Feo, G. Isaia, L. Masi, A. Amedei, F. Cioppi, V. Ghinoi, S.M. Bonghi, G. Di Fede, C. Sferrazza, G.B. Rini, D. Melchiorre, M. Matucci-Cerinic, and M.L. Brandi. 2004. Two novel mutations at exon 8 of the Sequestosome 1 (SQSTM1) gene in an Italian series of patients affected by Paget's disease of bone (PDB). *J Bone Miner Res.* 19:1013-1017.
- Fan, W., Z. Tang, D. Chen, D. Moughon, X. Ding, S. Chen, M. Zhu, and Q. Zhong. 2010. Keap1 facilitates p62-mediated ubiquitin aggregate clearance via autophagy. *Autophagy.* 6:614-621.
- Fecto, F., J. Yan, S.P. Vemula, E. Liu, Y. Yang, W. Chen, J.G. Zheng, Y. Shi, N. Siddique, H. Arrat, S. Donkervoort, S. Ajroud-Driss, R.L. Sufit, S.L. Heller, H.X. Deng, and T. Siddique. 2011. SQSTM1 mutations in familial and sporadic amyotrophic lateral sclerosis. *Arch Neurol.* 68:1440-1446.
- Foster, A.D., L.L. Flynn, C. Cluning, F. Cheng, J.M. Davidson, A. Lee, N. Polain, R. Mejzini, N. Farrawell, J.J. Yerbury, R. Layfield, P.A. Akkari, and S.L. Rea. 2021. p62 overexpression

- induces TDP-43 cytoplasmic mislocalisation, aggregation and cleavage and neuronal death. *Sci Rep.* 11:11474.
- Fracchiolla, D., J. Sawa-Makarska, and S. Martens. 2017. Beyond Atg8 binding: The role of AIM/LIR motifs in autophagy. *Autophagy.* 13:978-979.
- Fu, T., J. Liu, Y. Wang, X. Xie, S. Hu, and L. Pan. 2018. Mechanistic insights into the interactions of NAP1 with the SKICH domains of NDP52 and TAX1BP1. *Proc Natl Acad Sci U S A.* 115:E11651-e11660.
- Fujioka, Y., J.M. Alam, D. Noshiro, K. Mouri, T. Ando, Y. Okada, A.I. May, R.L. Knorr, K. Suzuki, Y. Ohsumi, and N.N. Noda. 2020. Phase separation organizes the site of autophagosome formation. *Nature.* 578:301-305.
- Galluzzi, L., E.H. Baehrecke, A. Ballabio, P. Boya, J.M. Bravo-San Pedro, F. Cecconi, A.M. Choi, C.T. Chu, P. Codogno, M.I. Colombo, A.M. Cuervo, J. Debnath, V. Deretic, I. Dikic, E.L. Eskelinen, G.M. Fimia, S. Fulda, D.A. Gewirtz, D.R. Green, M. Hansen, J.W. Harper, M. Jäättelä, T. Johansen, G. Juhasz, A.C. Kimmelman, C. Kraft, N.T. Ktistakis, S. Kumar, B. Levine, C. Lopez-Otin, F. Madeo, S. Martens, J. Martinez, A. Melendez, N. Mizushima, C. Münz, L.O. Murphy, J.M. Penninger, M. Piacentini, F. Reggiori, D.C. Rubinsztein, K.M. Ryan, L. Santambrogio, L. Scorrano, A.K. Simon, H.U. Simon, A. Simonsen, N. Tavernarakis, S.A. Tooze, T. Yoshimori, J. Yuan, Z. Yue, Q. Zhong, and G. Kroemer. 2017. Molecular definitions of autophagy and related processes. *Embo j.* 36:1811-1836.
- Galluzzi, L., and D.R. Green. 2019. Autophagy-Independent Functions of the Autophagy Machinery. *Cell.* 177:1682-1699.
- Gao, J., M. Ohtsubo, Y. Hotta, and S. Minoshima. 2014. Oligomerization of optineurin and its oxidative stress- or E50K mutation-driven covalent cross-linking: possible relationship with glaucoma pathology. *PLoS One.* 9:e101206.
- Gatica, D., V. Lahiri, and D.J. Klionsky. 2018. Cargo recognition and degradation by selective autophagy. *Nat Cell Biol.* 20:233-242.
- Glick, D., S. Barth, and K.F. Macleod. 2010. Autophagy: cellular and molecular mechanisms. *J Pathol.* 221:3-12.
- Grice, G.L., and J.A. Nathan. 2016. The recognition of ubiquitinated proteins by the proteasome. *Cell Mol Life Sci.* 73:3497-3506.
- Grumati, P., and I. Dikic. 2018. Ubiquitin signaling and autophagy. *J Biol Chem.* 293:5404-5413.
- Hara, T., A. Takamura, C. Kishi, S. Iemura, T. Natsume, J.L. Guan, and N. Mizushima. 2008. FIP200, a ULK-interacting protein, is required for autophagosome formation in mammalian cells. *J Cell Biol.* 181:497-510.
- Heath, R.J., G. Goel, L.A. Baxt, J.S. Rush, V. Mohanan, G.L.C. Paulus, V. Jani, K.G. Lassen, and R.J. Xavier. 2016. RNF166 Determines Recruitment of Adaptor Proteins during Antibacterial Autophagy. *Cell Rep.* 17:2183-2194.
- Hollenstein, D.M., and C. Kraft. 2020. Autophagosomes are formed at a distinct cellular structure. *Curr Opin Cell Biol.* 65:50-57.
- Hosokawa, N., T. Hara, T. Kaizuka, C. Kishi, A. Takamura, Y. Miura, S. Iemura, T. Natsume, K. Takehana, N. Yamada, J.L. Guan, N. Oshiro, and N. Mizushima. 2009. Nutrient-dependent mTORC1 association with the ULK1-Atg13-FIP200 complex required for autophagy. *Mol Biol Cell.* 20:1981-1991.

- Huang, K.-Y., T.-Y. Lee, H.-J. Kao, C.-T. Ma, C.-C. Lee, T.-H. Lin, W.-C. Chang, and H.-D. Huang. 2019. dbPTM in 2019: exploring disease association and cross-talk of post-translational modifications. *Nucleic acids research*. 47:D298-D308.
- Hyman, A.A., C.A. Weber, and F. Jülicher. 2014. Liquid-Liquid Phase Separation in Biology. *Annual Review of Cell and Developmental Biology*. 30:39-58.
- Haack, T.B., E. Ignatius, J. Calvo-Garrido, A. Iuso, P. Isohanni, C. Maffezzini, T. Lönnqvist, A. Suomalainen, M. Gorza, L.S. Kremer, E. Graf, M. Hartig, R. Berutti, M. Paucar, P. Svenningsson, H. Stranneheim, G. Brandberg, A. Wedell, M.A. Kurian, S.A. Hayflick, P. Venco, V. Tiranti, T.M. Strom, M. Dichgans, R. Horvath, E. Holinski-Feder, C. Freyer, T. Meitinger, H. Prokisch, J. Senderek, A. Wredenberg, C.J. Carroll, and T. Klopstock. 2016. Absence of the Autophagy Adaptor SQSTM1/p62 Causes Childhood-Onset Neurodegeneration with Ataxia, Dystonia, and Gaze Palsy. *Am J Hum Genet*. 99:735-743.
- Ichimura, Y., T. Kumanomidou, Y.S. Sou, T. Mizushima, J. Ezaki, T. Ueno, E. Kominami, T. Yamane, K. Tanaka, and M. Komatsu. 2008. Structural basis for sorting mechanism of p62 in selective autophagy. *J Biol Chem*. 283:22847-22857.
- Ichimura, Y., S. Waguri, Y.S. Sou, S. Kageyama, J. Hasegawa, R. Ishimura, T. Saito, Y. Yang, T. Kouno, T. Fukutomi, T. Hoshii, A. Hirao, K. Takagi, T. Mizushima, H. Motohashi, M.S. Lee, T. Yoshimori, K. Tanaka, M. Yamamoto, and M. Komatsu. 2013. Phosphorylation of p62 activates the Keap1-Nrf2 pathway during selective autophagy. *Mol Cell*. 51:618-631.
- Isogai, S., D. Morimoto, K. Arita, S. Unzai, T. Tenno, J. Hasegawa, Y.S. Sou, M. Komatsu, K. Tanaka, M. Shirakawa, and H. Tochio. 2011. Crystal structure of the ubiquitin-associated (UBA) domain of p62 and its interaction with ubiquitin. *J Biol Chem*. 286:31864-31874.
- Jain, A., T. Lamark, E. Sjøttem, K.B. Larsen, J.A. Awuh, A. Øvervatn, M. McMahon, J.D. Hayes, and T. Johansen. 2010. p62/SQSTM1 is a target gene for transcription factor NRF2 and creates a positive feedback loop by inducing antioxidant response element-driven gene transcription. *J Biol Chem*. 285:22576-22591.
- Jakobi, A.J., S.T. Huber, S.A. Mortensen, S.W. Schultz, A. Palara, T. Kuhm, B.K. Shrestha, T. Lamark, W.J.H. Hagen, M. Wilmanns, T. Johansen, A. Brech, and C. Sachse. 2020. Structural basis of p62/SQSTM1 helical filaments and their role in cellular cargo uptake. *Nat Commun*. 11:440.
- Jiang, S., B. Heller, V.S. Tagliabracci, L. Zhai, J.M. Irimia, A.A. DePaoli-Roach, C.D. Wells, A.V. Skurat, and P.J. Roach. 2010. Starch binding domain-containing protein 1/genethonin 1 is a novel participant in glycogen metabolism. *J Biol Chem*. 285:34960-34971.
- Johansen, T., B. Birgisdottir Å, J. Huber, A. Kniss, V. Dötsch, V. Kirkin, and V.V. Rogov. 2017. Methods for Studying Interactions Between Atg8/LC3/GABARAP and LIR-Containing Proteins. *Methods Enzymol*. 587:143-169.
- Johansen, T., and T. Lamark. 2011. Selective autophagy mediated by autophagic adapter proteins. *Autophagy*. 7:279-296.
- Johansen, T., and T. Lamark. 2020. Selective Autophagy: ATG8 Family Proteins, LIR Motifs and Cargo Receptors. *J Mol Biol*. 432:80-103.
- Jung, C.H., C.B. Jun, S.H. Ro, Y.M. Kim, N.M. Otto, J. Cao, M. Kundu, and D.H. Kim. 2009. ULK-Atg13-FIP200 complexes mediate mTOR signaling to the autophagy machinery. *Mol Biol Cell*. 20:1992-2003.

- Kageyama, S., S.R. Gudmundsson, Y.S. Sou, Y. Ichimura, N. Tamura, S. Kazuno, T. Ueno, Y. Miura, D. Noshiro, M. Abe, T. Mizushima, N. Miura, S. Okuda, H. Motohashi, J.A. Lee, K. Sakimura, T. Ohe, N.N. Noda, S. Waguri, E.L. Eskelinen, and M. Komatsu. 2021. p62/SQSTM1-droplet serves as a platform for autophagosome formation and anti-oxidative stress response. *Nat Commun.* 12:16.
- Kaushik, S., and A.M. Cuervo. 2016. AMPK-dependent phosphorylation of lipid droplet protein PLIN2 triggers its degradation by CMA. *Autophagy.* 12:432-438.
- Kaushik, S., and A.M. Cuervo. 2018. The coming of age of chaperone-mediated autophagy. *Nat Rev Mol Cell Biol.* 19:365-381.
- Khoury, G.A., R.C. Baliban, and C.A. Floudas. 2011. Proteome-wide post-translational modification statistics: frequency analysis and curation of the swiss-prot database. *Scientific reports.* 1:1-5.
- Kimura, T., A. Jain, S.W. Choi, M.A. Mandell, K. Schroder, T. Johansen, and V. Deretic. 2015. TRIM-mediated precision autophagy targets cytoplasmic regulators of innate immunity. *J Cell Biol.* 210:973-989.
- Kirkin, V., T. Lamark, T. Johansen, and I. Dikic. 2009a. NBR1 co-operates with p62 in selective autophagy of ubiquitinated targets. *Autophagy.* 5:732-733.
- Kirkin, V., T. Lamark, Y.S. Sou, G. Bjørkøy, J.L. Nunn, J.A. Bruun, E. Shvets, D.G. McEwan, T.H. Clausen, P. Wild, I. Bilusic, J.P. Theurillat, A. Øvervatn, T. Ishii, Z. Elazar, M. Komatsu, I. Dikic, and T. Johansen. 2009b. A role for NBR1 in autophagosomal degradation of ubiquitinated substrates. *Mol Cell.* 33:505-516.
- Kirkin, V., and V.V. Rogov. 2019. A Diversity of Selective Autophagy Receptors Determines the Specificity of the Autophagy Pathway. *Mol Cell.* 76:268-285.
- Klionsky, D.J. 2008. Autophagy revisited: a conversation with Christian de Duve. *Autophagy.* 4:740-743.
- Komatsu, M., H. Kurokawa, S. Waguri, K. Taguchi, A. Kobayashi, Y. Ichimura, Y.S. Sou, I. Ueno, A. Sakamoto, K.I. Tong, M. Kim, Y. Nishito, S. Iemura, T. Natsume, T. Ueno, E. Kominami, H. Motohashi, K. Tanaka, and M. Yamamoto. 2010. The selective autophagy substrate p62 activates the stress responsive transcription factor Nrf2 through inactivation of Keap1. *Nat Cell Biol.* 12:213-223.
- Kriegenberg, F., C. Ungermann, and F. Reggiori. 2018. Coordination of Autophagosome-Lysosome Fusion by Atg8 Family Members. *Curr Biol.* 28:R512-r518.
- Lahiri, P., V. Schmidt, C. Smole, I. Kufferath, H. Denk, P. Strnad, T. Rüllicke, L.F. Fröhlich, and K. Zatloukal. 2016. p62/Sequestosome-1 Is Indispensable for Maturation and Stabilization of Mallory-Denk Bodies. *PLoS One.* 11:e0161083.
- Lamark, T., and T. Johansen. 2021. Mechanisms of Selective Autophagy. *Annu Rev Cell Dev Biol.*
- Lamark, T., M. Perander, H. Outzen, K. Kristiansen, A. Øvervatn, E. Michaelsen, G. Bjørkøy, and T. Johansen. 2003. Interaction codes within the family of mammalian Phox and Bem1p domain-containing proteins. *J Biol Chem.* 278:34568-34581.
- Lamark, T., S. Svenning, and T. Johansen. 2017. Regulation of selective autophagy: the p62/SQSTM1 paradigm. *Essays in Biochemistry.* 61:609-624.
- Lau, A., X.J. Wang, F. Zhao, N.F. Villeneuve, T. Wu, T. Jiang, Z. Sun, E. White, and D.D. Zhang. 2010. A noncanonical mechanism of Nrf2 activation by autophagy deficiency: direct interaction between Keap1 and p62. *Mol Cell Biol.* 30:3275-3285.

- Lee, Y., T.F. Chou, S.K. Pittman, A.L. Keith, B. Razani, and C.C. Wehl. 2017. Keap1/Cullin3 Modulates p62/SQSTM1 Activity via UBA Domain Ubiquitination. *Cell Rep.* 19:188-202.
- Legge, G.B., M.A. Martinez-Yamout, D.M. Hambly, T. Trinh, B.M. Lee, H.J. Dyson, and P.E. Wright. 2004. ZZ domain of CBP: an unusual zinc finger fold in a protein interaction module. *J Mol Biol.* 343:1081-1093.
- Levine, B., and G. Kroemer. 2019. Biological Functions of Autophagy Genes: A Disease Perspective. *Cell.* 176:11-42.
- Li, J., R. Zhu, K. Chen, H. Zheng, H. Zhao, C. Yuan, H. Zhang, C. Wang, and M. Zhang. 2018. Potent and specific Atg8-targeting autophagy inhibitory peptides from giant ankyrins. *Nat Chem Biol.* 14:778-787.
- Li, L., M. Tong, Y. Fu, F. Chen, S. Zhang, H. Chen, X. Ma, D. Li, X. Liu, and Q. Zhong. 2021. Lipids and membrane-associated proteins in autophagy. *Protein & Cell.* 12:520-544.
- Li, W.W., J. Li, and J.K. Bao. 2012. Microautophagy: lesser-known self-eating. *Cell Mol Life Sci.* 69:1125-1136.
- Lim, J., M.L. Lachenmayer, S. Wu, W. Liu, M. Kundu, R. Wang, M. Komatsu, Y.J. Oh, Y. Zhao, and Z. Yue. 2015. Proteotoxic Stress Induces Phosphorylation of p62/SQSTM1 by ULK1 to Regulate Selective Autophagic Clearance of Protein Aggregates. *PLOS Genetics.* 11:e1004987.
- Linares, J.F., R. Amanchy, K. Greis, M.T. Diaz-Meco, and J. Moscat. 2011. Phosphorylation of p62 by cdk1 controls the timely transit of cells through mitosis and tumor cell proliferation. *Mol Cell Biol.* 31:105-117.
- Liu, W.J., L. Ye, W.F. Huang, L.J. Guo, Z.G. Xu, H.L. Wu, C. Yang, and H.F. Liu. 2016. p62 links the autophagy pathway and the ubiquitin-proteasome system upon ubiquitinated protein degradation. *Cell Mol Biol Lett.* 21:29.
- Long, J., T.P. Garner, M.J. Pandya, C.J. Craven, P. Chen, B. Shaw, M.P. Williamson, R. Layfield, and M.S. Searle. 2010. Dimerisation of the UBA domain of p62 inhibits ubiquitin binding and regulates NF-kappaB signalling. *J Mol Biol.* 396:178-194.
- Maeda, S., C. Otomo, and T. Otomo. 2019. The autophagic membrane tether ATG2A transfers lipids between membranes. *Elife.* 8.
- Mahmood, T., and P.C. Yang. 2012. Western blot: technique, theory, and trouble shooting. *N Am J Med Sci.* 4:429-434.
- Mandell, M.A., A. Jain, J. Arko-Mensah, S. Chauhan, T. Kimura, C. Dinkins, G. Silvestri, J. Münch, F. Kirchhoff, A. Simonsen, Y. Wei, B. Levine, T. Johansen, and V. Deretic. 2014. TRIM proteins regulate autophagy and can target autophagic substrates by direct recognition. *Dev Cell.* 30:394-409.
- Marchbank, K., S. Waters, R.G. Roberts, E. Solomon, and C.A. Whitehouse. 2012. MAP1B Interaction with the FW Domain of the Autophagic Receptor Nbr1 Facilitates Its Association to the Microtubule Network. *International Journal of Cell Biology.* 2012:208014.
- Marshall, R.S., Z. Hua, S. Mali, F. McLoughlin, and R.D. Vierstra. 2019. ATG8-Binding UIM Proteins Define a New Class of Autophagy Adaptors and Receptors. *Cell.* 177:766-781.e724.
- Matoba, K., T. Kotani, A. Tsutsumi, T. Tsuji, T. Mori, D. Noshiro, Y. Sugita, N. Nomura, S. Iwata, Y. Ohsumi, T. Fujimoto, H. Nakatogawa, M. Kikkawa, and N.N. Noda. 2020.

- Atg9 is a lipid scramblase that mediates autophagosomal membrane expansion. *Nature Structural & Molecular Biology*. 27:1185-1193.
- Matsumoto, G., T. Shimogori, N. Hattori, and N. Nukina. 2015. TBK1 controls autophagosomal engulfment of polyubiquitinated mitochondria through p62/SQSTM1 phosphorylation. *Hum Mol Genet*. 24:4429-4442.
- Matsumoto, G., K. Wada, M. Okuno, M. Kurosawa, and N. Nukina. 2011. Serine 403 phosphorylation of p62/SQSTM1 regulates selective autophagic clearance of ubiquitinated proteins. *Mol Cell*. 44:279-289.
- Mejlvang, J., H. Olsvik, S. Svenning, J.A. Bruun, Y.P. Abudu, K.B. Larsen, A. Brech, T.E. Hansen, H. Brenne, T. Hansen, H. Stenmark, and T. Johansen. 2018. Starvation induces rapid degradation of selective autophagy receptors by endosomal microautophagy. *J Cell Biol*. 217:3640-3655.
- Memisoglu, G., V.V. Eapen, Y. Yang, D.J. Klionsky, and J.E. Haber. 2019. PP2C phosphatases promote autophagy by dephosphorylation of the Atg1 complex. *Proc Natl Acad Sci U S A*. 116:1613-1620.
- Mercer, C.A., A. Kaliappan, and P.B. Dennis. 2009. A novel, human Atg13 binding protein, Atg101, interacts with ULK1 and is essential for macroautophagy. *Autophagy*. 5:649-662.
- Mijaljica, D., T.Y. Nazarko, J.H. Brumell, W.P. Huang, M. Komatsu, M. Prescott, A. Simonsen, A. Yamamoto, H. Zhang, D.J. Klionsky, and R.J. Devenish. 2012. Receptor protein complexes are in control of autophagy. *Autophagy*. 8:1701-1705.
- Mizushima, N., and B. Levine. 2010. Autophagy in mammalian development and differentiation. *Nat Cell Biol*. 12:823-830.
- Mizushima, N., B. Levine, A.M. Cuervo, and D.J. Klionsky. 2008. Autophagy fights disease through cellular self-digestion. *Nature*. 451:1069-1075.
- Mizushima, N., T. Yoshimori, and Y. Ohsumi. 2011. The role of Atg proteins in autophagosome formation. *Annu Rev Cell Dev Biol*. 27:107-132.
- Morita, K., Y. Hama, T. Izume, N. Tamura, T. Ueno, Y. Yamashita, Y. Sakamaki, K. Mimura, H. Morishita, W. Shihoya, O. Nureki, H. Mano, and N. Mizushima. 2018. Genome-wide CRISPR screen identifies TMEM41B as a gene required for autophagosome formation. *J Cell Biol*. 217:3817-3828.
- Nakamura, S., J. Hidema, W. Sakamoto, H. Ishida, and M. Izumi. 2018. Selective Elimination of Membrane-Damaged Chloroplasts via Microautophagy. *Plant Physiology*. 177:1007-1026.
- Newman, A.C., C.L. Scholefield, A.J. Kemp, M. Newman, E.G. McIver, A. Kamal, and S. Wilkinson. 2012. TBK1 kinase addiction in lung cancer cells is mediated via autophagy of Tax1bp1/Ndp52 and non-canonical NF- κ B signalling. *PLoS One*. 7:e50672.
- Nguyen, T.N., B.S. Padman, J. Usher, V. Oorschot, G. Ramm, and M. Lazarou. 2016. Atg8 family LC3/GABARAP proteins are crucial for autophagosome-lysosome fusion but not autophagosome formation during PINK1/Parkin mitophagy and starvation. *J Cell Biol*. 215:857-874.
- Nishimura, T., and S.A. Tooze. 2020. Emerging roles of ATG proteins and membrane lipids in autophagosome formation. *Cell Discov*. 6:32.
- Noda, N.N. 2021. Atg2 and Atg9: Intermembrane and interleaflet lipid transporters driving autophagy. *Biochim Biophys Acta Mol Cell Biol Lipids*. 1866:158956.

- Noda, N.N., H. Kumeta, H. Nakatogawa, K. Satoo, W. Adachi, J. Ishii, Y. Fujioka, Y. Ohsumi, and F. Inagaki. 2008. Structural basis of target recognition by Atg8/LC3 during selective autophagy. *Genes Cells*. 13:1211-1218.
- Noda, N.N., Z. Wang, and H. Zhang. 2020. Liquid-liquid phase separation in autophagy. *J Cell Biol*. 219.
- Nthiga, T.M., B. Kumar Shrestha, E. Sjøttem, J.A. Bruun, K. Bowitz Larsen, Z. Bhujabal, T. Lamark, and T. Johansen. 2020. CALCOCO1 acts with VAMP-associated proteins to mediate ER-phagy. *Embo j*. 39:e103649.
- Nthiga, T.M., B.K. Shrestha, J.A. Bruun, K.B. Larsen, T. Lamark, and T. Johansen. 2021. Regulation of Golgi turnover by CALCOCO1-mediated selective autophagy. *J Cell Biol*. 220.
- Ohsumi, Y. 2014. Historical landmarks of autophagy research. *Cell Res*. 24:9-23.
- Oku, M., and Y. Sakai. 2018. Three Distinct Types of Microautophagy Based on Membrane Dynamics and Molecular Machineries. *Bioessays*. 40:e1800008.
- Omar, F.M., Y. Ichimura, S. Kageyama, A.H. El-Gowily, Y.S. Sou, M. Koike, N.N. Noda, and M. Komatsu. 2021. Droplets of amyotrophic lateral sclerosis-associated p62/SQSTM1 mutants show slower inner fluidity. *bioRxiv 2021.06.07.447422 doi: <https://doi.org/10.1101/2021.06.07.447422>*.
- Onyike, C.U., and J. Diehl-Schmid. 2013. The epidemiology of frontotemporal dementia. *Int Rev Psychiatry*. 25:130-137.
- Otomo, T., S. Chowdhury, and G.C. Lander. 2018. The rod-shaped ATG2A-WIPI4 complex tethers membranes in vitro. *Contact (Thousand Oaks)*. 1.
- Overå, K.S., J. Garcia-Garcia, Z. Bhujabal, A. Jain, A. Øvervatn, K.B. Larsen, V. Deretic, T. Johansen, T. Lamark, and E. Sjøttem. 2019. TRIM32, but not its muscular dystrophy-associated mutant, positively regulates and is targeted to autophagic degradation by p62/SQSTM1. *J Cell Sci*. 132.
- Pan, J.A., Y. Sun, Y.P. Jiang, A.J. Bott, N. Jaber, Z. Dou, B. Yang, J.S. Chen, J.M. Catanzaro, C. Du, W.X. Ding, M.T. Diaz-Meco, J. Moscat, K. Ozato, R.Z. Lin, and W.X. Zong. 2016. TRIM21 Ubiquitylates SQSTM1/p62 and Suppresses Protein Sequestration to Regulate Redox Homeostasis. *Mol Cell*. 61:720-733.
- Pankiv, S., E.A. Alemu, A. Brech, J.A. Bruun, T. Lamark, A. Overvatn, G. Bjørkøy, and T. Johansen. 2010. FYCO1 is a Rab7 effector that binds to LC3 and PI3P to mediate microtubule plus end-directed vesicle transport. *J Cell Biol*. 188:253-269.
- Pankiv, S., T.H. Clausen, T. Lamark, A. Brech, J.A. Bruun, H. Outzen, A. Øvervatn, G. Bjørkøy, and T. Johansen. 2007. p62/SQSTM1 binds directly to Atg8/LC3 to facilitate degradation of ubiquitinated protein aggregates by autophagy. *J Biol Chem*. 282:24131-24145.
- Park, C., Y. Suh, and A.M. Cuervo. 2015. Regulated degradation of Chk1 by chaperone-mediated autophagy in response to DNA damage. *Nat Commun*. 6:6823.
- Parzych, K.R., and D.J. Klionsky. 2014. An overview of autophagy: morphology, mechanism, and regulation. *Antioxid Redox Signal*. 20:460-473.
- Peng, H., F. Yang, Q. Hu, J. Sun, C. Peng, Y. Zhao, and C. Huang. 2020. The ubiquitin-specific protease USP8 directly deubiquitinates SQSTM1/p62 to suppress its autophagic activity. *Autophagy*. 16:698-708.
- Peng, H., J. Yang, G. Li, Q. You, W. Han, T. Li, D. Gao, X. Xie, B.H. Lee, J. Du, J. Hou, T. Zhang, H. Rao, Y. Huang, Q. Li, R. Zeng, L. Hui, H. Wang, Q. Xia, X. Zhang, Y. He, M. Komatsu,

- I. Dikic, D. Finley, and R. Hu. 2017. Ubiquitylation of p62/sequestosome1 activates its autophagy receptor function and controls selective autophagy upon ubiquitin stress. *Cell Res.* 27:657-674.
- PhosphoSitePlus. 2003. PhosphoSitePlus. Vol. 2003.
- Pilli, M., J. Arko-Mensah, M. Ponpuak, E. Roberts, S. Master, M.A. Mandell, N. Dupont, W. Ornatowski, S. Jiang, S.B. Bradfute, J.A. Bruun, T.E. Hansen, T. Johansen, and V. Deretic. 2012. TBK-1 promotes autophagy-mediated antimicrobial defense by controlling autophagosome maturation. *Immunity.* 37:223-234.
- Ponting, C.P., D.J. Blake, K.E. Davies, J. Kendrick-Jones, and S.J. Winder. 1996. ZZ and TAZ: new putative zinc fingers in dystrophin and other proteins. *Trends Biochem Sci.* 21:11-13.
- Prabakaran, T., C. Bodda, C. Krapp, B.C. Zhang, M.H. Christensen, C. Sun, L. Reinert, Y. Cai, S.B. Jensen, M.K. Skouboe, J.R. Nyengaard, C.B. Thompson, R.J. Lebbink, G.C. Sen, G. van Loo, R. Nielsen, M. Komatsu, L.N. Nejsum, M.R. Jakobsen, M. Gyrd-Hansen, and S.R. Paludan. 2018. Attenuation of cGAS-STING signaling is mediated by a p62/SQSTM1-dependent autophagy pathway activated by TBK1. *Embo j.* 37.
- Puri, C., M. Vicinanza, A. Ashkenazi, M.J. Gratian, Q. Zhang, C.F. Bento, M. Renna, F.M. Menzies, and D.C. Rubinsztein. 2018. The RAB11A-Positive Compartment Is a Primary Platform for Autophagosome Assembly Mediated by WIPI2 Recognition of PI3P-RAB11A. *Dev Cell.* 45:114-131.e118.
- Quintavalle, C., S. Di Costanzo, C. Zanca, I. Tasset, A. Fraldi, M. Incoronato, P. Mirabelli, M. Monti, A. Ballabio, P. Pucci, A.M. Cuervo, and G. Condorelli. 2014. Phosphorylation-regulated degradation of the tumor-suppressor form of PED by chaperone-mediated autophagy in lung cancer cells. *J Cell Physiol.* 229:1359-1368.
- Ramazi, S., and J. Zahiri. 2021. Post-translational modifications in proteins: resources, tools and prediction methods. *Database.* 2021.
- Richter, B., D.A. Sliter, L. Herhaus, A. Stolz, C. Wang, P. Beli, G. Zaffagnini, P. Wild, S. Martens, S.A. Wagner, R.J. Youle, and I. Dikic. 2016. Phosphorylation of OPTN by TBK1 enhances its binding to Ub chains and promotes selective autophagy of damaged mitochondria. *Proc Natl Acad Sci U S A.* 113:4039-4044.
- Ro, S.H., I.A. Semple, H. Park, H. Park, H.W. Park, M. Kim, J.S. Kim, and J.H. Lee. 2014. Sestrin2 promotes Unc-51-like kinase 1 mediated phosphorylation of p62/sequestosome-1. *Febs j.* 281:3816-3827.
- Rogov, V., V. Dötsch, T. Johansen, and V. Kirkin. 2014. Interactions between autophagy receptors and ubiquitin-like proteins form the molecular basis for selective autophagy. *Mol Cell.* 53:167-178.
- Russell, R.C., Y. Tian, H. Yuan, H.W. Park, Y.-Y. Chang, J. Kim, H. Kim, T.P. Neufeld, A. Dillin, and K.-L. Guan. 2013. ULK1 induces autophagy by phosphorylating Beclin-1 and activating VPS34 lipid kinase. *Nature Cell Biology.* 15:741-750.
- Sahu, R., S. Kaushik, C.C. Clement, E.S. Cannizzo, B. Scharf, A. Follenzi, I. Potolicchio, E. Nieves, A.M. Cuervo, and L. Santambrogio. 2011. Microautophagy of cytosolic proteins by late endosomes. *Dev Cell.* 20:131-139.
- Sánchez-Martín, P., Y.S. Sou, S. Kageyama, M. Koike, S. Waguri, and M. Komatsu. 2020. NBR1-mediated p62-liquid droplets enhance the Keap1-Nrf2 system. *EMBO Rep.* 21:e48902.

- Sanchez-Wandelmer, J., and F. Reggiori. 2013. Amphisomes: out of the autophagosome shadow? *Embo j.* 32:3116-3118.
- Schlütermann, D., N. Berleth, J. Deitersen, N. Wallot-Hieke, O. Friesen, W. Wu, F. Stuhldreier, Y. Sun, L. Berning, A. Friedrich, M.J. Mendiburo, C. Peter, C. Wiek, H. Hanenberg, A. Stefanski, K. Stühler, and B. Stork. 2021. FIP200 controls the TBK1 activation threshold at SQSTM1/p62-positive condensates. *Scientific Reports.* 11:13863.
- Schuck, S. 2020. Microautophagy - distinct molecular mechanisms handle cargoes of many sizes. *J Cell Sci.* 133.
- Schwanhäusser, B., D. Busse, N. Li, G. Dittmar, J. Schuchhardt, J. Wolf, W. Chen, and M. Selbach. 2013. Corrigendum: Global quantification of mammalian gene expression control. *Nature.* 495:126-127.
- Seglen, P.O., P.B. Gordon, I. Holen, and H. Høyvik. 1991. Hepatocytic autophagy. *Biomed Biochim Acta.* 50:373-381.
- Sehgal, P.B., J. Westley, K.M. Lerea, S. DiSenso-Browne, and J.D. Etlinger. 2020. Biomolecular condensates in cell biology and virology: Phase-separated membraneless organelles (MLOs). *Anal Biochem.* 597:113691.
- Shpilka, T., H. Weidberg, S. Pietrokovski, and Z. Elazar. 2011. Atg8: an autophagy-related ubiquitin-like protein family. *Genome Biol.* 12:226.
- Simonsen, A., and S.A. Tooze. 2009. Coordination of membrane events during autophagy by multiple class III PI3-kinase complexes. *J Cell Biol.* 186:773-782.
- Sun, D., R. Wu, P. Li, and L. Yu. 2020. Phase Separation in Regulation of Aggrephagy. *Journal of Molecular Biology.* 432:160-169.
- Sun, D., R. Wu, J. Zheng, P. Li, and L. Yu. 2018. Polyubiquitin chain-induced p62 phase separation drives autophagic cargo segregation. *Cell Res.* 28:405-415.
- Suzuki, K., Y. Kubota, T. Sekito, and Y. Ohsumi. 2007. Hierarchy of Atg proteins in pre-autophagosomal structure organization. *Genes Cells.* 12:209-218.
- Svenning, S., T. Lamark, K. Krause, and T. Johansen. 2011. Plant NBR1 is a selective autophagy substrate and a functional hybrid of the mammalian autophagic adapters NBR1 and p62/SQSTM1. *Autophagy.* 7:993-1010.
- Tamargo-Gómez, I., G.G. Martínez-García, M.F. Suárez, V. Rey, A. Fueyo, H. Codina-Martínez, G. Bretones, X.M. Caravia, E. Morel, N. Dupont, R. Cabo, C. Tomás-Zapico, S. Souquere, G. Pierron, P. Codogno, C. López-Otín, F. Fernández Á, and G. Mariño. 2021. ATG4D is the main ATG8 delipidating enzyme in mammalian cells and protects against cerebellar neurodegeneration. *Cell Death Differ.*
- Tekirdag, K., and A.M. Cuervo. 2018. Chaperone-mediated autophagy and endosomal microautophagy: Joint by a chaperone. *J Biol Chem.* 293:5414-5424.
- Thurston, T.L., G. Ryzhakov, S. Bloor, N. von Muhlinen, and F. Randow. 2009. The TBK1 adaptor and autophagy receptor NDP52 restricts the proliferation of ubiquitin-coated bacteria. *Nat Immunol.* 10:1215-1221.
- Tonelli, C., I.I.C. Chio, and D.A. Tuveson. 2018. Transcriptional Regulation by Nrf2. *Antioxid Redox Signal.* 29:1727-1745.
- Tooze, S.A., and T. Yoshimori. 2010. The origin of the autophagosomal membrane. *Nat Cell Biol.* 12:831-835.
- Tsukada, M., and Y. Ohsumi. 1993. Isolation and characterization of autophagy-defective mutants of *Saccharomyces cerevisiae*. *FEBS Lett.* 333:169-174.

- Tuck, P.S., R. Layfield, J. Walker, B. Mekkyail, and R. Francis. 2017. Adult Paget's disease of bone: a review. *Rheumatology (Oxford)*. 56:2050-2059.
- Tumbarello, D.A., P.T. Manna, M. Allen, M. Bycroft, S.D. Arden, J. Kendrick-Jones, and F. Buss. 2015. The Autophagy Receptor TAX1BP1 and the Molecular Motor Myosin VI Are Required for Clearance of Salmonella Typhimurium by Autophagy. *PLoS Pathog.* 11:e1005174.
- Turco, E., M. Witt, C. Abert, T. Bock-Bierbaum, M.-Y. Su, R. Trapannone, M. Sztacho, A. Danieli, X. Shi, G. Zaffagnini, A. Gamper, M. Schuschnig, D. Fracchiolla, D. Bernklau, J. Romanov, M. Hartl, J.H. Hurley, O. Daumke, and S. Martens. 2019. FIP200 Claw Domain Binding to p62 Promotes Autophagosome Formation at Ubiquitin Condensates. *Molecular Cell*. 74:330-346.e311.
- Turco E. , F.I., Martens S. 2020. FIP200 organizes the autophagy machinery at p62-ubiquitin condensates beyond activation of the ULK1 kinase. *BioRxiv*.
- Ueda, H., S. Abbi, C. Zheng, and J.L. Guan. 2000. Suppression of Pyk2 kinase and cellular activities by FIP200. *J Cell Biol.* 149:423-430.
- Varshavsky, A. 2011. The N-end rule pathway and regulation by proteolysis. *Protein Sci.* 20:1298-1345.
- von Muhlinen, N., M. Akutsu, B.J. Ravenhill, Á. Foeglein, S. Bloor, T.J. Rutherford, S.M. Freund, D. Komander, and F. Randow. 2012. LC3C, bound selectively by a noncanonical LIR motif in NDP52, is required for antibacterial autophagy. *Mol Cell*. 48:329-342.
- Walsh, C.T., and Roberts. 2006. Posttranslational Modification of Proteins: Expanding Nature's Inventory. *Biochemistry and Molecular Biology*. 34:459-462.
- Wang, Z., and H. Zhang. 2019. Phase Separation, Transition, and Autophagic Degradation of Proteins in Development and Pathogenesis. *Trends Cell Biol.* 29:417-427.
- Wei, Y., M. Liu, X. Li, J. Liu, and H. Li. 2018. Origin of the Autophagosome Membrane in Mammals. *Biomed Res Int.* 2018:1012789.
- Wild, P., H. Farhan, D.G. McEwan, S. Wagner, V.V. Rogov, N.R. Brady, B. Richter, J. Korac, O. Waidmann, C. Choudhary, V. Dötsch, D. Bumann, and I. Dikic. 2011. Phosphorylation of the autophagy receptor optineurin restricts Salmonella growth. *Science*. 333:228-233.
- Wu, F., Y. Watanabe, X.Y. Guo, X. Qi, P. Wang, H.Y. Zhao, Z. Wang, Y. Fujioka, H. Zhang, J.Q. Ren, T.C. Fang, Y.X. Shen, W. Feng, J.J. Hu, N.N. Noda, and H. Zhang. 2015. Structural Basis of the Differential Function of the Two C. elegans Atg8 Homologs, LGG-1 and LGG-2, in Autophagy. *Mol Cell*. 60:914-929.
- Wyant, G.A., M. Abu-Remaileh, E.M. Frenkel, N.N. Laqtom, V. Dharamdasani, C.A. Lewis, S.H. Chan, I. Heinze, A. Ori, and D.M. Sabatini. 2018. NUFIP1 is a ribosome receptor for starvation-induced ribophagy. *Science*. 360:751-758.
- Xie, Y., R. Kang, X. Sun, M. Zhong, J. Huang, D.J. Klionsky, and D. Tang. 2015. Posttranslational modification of autophagy-related proteins in macroautophagy. *Autophagy*. 11:28-45.
- Xie, Z., and D.J. Klionsky. 2007. Autophagosome formation: core machinery and adaptations. *Nat Cell Biol.* 9:1102-1109.
- Yang, Y., G. Wang, X. Huang, and Z. Du. 2014. Expression, purification and crystallization of the SKICH domain of human TAX1BP1. *Acta Crystallogr F Struct Biol Commun.* 70:619-623.

- Yang, Z., and D.J. Klionsky. 2010. Mammalian autophagy: core molecular machinery and signaling regulation. *Current Opinion in Cell Biology*. 22:124-131.
- You, Z., W.-X. Jiang, L.-Y. Qin, Z. Gong, W. Wan, J. Li, Y. Wang, H. Zhang, C. Peng, T. Zhou, C. Tang, and W. Liu. 2019a. Requirement for p62 acetylation in the aggregation of ubiquitylated proteins under nutrient stress. *Nature Communications*. 10:5792.
- You, Z., W.X. Jiang, L.Y. Qin, Z. Gong, W. Wan, J. Li, Y. Wang, H. Zhang, C. Peng, T. Zhou, C. Tang, and W. Liu. 2019b. Requirement for p62 acetylation in the aggregation of ubiquitylated proteins under nutrient stress. *Nat Commun*. 10:5792.
- Young, A.R., M. Narita, M. Ferreira, K. Kirschner, M. Sadaie, J.F. Darot, S. Tavaré, S. Arakawa, S. Shimizu, F.M. Watt, and M. Narita. 2009. Autophagy mediates the mitotic senescence transition. *Genes Dev*. 23:798-803.
- Zachari, M., and I.G. Ganley. 2017. The mammalian ULK1 complex and autophagy initiation. *Essays Biochem*. 61:585-596.
- Zaffagnini, G., A. Savova, A. Danieli, J. Romanov, S. Tremel, M. Ebner, T. Peterbauer, M. Sztacho, R. Trapannone, A.K. Tarafder, C. Sachse, and S. Martens. 2018. p62 filaments capture and present ubiquitinated cargos for autophagy. *Embo j*. 37.
- Zhang, D.D. 2010. The Nrf2-Keap1-ARE signaling pathway: The regulation and dual function of Nrf2 in cancer. *Antioxid Redox Signal*. 13:1623-1626.
- Zhang, Y., S.R. Mun, J.F. Linares, J. Ahn, C.G. Towers, C.H. Ji, B.E. Fitzwalter, M.R. Holden, W. Mi, X. Shi, J. Moscat, A. Thorburn, M.T. Diaz-Meco, Y.T. Kwon, and T.G. Kutateladze. 2018. ZZ-dependent regulation of p62/SQSTM1 in autophagy. *Nat Commun*. 9:4373.
- Zhang, Y., S.R. Mun, J.F. Linares, C.G. Towers, A. Thorburn, M.T. Diaz-Meco, Y.T. Kwon, and T.G. Kutateladze. 2019. Mechanistic insight into the regulation of SQSTM1/p62. *Autophagy*. 15:735-737.

All the images that have been used, contain the reference from the source that they have been copied and they have permission (where it was needed) from the Copyright Clearance Center's RightsLink®







PAPER-I

ARTICLE

<https://doi.org/10.1038/s41467-020-14343-8>

OPEN

Structural basis of p62/SQSTM1 helical filaments and their role in cellular cargo uptake

Arjen J. Jakobi ^{1,2,3,8}, Stefan T. Huber ^{1,8,9}, Simon A. Mortensen^{1,4,5,9}, Sebastian W. Schultz⁶, Anthimi Palara⁷, Tanja Kuhm^{1,8}, Birendra Kumar Shrestha⁷, Trond Lamark ⁷, Wim J.H. Hagen¹, Matthias Wilmanns ^{2,3}, Terje Johansen ⁷, Andreas Brech⁶ & Carsten Sachse ^{1,4,5*}

p62/SQSTM1 is an autophagy receptor and signaling adaptor with an N-terminal PB1 domain that forms the scaffold of phase-separated p62 bodies in the cell. The molecular determinants that govern PB1 domain filament formation *in vitro* remain to be determined and the role of p62 filaments inside the cell is currently unclear. We here determine four high-resolution cryo-EM structures of different human and Arabidopsis PB1 domain assemblies and observed a filamentous ultrastructure of p62/SQSTM1 bodies using correlative cellular EM. We show that oligomerization or polymerization, driven by a double arginine finger in the PB1 domain, is a general requirement for lysosomal targeting of p62. Furthermore, the filamentous assembly state of p62 is required for autophagosomal processing of the p62-specific cargo KEAP1. Our results show that using such mechanisms, p62 filaments can be critical for cargo uptake in autophagy and are an integral part of phase-separated p62 bodies.

¹European Molecular Biology Laboratory (EMBL), Structural and Computational Biology Unit, Meyerhofstraße 1, 69117 Heidelberg, Germany. ²European Molecular Biology Laboratory (EMBL), Hamburg Unit c/o DESY, Notkestraße 85, 22607 Hamburg, Germany. ³The Hamburg Centre for Ultrafast Imaging (CUI), Luruper Chaussee 149, 22761 Hamburg, Germany. ⁴Ernst-Ruska Centre for Microscopy and Spectroscopy with Electrons (ER-C-3/Structural Biology), Forschungszentrum Jülich, 52425 Jülich, Germany. ⁵JuStruct: Jülich Center for Structural Biology, Forschungszentrum Jülich, 52425 Jülich, Germany. ⁶Department of Molecular Cell Biology, Institute for Cancer Research, Oslo University Hospital, Montebello, N-0379 Oslo, Norway. ⁷Molecular Cancer Research Group, Institute of Medical Biology, University of Tromsø - The Arctic University of Norway, 9037 Tromsø, Norway. ⁸Present address: Department of Bionanoscience, Kavli Institute of Nanoscience, Delft University of Technology, Van der Maasweg 9, 2629 HZ Delft, The Netherlands. ⁹These authors contributed equally: Stefan T. Huber, Simon A. Mortensen. *email: c.sachse@fz-juelich.de

p62/SQSTM1 (from hereon p62) is a multifunctional adaptor protein that acts as a central scaffold protein in different cellular processes, such as autophagy and signaling¹. p62 has a tendency to cluster, and in human cells, is often observed in discrete punctae known as p62 bodies². The formation of these bodies is dependent on the amino-terminal PB1 domain of p62². PB1 domains are protein interaction modules with critical roles in the assembly of protein complexes involved in autophagy, signaling, cell division, and redox processes³, as well as the auxin-response pathway in plants⁴. PB1 domains form homotypic interactions via conserved electrostatic motifs molded by basic or acidic surface patches on opposite faces of their ubiquitin-like β -grasp fold^{2,5}. According to their interaction profile, PB1 domains are classified into type A (acidic, OPCA motif), type B (basic), or mixed-type AB members⁵. While type A and type B PB1 domains can form heterodimeric protein complexes, type AB members can mediate interactions with either PB1 domain type or engage in homotypic interactions to form homo-oligomers or hetero-oligomers^{2,6}. More recently, PB1-mediated self-interaction of p62/SQSTM1 was found to result in the formation of filamentous polymers⁷ with helical symmetry *in vitro*⁸.

p62 has been shown to function in autophagy and cellular signaling. Autophagy is a degradative cellular housekeeping pathway by which cytoplasmic materials are engulfed in a double-membrane vesicle termed the autophagosome and delivered to the lysosomal compartment⁹. Substrates for autophagy are not limited by molecular size and include large protein aggregates, intracellular pathogens, and cellular organelles. Selective autophagy has been characterized as the process that specifically directs cytosolic substrates to the formation site of autophagosomal membranes^{10,11}. As an autophagy receptor, p62 links cargo proteins with the autophagosome membrane. PB1-mediated oligomerization of p62 is essential for its function as a selective autophagy receptor¹² and thought to facilitate co-aggregation of ubiquitylated cargo¹³. The C-terminal UBA domain of p62 captures ubiquitinated cargo, and the LIR motif guides the cargo-receptor complex to Atg8/LC3, which is anchored to the surface of the autophagosomal membrane^{14,15}. Importantly, in addition to the selective autophagy degradation of ubiquitinated cargo, p62 is also involved in the degradation of other substrates such as KEAP1 known as a regulator of the antioxidative stress response transcription factor NRF2. KEAP1 binds directly to a specific motif in p62, i.e., the KEAP1-interacting region (KIR)^{16,17}. In signaling, p62 bodies constitute an interaction hub for the kinases MEKK3, MEK5, and aPKCs, which also contain PB1 domains², in addition to triggering the NF- κ B pathway through the polyubiquitination of tumor necrosis factor (TNF) receptor-associated factor 6 (TRAF6)¹⁸.

Due to p62's involvement in protein homeostasis, the impairment of autophagy or oxidative stress results in aggregation or upregulation of p62, including increased body formation^{19,20}. Recently, we and others independently found that p62 reconstituted with other components of the autophagy pathway, such as ubiquitinated model cargo, and the selective autophagy receptor NBR1, spontaneously coalesces into p62 bodies *in vitro*²¹ and shows the characteristics of liquid-liquid-phase separation *in vivo*²². These studies established that oligomerization by the N-terminal PB1 domain of p62 is an essential requirement for recapitulating phase separation *in vitro*, as well as for cargo uptake *in vivo*^{12,22}.

The exact structural requirements and physiological conditions under which p62-PB1 domains self-assemble or engage in hetero-PB1 complexes are currently unclear. Furthermore, it is not known what assembly state of p62 is required for biological functions such as cargo uptake in autophagy or the formation of phase-separated compartments *in vivo*. Based on high-

resolution electron cryo-microscopy (cryo-EM) and crystal structures, cellular EM, biochemical, and cellular characterization, we here revealed the structural basis for polymeric PB1 self-assembly and defined the relevance of symmetry and spatial arrangement of the polymeric assembly state for p62 autophagy function *in vivo*.

Results

p62, TFG1, and AtNBR1-PB1 domains form filamentous polymers. Based on our previous finding that p62 is capable of forming homo-oligomeric filamentous assemblies⁸, we set out to understand whether related AB-type PB1 domains possess a similar property to self-assemble. With reference to sequence alignments (Fig. 1a), we expressed and purified PB1 domains from human p62¹⁻¹⁰², p62¹⁻¹²², TFG1¹⁻⁹⁵ (Trk-fused gene 1), the atypical protein kinase PKC ζ ¹¹⁻¹⁰¹, as well as the evolutionary-related PB1 domain of the NBR1¹⁻⁹⁴ autophagy receptor from *Arabidopsis thaliana* (AtNBR1)²³. p62, TFG1, PKC ζ , and AtNBR1 are multi-domain proteins that share the N-terminal PB1 domain with additional functional C-terminal domains (Fig. 1b). In order to assess whether these PB1 domain-containing proteins are capable of forming high-molecular-weight assemblies, we performed sedimentation assays by ultracentrifugation. The PB1 domains of TFG1¹⁻⁹⁵, AtNBR1¹⁻⁹⁴, p62¹⁻¹⁰², and p62¹⁻¹²² were found in the pellet fraction, whereas PB1 domains from PKC ζ remained soluble (Fig. 1c), which is in agreement with our previous study, showing that both p62¹⁻¹⁰² and p62¹⁻¹²² form filamentous structures⁸. Furthermore, we visualized the pelleted fractions by using negative staining electron microscopy (EM) and observed elongated filamentous or tubular assemblies for the PB1 domains of p62¹⁻¹²², TFG1, and AtNBR1 that measure 145 ± 5 , 900 ± 52 , and 120 ± 4 Å in diameter, respectively (Fig. 1d). Closer inspection of the sequence alignments revealed that all three of these PB1 domains share the tandem arginine motif close to the canonical lysine residue of the basic motif in B-type PB1 domains. By contrast, this tandem arginine motif is absent in AB-type PB1 sequences of PKC ζ that does not form filamentous or tubular structures, suggesting a critical role for self-assembly.

Cryo-EM structures of AtNBR1 and p62-PB1 filaments. Of the three PB1 assemblies studied, AtNBR1¹⁻⁹⁴ (AtNBR1-PB1) and p62¹⁻¹²² (p62-PB1) formed homogeneous filaments of constant diameter that appeared best suited for high-resolution structure investigation by cryo-EM. Therefore, we vitrified filaments of purified AtNBR1-PB1 and p62-PB1 domains and imaged the samples by cryo-EM (Fig. 2a, b). Image classification of segmented PB1 helices revealed that both AtNBR1-PB1 and p62-PB1 polymerize in two different tubular morphologies: a projection class with a ladder-like pattern, we term L-type, and a projection class with a serpent-like one, we term S-type (Fig. 2c; Supplementary Fig. 1A-C). L-type and S-type helices partition approximately evenly, i.e., 40–60% and 55–45% for p62-PB1 and AtNBR1-PB1 samples, respectively. Further analysis revealed that the occurrence of L-type or S-type assemblies is persistent along the individual helices in micrographs of AtNBR1-PB1, whereas for p62-PB1 filaments regularly displayed transitions from L-type to S-type symmetry (Supplementary Fig. 1D). In an effort to understand the underlying structures of L-type and S-type projections, we analyzed the averaged power spectra from in-plane rotated segments and from class averages. The best Fourier spectra of AtNBR1-PB1 and p62-PB1 showed discrete layer-line reflections up to 5.9 and 4.7 Å, suggesting a helical organization and preservation of structural order up to high resolution (Supplementary Fig. 1E, F). The comparison of the Fourier spectra

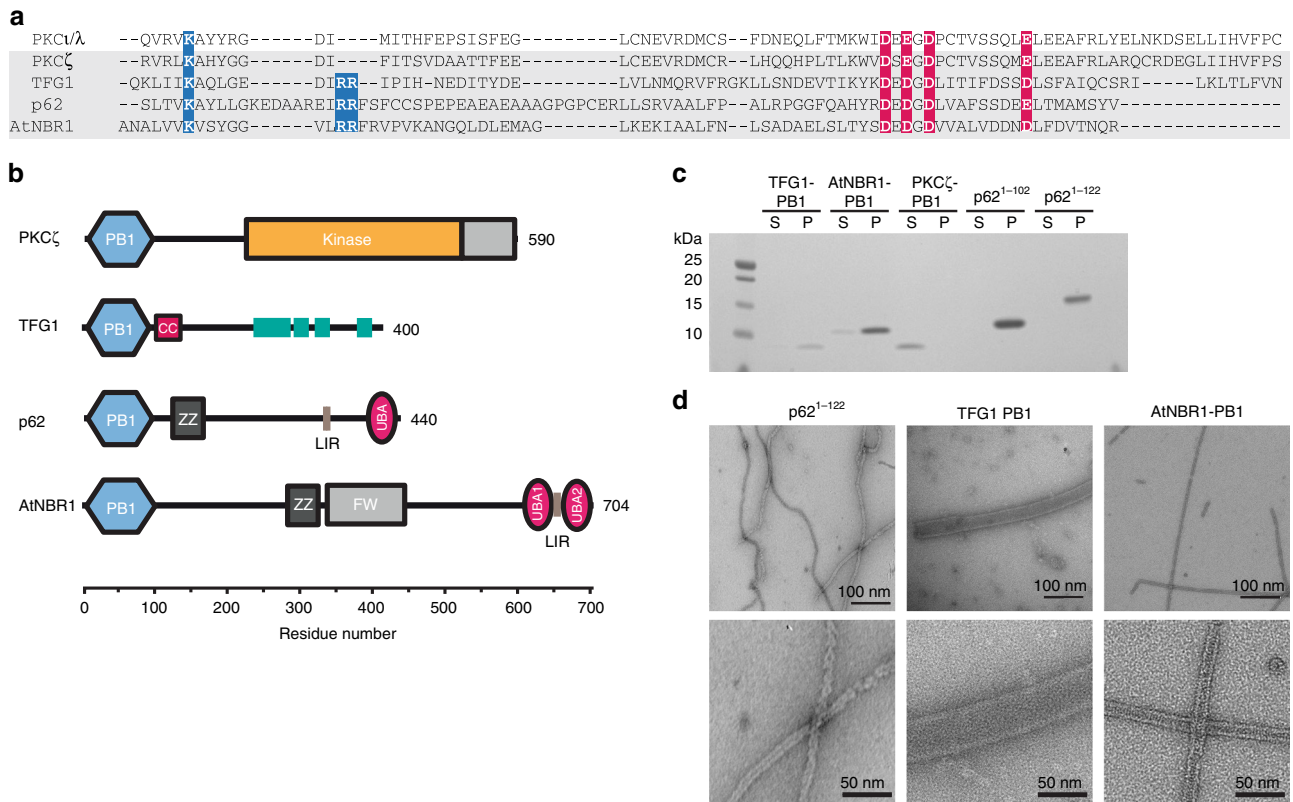


Fig. 1 Type A/B PB1 domains and their capability to form polymers. **a** Sequence alignment of the type A/B PB1 domains with highlighted tandem arginine motif (blue) in addition to basic (blue) and acidic residues (red). **b** Domain architecture of PKC ζ , TFG1, p62, and AtNBR1 proteins. **c** Pelletation assay of purified type A, B, or AB PB1 domains: TFG1, AtNBR1, PKC ζ , p62¹⁻¹⁰², and p62¹⁻¹²². Corresponding lanes of soluble (S) and pellet (P) fraction are shown. Only PKC ζ remains soluble, whereas TFG1, AtNBR1, and p62 are found in the pellet. Source data are provided as a Source Data file. **d** Electron micrographs of negatively stained specimens reveal elongated filamentous p62¹⁻¹²², tubular polymers of TFG1 and AtNBR1 of 145 ± 5, 900 ± 52, and 120 ± 4 Å nm in diameter, respectively.

confirmed that L-type and S-type structures are differently organized in their helical lattice. By indexing the layer lines in the Fourier spectra of AtNBR1-PB1 filaments, we concluded that L-type is a two-stranded helix with a pitch of 77.2 Å and 11.47 subunits/turn, whereas S-type is a single double-stranded helix with a pitch of 68.2 Å and 11.55 subunits/turn. For p62-PB1, we observed a four-stranded L-type assembly and a three-stranded S-type assembly. In the latter S-type, one of the three helical rungs is propagating in an antiparallel orientation, related to the central rung by local dihedral symmetry. The L-type here has a pitch of 135.9 Å with 14.16 subunits/turn, and S-type has a pitch of 138.6 Å with 13.60 subunits/turn. Using the derived symmetries, we determined the 3.5/3.9- (L-type, p62/AtNBR1) and 4.0/4.4 Å- (S-type, p62/AtNBR1) resolution structures (Fig. 2c, Tables 1, 2; Supplementary Fig. 1G, H). All four structures form tubules of ~120 Å and 150-Å width with an inner diameter of 45 Å and 70 Å for AtNBR1-PB1 and p62-PB1, respectively. In all reconstructions, the main chain of the PB1 domain could be resolved with α -helical pitch features and individual β -strands separated. The overall fold of the asymmetric unit was found compatible with the NMR structure of the p62-PB1 monomer^{24,25} (Fig. 3a, b). In the absence of prior structural information, we traced the AtNBR1-PB1 de novo. This de novo-built model is in close agreement with the 1.6-Å crystal structure of a polymerization-deficient AtNBR1-PB1 mutant, which we solved in parallel (Table 3; Supplementary Fig. 2A). The relative orientation between adjacent subunits is very similar in the respective S-type and L-type assemblies of AtNBR1-PB1 and p62-PB1 (Supplementary Fig. 2B). The β 1- α 1 loop in p62 is

flexible and only visible in the L-type assembly density (Supplementary Fig. 2C). Expanding the asymmetric unit by using the helical parameters of the L-type and S-type structures allowed analysis of the interface between repeating units. Despite overall similar interaction modes, the AtNBR1 and p62 assemblies showed differences in relative domain rotation between adjacent subunits and with respect to the helical axis (Fig. 3c). In agreement with sequence analysis (see Fig. 1a), the electrostatic potential mapped onto the molecular surface of the structures revealed that opposing charged surfaces mediate the PB1-PB1 interactions in the helical repeat (Fig. 3d). In addition, we more closely examined the interface of homomeric interactions in the helical assemblies. The main interactions are formed between a double arginine finger formed by two neighboring arginine residues in strand β 2 (R19-R20^{AtNBR1}/R21-22^{p62}) stabilizing strong salt bridges to acidic residues (D60/D62/D64/D73^{AtNBR1} or D69/D71/D73/E82^{p62}) in the OPCA motif located in the β 2- β 3 loop and the α 2 helix (Fig. 3e). These interactions are assisted by the canonical-type B lysine (K11^{AtNBR1} and K7^{p62}) in strand β 1. Free-energy calculations using the PDBePISA server²⁶ suggest that a large part of the interface free energy is contributed by the double arginine finger. In addition to the canonical transverse interactions, the helices are further stabilized by longitudinal interactions Y14^{AtNBR1}/N28^{AtNBR1} or K102^{p62}/D92^{p62} and R59^{p62}/D93^{p62} to subunits of neighboring strands along the helical axis (Supplementary Fig. 2D, E). The importance of electrostatic interactions on filament stability is further supported by the observation that increased ionic strength impedes stable filament formation and is sensitive to pH (Supplementary

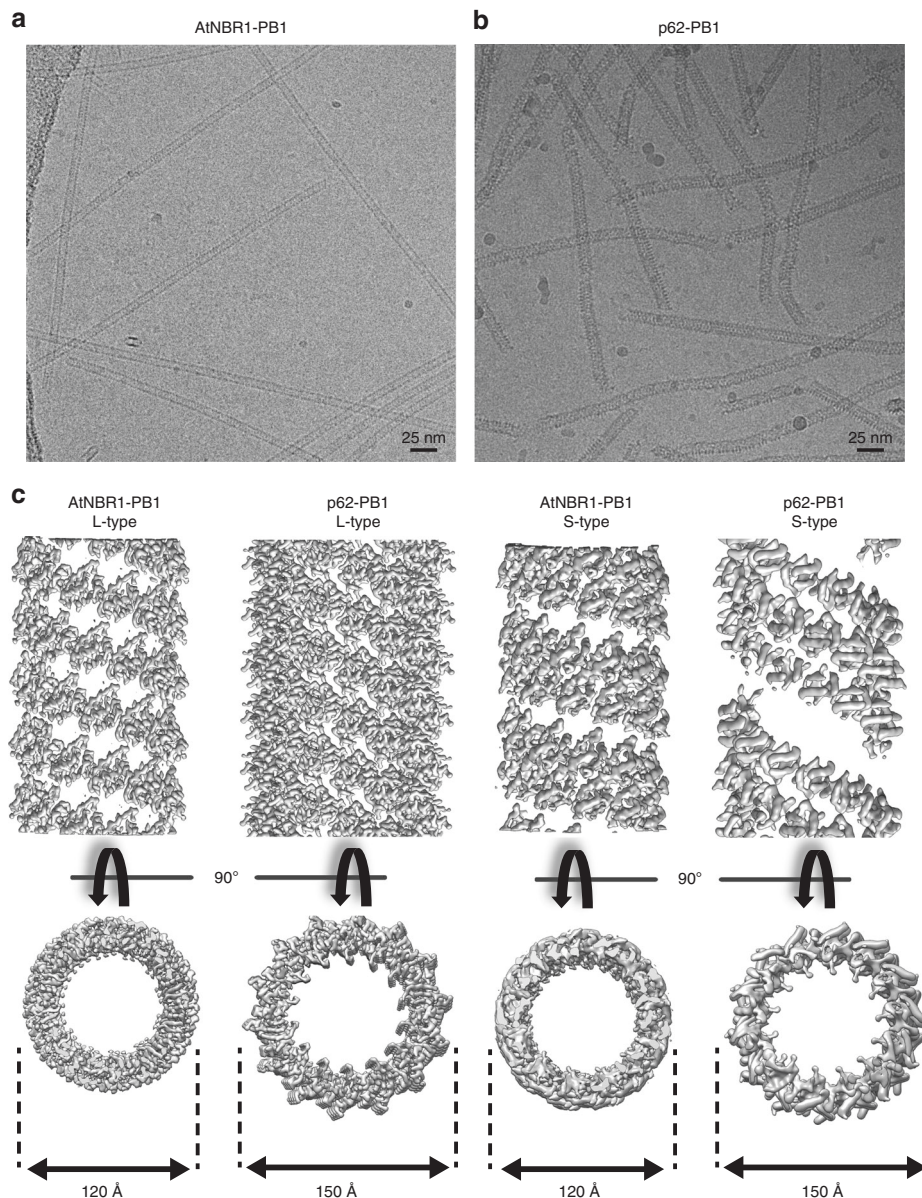


Fig. 2 Cryo-EM structures of AtNBR1¹¹⁻⁹⁴ and p62¹⁻¹²². **a** Electron cryo-micrograph of AtNBR1-PB1¹⁻⁹⁴ and **(b)** p62-PB1¹⁻¹²² assemblies. **c** Side and top views for determined cryo-EM structures of L-type AtNBR1-PB1 (far left), p62-PB1 (left), and S-type assembly of AtNbr-PB1 (right), p62-PB1 (far right).

Fig. 3A–H). To validate our structural interpretation, we performed pull-down experiments using MBP-tagged wild-type AtNBR1–PB1 as a prey and a series of AtNBR1–PB1 interface mutants as bait (Fig. 3f). All interface mutants decrease binding significantly compared with the wild type, and binding is completely abrogated in mutants lacking the double arginine finger, in agreement with observations in cellular assays^{2,23}. Together, the cryo-EM structures of two PB1 domain assemblies reveal that in addition to the canonical-type electrostatic AB interactions, the self-polymerization property is linked to the presence of a double arginine finger.

PB1 domain interactions in the context of filamentous p62.

After establishing the molecular basis of PB1 domain homopolymerization, we wanted to understand how these assemblies interact with other PB1 domains of the A and B types that have been shown to co-localize with p62 punctae². We therefore expressed and purified A-type human PB1 domains of

MEK5⁵⁻¹⁰⁸ and NBR1¹⁻⁸⁵, the B-type PB1 domain of MEKK3⁴³⁻¹²⁷, and the AB-type PB1 domain of PKCζ¹¹⁻¹⁰¹ and determined their binding affinities for polymerization-deficient p62¹⁻¹⁰² (D69A/D73A)⁵ by isothermal titration calorimetry (ITC). These PB1 domains show 2–10-fold lower binding affinity to p62 compared with its self-interaction dissociation constant (K_D) of 6 nM²⁷, with K_D of 8.9 ± 0.9 nM, 12.6 ± 0.4 nM, 26.8 ± 0.5 nM, and 105 ± 1.3 nM determined for PKCζ²⁷, NBR1, MEKK3, and MEK5, respectively (Fig. 4a). Moreover, other PB1 interactions, such as binding of NBR1–PB1 to MEKK3, have also been measured and have even lower affinity (K_D of 13.3 μM). We therefore hypothesized that binding of p62-interacting PB1 domains could compete with p62 self-polymerization and affect the assembly structures of p62–PB1 filaments. We found that NBR1–PB1 strongly interacts with p62–PB1 filaments and shortens p62–PB1 filaments on average to less than half the starting length (Fig. 4b, c). Surprisingly, MEKK3, MEK5, and PKCζ–PB1 showed no effect on the pelletation behavior of p62 assemblies, although having only marginally lower affinities than

NBR1 (Fig. 4d). To further analyze the interactions, we turned to negative staining EM. In agreement with the co-sedimentation data, for PB1 domains other than NBR1 we did not observe any effect on the morphology of p62-PB1 filaments and the measured filament lengths. In order to increase the sensitivity of detecting interactions with p62-PB1 filaments, we also imaged p62-PB1 filaments incubated with nanogold-labeled NBR1, MEKK3, MEK5, and PKC ζ PB1 domains using negative staining EM (Fig. 4e). For all PB1 domains, the micrographs confirmed end-on binding of the PB1

domains to p62-PB1 polymers or to oligomeric, ring-like structures. Interestingly, NBR1, MEK5, and PKC ζ PB1 domains preferably bind to one end of the filament (Fig. 4f), consistent with an overall polar assembly observed in the 3D reconstructions of p62-PB1 filaments (see Fig. 2). MEKK3-PB1 (type B) was not observed at p62-PB1 filament ends, but occasionally found at oligomeric ring-like structures. Biochemical interaction studies suggest that assembled filamentous p62 can display significantly lower apparent binding affinities for interacting PB1 domains than when present in the monomeric form.

Table 1 Cryo-EM data collection and helical reconstruction.

	AtNBR1-PB1¹⁻⁹⁴ (S-type: EMD-10500, L-type: EMD-10499)	p62-PB1¹⁻¹²² (S-type: EMD-10502, L-type: EMD-10501)
<i>Data collection and processing</i>		
Magnification	105kx	130kx
Voltage (kV)	300	300
Electron exposure (e ⁻ /Å)	17	40
Defocus range (μm)	1.0–4.0	0.5–2.5
Pixel size (Å)	1.386	1.040
Symmetry imposed	S-type: C1 L-type: C2	S-type: C1 L-type: C2
Final no. of segments	S-type: 18,021 L-type: 25,387	S-type: 51,679 L-type: 51,853
Helical rise (Å)	S-type: 5.905 L-type: 6.721	S-type: 9.78 L-type: 4.787 (9.574)*
Helical twist (°)	S-type: -31.17 L-type: -31.44	S-type: -26.48 L-type: 77.29 (-25.42)*
Global map resolution (Å, FSC = 0.143)	S-type: 4.4 L-type: 3.9	S-type: 4.0 L-type: 3.5
Local map resolution range (Å)	S-type: 4.0–4.7 L-type: 3.4–4.1	S-type: 3.7–4.4 L-type: 3.3–4.4

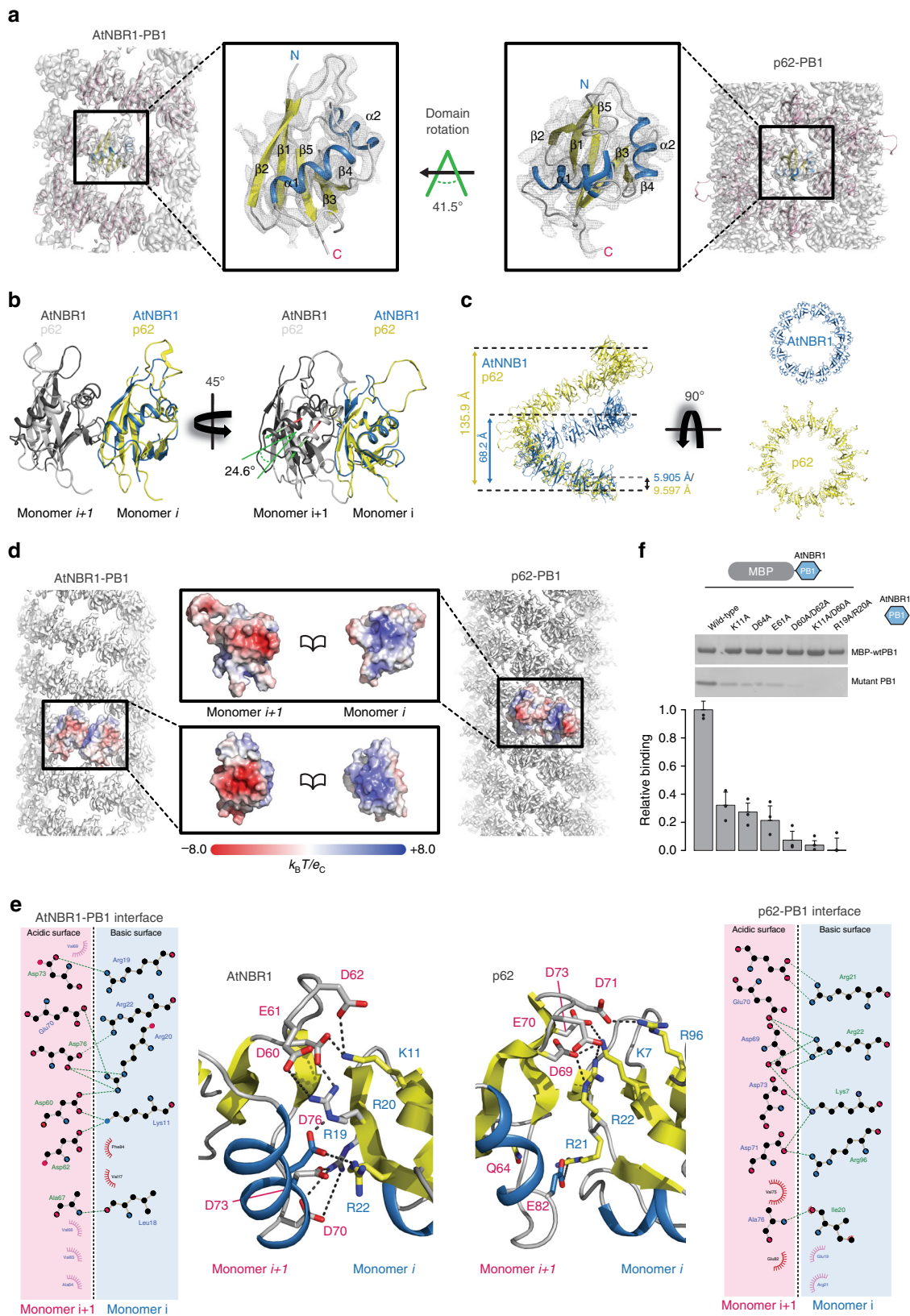
*Equivalent notation for asymmetric unit of two monomers as described in the main text

Cellular p62 bodies consist of filamentous structures. Although self-oligomerization of p62 has been shown to be essential for targeting of p62 to the autophagosome¹², it is unclear whether the filamentous assemblies observed in vitro are involved in this process or even occur inside of cells. We used correlative light and electron microscopy (CLEM) to study the ultrastructure of p62 bodies in a targeted manner. In order to enrich endogenous p62 bodies in RPE1 cells, we overexpressed a human NBR1-D50R mutant that abolishes the interaction with p62². Co-sedimentation experiments, in which the relative amount of p62 in the monomeric and polymeric state are determined, indeed showed that wild-type NBR1 solubilizes filamentous p62-PB1, whereas the D50R mutant does not (Fig. 5a). In RPE1 cells, the NBR1-D50R mutant consistently produced larger p62 clusters possibly by promoting self-polymerization as observed in vitro (Supplementary Fig. 4A). In such cells, we localized p62 to punctate areas of 0.5 ± 0.1 -μm diameter by fluorescence microscopy and visualized their ultrastructure by electron tomography (Fig. 5b, Supplementary Fig. 4B, C). The electron micrographs revealed that p62 bodies have a distinct appearance that is well differentiable from the cytosol with an electron-dense boundary of ~60-nm thickness surrounding the body (Fig. 5c, d). We thresholded the interior density and found that the p62 bodies are composed of a dense meshwork of filamentous assemblies (Fig. 5e). Quantitative analysis of thresholded images confirmed the presence of elongated filament-like structures with an average diameter of 15 nm compatible in dimensions with the helical p62 structures observed in vitro⁸. We estimated the length of these structures by tracing individual filaments in

Table 2 Model refinement statistics.

	AtNBR1-PB1¹⁻⁹⁴ (S-type: PDB ID 6TGP, L-type: PDB ID 6TGN)	p62-PB1¹⁻¹²² (S-type: PDB ID 6TH3, L-type: PDB ID 6TGY)
<i>Model refinement</i>		
Initial model used (PDB code)	PDB-6TGS (X-ray model)	PDB ID 2KKC#
Model resolution (Å, FSC = 0.5)	S-type: 5.5 L-type: 4.3	S-type: 4.0 L-type: 3.6
Map-sharpening B-factor (Å ²)	S-type: -300 L-type: -200	S-type: -193 L-type: -139
<i>Model composition</i>		
Non-hydrogen atoms	669 (S-/L-type)	808 (S-/L-type)
Protein residues	88 (S-/L-type)	104 (S-/L-type)
<i>R.m.s. deviations</i>		
Bond lengths (Å)	0.009/0.008 (S-/L-type)	0.006/0.007 (S-/L-type)
Bond angles (°)	1.16/1.161 (S-/L-type)	1.22/1.24 (S-/L-type)
<i>Validation</i>		
MolProbity score	2.41/2.29 (S-/L-type)	1.94/1.64 (S-/L-type)
Clashscore*	7.59/6.41 (S-/L-type)	4.89/1.88/ (S-/L-type)
Rotamer outliers (%)	1.41/1.41 (S-L-type)	0.00/0.63 (S-/L-type)
<i>Ramachandran plot</i>		
Favored (%)	93.21/94.19 (S-/L-type)	83.33/83.33 (S-/L-type)
Allowed (%)	6.79/5.81 (S-/L-type)	16.67/16.67 (S-/L-type)
Disallowed (%)	0.00 (S-/L-type)	0.00 (S-/L-type)

*Computed for 9-mer
#Saio et al.²⁴



sequential tomogram slices (Fig. 5f). CLEM visualization of p62 bodies in cells under endogenous p62 levels confirms the presence of filamentous assemblies.

The effect of different p62 assemblies on autophagy clearance. We next set out to assess the relevance of symmetry and assembly

state of PB1-mediated filaments for biological function within cellular p62 bodies and lysosomal targeting through the autophagy pathway. In the comparison of PB1 assemblies visualized by negative staining EM, TFG1 showed the most striking difference to p62 assemblies both in size and apparent symmetry (see Fig. 1d). Therefore, we reasoned that a p62 chimera, in which

Fig. 3 Structural basis of PB1 polymer formation. **a** Cryo-EM structures of AtNBR1-PB1 (left) and p62-PB1 filaments are shown with atomic ribbon models (α -helix: blue and β -strands: yellow) superposed on the density. Close-ups show that both PB1 domains display the canonical ubiquitin-like fold (center left and center right). The arrow indicates the rotation of the p62-PB1 subunit relative to the AtNBR1-PB1 subunit in their respective assemblies. **b, c** Differences in the PB1-PB1 interface give rise to different helical architectures. (Left) Monomer *i* of AtNBR1 (blue) and monomer *i* of p62 (yellow) were superposed to visualize the degree of domain rotation toward the next monomer along the helical rung (monomer *i* + 1). (Right) Adjacent subunits along the helical rung for AtNBR1 display a 25° inward rotation compared with adjacent subunits of p62, explaining the observed differences in helical symmetry and diameter of AtNBR1-PB1 and p62-PB1 filaments, respectively. **c** **d** Electrostatic potential surface of the determined AtNBR1-PB1 and p62-PB1 structures. For both structures, the propagation of the helical structure is mediated and stabilized by positively (blue) and negatively charged (red) surfaces on opposite faces of the PB1 fold. **e** Schematic illustration and detailed interactions of the PB1-PB1 interface as determined from the AtNBR1-PB1 and p62-PB1 cryo-EM structures, respectively. The structures are shown in cartoon representation highlighting key electrostatic residue contacts shown as sticks. **f** In vitro pull-down with maltose-binding protein (MBP)-tagged wild-type AtNBR1-PB1 of structure-based AtNBR1-PB1 domain mutants. Error bars represent standard deviation (SD) of three independent experiments. Source data are provided as a Source Data file.

Table 3 X-ray crystallography data collection and refinement statistics.

Data collection statistics

Wavelength	
Resolution range	37.9–1.53 (1.59–1.53)
Space group	P 21 21 2
Unit cell	43.13 79.44 24.14 90 90 90
Total reflections	25,830 (2499)
Unique reflections	13,035 (1271)
Multiplicity	2.0 (2.0)
Completeness (%)	99.22 (99.30)
Mean I/ σ (I)	10.45 (1.42)
Wilson B-factor	20.99
R-merge	0.02799 (0.4132)
R-meas	0.03958 (0.5844)
R-pim	0.02799 (0.4132)
CC1/2	0.999 (0.655)
CC*	1.00 (0.89)

Model refinement

Reflections used in refinement	13,030 (1271)
Reflections used for R-free	669 (53)
R-work	0.2456 (0.3525)
R-free	0.2776 (0.4166)
CC (work)	0.927 (0.750)
CC (free)	0.902 (0.462)

Model refinement

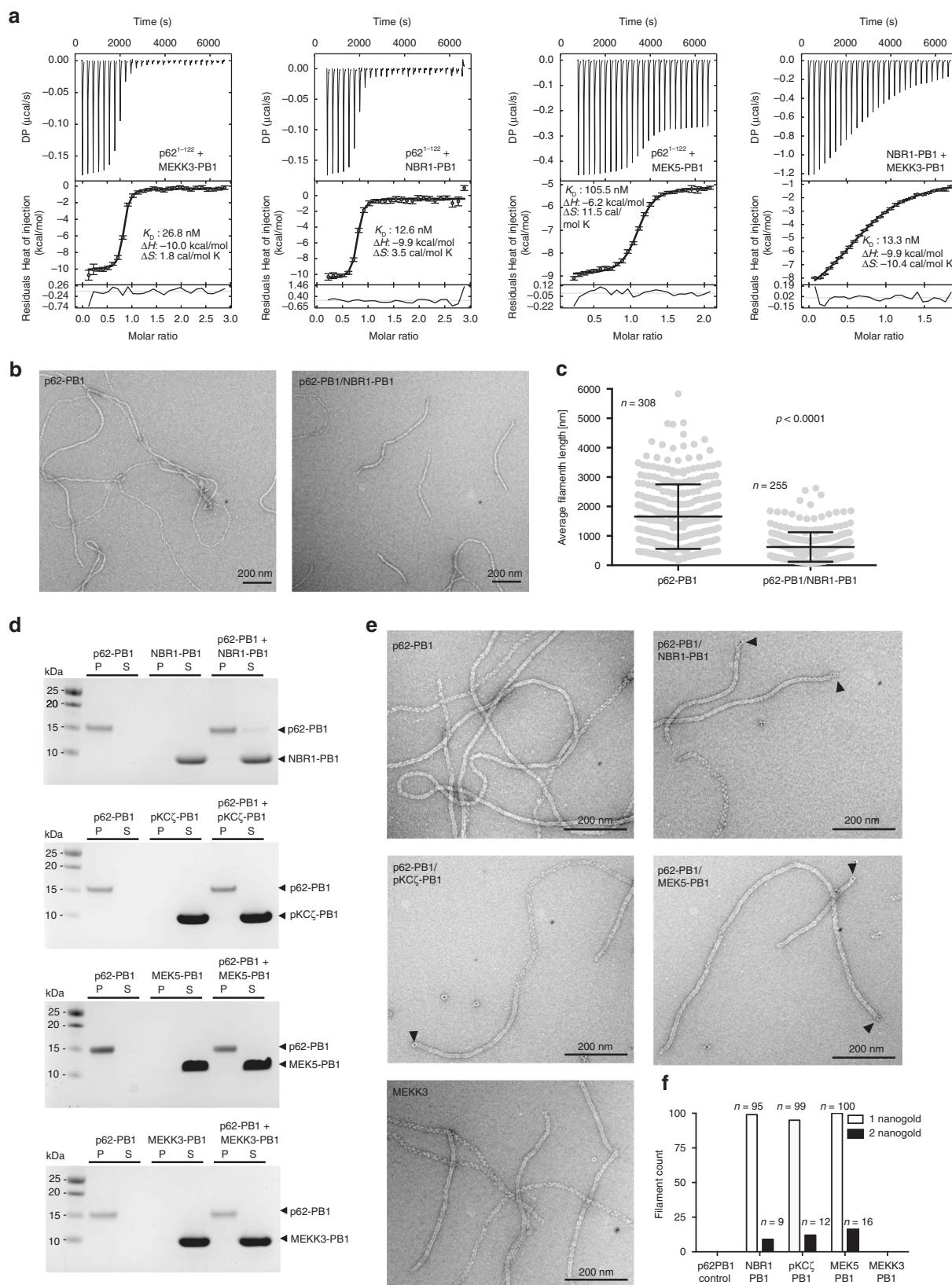
Number of non-hydrogen atoms	816
Macromolecules	723
Ligands	52
Solvent	41
Protein residues	88
RMS (bonds)	0.007
RMS (angles)	0.79
Ramachandran	
Favored (%)	100.00
Allowed (%)	0.00
Outliers (%)	0.00
Rotamer outliers (%)	6.49
Clashscore	2.97
Average B-factor	32.42
Macromolecules	30.25
Ligands	51.32
Solvent	46.80

*Statistics for the highest-resolution shell are shown in parentheses

we exchange the native PB1 domain for TFG1-PB1, could clarify the role of the helical PB1 scaffold in autophagy clearance. We generated two p62 chimeras by fusing the TFG1-PB1 domain to either p62 (123–408) or p62 Δ 123–319 (mini-p62), containing only the p62 LIR motif and UBA domain (Fig. 6a) and visualized the resulting assemblies by negative staining EM (Fig. 6b). The

TFG1:p62 chimera forms 48-nm wide filaments, which is approximately three times the diameter of WT-p62 filaments and possesses a helical architecture clearly different from that of WT-p62 filaments. The TFG1-mini-p62 chimera forms defined, ring-shaped oligomers with ~12 nm in diameter. To test whether the TFG1-p62 fusion constructs are able to form p62 bodies in cells, we expressed the chimeras fused to an N-terminal GFP tag in HeLa cells deficient of endogenous p62. As controls, we also expressed GFP-tagged WT-p62 and the mini-p62 construct (p62 Δ 123–319) (Fig. 6c). The transfected cells were analyzed by confocal fluorescence microscopy 24 h and 48 h post transfection. All constructs formed p62 bodies, with the majority of dots having a diameter in the range of 0.1–0.5 μ m. We further classified GFP-positive punctae according to frequency of occurrence, the tendency to cluster, and the morphological appearance (Fig. 6c, d; Supplementary Fig. 5A).

We next asked whether TFG1-p62 could perform the biological function of p62. We first assessed whether TFG1-p62 can be turned over by autophagy and targeted to acidified cellular compartments by using the “traffic light” reporter. Here, the mCherry-YFP tandem tag is fused to the target protein, and the acidification of the construct in lysosomes is monitored by appearance of red punctae. Although both TFG1-p62 chimeras displayed a diffuse yellow fraction, they were almost as efficiently degraded by autophagy as the WT and mini-p62 constructs (Fig. 6e, f; Supplementary Fig. 5B–F). We then asked if the TFG1-p62 chimera was able to act as a cargo receptor for a p62-specific substrate, KEAP1, and mediate autophagy degradation. KEAP1 was shown to be entirely diffusely localized when expressed in cells lacking p62¹⁶. We first verified that purified KEAP1-DC domain still binds to the p62-TFG1 chimeras by using a pull-down assay (Supplementary Fig. 5G). Next, we monitored co-localization in cells and found that in analogy to biochemical binding data, the TFG1-p62 chimera, WT, and mini-p62 constructs co-aggregated with KEAP1 in cells, but only the WT and mini-p62 constructs could mediate acidification of tandem tagged KEAP1 when co-expressed as Myc-tagged constructs in the p62 KO HeLa cells. At the same time, no autophagic turnover of mCherry-YFP-KEAP1, however, was observed upon co-expression with chimera Myc-TFG1-p62 or Myc-TFG1-mini-p62 (Fig. 6g, h; Supplementary Fig. 6A–D). When we compromised the formation of PB1 domain-mediated filament assemblies by mutating p62’s double arginine finger (R21A/R22A), p62 was completely diffusely localized and not degraded by autophagy (Supplementary Fig. 7A, B, Supplementary Fig. 8, Supplementary Movies 1, 2). This mutant also failed to mediate aggregation and autophagic degradation of KEAP1 in co-transfected cells (Supplementary Fig. 7C). In conclusion, although TFG1-p62 chimera can be degraded by autophagy despite their assembly into nonnative polymers, these assemblies are evidently unable to mediate degradation of the p62-specific substrate KEAP1 in analogy to the polymerization-deficient double arginine finger mutant of p62.



Discussion

The PB1 domain is a common interaction module present in all kingdoms of life and found in various proteins involved in membrane trafficking, redox regulation, cell division, as well as in signaling. In this study, we focused on the structure in addition to the biological and functional relevance of the p62-PB1 domain in

the context of polymeric assemblies. The overall ubiquitin-like fold of the PB1 domain has been determined, and different interface types through acidic and basic patches have been identified in earlier studies^{2,5}. Our cryo-EM structures of filamentous p62 and AtNBR1-PB1 assemblies revealed that the presence of a tandem arginine sequence in the basic motif of type

Fig. 4 Interactions of p62-PB1 with other PB1 domain proteins. **a** Quantitative determination of PB1-binding affinities by isothermal titration calorimetry. Data represent mean and standard deviations from three independent experiments. **b** Representative electron micrographs of negatively stained p62-PB1¹⁻¹²² (left) incubated with human NBR1-PB1 (right). **c** Quantification of lengths of P62-PB1¹⁻¹²² filaments before and after incubation with NBR1-PB1. Source data are provided as a Source Data file. **d** Co-sedimentation assays of p62-PB1¹⁻¹²² with NBR1-PB1, PKC ζ -PB1, MEK5-PB1, and MEK3-PB1 (S = supernatant; P = pellet). Control experiments of p62-PB1¹⁻¹²² and the respective PB1 interactor alone are also shown. Source data are provided as a Source Data file. **e** Representative electron micrographs of negatively stained p62-PB1¹⁻¹²² with nanogold-labeled NBR1-PB1, PKC ζ -PB1, MEK5-PB1, or MEK3-PB1. **f** Quantification of p62-PB1¹⁻¹²² filaments displaying one or two nanogold-labeled PB1 interaction domains. Source data are provided as a Source Data file.

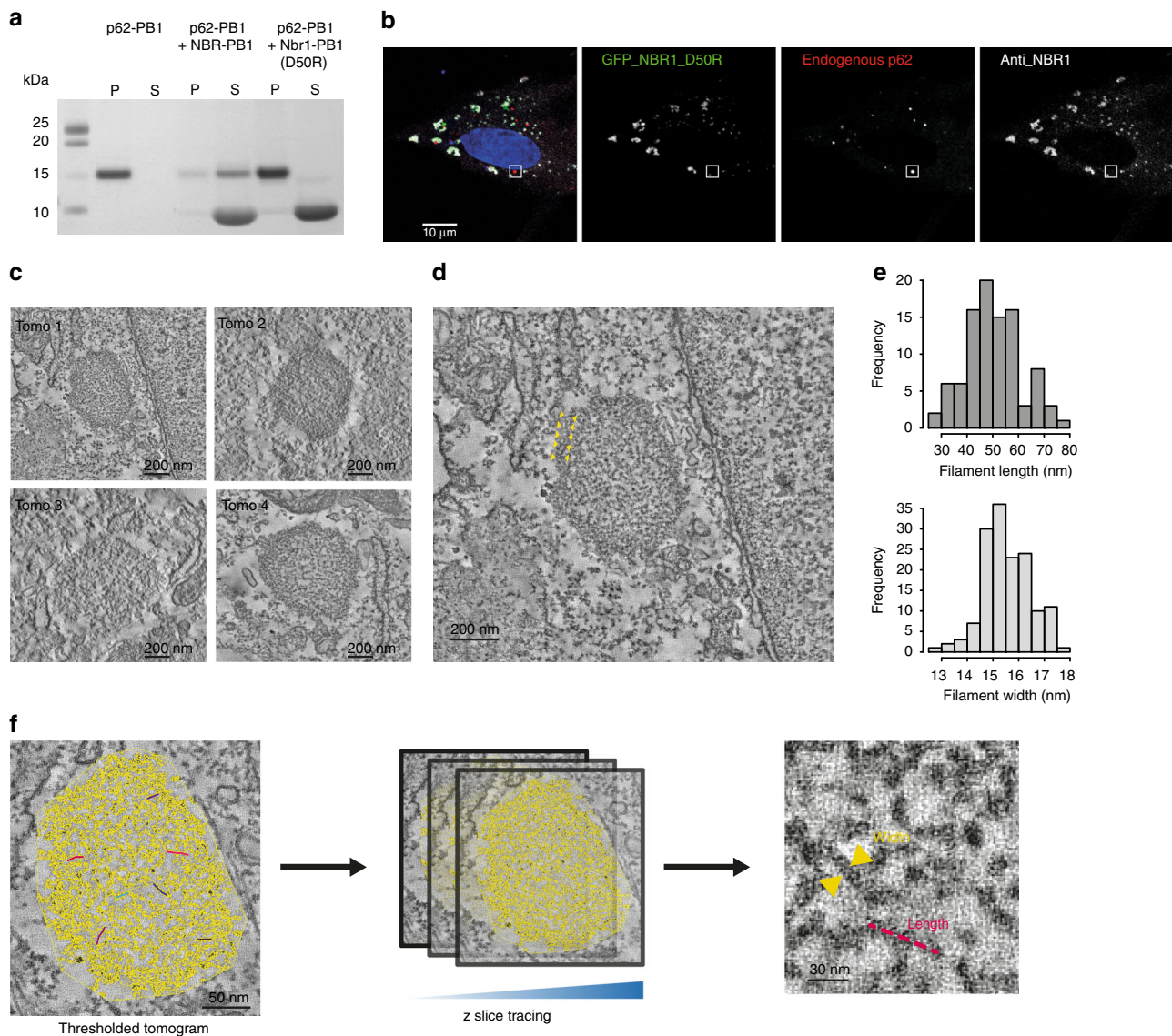
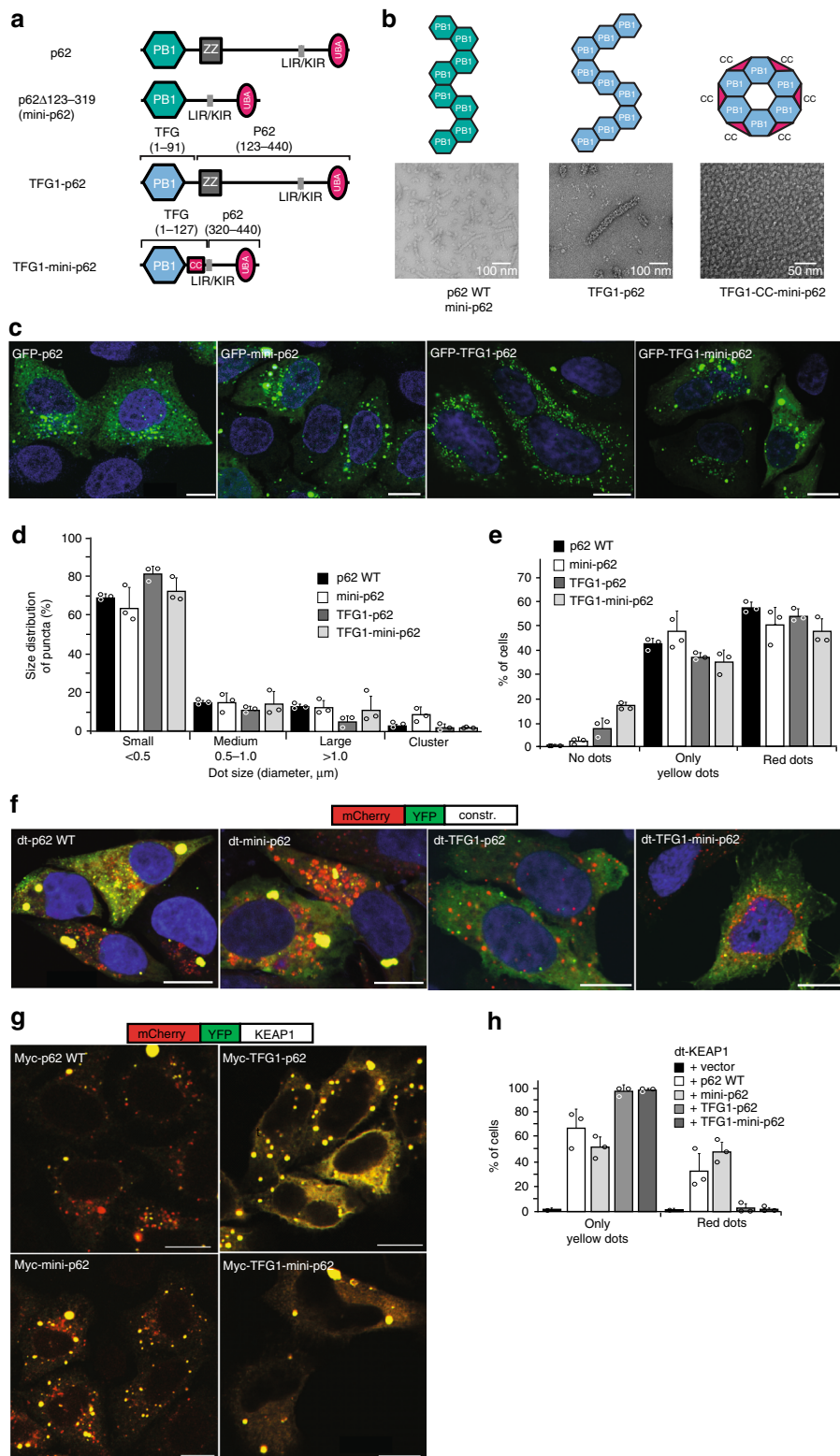


Fig. 5 CLEM visualization of p62 bodies in cells. **a** Effect of human NBR1-D50R mutation on p62 filaments. SDS-PAGE analysis of pelletation assay showing that p62-PB1 filaments are not disrupted by NBR1-PB1 with a D50R mutation (P = pellet; S = supernatant). Source data are provided as a Source Data file. **b** Representative confocal fluorescence images showing NBR1 (green) and endogenous p62 (red) in RPE1 cells. Co-localization analysis of fixed RPE1 cells stably expressing NBR1(D50R) shows no overlap of NBR1(D50R) with p62 bodies. **c** Representative electron tomogram slices of p62 bodies localized by CLEM. **d** Enlarged view of a representative tomogram slice from the highlighted p62 body in (b) reveals the filament-like meshwork of p62 bodies. Note the apparent phase separation of the p62 body from the cytosol. The ring of increased density surrounding the bodies is indicated by yellow arrows. **e** Distribution of estimated filament length and width from tracing in thresholded tomograms. Source data are provided as a Source Data file. **f** Schematic illustration of width and length measurements performed in thresholded tomograms (yellow pixels).

AB interfaces is required to stabilize a polymeric assembly. Although the exact composition of the interface between opposed and electrostatically complementary surfaces is distinctly different for the two PB1 assemblies, the main functional acidic and basic residues including the essential double arginine finger are conserved (Fig. 3). Furthermore, we observed that the propagation of

the helical rung is also distinctly different in p62 and AtNBR1 assemblies, with small changes in primary structure giving rise to large differences in quaternary structure. This property has been characterized in other sequence-related helical systems²⁸. Interestingly, we also found that the polymeric PB1 domain structures of human p62 and AtNBR1 are assembled from a common helical



rung into two morphologically distinct organization types, i.e., in the form of differently organized helical rungs. We speculate that this observed plasticity of assembling a common helical rung is a consequence of flexibility in forming the longitudinal PB1–PB1 interactions in the loop regions. As the constructs used here for structure determination and cellular assays were limited to PB1 domains of AtNBR1 and p62, the relevance and functional consequences of these different morphological arrangements within

cellular polymeric assemblies remain open. Full-length p62 was shown to be flexible, and at this stage too disordered to be amenable to 3D reconstructions⁸. In line with our previous analysis, the PB1 domain directs the C-terminus either to the outside or the inside of the helical assembly, depending on the exact helical arrangement. It is possible to envision that different morphological arrangements affect the availability of critical interaction motifs outside the PB1 domain, i.e., LIR and KIR motifs as well as the UBA domain.

Fig. 6 Cellular assays of p62 polymeric state. **a** Schematic illustration of used p62 constructs and chimeras with p62-PB1 (green) and TFG1-PB1 (blue). **b** Representative, negatively stained electron micrographs of purified p62 constructs and chimeras from (a), including illustration of polymeric and oligomeric forms observed by negative staining electron microscopy. **c** Confocal fluorescent images of HeLa p62 (KO) cells expressing GFP-tagged constructs and chimeras. All examined constructs form punctate structures. **d** Quantification of the number of p62 bodies forming dots of various sizes. **e** Quantification of cells displaying yellow and red dots in (f). **f** Representative confocal fluorescence images of HeLa p62 (KO) cells expressing mCherry-YFP-tagged (dt-tagged) p62 constructs and chimeras. The appearance of red puncta (as an indicator of lysosomal localization) for all constructs indicates that all constructs and chimeras can be processed by autophagy. Punctae were counted and classified based on more than 100 cells in each condition in three independent experiments. **g** Representative confocal fluorescence images of HeLa p62 (KO) cells expressing the respective p62 constructs and chimeras, as well as mCherry-YFP-tagged KEAP1. **h** Statistics of appearance of lysosome-localized and cytosolic dots for mCherry-YFP-tagged KEAP1. The error bars in **d**, **e**, and **h** represent standard deviations of the mean.

Previous studies showed that purified full-length p62 can also form helical filaments^{7,8}. The existence of these assembly structures inside of cells, however, had not been demonstrated. Therefore, we used the CLEM technique to identify and visualize the ultrastructural organization of p62 found in large clusters known as p62 bodies. Image analysis confirmed that p62 bodies consist of a meshwork of short filamentous structures. The principal dimension of the observed structures is consistent in width and length with previous measurements *in vitro*⁸. The structures are compatible with recently observed aggregates of p62 in brain neurons and neuroepithelial cells²⁰. Due to the limited length and flexibility, p62 filaments pack loosely into a spheroid-shaped, meshwork-like superstructure. The observed bodies with average dimensions below micrometers in size aggregate in structures that appear morphologically separated from the cytosol (Fig. 5), suggestive of phase separation as observed previously in reconstitution experiments^{21,22}. The observed body structures of hundreds of nanometers are also significantly larger than individual filaments with on average 30 nm length. When organized in such large superstructures, p62 bodies are more similar in dimension to typical molecular cargo, such as protein aggregates, viruses, and organelles when compared with receptor oligomers or filament assemblies alone.

The organization of p62 in filamentous assemblies has direct functional consequences for the interaction with a series of binding partners in the context of autophagy as well as signaling. It has been demonstrated that a polymeric organization of p62 can enhance low-affinity interactions to highly avid interactions¹³. In addition, using p62-interacting PB1 domains from MEK5, PKC ζ , and MEKK3 kinases, we show that p62 polymeric assemblies can be capped on one end or dissociate into smaller, ring-like structures. The intact p62 filaments occlude the bulk of PB1 interaction sites that are accessible in its monomeric state⁵ (Fig. 4). Conversely, we show that end binding of NBR1 to p62 filaments leads to disassembly and shortening, which can thereby modulate the length of the filamentous structure. As NBR1 binding has been shown to promote p62 body formation *in vitro*^{21,22} to co-localize with p62 bodies *in vivo*²⁹, we hypothesize that this filament-end interaction by NBR1 cross-links shorter filaments more effectively into larger structures and thereby also affects the size of p62 bodies in cells. We speculate that other interactors have similar effects on the size and dynamics of p62 bodies as they may occur in phase separation processes. The size of bodies will also control the availability of interaction sites. The here presented structures and interaction studies of PB1–p62 filaments reveal a series of regulation mechanisms that are critical in the functional context of p62's action in autophagy and signaling.

In order to understand how the assembly state, the specific symmetry, and subunit arrangement of this state affect p62's biological function, we tested a series of chimera variants of p62 for their efficiency with regard to cargo uptake and autophagic degradation in the cell. The experiments showed that polymeric

as well as oligomeric ring-like scaffolds from related PB1 domains fused to the C-terminal functional domains of p62 can be taken up by the autophagy machinery almost as efficiently as WT-p62. Interestingly, this is not the case for variants of p62 that are monomeric and diffuse in the cytosol¹². Our results suggest that structures organized in larger oligomeric clusters are sufficient to mediate self-disposal of p62 (Fig. 6), presumably due to increased avidity of accessible LIR motifs and UBA domains. The specific uptake of the model cargo KEAP1, however, could only be accomplished by WT-p62 and mini-p62 retaining the structural context of native p62 assemblies. Other TFG1-PB1-p62 chimera polymers were not capable of transferring KEAP1 to the lysosome. The dependency of the native p62-PB1 domain for filament assemblies and KEAP1 degradation was further illustrated by the monomeric double arginine finger (R21A/R22A) mutant of p62. This mutant was completely diffusely localized, not degraded by autophagy, and unable to mediate degradation of KEAP1 by autophagy. In conclusion, larger p62 assemblies, including ring-like structures and filaments, are essential for disposal of autophagy cargo. Moreover, the precise structural context of the filament assembly is affecting the ability to degrade KEAP1-containing aggregates, and possibly other p62-specific cargoes.

Methods

Protein purification. AtNBR1 residues 1–94 (NBR1–PB1), p62 residues 1–122 (p62–PB1), and TFG1 residues 1–95 (TFG1–PB1) were cloned into a pETM44 expression vector containing a N-terminal His₆ tag, followed by a maltose-binding protein (MBP) tag and a recognition sequence for 3C protease. Proteins were expressed in *E. coli* BL21 (DE3) (obtained from Protein Expression and Purification Core Facility EMBL) using auto-induction in lactose-containing media³⁰. After 18 h, cells were harvested by centrifugation, resuspended in lysis buffer (50 mM HEPES, pH 8.0, 0.5 M NaCl, 0.05 mM TCEP, and 0.1% (v/v) Triton X-100), and lysed by three cycles of rapid freeze–thawing in liquid nitrogen. After removal of cell debris by centrifugation, recombinant proteins were purified by Ni-NTA affinity chromatography, and diafiltrated into 50 mM HEPES, pH 7.5, 0.1 M NaCl, and 0.05 mM TCEP followed by proteolytic cleavage of the His₆/MBP by incubation with 1:200 mol/mol 3C protease at ambient temperature. After 1 h, the cleavage solution was incubated with Talon resin (Clontech) for 15 min, and the resin subsequently sedimented by centrifugation. The supernatant contained the respective PB1 domains in high purity. p62 residues 1–122 (p62–PB1) were cloned into pOPTM and expressed as an MBP fusion protein in *E. coli* BL21 (DE3) using auto-induction (Studier 2005). NBR1 residues 1–85 (NBR1–PB1), pKC ζ residues 11–101 (pKC ζ –PB1), MEK5 residues 5–108 (MEK5–PB1), and MEKK3 residues 43–127 (MEKK3–PB1) were cloned into the pETM11 containing an N-terminal His₆ tag followed by a recognition sequence for TEV protease. Proteins were expressed in *E. coli* BL21 (DE3) using auto-induction (Studier 2005). For the gold-labeling experiments, the His₆ tag was not removed to allow binding of 5 nm Ni-NTA-Nanogold® (Nanoprobes). For consistency, the His₆ tag was also kept on the proteins for the co-pelletation assay.

Thermal unfolding assays. Thermal denaturation assays were performed essentially as described previously³¹. Briefly, protein was dialyzed into 15 mM HEPES (pH 7.5), 150 mM NaCl for pH screening, or 100 mM HEPES (pH 7.5) for ionic strength screening. All additives were dissolved in 50 mM HEPES (pH 7.5). A volume of 12.5 μ l of a solution containing 500 ng of protein was diluted in H₂O with 5x Sypro Orange (Sigma-Aldrich) and immediately mixed with an equal volume of assay condition. All conditions were assessed in triplicate. Fluorescence increase was monitored on a MyiQ real-time PCR instrument (BioRad). Assays were performed over a temperature range of 15–90 °C using a ramp rate of 1 °C

min⁻¹ in steps of 0.5 °C. Fluorescence data from triplicate measurements were baseline corrected individually, and unfolding curves were normalized to maximum fluorescence to give fractional denaturation curves. The apparent T_m was determined as the inflection point of a sigmoidal fit to the normalized fluorescence signal using a customized routine in R.

Quantification of PB1-binding affinities. Isothermal titration calorimetry (ITC) experiments were carried out with a VP-ITC system (MicroCal). Experiments were performed at 25 °C in 10 mM HEPES (pH 7.5), 150 mM NaCl. Purified p62¹⁻¹²² D69A/D73A was placed in the reaction cell at a concentration of 5–20 μM with either MEK5 or NBR1 at a concentration of 25–100 μM in the injection syringe. Injections of 10 μl of syringe solution were performed at 4-min intervals. Integration of the raw thermogram data, baseline correction, and data processing were performed with the NITPIC³² and SEDPHAT³³ software packages. The data were corrected by the heat of injection calculated from the basal heat remaining after saturation. A one-site binding mode was used to fit the data using a nonlinear least-squares algorithm³⁴. The values reported are the mean of three independent measurements, and errors represent the corresponding standard deviation.

Co-pelleting assay. Co-pelleting assay was performed according to the F-actin binding co-sedimentation assay from Cytoskeleton Inc. In brief, p62-PB1¹⁻¹²², potential binding partner, or p62-PB1¹⁻¹²² together with potential binding partner, were incubated for 1 h on ice followed by centrifugation at 49,000 g, 4 °C for 30 min in a TLA-100 rotor. The pellet and supernatant were assayed by SDS-PAGE and stained with Coomassie.

Negative staining EM and filament-length measurements. p62-PB1¹⁻¹²² was incubated with different binding partners for 1 h on ice followed by 30 min of incubation with 5 nm Ni-NTA-Nanogold® (diluted 1:25). Excess nanogold was removed through pelleting of filaments by ultracentrifugation at 49,000 g, 4 °C for 30 min in a TLA-100 rotor, and the pellet fraction was resuspended in 20 mM HEPES, pH 8, 50 mM NaCl. The sample (3.6 μl) was applied to a glow-discharged carbon-coated EM grid and blotted according to the side-blotting method³⁵. Grids were imaged using a Morgagni 268 transmission electron microscope (FEI) operated at 100 kV with a side-mounted 1 K CCD camera. Filament lengths for p62-PB1¹⁻¹²² and p62-PB1¹⁻¹²²/HsNBR1¹⁻⁸⁵ were measured using Fiji³⁶, and statistical analysis was done using a two-tailed unpaired *t* test with Welch's correction in GraphPad Prism 6.0.

Pull-down assay. MBP-tagged AtNBR1–PB1¹⁻⁹⁴ and mutant AtNBR1 residues 1–94 (AtNBR1–PB1) were expressed as described above and buffer-exchanged into 15 mM Tris (pH 7.5), 150 mM NaCl. For the AtNBR1 pull-down experiments, 50 μl of amylose resin (NEB) was incubated for 10 min with MBP–AtNBR1–PB1, followed by 5-min incubations with a 4:1 molar excess of mutant AtNBR1–PB1. Beads were washed with 15 mM HEPES (pH 7.5), 500 mM NaCl, eluted with 15 mM HEPES (pH 7.5), 150 mM NaCl, and 30 mM maltose, and fractions were analyzed by SDS-PAGE. p62, TFG1-mini-p62, and TFG1-p62 were purified as described and applied to size-exclusion chromatography on a Superdex 75 16/60 in 20 mM Tris (pH 8), 100 mM NaCl. Human KEAP1–DC³⁰⁹⁻⁶²⁴ was cloned into pET-28a(+) with a N-terminal 6×His tag, purified on Ni-NTA resin, and buffer-exchanged into 20 mM Tris (pH 8), 100 mM NaCl. Approximately 100 μl of amylose resin (NEB) was incubated for 30 min with either of the MBP-containing proteins at room temperature, followed by 30-min incubations with a 3:1 molar excess of KEAP1–DC³⁰⁹⁻⁶²⁴. Beads were washed with 20 mM Tris (pH 8), 1 M NaCl, and eluted with 20 mM Tris (pH 8), 100 mM NaCl, and 20 mM maltose. Fractions were analyzed by SDS-PAGE.

Electron cryo-microscopy. For AtNBR1¹⁻⁹⁴, a total of 3.0 μl of 0.4 mg ml⁻¹ AtNBR1–PB1 was applied to glow-discharged C-flat grids (CF-1.2/1.3–2 C, 400-mesh holey carbon on copper; Protochips) on a Leica GP2 vitrification robot (Leica, Germany) at 95% humidity and 25 °C. The sample was incubated for 10 s on the grid before blotting for 2 s from the back side of the grid and immediately flash-frozen in liquid ethane. Micrographs were acquired at 300 kV using an FEI Titan Krios (Thermo Fisher Scientific) equipped with a Falcon II direct detector at a magnification of 59,000, corresponding to a pixel size of 1.386 Å at the specimen level. Image acquisition was performed with EPU Software (Thermo Fisher Scientific), and micrographs were collected at an underfocus varying between 0.5 and 4.5 μm. We collected a total of seven frames accumulating to a dose of 14 e⁻ Å⁻² over 0.82 s. In total, 742 micrographs were acquired, of which we selected 684 for further processing after discarding micrographs that did not show Thon rings exceeding 6 Å.

For p62¹⁻¹²², L-type filaments were enriched by the following procedure: 0.2 mg of p62-PB1 (100 μl) was ammonium sulfate precipitated (25% v/v) and incubated o/n at 4 °C. The sample was spun at 17,000 g for 15 min at 4 °C, and the pellet was resuspended in 50 mM TRIS (pH 7.5), 100 mM NaCl, and 4 mM DTT. This ammonium sulfate precipitation was repeated a second time. In the final step, the sample was centrifuged at 49,000 g for 45 min at 4 °C, and the pellet resuspended in 25 μl. A total of 3.6 μl of the resulting p62-PB1¹⁻¹²² solution was applied to glow-discharged Quantifoil R2/1 Cu 400-mesh grids on a Vitrobot Mark IV (Thermo

Fisher Scientific) at 10 °C and 100% humidity. The sample was blotted for 5 s from both sides, and flash-frozen in liquid ethane after a drain time of 1 s. Micrographs were acquired at 300 kV using a FEI Titan Krios (Thermo Fisher Scientific) with a K2 Summit detector (Gatan, Inc.), a pixel size of 1.04 Å, and an underfocus ranging from 0.5 to 2.5 μm. In total, 40 frames were collected in counting mode with a dose rate of 4.5 e⁻ Å⁻² s and a total dose of 40 e⁻ Å⁻². In total, 2277 micrographs were automatically collected, and 856 micrographs without ice contamination or carbon chosen for further processing.

Image processing. For the AtNBR1 dataset, movie frames were aligned using MOTIONCORR³⁷. The resulting frame stacks and integrated images (total frame sums) were used for further processing. The contrast-transfer function of the micrographs was determined with CTFIND4³⁸ using the integrated images. Helix coordinates were picked using e2helixboxer.py from the EMAN2 package³⁹. Initially a subset of 100 images was selected for preliminary processing in SPRING⁴⁰. Briefly, overlapping helix segments of 350 × 350 Å dimensions were excised from the frame-aligned images with a mean step size of 60 Å using the SEGMENT module in SPRING. In-plane rotated, phase-flipped segments were subjected to 2D classification by k-means clustering as implemented in SPARX⁴¹. During a total of five iterations, the segments were classified and iteratively aligned against a subset of class averages chosen based on the quality of their power spectra. Class averages revealed two distinct helix types referred to as S-type and L-type. We determined the helical symmetry for the L-type helices by indexing of the power spectra obtained from the 2D classification. The final symmetry parameters were determined with a symmetry search grid using SEGMENTREFINED3GRID. For 3D refinement and reconstruction, the excised segments were convolved with the CTF and no in-plane rotation was applied prior to reconstruction. Starting from the symmetry parameters obtained for the L-type helix, symmetry parameters of the S-type helix were refined. The maximum of the mean cross-correlation peak between computed and experimental power spectra was found at a pitch of 70 Å, 11.55 units per turn for the two-start L-type helix, and a pitch of 68.2 Å, 11.55 units per turn for the one-start S-type helix. Using the refined symmetry parameters, we performed a competitive high-resolution multi-model structure refinement using all 684 images with a final resolution of 4.5/3.9 Å and 5.0/4.4 Å (FSC 0.5/0.143)⁴² for the two-start (L-type) and one-start (S-type) helix reconstructions (Table 2).

For the p62¹⁻¹²² data set, movie frames were aligned in RELION^{34,35} using 5 × 5 patches. The contrast-transfer function of the micrographs was determined with Gctf⁴⁴. Helix coordinates were automatically picked in RELION3 and segments extracted with a step of 22.5 Å, binning 2, and an unbinned box size of 256 pixels. 2D classification with 100 classes was performed and classes were selected that showed secondary structure features. Two separate subsequent 2D classifications were performed with two distinct groups of 2D classes belonging to an S-type and L-type pattern. Using SEGCLASSRECONSTRUCT from the SPRING package⁴⁰ a series of putative helical symmetry solutions could be obtained. In addition to running a series of refinements with these symmetry solutions, a C1 reconstruction provided additional hints for symmetry parameters. Imposition of wrong symmetry parameters led to smeared density features, whereas only the correct symmetries for both filament types led to recognizable high-resolution side-chain features. Helical symmetry was automatically refined in RELION to 77.3° helical rotation and 4.8 Å rise for the S-type and 26.5° rotation and 9.8 Å rise for the L-type, respectively (Table 2). Focussed refinement was performed using a mask covering the central 25% of the filament along the helical axis. This approach improved the resulting resolution for the L-type, but not for the S-type. The final resolution was estimated at 3.5 Å and 4.0 Å using the FSC and the 0.143 criterion cutoff⁴², for the L- and S-types, respectively.

Atomic model building and refinement. For visual display and model building, the AtNBR1 EM density map of the individual reconstructions was initially filtered to 3.9 Å and 4.4 Å, respectively, and sharpened using a B-factor of –200 Å². The AtNBR1–PB1 subunit model was built into the 3.9 Å density map of the L-type arrangement de novo in COOT⁴⁵. Residues 81–85 could not be built de novo due to weak density, but were added based on the high-resolution crystal structure obtained in this study, which showed good agreement with the weak density. For the p62-PB1 (3–102) map, the NMR structure from *rattus norvegicus* (PDB ID 2kkc [<https://doi.org/10.2210/pdb2kkc/pdb>]) was rigid-body fitted into the RELION-postprocessed density of the L-type filament and then manually adjusted to the human sequence in COOT⁴⁵. The models were expanded using helical symmetry, and a nine-subunit segment was excised to serve as a refinement target, taking into account interactions along the azimuthal propagation and lateral interactions along the helical axis. Following real-space refinement in PHENIX⁴⁶, we used model-based density scaling⁴⁷ to generate locally sharpened maps and completed the model in COOT followed by further iterations of real-space refinement. The final monomer atomic model from the L-type arrangement was rigid-body fitted into the S-type density, and refinement of the model was performed as described above (Table 3).

X-ray crystallography. Crystals of AtNBR1¹⁻⁹⁴ carrying a D60A/D62A mutation were grown using hanging drop vapor diffusion at 292 K by mixing equal volumes of 11 mg ml⁻¹ protein and reservoir solution. Within 10 h, crystals appeared as

needle clusters in 0.085 M MES (pH 6.5), 18.2% (w/v) PEG20000. Isolated needles ($10 \times 2 \times 4 \mu\text{m}$) were obtained by streak seeding with a cat whisker into 0.1 M MES (pH 6.5), 18–20% (w/v) PEG20000, or 0.1 M sodium cacodylate (pH 6.5), 0.2 M $(\text{NH}_4)_2\text{SO}_4$, and 30–33% PEG8000. For cryo-protection, crystals were soaked in the crystallization condition supplemented with 15% (v/v) glycerol. Diffraction data were collected on the ID23-2 microfocuss beamline at the European Synchrotron Radiation Facility (ESRF) and processed with XDS⁴⁸ and AIMLESS⁴⁹. Initial attempts to solve the crystal structure using the cryo-EM atomic model were unsuccessful. The crystal structure was solved using molecular replacement using the monomer density from the L-type cryo-EM reconstruction as the search model. Briefly, the monomer density was obtained by cutting out density extending 4.5 Å beyond the atomic coordinates. The extracted map segment was centered in a P1 unit cell extending over three times the maximum map dimension, converted to structure factors using an in-house, customized CCTBX⁵⁰ routine, and used for automated molecular replacement in PHASER⁵¹. The top-scoring solution had a translation function Z score of 16.5. Henderson–Lattmann coefficients were generated from the figure of merit (FOM) obtained from the PHASER solution and employed for phase extension using the high-resolution X-ray crystallographic data by density modification in RESOLVE⁵², yielding excellent electron density. Using the 1.9 Å data, the model was built using Arp/Warp⁵³ and completed manually in COOT. Table 1 summarizes data collection and refinement statistics.

Correlative light and electron microscopy. For CLEM, RPE1 cells (ATCC CRL-4000) were transiently transfected with pDest-EGFP-NBR1(D50R)²⁹ and grown on photo-etched coverslips (Electron Microscopy Sciences, Hatfield, USA). Cells were fixed in 4% formaldehyde, 0.1% glutaraldehyde/0.1 M PHEM (80 mM PIPES, 25 mM HEPES, 2 mM MgCl_2 , and 10 mM EGTA, pH 6.9), for 1 h. The coverslips were then washed in PBS containing 0.005% saponin and stained with the indicated primary antibodies for 1 h (rabbit anti-p62 (MBL, PM045), mouse anti-NBR1 (Santa Cruz, #sc-130380)), washed three times in PBS/saponin, stained with secondary antibodies (from Jackson ImmunoResearch Laboratories) for 1 h, washed three times in PBS, and shortly rinsed in water. The cells were mounted with Mowiol containing $2 \mu\text{g ml}^{-1}$ Hoechst 33342 (Sigma-Aldrich). Mounted coverslips were examined with a Zeiss LSM780 confocal microscope (Carl Zeiss MicroImaging GmbH, Jena, Germany) utilizing a Laser diode 405–30 CW (405 nm), an Ar-Laser Multiline (458/488/514 nm), a DPSS-561 10 (561 nm), and a HeNe laser (633 nm). The objective used for confocal microscopy was a Zeiss plan-Apochromat 63 \times /1.4 Oil DIC III. Cells of interest were identified by fluorescence microscopy and a Z stack was acquired. The relative positioning of the cells on the photo-etched coverslips was determined by taking a DIC image. The coverslips were removed from the object glass, washed with 0.1 M PHEM buffer, and fixed in 2% glutaraldehyde/0.1 M PHEM for 1 h. Cells were postfixed in osmium tetroxide, stained with tannic acid, dehydrated stepwise to 100% ethanol, and flat-embedded in Epon. Serial sections (~100–200 nm) were cut on an Ultracut UCT ultra-microtome (Leica, Germany), collected on formvar-coated mesh grids, and post-stained with lead citrate.

Electron tomography from cellular sections. Samples were observed using a FEI Talos F200C electron microscope (Thermo Fisher Scientific). Image series were taken between -60° and 60° with 2° increment. Single-tilt or double-tilt series (as indicated in the text above) were recorded with a Ceta 16 M camera. Single-axis tomograms were computed using weighted back projection, and when applicable, merged into a dual-axis tomogram using the IMOD⁵⁴ package. Display and animation of segmentation of tomograms were performed using a scripted workflow in ImageJ⁵⁶ and IMARIS.

Autophagy and p62 turnover assays. The following antibodies were used: mouse anti-Myc antibody (Cell Signaling, Cat. #2276#, 1:8000 for western blots and 1:5000 for confocal imaging); rabbit anti-GFP antibody (Abcam, ab290, 1:5000); guinea pig anti-p62 antibody (Progen, Cat. #Gp62-C#, 1:5000); rabbit anti-actin antibody (Sigma, Cat. #A2066#, 1:1000); Alexa Fluor[®] 647-conjugated goat anti-mouse IgG (A21236, 1:1000); HRP-conjugated goat anti-mouse IgG (1:5000); goat anti-rabbit IgG (1:5000); goat anti-guinea pig IgG (1:5000).

Generation of HeLa cells KO for p62 and stable cell lines. To generate CRISPR/Cas9 p62 gRNA plasmid, sense and antisense p62 gRNA was annealed and then inserted into plasmid pX330 (Ref PMID: 23287718). For generation of CRISPR/Cas9 p62 KO cells, ~30,000 HeLa cells (ATCC CCL2) were seeded per well into 24-well plates and transfected with plasmid pX330 p62 gRNA using Metafectene Pro (Biontex T040). For clonal selection, cells were treated with 500 ng ml^{-1} of puromycin 24 h after transfection for 48–72 h. Later, single cells were sorted into a 96-well plate using FACS (fluorescence-activated cell sorting). These clones were allowed to grow for 7–10 days before screening for KO using immunoblotting. The following sense 5'-CACGTCATCCTTCACGTAGGACA-3' and antisense 5'-AAACTGTCCTACGTGAAGGATGAC-3' gRNAs were used.

HeLa FlpIn T-Rex p62 KO cells⁵⁵ were used to make stable cell lines expressing GFP-p62 or GFP-p62 R21A/R22A. First, p62 and p62 R21A/R22A were transferred

into the destination vector pDest-FRT/TO-GFP-C1⁵⁶ by Gateway LR recombination reactions. Then stable cell lines were made using the manufacturer's instructions (Invitrogen, V6520-20). Briefly, the HeLa FlpIn T-Rex p62 KO cell line was transfected with pDest-FRT/TO-EGFP-p62 or pDest-FRT/TO-EGFP-p62 R21A/R22A. Forty-eight hours post transfection, colonies of cells with the gene of interest integrated into FRT site were selected using $200 \mu\text{g/ml}$ of Hygromycin (Calbiochem, 400051). To induce expression of the gene of interest, $1 \mu\text{g/ml}$ of tetracycline was added for 24 h. Analyses of degradation of EGFP-p62 or EGFP-p62 R21A/R22A by flow cytometry were done as previously described⁵⁷.

Construction of plasmids. The gateway entry clones pENTR-p62, pENTR-p62 R21A/R22A, and pENTR-p62 Δ 123–319 (mini-p62) have been described previously². pENTR-p62 Δ 123–319 was made by deletion of pENTR-p62. TFG1-p62 fusion constructs were produced by InFusion PCR. To subclone the TFG1-p62 fusion constructs into an ENTRY vector, a NcoI site was inserted into the start codon of p62 in pENTR-p62, creating pENTR-p62_{CCATGG}. The start codons in TFG1-p62 (AJD152) and TFG1-mini-p62 (AJD157) already have NcoI sites, and there is an additional NcoI site close to the end of the p62 cDNA sequence in pENTR-p62, TFG1-p62, and TFG1-mini-p62. To replace wild-type p62 of pENTR-p62_{CCATGG}, TFG1-p62 and TFG1-mini-p62 (AJD152 and AJD157) were subcloned as NcoI fragments into pENTR-p62_{CCATGG} cut with NcoI, creating pENTR-TFG1-p62 and pENTR-TFG1-mini-p62, respectively. Gateway LR recombination reactions were performed as described in the Gateway cloning technology instruction manual (Thermo Fisher Scientific, 11791020). Gateway expression clones pDest-Myc-p62, pDest-EGFP-p62, and pDest-mCherry-EGFP-KEAP1 have been described previously^{2,16}. pDest-TFG1-Myc-p62 Δ 123–319, pDest-Myc-TFG1-p62, and pDest-Myc-TFG1-mini-p62 were made by Gateway LR reactions using destination vector pDest-Myc (mammalian expression of N-terminal Myc-tagged proteins²). pDest-EGFP-p62 Δ 123–319, pDest-EGFP-TFG1-p62, and pDest-EGFP-TFG1-mini-p62 were made using destination vector pDest-EGFP-C1 (mammalian expression of N-terminal EGFP-tagged proteins²). pDest-mCherry-EYFP-p62, pDest-mCherry-EYFP-p62 Δ 123–319, pDest-mCherry-EYFP-TFG1-p62, and pDest-mCherry-EYFP-TFG1-mini-p62 were made using destination vector pDest-mCherry-EYFP⁵⁸ (mammalian expression of N-terminal mCherry-EYFP double-tagged proteins).

Cell culture and transfections. HeLa p62 KO cells were cultured in Eagle's minimum essential medium with 10% fetal bovine serum (Biocrom AG, S0615), non-essential amino acids, 2 mM L-glutamine, and 1% streptomycin–penicillin (Sigma, P4333). For transfection the same media was used but without 1% streptomycin–penicillin. Cells were fixed in 4% PFA for 20 min at room temperature. For immunostaining, cells were permeabilized with cold methanol for 5 min at room temperature, blocked in 3% goat serum/PBS, and incubated at room temperature with antibodies. For DNA staining 1:4000 dilution was used in PBS of DAPI (Thermo Fisher Scientific; pr.66248). Samples were mounted using Mowiol 4-88 (Calbiochem 475904). Cells were examined using a Zeiss LSM780 or LSM800 microscope with a 63×1.4 oil objective or a Leica TCS SP8 confocal microscope, 40×1.3 oil objective.

Western blot analyses. Transfected HeLa p62 KO cells were harvested in 50 mM Tris, pH 7.4, 2% SDS, and 1% glycerol. Cell lysates were cleared by centrifugation, and supernatants resolved by SDS-PAGE and transferred to Hybond-ECL nitro-cellulose membrane (GE Healthcare). The membrane was blocked with 5% nonfat dry milk in PBS-T, incubated with primary antibody overnight, and HRP-conjugated secondary antibody for 1 h at room temperature. Proteins were detected by immunoblotting with a chemiluminescence Luminol kit (SC-2048, Santa Cruz Biotechnology) using a LumiAnalyst Imager (Roche Applied Sciences).

Reporting summary. Further information on research design is available in the Nature Research Reporting Summary linked to this article.

Data availability

The PDB accession number for the atomic coordinates and structure factors of the reported AtNBR1-PB1 X-ray crystal structure is PDB ID 6TGS. Raw X-ray diffraction images of the AtNBR1-PB1 crystal structure (PDB ID 6TGS [<https://doi.org/10.22101/pdb6tgs/pdb>]) have been deposited under <https://doi.org/10.5281/zenodo.3556558>. The EMDB accession numbers for the L- and S-type AtNBR1-PB1 cryo-EM maps and models are EMD-10499/EMD-10500 and the corresponding PDB IDs 6TGN [<https://doi.org/10.22101/pdb6tgn/pdb>]/6TGP [<https://doi.org/10.22101/pdb6tgp/pdb>]. For the L- and S-type p62-PB1 cryo-EM maps and atomic coordinate models EMD-10501/EMD-10502 and PDB IDs 6TGY [<https://doi.org/10.22101/pdb6tgy/pdb>]/6TH3 [<https://doi.org/10.22101/pdb6th3/pdb>] have been assigned, respectively. The source data underlying Figs. 1C, 3F, 4C, 4D, 4F, 5A, 5E, and Supplementary Figs. 5F, 7D, 7E, and 7F are provided as a Source Data file. All relevant data are available from the corresponding author upon reasonable request.

Received: 28 May 2019; Accepted: 2 January 2020;
Published online: 23 January 2020

References

- Katsuragi, Y., Ichimura, Y. & Komatsu, M. p62/SQSTM1 functions as a signaling hub and an autophagy adaptor. *FEBS J.* **282**, 4672–4678 (2015).
- Lamark, T. et al. Interaction codes within the family of mammalian Phox and Bem1p domain-containing proteins. *J. Biol. Chem.* **278**, 34568–34581 (2003).
- Moscat, J., Diaz-Meco, M. T., Albert, A. & Campuzano, S. Cell signaling and function organized by PB1 domain interactions. *Mol. Cell* **23**, 631–640 (2006).
- Korasick, D. A. et al. Molecular basis for AUXIN RESPONSE FACTOR protein interaction and the control of auxin response repression. *Proc. Natl Acad. Sci. USA* **111**, 5427–5432 (2014).
- Wilson, M. I., Gill, D. J., Perisic, O., Quinn, M. T. & Williams, R. L. PB1 domain-mediated heterodimerization in NADPH oxidase and signaling complexes of atypical protein kinase C with Par6 and p62. *Mol. Cell* **12**, 39–50 (2003).
- Sumimoto, H., Kamakura, S. & Ito, T. Structure and function of the PB1 domain, a protein interaction module conserved in animals, fungi, amoebas, and plants. *Sci. STKE* **2007**, re6 (2007).
- Paine, M. G., Babu, J. R., Seibenhener, M. L. & Wooten, M. W. Evidence for p62 aggregate formation: role in cell survival. *FEBS Lett.* **579**, 5029–5034 (2005).
- Ciuffa, R. et al. The selective autophagy receptor p62 forms a flexible filamentous helical scaffold. *Cell Rep.* **11**, 748–758 (2015).
- Mizushima, N. & Komatsu, M. Autophagy: renovation of cells and tissues. *Cell* **147**, 728–741 (2011).
- Johansen, T. & Lamark, T. Selective autophagy mediated by autophagic adapter proteins. *Autophagy* **7**, 279–296 (2011).
- Kraft, C., Peter, M. & Hofmann, K. Selective autophagy: ubiquitin-mediated recognition and beyond. *Nat. Cell Biol.* **12**, 836–841 (2010).
- Itakura, E. & Mizushima, N. p62 Targeting to the autophagosome formation site requires self-oligomerization but not LC3 binding. *J. Cell Biol.* **192**, 17–27 (2011).
- Wurzer, B. et al. Oligomerization of p62 allows for selection of ubiquitinated cargo and isolation membrane during selective autophagy. *eLife* **4**, 1687 (2015).
- Bjorkoy, G. et al. p62/SQSTM1 forms protein aggregates degraded by autophagy and has a protective effect on huntingtin-induced cell death. *J. Cell Biol.* **171**, 603–614 (2005).
- Pankiv, S. et al. p62/SQSTM1 binds directly to Atg8/LC3 to facilitate degradation of ubiquitinated protein aggregates by autophagy. *J. Biol. Chem.* **282**, 24131–24145 (2007).
- Jain, A. et al. p62/SQSTM1 is a target gene for transcription factor NRF2 and creates a positive feedback loop by inducing antioxidant response element-driven gene transcription. *J. Biol. Chem.* **285**, 22576–22591 (2010).
- Komatsu, M. et al. The selective autophagy substrate p62 activates the stress responsive transcription factor Nrf2 through inactivation of Keap1. *Nat. Cell Biol.* **12**, 213–223 (2010).
- Duran, A. et al. The signaling adaptor p62 is an important NF- κ B mediator in tumorigenesis. *Cancer Cell* **13**, 343–354 (2008).
- Carroll, B. et al. Oxidation of SQSTM1/p62 mediates the link between redox state and protein homeostasis. *Nat. Commun.* **9**, 256–11 (2018).
- Sukseree, S. et al. Filamentous aggregation of sequestosome-1/p62 in brain neurons and neuroepithelial cells upon Tyr-Cre-mediated deletion of the autophagy gene Atg7. *Mol. Neurobiol.* **55**, 8425–8437 (2018).
- Zaffagnini, G. et al. p62 filaments capture and present ubiquitinated cargos for autophagy. *EMBO J.* **37**, e98308 (2018).
- Sun, D., Wu, R., Zheng, J., Li, P. & Yu, L. Polyubiquitin chain-induced p62 phase separation drives autophagic cargo segregation. *Cell Res.* **28**, 405–415 (2018).
- Svenning, S., Lamark, T., Krause, K. & Johansen, T. Plant NBR1 is a selective autophagy substrate and a functional hybrid of the mammalian autophagic adapters NBR1 and p62/SQSTM1. *Autophagy* **7**, 993–1010 (2011).
- Saio, T., Yokochi, M. & Inagaki, F. The NMR structure of the p62 PB1 domain, a key protein in autophagy and NF- κ B signaling pathway. *J. Biomol. NMR* **45**, 335–341 (2009).
- Saio, T., Yokochi, M., Kumeta, H. & Inagaki, F. PCS-based structure determination of protein-protein complexes. *J. Biomol. NMR* **46**, 271–280 (2010).
- Krissinel, E. & Henrick, K. Inference of macromolecular assemblies from crystalline state. *J. Mol. Biol.* **372**, 774–797 (2007).
- Ren, J., Wang, J., Wang, Z. & Wu, J. Structural and biochemical insights into the homotypic PB1-PB1 complex between PKC ζ and p62. *Sci. China Life Sci.* **57**, 69–80 (2014).
- Egelman, E. H. et al. Structural plasticity of helical nanotubes based on coiled-coil assemblies. *Structure* **23**, 280–289 (2015).
- Kirkin, V. et al. A role for NBR1 in autophagosomal degradation of ubiquitinated substrates. *Mol. Cell* **33**, 505–516 (2009).
- Studier, F. W. Protein production by auto-induction in high density shaking cultures. *Protein Expr. Purif.* **41**, 207–234 (2005).
- Jakobi, A. J., Mashaghi, A., Tans, S. J. & Huizinga, E. G. Calcium modulates force sensing by the von Willebrand factor A2 domain. *Nat. Commun.* **2**, 385 (2011).
- Scheuermann, T. H. & Brautigam, C. A. High-precision, automated integration of multiple isothermal titration calorimetric thermograms: new features of NITPIC. *Methods* **76**, 87–98 (2015).
- Zhao, H., Piszczek, G. & Schuck, P. SEDPHAT—a platform for global ITC analysis and global multi-method analysis of molecular interactions. *Methods* **76**, 137–148 (2015).
- Brautigam, C. A., Zhao, H., Vargas, C., Keller, S. & Schuck, P. Integration and global analysis of isothermal titration calorimetry data for studying macromolecular interactions. *Nat. Protoc.* **11**, 882–894 (2016).
- Ohi, M., Li, Y., Cheng, Y. & Walz, T. Negative staining and image classification—powerful tools in modern electron microscopy. *Biol. Proc. Online* **6**, 23–34 (2004).
- Schindelin, J. et al. Fiji: an open-source platform for biological-image analysis. *Nat. Methods* **9**, 676–682 (2012).
- Li, X. et al. Electron counting and beam-induced motion correction enable near-atomic-resolution single-particle cryo-EM. *Nat. Methods* **10**, 584–590 (2013).
- Rohou, A. & Grigorieff, N. CTFIND4: fast and accurate defocus estimation from electron micrographs. *J. Struct. Biol.* **192**, 216–221 (2015).
- Tang, G. et al. EMAN2: an extensible image processing suite for electron microscopy. *J. Struct. Biol.* **157**, 38–46 (2007).
- Desfosses, A., Ciuffa, R., Gutsche, I. & Sachse, C. SPRING—an image processing package for single-particle based helical reconstruction from electron cryomicrographs. *J. Struct. Biol.* **185**, 15–26 (2014).
- Hohn, M. et al. SPARX, a new environment for Cryo-EM image processing. *J. Struct. Biol.* **157**, 47–55 (2007).
- Rosenthal, P. B. & Henderson, R. Optimal determination of particle orientation, absolute hand, and contrast loss in single-particle electron cryomicroscopy. *J. Mol. Biol.* **333**, 721–745 (2003).
- Zivanov, J. et al. New tools for automated high-resolution cryo-EM structure determination in RELION-3. *eLife* **7**, 163 (2018).
- Zhang, K. Gctf: real-time CTF determination and correction. *J. Struct. Biol.* **193**, 1–12 (2016).
- Emsley, P. & Cowtan, K. Coot: model-building tools for molecular graphics. *Acta Crystallogr. D. Biol. Crystallogr.* **60**, 2126–2132 (2004).
- Adams, P. D. et al. PHENIX: a comprehensive Python-based system for macromolecular structure solution. *Acta Crystallogr. D. Biol. Crystallogr.* **66**, 213–221 (2010).
- Jakobi, A. J., Wilmanns, M. & Sachse, C. Model-based local density sharpening of cryo-EM maps. *eLife* **6**, e27131 (2017).
- Kabsch, W. Integration, scaling, space-group assignment and post-refinement. *Acta Crystallogr. D. Biol. Crystallogr.* **66**, 133–144 (2010).
- Evans, P. R. & Murshudov, G. N. How good are my data and what is the resolution? *Acta Crystallogr. D. Biol. Crystallogr.* **69**, 1204–1214 (2013).
- Grosse-Kunstleve, R. W., Sauter, N. K., Moriarty, N. W. & Adams, P. D. The Computational Crystallography Toolbox: crystallographic algorithms in a reusable software framework. *J. Appl. Crystallogr.* **35**, 126–136 (2002).
- Mccooy, A. J. et al. Phaser crystallographic software. *J. Appl. Crystallogr.* **40**, 658–674 (2007).
- Terwilliger, T. C. et al. Model morphing and sequence assignment after molecular replacement. *Acta Crystallogr. D. Biol. Crystallogr.* **69**, 2244–2250 (2013).
- Langer, G., Cohen, S. X., Lamzin, V. S. & Perrakis, A. Automated macromolecular model building for X-ray crystallography using ARP/wARP version 7. *Nat. Protoc.* **3**, 1171–1179 (2008).
- Kremer, J. R., Mastronarde, D. N. & McIntosh, J. R. Computer visualization of three-dimensional image data using IMOD. *J. Struct. Biol.* **116**, 71–76 (1996).
- Overå, K. et al. TRIM32, but not its muscular dystrophy-associated mutant, positively regulates and is targeted to autophagic degradation by p62/SQSTM1. *J. Cell Sci.* **132**, jcs236596 (2019).
- Alemu, E. A. et al. ATG8 family proteins act as scaffolds for assembly of the ULK complex: sequence requirements for LC3-interacting region (LIR) motifs. *J. Biol. Chem.* **287**, 39275–39290 (2012).
- Larsen, K. B. et al. A reporter cell system to monitor autophagy based on p62/SQSTM1. *Autophagy* **6**, 784–793 (2010).
- Bhujabal, Z. et al. FKBP8 recruits LC3A to mediate Parkin-independent mitophagy. *EMBO Rep.* **18**, 947–961 (2017).

Acknowledgements

We thank the European Synchrotron Radiation Facility (ESRF, Grenoble, France), the EMBL beamlines at PETRA-III (DESY, Hamburg, Germany), and the beamline scientists at ESRF ID23-2 and EMBL-DESY P14 for excellent support. The project was financially supported by the Boehringer Ingelheim Fund's Exploration Grant. A.J.J. acknowledges financial support by an EMBL Interdisciplinary Postdoc (EIPOD) fellowship under Marie Curie Actions (PCOFUND-GA-2008-229597), a Marie Skłodowska-Curie IEF

fellowship (PIEF-GA-2012-331285), the Deutsche Forschungsgemeinschaft (DFG) through the excellence cluster “The Hamburg Center for Ultrafast Imaging (CUI)—Structure, Dynamics and Control of Matter at the Atomic Scale” (EXC1074), and the Joachim Herz Foundation. Work in the lab of T.J. was funded by grants from the FRIBIOMED (grant number 214448) and the TOPPFORSK (grant number 249884) programs of the Research Council of Norway to T.J.

Author contributions

A.J.J. and C.S. designed research. A.J.J., T.K. and S.M. purified proteins and performed biochemical/biophysical characterization. A.J.J., W.J.H.H. and S.T.H. determined the cryo-EM structures. A.J.J. and M.W. determined the X-ray crystal structure. S.W.B. and A.B. performed and evaluated cellular EM. A.P., B.K.S., T.L. and T.J. designed and carried out experiments using cellular light microscopy. A.J.J. and C.S. wrote the paper with major input from all other authors.

Competing interests

The authors declare no competing interests.

Additional information

Supplementary information is available for this paper at <https://doi.org/10.1038/s41467-020-14343-8>.

Correspondence and requests for materials should be addressed to C.S.

Peer review information *Nature Communications* thanks Masaaki Komatsu, Matthias Wolf and the other, anonymous, reviewer(s) for their contribution to the peer review of this work. Peer reviewer reports are available.

Reprints and permission information is available at <http://www.nature.com/reprints>

Publisher's note Springer Nature remains neutral with regard to jurisdictional claims in published maps and institutional affiliations.



Open Access This article is licensed under a Creative Commons Attribution 4.0 International License, which permits use, sharing, adaptation, distribution and reproduction in any medium or format, as long as you give appropriate credit to the original author(s) and the source, provide a link to the Creative Commons license, and indicate if changes were made. The images or other third party material in this article are included in the article's Creative Commons license, unless indicated otherwise in a credit line to the material. If material is not included in the article's Creative Commons license and your intended use is not permitted by statutory regulation or exceeds the permitted use, you will need to obtain permission directly from the copyright holder. To view a copy of this license, visit <http://creativecommons.org/licenses/by/4.0/>.

© The Author(s) 2020

Supplementary Information

Structural basis of p62/SQSTM1 helical filaments and their role in cellular cargo uptake

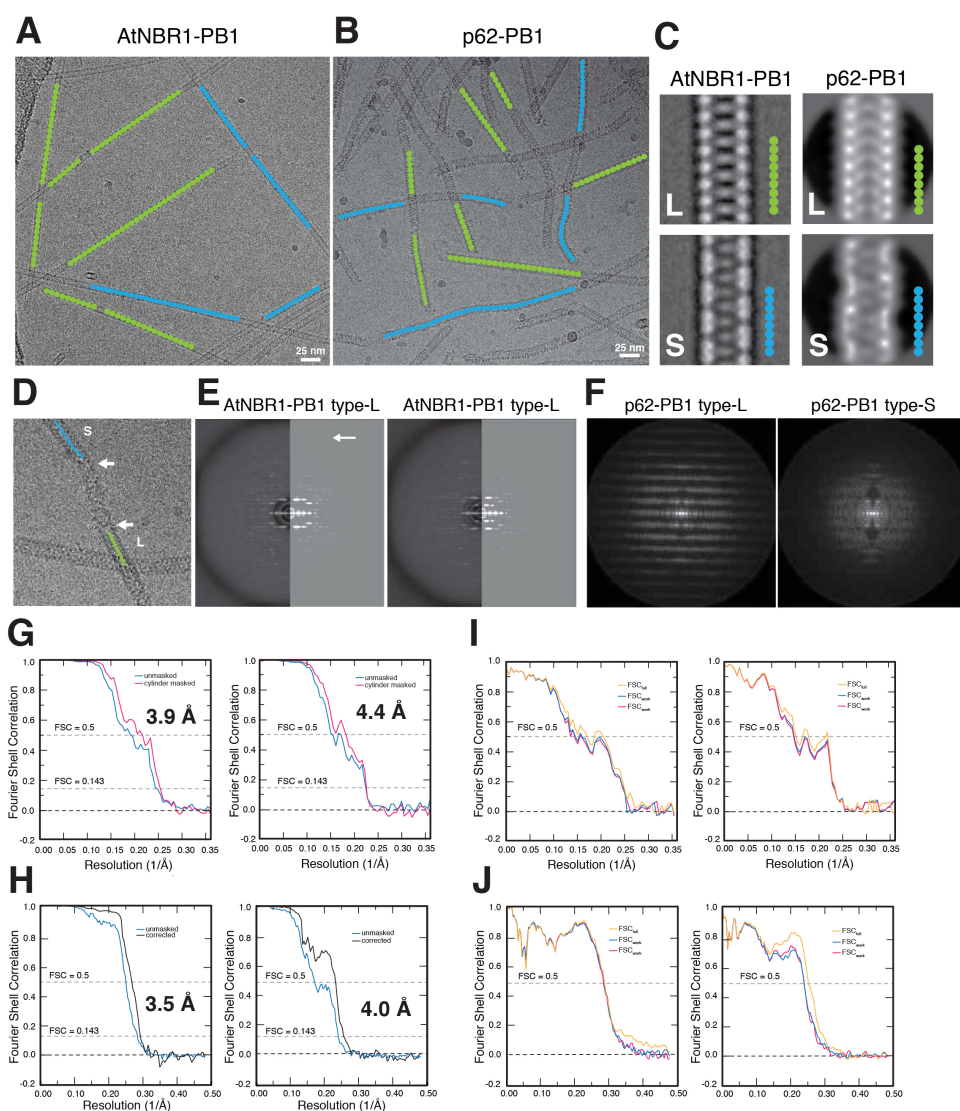
Arjen J. Jakobi et al.

Supplementary Tables

Supplementary Table 1. Primer sequences used in this manuscript.

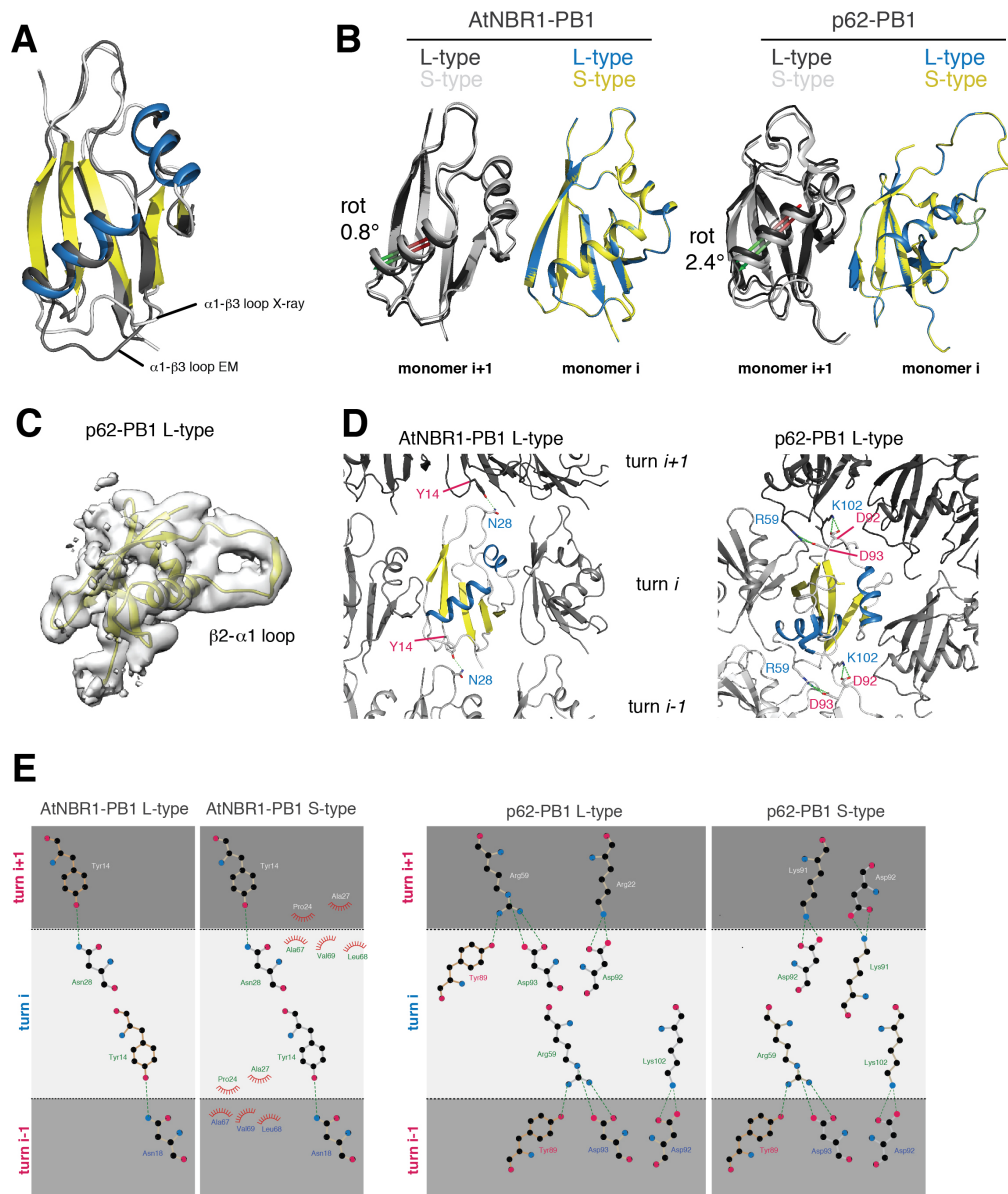
Primer name	sequence (5' -> 3')
AtNBR1 M1 fw	gcttccatgggcatggagtctactgctaacgcactcg
AtNBR1 K11a fw	gctaacgcactcgtcgtcgccgtgagctatggagggtg
AtNBR1 K11A rv	cacacctccatagctcacggcgacgacgagtgcgtagc
AtNBR1 R19A_R20A fw	gtgagctatggagggtgcttgccgctcagggtgcctgttaaagc
AtNBR1 R19A_R20A rv	gctttaacaggcaccctgaaggccgaagcacacctccatagctcac
AtNBR1 D60A fw	gagtctgacttactctgctgaggatggggatgtgg
AtNBR1 D60A rv	ccacatccccatcctcagcagagtaagtcagactc
AtNBR1 E61A fw	gtctgacttactctgatgaggatggggatgtgg
AtNBR1 E61A rv	ccacatccccatccgcatcagagtaagtcagac
AtNBR1 D60A_D62A fw	gagtctgacttactctgctgaggctggggatgtggtgccctgt
AtNBR1 D60A_D62A rv	acaagggcaaccacatccccagcctcagcagagtaagtcagactc
AtNBR1 D64A fw	ctgatgaggatggggctgtggtgccctgt
AtNBR1 D64A rv	acaagggcaaccacaGccccatcctcatcag
AtNBR1 S94 rv	gcttgccggccgcttattaggacacgccagcgttcacattg
TFG M1 fw	gcttccatgggcaacggacagttggatctaagtggg
TFG R95 rv	gcttgccggccgcttattatctggctggccattaacaaataatg
PKCz G11 fw	gcttccatgggacagcggcgccgctccgcc
PKCz E101 rv	gcttgccggccgcttattactcaggggtgctcgggaaaac
NBR1 D50R fw	gatggatacctctcatttctcagcaggtattttattgaatagtattc
NBR1 D50R rv	gaatactattcaataaaaatacctgcgtgaggaaaatgaagaggatccatc
p62 M1 fw	gcttccatgggacgctcgtcaccgtgaaggc
p62 K102 rv	gcttgccggccgcttattttctttaatgtagattcgg
p62 V122 rv	gcttgccggccgcttattacaccatgttgccggggcgccctcc
TFG-P62 fw	tctgttccaggggccatggccatgaacggacagttggatctaa
TFG-P62 rv	gcagccatcgagatcacattgggattaacaaataatgtcagtttcagt
TFG-CC-min-pP62 fw	tctgttccaggggccatggccatgaacggacagttggatctaa
TFG-CC-min-pP62 rv	actccatctgttctcagggcgtccaggtggtccaagct
MEK5 A5 fw	ttcagggcgccatggcgcccttgccccttct
MEK5 A108 rv	gctcgagtgcggccgctcaggctcttgaaatctcgcag

Supplementary Figures



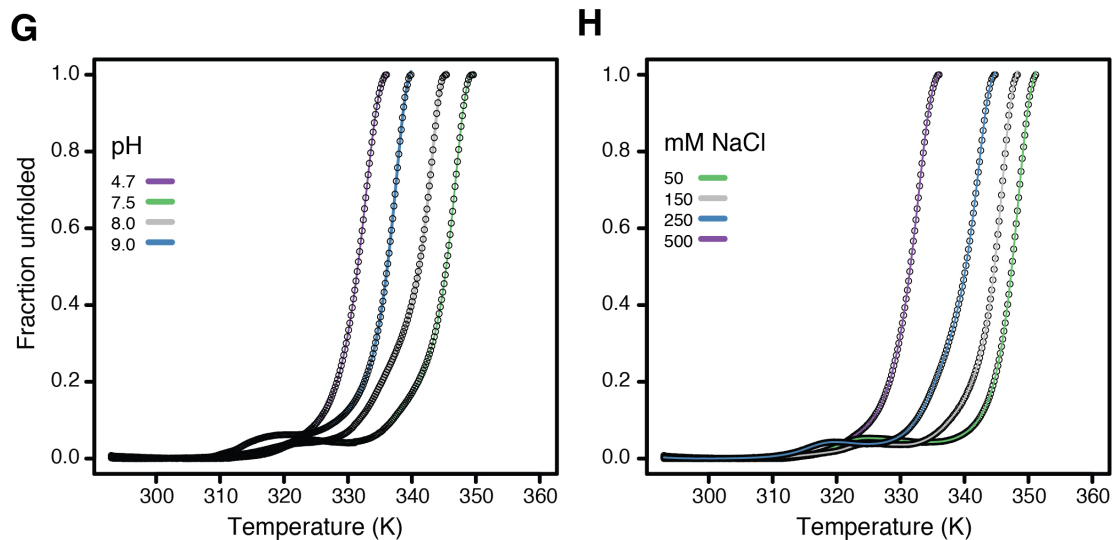
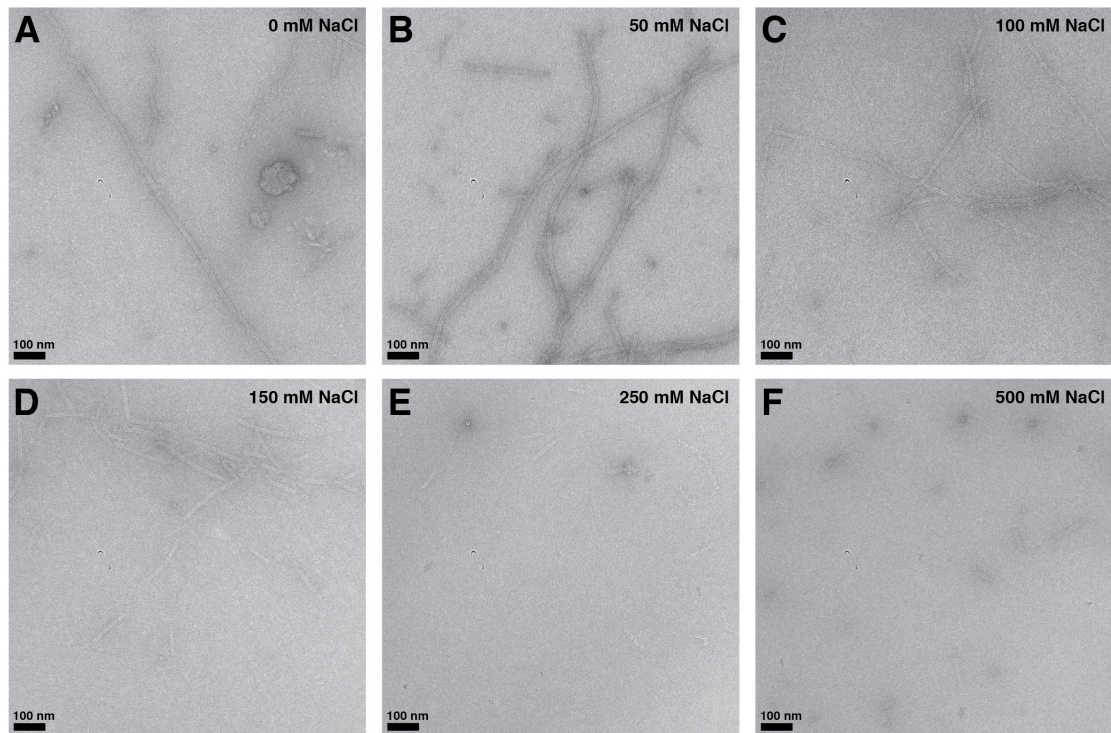
Supplementary Figure 1. Electron cryo-microscopy of AtNBR1-PB1 and p62-PB1.

(A) Representative micrographs of AtNBR1-PB1 with helix traces of segment centers classified as L-type (green) or S-type (blue) superposed. (B) Representative micrographs of p62-PB1 with center traces of segments classified as L-type (green) or S-type (blue) superposed. (C) Low-pass filtered class averages of L-type (top) and S-type (bottom) AtNBR1-PB1 and p62-PB1 assemblies. (D) Representative image showing transitions between L and S-type assemblies for p62-PB1 (E) Side-by-side power spectra of L-type (top) and S-type (bottom) AtNBR1-PB1 assemblies with the power of sum of segments (left) and that simulated from re-projection of the 3D structure (right). Arrows indicate high-resolution meridional layer lines. (F) Power spectra of L-type (top) and S-type (bottom) p62-PB1 assemblies with the summed power spectra of the 2D classes. (G) Fourier shell correlation for 3D reconstruction of L-type (left) and S-type (right) AtNBR1-PB1 assemblies. (H) Fourier shell correlation for 3D reconstruction of L-type (left) and S-type (right) p62-PB1 assemblies. (I) Model vs. map Fourier shell correlation for L-type (left) and S-type (right) AtNBR1-PB1 assemblies. (J) Model vs. map Fourier shell correlation for L-type (left) and S-type (right) p62-PB1 assemblies.



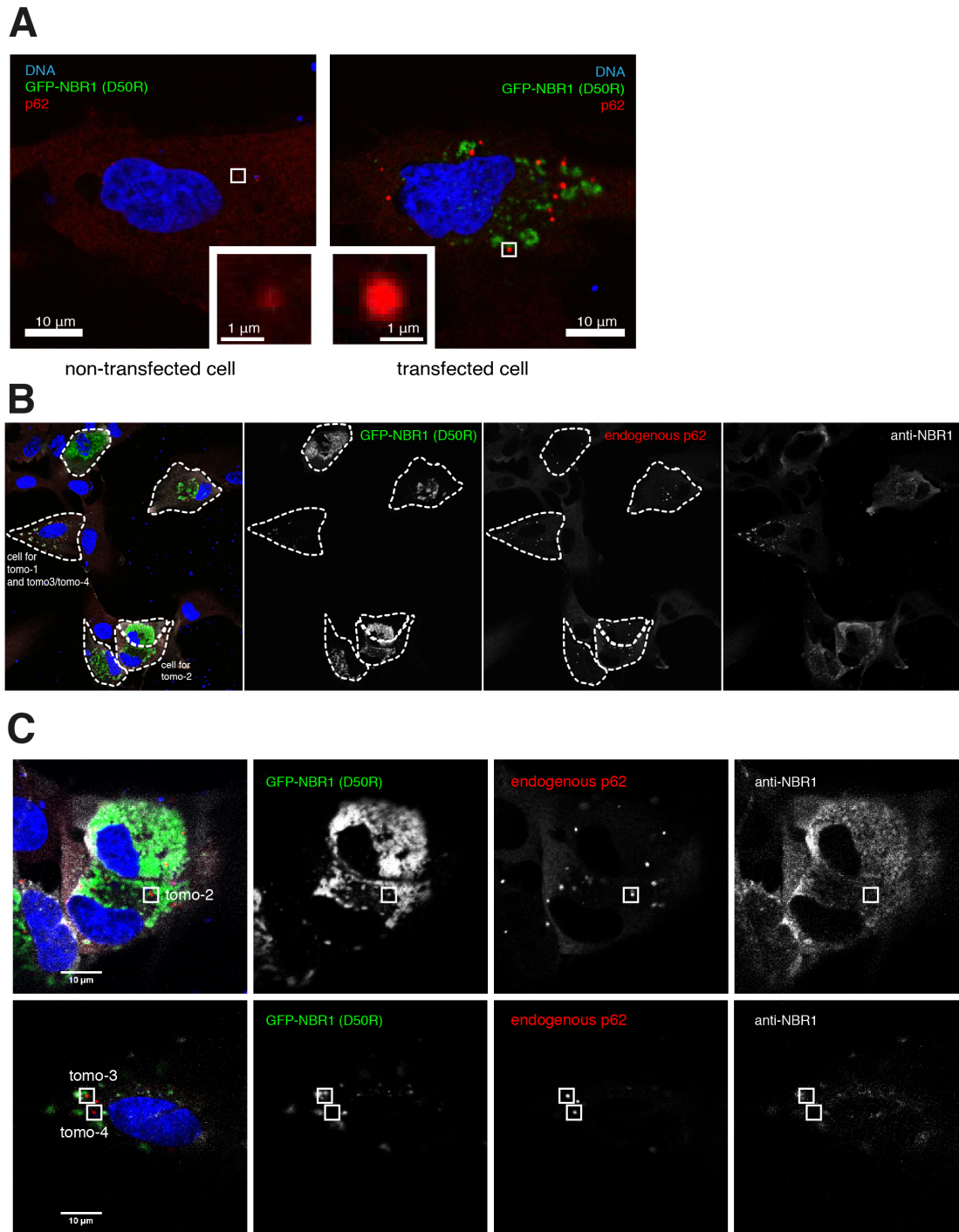
Supplementary Figure 2. Atomic models from crystal and cryo-EM structures of AtNBR1-PB1¹⁻⁹⁴ and p62-PB1¹⁻¹²².

(A) Superposition of cartoon representation of atomic models from the 1.6 Å crystal structure of AtNBR1-PB1 and the de novo-built model based on the 3.9 Å cryo-EM AtNBR1-PB1 density map (α -helix: blue, β -strands: yellow). Marked differences are observed in loop regions mediating lateral contacts. (B) Superposition of atomic models for L-type (blue) and S-type (yellow) assemblies for AtNBR1-PB1 (left) and p62-PB1 (right). Monomer *i* for each assembly is superposed and the difference in rotation of adjacent subunit *i*+1 are indicated. Only minor differences are observed. (C) LocScale map for L-type p62-PB1 cropped around one monomer. (D) Lateral contacts formed along the helical axis shown for AtNBR1-PB1 (left) and p62-PB1 (right). Subunits are shown in cartoon representation and relevant residue contacts are highlighted with side-chains shown as stick. (E) Schematic representation of common longitudinal contacts formed in AtNBR1-PB1 and p62-PB1 helices.



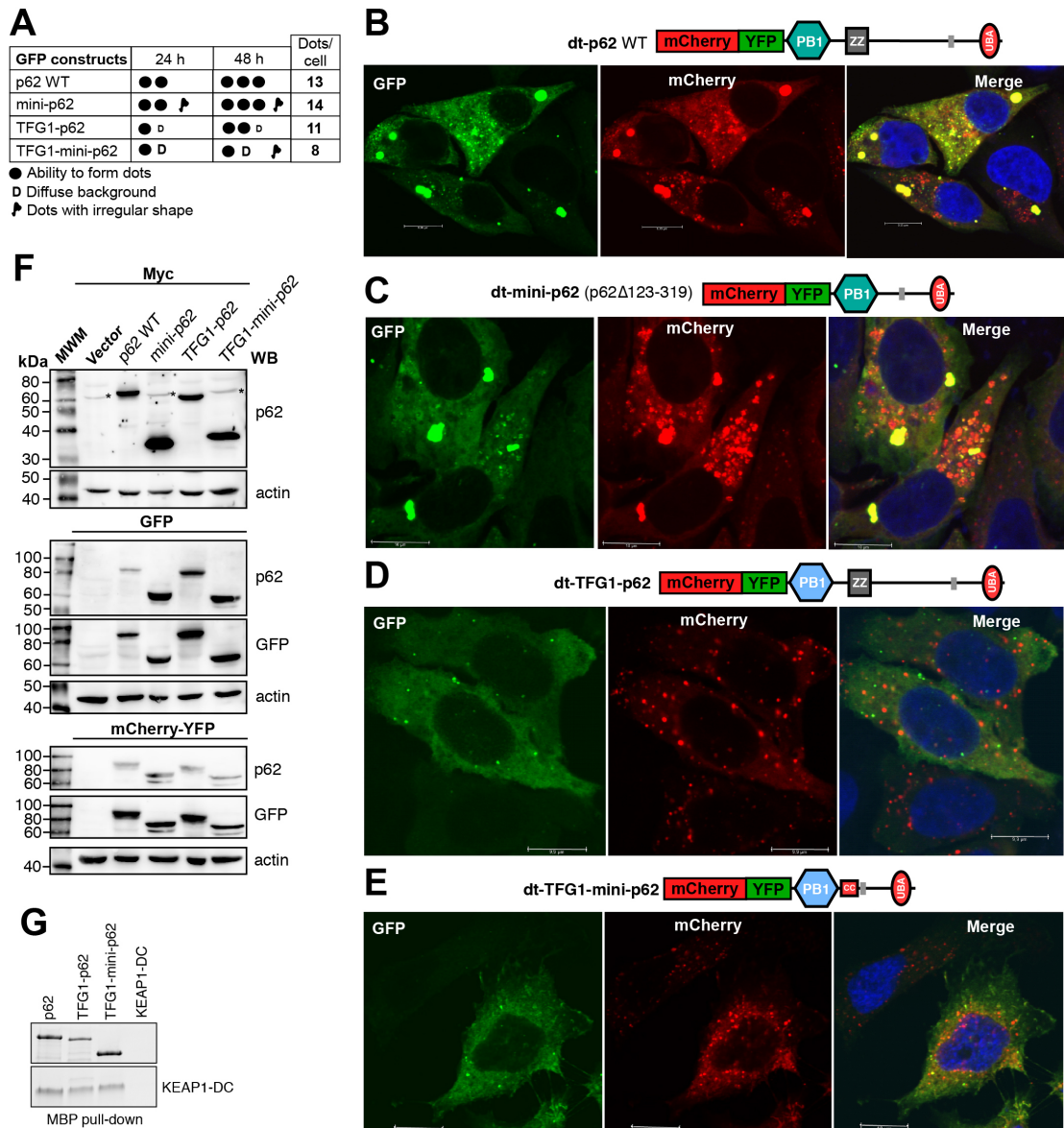
Supplementary Figure 3. Electrostatic interactions drive type PB1 filament formation.

(A-F) Negative-stain electron micrographs of AtNBR1-PB1 at increasing NaCl concentrations (A, 0 mM; B, 50 mM; C, 100 mM; D, 150 mM; E, 250 mM; F, 500 mM) illustrate how ionic strength weakens PB1 homo-oligomerization and affects filament length. (G/H) Thermofluor protein unfolding curves demonstrate that high ionic strength, as well as low and high pH destabilize a thermodynamically favorable (filamentous) state of AtNBR1-PB1.

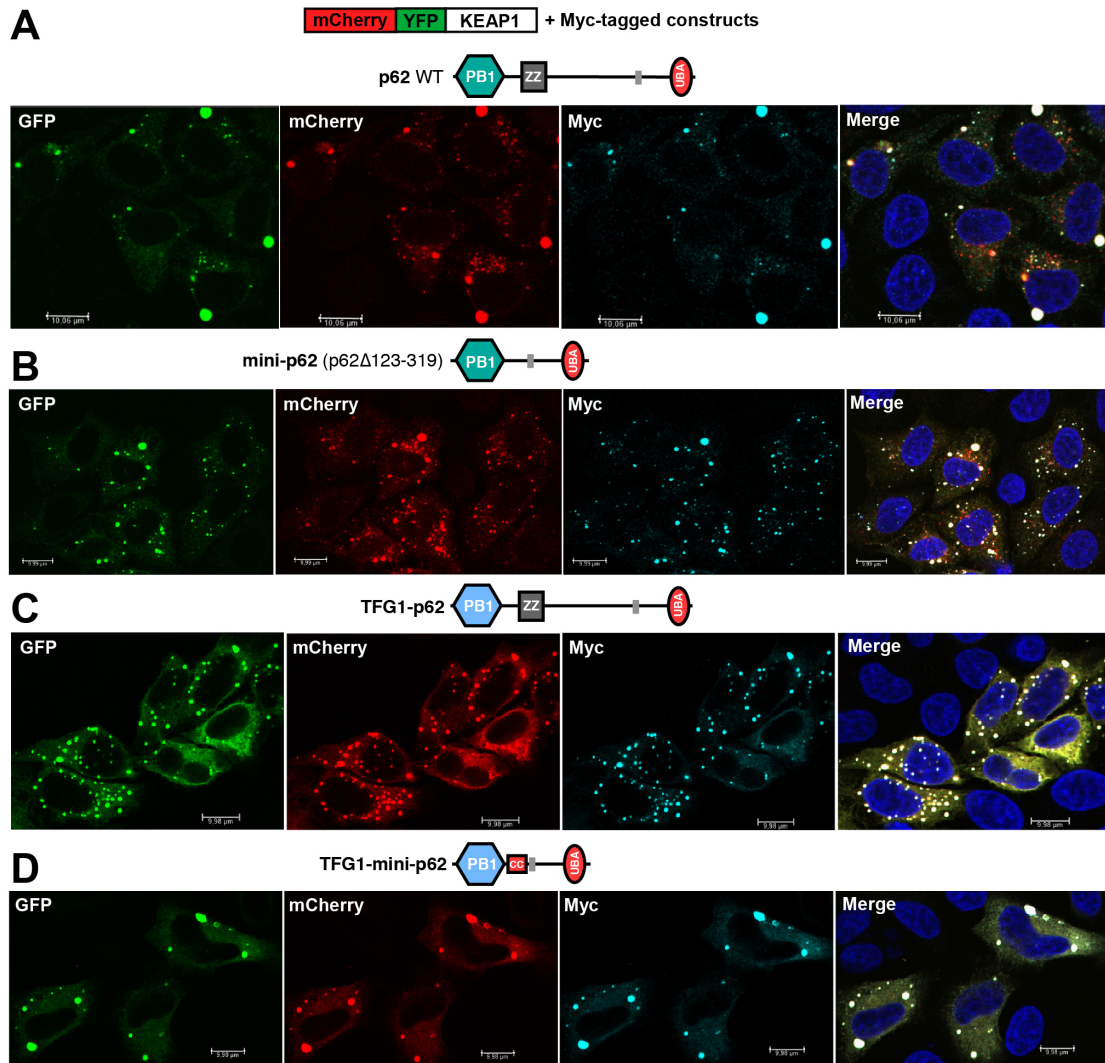


Supplementary Figure 4. Fluorescence images of RPE1 cells.

(A) Representative confocal fluorescence image of RPE1 cells expressing or not expressing NBR1(D50R): DNA (blue), NBR1 (D50R) (green) and endogenous p62 (red). Note the difference in average dot size of mCherry-p62 observed for both cases. (B) Overview fluorescence image showing the cells used for tomogram acquisition. Cells are outlined and the tomogram number is indicated. (C) Close-up view of cells in (B) indicating the subcellular position for tomogram acquisition.

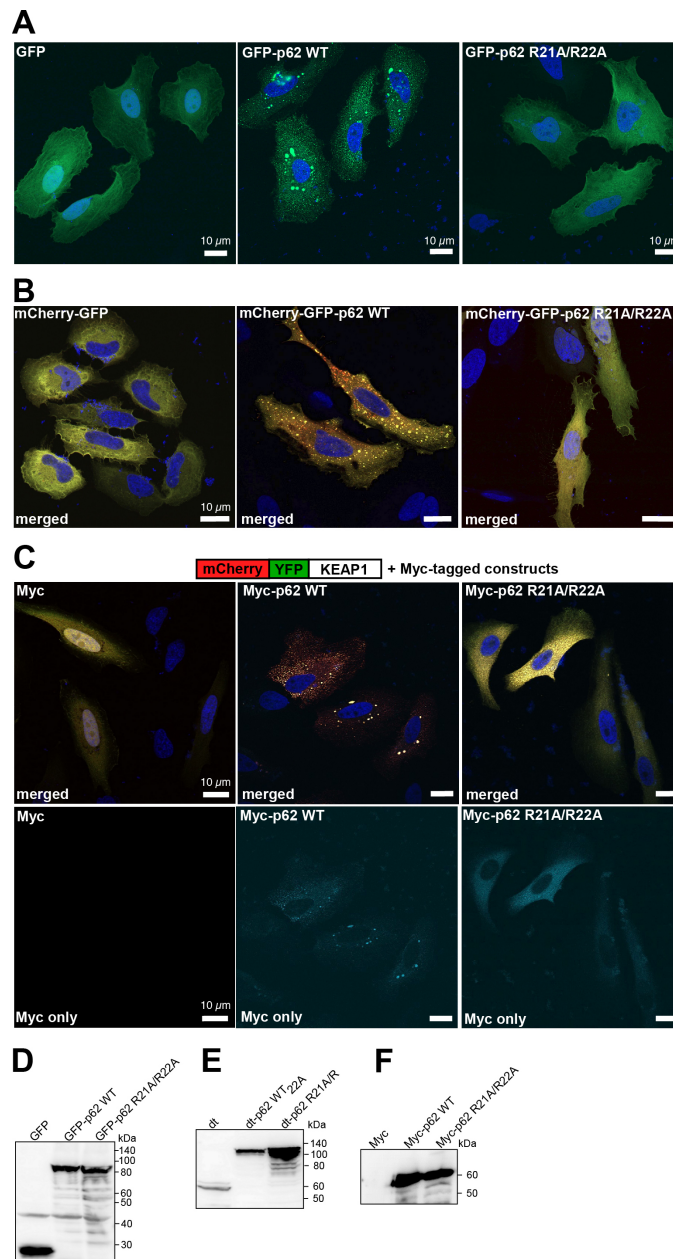


Supplementary Figure 5. Chimera variants of p62 with the PB1 domain exchanged with a related domain from TFG is efficiently degraded by autophagy. (A) Graphic presentation of phenotypes observed by confocal imaging of cells transfected with p62 constructs fused to GFP (number of dots, morphology of dots, and amount of diffuse protein). Cells were analyzed 24h and 48h after transfection. (B-E) Representative confocal images of HeLa p62 KO cells transiently transfected with the indicated p62 constructs fused to the mCherry-YFP double tag. Efficient degradation by autophagy is indicated by the accumulation of red-only dots. Scale bars, 10 μ m. (F) Representative western blots using extracts from HeLa cells transiently transfected with the indicated p62 constructs fused to Myc (top), GFP (middle) or mCherry-YFP (bottom). p62, GFP or actin antibodies were used as indicated. Source data are provided as a Source Data file. (G) SDS-PAGE of pull-down fractions for KEAP1-DC using MBP-tagged TFG1-P62 chimera constructs. Source data are provided as a Source Data file.



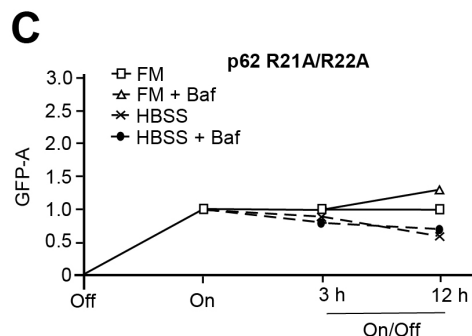
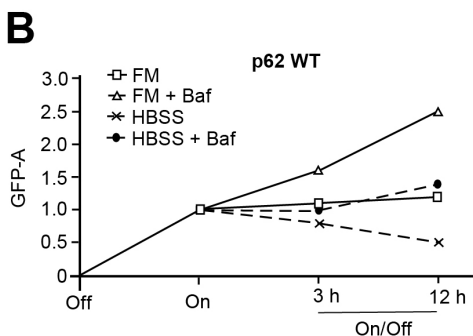
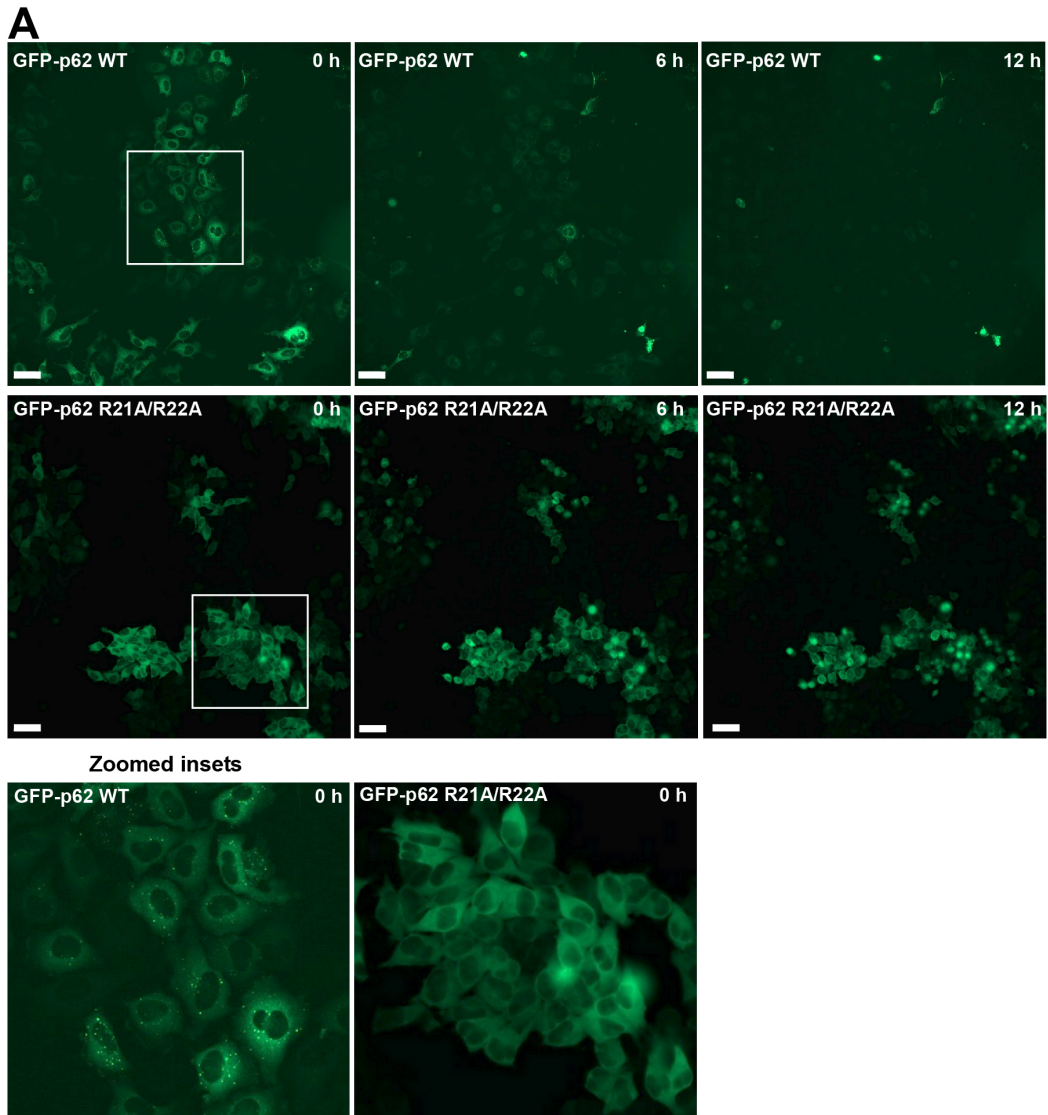
Supplementary Figure 6. p62-mediated degradation of co-expressed KEAP1 depends on the native PB1 domain of p62.

(A-D) Representative confocal images of HeLa p62 KO cells transiently co-transfected with mCherry-YFP tagged KEAP1 and the indicated p62 constructs fused to Myc. Degradation of KEAP1 by autophagy (accumulation of red-only dots) is seen in cells co-transfected with full-length p62 or a mini-p62 deleted for residues 123-319, but not in cells co-transfected with chimera constructs containing the PB1 domain of TFG1. Scale bars, 10 μ m.



Supplementary Figure 7. The double arginine finger in the PB1 domain is essential for aggregation and autophagy degradation of p62 and its substrate KEAP1.

(A-C) Representative confocal fluorescence images of HeLa p62 (KO) cells expressing GFP only (left), GFP-tagged p62 WT (center) or p62 R21A/R22A (right) (A), and of HeLa p62 (KO) cells expressing mCherry-GFP tagged p62 WT, p62 R21A/R22A or mCherry-GFP alone (B). As seen in (A) the R21A/R22A mutant is unable to form punctate structures and the lack of red dots (B) indicates that this construct is not turned over by autophagy. (C) Representative confocal fluorescence images of HeLa p62 (KO) cells expressing the corresponding myc-tagged p62 WT and p62 R21A/R22A as well as mCherry-YFP-KEAP1. The R21A/R22A mutant does not form aggregates with KEAP1 and is unable to induce lysosomal-localization of mCherry-YFP-KEAP1. Scale bars, 10 μ m. (D-F) Western blots of extracts from HeLa cells expressing GFP-tagged (D), mCherry-GFP-tagged (dt) (E) or Myc-tagged (F) p62 WT or p62 R21A/R22A constructs. GFP (D and E) and MYC antibodies (F) were used. Source data are provided as a Source Data file.



Supplementary Figure 8. The double arginine finger in the PB1 domain is required for autophagy degradation of p62.

(A) Representative still images from movies of HeLa FlpIn T-Rex p62 KO cell lines stably expressing either GFP, GFP-p62 WT or GFP-p62 R21A/R22A at 0 h, 6h and 12h incubation in starvation medium (HBSS). Expression was turned on with tetracycline for 24h before the experiment. Scale bars, 50 μ m. Flow cytometry data showing the GFP fluorescence intensity of (B) GFP-p62 WT and (C) GFP-p62 R21A/R22A after 3h or 12h incubation in full medium (FM), FM + Bafilomycin A1 (Baf), HBSS or HBSS + Baf. Cells were untreated (Off) or treated with tetracycline for 24h (On) before the experiment in order to induce the expression of the GFP proteins.

PAPER-II

Replacement of the p62 LIR with the FYCO1- or ULK1 LIR blocks starvation-induced autophagic degradation of p62

Anthimi Palara, , Hallvard Lauritz Olsvik, Mireia Nàger, Aud Karin Øvervatn, Gry Evjen, Kenneth Bowitz Larsen, Trond Lamark and Terje Johansen

Autophagy Research Group, Department of Medical Biology, University of Tromsø – The Arctic University of Norway, 9037 Tromsø, Norway.

Correspondence to: Trond Lamark, Email: trond.lamark@uit.no or Terje Johansen, Email: terje.johansen@uit.no

Keywords: autophagy, GABARAP, LC3B, LIR, p62

ABSTRACT

Selective autophagy depends on the binding of selective autophagy receptors (SARs) to ATG8 family proteins. The binding depends on a LC3 interaction region (LIR) motif in the SAR. There are six different ATG8 family proteins in mammals, and the majority of characterized SARs interact with only a subset among them. However, the important mammalian SAR SQSTM1/p62 interacts strongly with all these ATG8 proteins. This raises the question whether they can all be utilized by p62 in selective autophagy. To address this, we replaced the broad specificity LIR motif of p62 with two alternative LIR motifs having a more narrow specificity, and these chimera constructs were tested in selective autophagy assays. We only partially succeeded in making chimera constructs with the expected binding specificity. Our study therefore failed to answer whether a specific subset of ATG8 proteins are responsible for the degradation of p62 and selected cargos by autophagy. The chimera constructs were degraded in full medium, but degradation upon starvation was strongly affected. In the p62 molecule, the LIR motif is adjacent to other important protein binding motifs. We therefore propose that these motifs together form an extended structure that is evolutionary conserved and sensitive to the substitutions we did when making the chimera constructs.

INTRODUCTION

Mammalian ATG8 proteins endorse autophagosome formation and subsequent fusion with lysosomes. In selective autophagy, ATG8 proteins are additionally required for the docking of selected cargos like nonfunctional proteins and damaged organelles to the inner membrane surface of a phagophore (Nguyen et al., 2016; Weidberg et al., 2010). Selective autophagy is mediated by selective autophagy receptors (SARs) like p62 that identify and bind to the cargo and simultaneously bind to ATG8 proteins that are lipidated to the inner membrane surface of the phagophore (Birgisdottir Å et al., 2013; Johansen and Lamark, 2020; Wirth et al., 2019) . The binding of a SAR to the ATG8 depends on a LC3 interaction region (LIR) motif in the SAR, and this interaction is absolutely required for the degradation of the cargo and the associated SAR by autophagy (Birgisdottir Å et al., 2013; Johansen and Lamark, 2020). There are six different ATG8 family proteins in mammalian cells, and these are separated into two main groups: the MAP1LC3/LC3 (microtubule-associated protein 1 light chain 3) subfamily, which includes LC3A, LC3B and LC3C and the GABARAP (gamma-aminobutyric acid

receptor associated protein6) subfamily, which includes GABARAP, GABARAPL1 and GABARAPL2 (Johansen and Lamark, 2020; Popelka and Klionsky, 2018).

The LIR is evolutionary conserved and identified in many proteins. The consensus for the core motif is $\Phi XX\Psi$, where Φ corresponds to tryptophan(W), tyrosine(F) or phenylalanine(Y), Ψ represents leucine(L), isoleucine(I) or valine(V) and finally X is for any other amino acid. The Φ and Ψ residues in the core motif interacts with two hydrophobic pockets in the C-terminal ubiquitin-like domain of the ATG8 protein. In addition, a LIR motif contains one or several acidic residues that are located inside or adjacent to the core motif, and these residues form electrostatic interactions with basic residues in the ATG8 protein (Birgisdottir Á et al., 2013; Johansen and Lamark, 2020). ATG8 family proteins have a short N-terminal two helical extension followed by a C-terminal ubiquitin-like domain, and essential basic residues may be localized in both these compartments (Shpilka et al., 2011). There is a considerable variation among different LIR containing proteins in binding affinity and binding preference. For example, the LIR of the core autophagy protein ULK1 has a strong preference for the GABARAP subfamily. In contrast to this, the LIR of the Rab7 effector FYCO1 (FYVE and coiled-coil domain-containing1), involved in the transport of autophagosomes and lysosomes, has a strong preference for LC3A and -B (Olsvik et al., 2015; Pankiv et al., 2010; Shpilka et al., 2011). The basic residues that are engaged in electrostatic interactions are only partially conserved in the ATG8 proteins, and the binding preference of a LIR motif is mainly decided by whether electrostatic interactions are formed or not.

The first mammalian SARs to be identified were the sequestosome-like receptors p62/SQSTM1 (p62) and NBR1 (Bjørkøy et al., 2005; Kirkin et al., 2009). These proteins were found to interact equally well with all human ATG8 proteins (Kirkin et al., 2009; Pankiv et al., 2007) (, suggesting that all ATG8 proteins can be utilized by these proteins. The strong co-localization of p62 bodies and p62 or NBR1 containing autophagy structures with LC3B indicate that LC3B is probably the main ATG8 used by these SARs in selective autophagy pathways. However, p62 is degraded by autophagy in cells lacking LC3B (Nguyen et al., 2016), and the efficient binding of p62 to other ATG8 proteins suggest that ATG8 proteins of the GABARAP subfamily can also be used by p62. To test this, we created chimeric variants of p62, with the LIR region of p62 replaced by LIR motifs with a narrower binding specificity, i. e. the LIR motifs of ULK1 and FYCO1. The chimeric variants were then expressed in cells and their degradation by autophagy analyzed.

MATERIALS AND METHODS

Plasmids

All plasmid construct used in this study are listed in Table 1. The constructs were made by using conventional cloning techniques and the Gateway recombination system. Mutagenesis was performed using oligonucleotides from ThermoFisher and following PCR mutagenesis protocol by the same company. All constructs were verified by sequencing (BigDye, applied Biosystems).

The two p62 chimera constructs pENTR-p62-LIR(ULK1) and pENTR-p62-LIR(FYCO1) were created by replacing the native LIR motif in p62 with a LIR motif from ULK1 (Alemu et al., 2012) or FYCO1 (Pankiv et al., 2010 FYCO1 paper), respectively. First, a KpnI site (GGATCC) was generated by site-directed mutagenesis, changing the sequence upstream of the LIR motif in pENTR-p62 (codons 334 and 335 from GGAGAT to GGTACC). Second, the mutated pENTR-p62 construct was cut with KpnI and AccI (native site downstream of the LIR motif), followed by 0.7% agarose gel electrophoresis and isolation of the linearized plasmid from the gel. Third, oligonucleotides encompassing the LIR motifs of ULK1 and FYCO1 proteins were ordered by ThermoFisher, hybridized and subcloned into the linearized plasmid.

Table1: Plasmids used in this study

pENTR-p62	(Lamark et al., 2003)	
pENTR-p62-LIR(ULK1)	This study	Traditional cloning
pENTR-p62-LIR(FYCO1)	This study	Traditional cloning
pDest-myc	(Lamark et al., 2003)	
pDest-myc-p62	(Lamark et al., 2003)	
pDest-myc-KEAP1	(Jain et al., 2010)	
pDest-myc-p62-LIR(ULK1)	This study	Gateway cloning
pDest-myc-p62-LIR(FYCO1)	This study	Gateway cloning
pGEX-2T (GST-fusion vector)	Amersham Pharmacia-Biotec	
pGEX-2T-p62	(Lamark et al., 2003)	
pDest15	Invitrogen	
pDest15- p62-LIR(ULK1)	This study	Gateway cloning

pDest15- p62-LIR(FYCO1)	This study	Gateway cloning
pDest15-LC3A	(Pankiv et al., 2007)	
pDest15-LC3B	(Pankiv et al., 2007)	
pDest15-LC3C	(Pankiv et al., 2007)	
pDest15-GABARAP	(Pankiv et al., 2007)	
pDest15-GABARAPL1	(Pankiv et al., 2007)	
pDest15-GABARAPL2	(Pankiv et al., 2007)	
pDest-mCherry-EYFP-KEAP1	(Jakobi et al., 2020)	
pDest-LTR-EGFP	(Skytte Rasmussen et al., 2017)	
pDest-LTR-EGFP-p62	This study	Gateway cloning
pDest-LTR-EGFP-LIR(ULK1)	This study	Gateway cloning
pDest-LTR-EGFP-p62-LIR(FYCO1)	This study	Gateway cloning

Generation of stable cell lines

For the creation of stable cell lines p62 KO murine embryo fibroblasts (MEFs) were used (Komatsu et al., 2007). The p62, p62-LIR(ULK1) and p62-LIR(FYCO1) constructs were cloned by gateway into pDest-LTR-EGFP, which is a retroviral mammalian vector. Viral supernatant from HEK293 plate E cells was harvested, filtered through a 0.45 μ M filter, and added to p62 KO MEFs 24, 48 and 72 hours post transfection. MEFs were reseeded in a medium containing 100 μ g/ml blastisidine S HCl (Thermo Fisher Scientific, R210-01). Doxycycline was used to control the induction of the protein expression. The induction of the tagged proteins was achieved by treating the cells with the indicated amount of doxycycline for 24 hours before the experiments were performed.

Mammalian cell culture

Cells were cultured in DMEM (Sigma-Aldrich, D6046) supplemented with 10% fetal bovine serum (Biochrom S0615) and 1% streptomycin-penicillin (Sigma-Aldrich P4333), and 100ng/ml blastisidine S HCl (Gilbo #A11139-03) was added after 2 splits to preserve the

expression of the tagged protein in the cells. The incubation conditions were : temperature at 37°C and 5% CO₂.

Antibodies

For immunostaining and immunoblotting experiments, the following primary and secondary antibodies were used:

Primary antibodies: Rabbit anti-p62 (MBL PM045), rabbit anti-actin (Sigma-Aldrich A2066), rabbit anti-LC3B (MBL PM036).- Secondary antibodies: HRP-conjugated polyclonal goat anti-rabbit (BD Bioscience Cat#554021).

Reagents\Chemicals

List of the reagents used in this study:

BafilomycinA1, Santa Cruz Biotech SC-201550, Reticulocyte Lysate System, Promega #14610, Ponceau S, Sigma #P3504, Dulbecco's modified Eagle's medium, Sigma-Aldrich #D6046, HBSS, Sigma-Aldrich #H9269, Pen\Step, Sigma-Aldrich #P4333, Metafectene Pro, BionTex #T040, Fetal bovine serum, Biochrom #S0615, SuperSignal West Femto Chemiluminescent Thermo Scientific 34096, Blastidicin S HCl, Gilbo #A11139-03, Coomassie Brilliant Blue R-250 Dye, Thermo Scientific 20278, DAPI, Thermo Scientific 62248, Isopropyl β - d-1-thiogalactopyranoside (IPTG), Sigma-Aldrich I6758, ³⁵S -methionine, PerkinElmer NEG709A500UC

GST- pulldown assays

GST pulldown assays were performed with *in vitro* translated proteins or cell extracts. GST fusion proteins were expressed in *Escherichia coli* SoluBL21(DE3) (Genlantis #C700200) in LB medium. Bacteria were grown to an OD₆₀₀ of 0,5-0,9, and GST or GST fusion protein expression induced by the addition of 0.5 mM IPTG. Cells were grown at 37°C for at least 4 hours and the cultures centrifuged for 10 minutes at 3500rpm. Pellets were sonicated in lysis buffer (20mM Tris-HCl pH 7.5, 10mM EDTA, 5mM EGTA, 150mM NaCl). GST-fusion proteins were isolated and purified on glutathione-Sepharose 4 Fast Flow beads (GE

Healthcare,17513201), by incubating in a rotator at 4°C for 1 hour, followed by 3 times washing with NETN buffer (50mM Tris pH 8.0, 150mM NaCl, 1 mM EDTA, 0,5% NP-40). Fusion protein-bound beads were used immediately in GST pulldown assays or stored in NETN at 4°C.

In vitro translation of Myc-tagged proteins expressed from a T7 polymerase promoter was performed using the TNT coupled Reticulocyte Lysate System (Promega L4610). *In vitro* transcription and translation were performed in the presence of T7 polymerase and radioactive ³⁵S-methionine and T7 polymerase. To reduce unspecific binding, the *in vitro* translated proteins were first mixed and rotated for 30 min at 4°C with empty beads held in NETN buffer added Mini EDTA-free protease inhibitors. Then, the precleared lysates were mixed with beads loaded with selected GST fusion proteins and rotated for 1-2 hours at 4°C. The beads were washed 5 times with cold NETN buffer without inhibitors. The beads were then resuspended in loading buffer (100mM Tris pH7.4, 4% SDS, 20% Glycerol, 0.2% bromophenol blue and 200mM DTT (Sigma #D0632) and boiled for 10 minutes to break the protein interactions and eluate the proteins from the beads. The beads were pelleted, and the supernatants analyzed by SDS-PAGE. GST fusion proteins were detected by staining of gels with Coomassie Brilliant Blue R-250 (Thermo Fisher Scientific #20278). Gels were vacuum dried for 1h, and the ³⁵S-labeled proteins detected and analyzed using the Fujifilm bioimaging analyzer BAS-5000 (Fujifilm).

For GST pulldown assays performed with cell extracts, cells were seeded in 10cm dishes, one day in advance, and doxycycline was added too, to promote the expression of the tagged protein. Next day cells were lysed and harvested in RIPA buffer. Cell extracts were centrifuged, and 3% of the amount was kept as input. The rest of the supernatant was added to the beads for 1-2 hours incubation at 4°C with rotation. Afterwards, beads were collected by centrifugation. Beads were washed five times with RIPA buffer. Samples were run on 8 or 10% SDS-PAGE and blotted on a 0.2 µm PVDF membrane (Amersham, GE10600021), followed by Ponceau S staining. Blocking was made by 5% nonfat dry milk in PBS-Tween 20 (0.1%). Membranes were incubated for one day at 4°C with rotation. Secondary antibody incubation was performed in room temperature for 1,5 hours in PBS-Tween 20 containing a secondary antibody. Blots were developed using LAS-4000 (Fujifilm).

Western blotting

Cells were lysed in 5x Laemmli buffer (50mM Tris pH 7.4, 5% SDS, 10% Glycerol, 200mM DTT (Sigma #D0632), heated for 5 minutes and then sonicated for 10sec. Protein levels were measure with the BCA assay. Bromophenol blue (0.1%) and DTT (100mM) were added to the lysates after the protein measurements, and the samples were run on 8 or 10% SDS polyacrylamide gels and blotted on a 0.2 μ m PVDF membrane (Amersham, GE10600021). Ponceau S staining was performed as a preliminary control for the loading. For blocking of membranes, 5% nonfat milk in PBS-Tween 20(0.1%) was used. Membranes were incubated for one day in 4°C with rotation. Secondary antibody incubation was performed in room temperature for 1,5 hours in PBS-Tween 20 containing secondary antibody. Blots were developed using LAS-4000 (Fujifilm).

Transient Transfection

Cells were seeded and induced with doxycycline 24 hours before the transfection. Cells were transiently transfected overnight with 50ng of DNA. Transfection medium was changed early the next morning with normal full media containing doxycycline. Cells were fixed with 4% formaldehyde 48 hours after transfection.

Immunofluorescence

Cells were placed on glass coverslips (VWR #6310150) and induced with doxycycline 24 hours in advance. Cells were fixed in 4% formaldehyde (PFA) for 15 minutes at room temperature and then permeabilized with 0.1% Triton X-100 in PBS at room temperature for 5 minutes. 3% goat serum diluted in PBS was used for blocking. Blocking period was 1 hour in room temperature. Samples were stained with primary antibody which was diluted in 1% goat serum in PBS. Incubation with the primary antibody was for 1-2 hours at room temperature. Incubation with AlexaFluor labelled secondary antibodies was for 1 hour at room temperature. Three washes with PBS were done before each staining step with antibodies. During the last 10 minutes, before the end of the staining with the secondary antibody, 1 μ g/ml DAPI was added to the samples. Finally, samples were washed 4 times in PBS and one time with pure water before they were mounted in 10 μ l of Mowiol and placed on a glass microscope slide.

Light microscopy

Fixed cells were imaged on an Zeiss Axio Observer Z.1 microscope, outfitted with a LSM800 scanner for confocal microscopy (Carl Zeiss microscopy). Images were taken in ZEN software using 63x NA1.4 oil immersion lens for coverslips. Optimal settings were determined by using the Best signal Setup functions in ZEN Blue software.

Quantification of data and statistical analysis

Confocal imaging data were quantified using Volocity software. Data in all figures are presented as mean +/- SD from minimum 3 biological independent experiments, unless otherwise stated. Dot plots were made in PRISM (Graphpad) and the statistical significance was also evaluated by the same software (ns $P > 0.05$, * $P \leq 0.05$, ** ≤ 0.01 , *** $0.01 \leq P \leq 0.001$, **** $P \leq 0.001$) by using one -way ANOVA nonparametric test or group comparison for unpaired t-test with Welch's correction for groups comparison when SDs are not equals.

RESULTS

p62 LIR chimera constructs with altered binding preference for ATG8 family proteins

The LIR interaction of p62 with ATG8 family proteins is essential for the degradation of p62 by autophagy and for its function as an autophagy receptor (Pankiv et al., 2007). The LIR motif in p62 has a broad specificity (Pankiv et al., 2007), but LC3B is believed to be the main partner of p62 in selective autophagy (Bjørkøy et al., 2005; Maruyama et al., 2014; Shvets et al., 2011) Shvets et al., 2011; Maruyama et al., 2014). However, p62 is degraded also in cells lacking LC3B (Nguyen et al., 2016), suggesting that other ATG8 family members may also be utilized by p62. To test if the binding preference of the LIR motif is important for the degradation of p62 by selective autophagy, we made two chimera p62 mutant constructs with the LIR motif in p62 replaced with LIR motifs having a more restricted binding specificity, i. e. the motifs of ULK1 and FYCO1 (**Figure 1A**). The motif in ULK1 has a preference for the GABARAP subfamily (Alemu et al., 2012), while the motif in FYCO1 has a preference for the LC3 subfamily (Cheng et al., 2016; Olsvik et al., 2015).

The LIR motif in p62 is part of an evolutionary conserved region of >22 residues that also includes the KEAP1 interacting region (KIR) motif (Jain et al., 2010). The sequence of the

conserved region is shown in figure 1A, with the core LIR (WTHL) and KIR (STGE) motifs underlined. This part of p62 can also bind to FIP200, and a replacement of the LIR motif may therefore affect the interaction of p62 with KEAP1 and/or FIP200. As an attempt to avoid or minimize such side effects, the region deleted from p62 and replaced by another LIR motif was limited to the core motif and a few residues adjacent to the core motif (**Figure 1A**). The risk is that the inserted LIR fragment may then lack more distant residues determining its binding preference (Olsvik et al., 2015), and there is also a risk that p62 residues that contribute to the ATG8 binding are not deleted. To verify that the LIR chimera p62 constructs had an ATG8 binding preference reflecting the characteristics of the inserted LIR motif, the binding of p62-LIR(ULK1) and p62-LIR(FYCO1) were tested by *in vitro* GST pulldown assays. Myc-tagged p62 constructs were *in vitro* transcribed and translated in the presence of [³⁵S]methionine and subjected to GST pulldown experiments with recombinant ATG8 family proteins fused to GST and immobilized on Sepharose beads (**Figure 1B-D**).

A previous study of the isolated LIR motif in ULK1 (residues 358-370) revealed a strong preference for the GABARAP subfamily, and within the GABARAP subfamily the binding preference was GABARAP > GABARAP > GABARAPL2 (Alemu et al., 2012). The same binding pattern for the GABARAP subfamily was seen for the chimera p62-LIR(ULK1) construct (**Figure 1C and -E**). Another feature recapitulated in the p62-LIR(ULK1) construct was a lack of binding to LC3A or -B. The p62-LIR(ULK1) chimera also interacted strongly with LC3C (**Figure 1C and -E**), and this differs from the isolated LIR in ULK1 that did not interact with LC3C (Alemu et al., 2012) .

The insertion of the LIR motif from FYCO1 into p62 did not recapitulate the expected binding characteristics previously seen for the isolated FYCO1 LIR (residues 1276-1294) that only interacted with LC3A and -B. p62-LIR(FYCO1) interacted with LC3A and -B, but it also interacted with LC3C, GABARAP and GABARAPL1 (**Figure 1D and E**). The FYCO1 LIR chimera construct displayed a rather broad specificity and our attempts to make a p62 construct with a preference for the LC3 subfamily therefore failed. The reason is unclear, but our assumption is that the FYCO1 fragment replacing the LIR motif in p62 is too small to recapitulate the binding preference of the FYCO1 LIR.

Impaired KEAP1 binding of p62 LIR chimera constructs

WT p62 and the p62 LIR chimera constructs were stably expressed as GFP fusions in p62 KO MEFs under control of a DOX inducible promoter. Expression in cells was verified by western blotting of cell extracts from cells treated or not with bafilomycin A1 (BafA1), an inhibitor of autophagosome degradation (**Figure 2A**). Confocal imaging of cells expressing GFP-tagged p62 LIR chimera constructs verified that both formed p62 bodies (**Figure 2B**). The number of p62 bodies was higher in cells expressing GFP-p62-LIR(ULK1) and GFP-p62-LIR(FYCO1) than in cells expressing WT GFP-p62 (**Figure 2C**), but the average size of the structures was similar for all constructs (**Figure 2D**). The western blot experiments indicated a higher expression level of the chimeric p62 constructs (**Figure 2A**), and visual imaging of cells expressing GFP-p62-LIR(ULK1) or GFP-p62-LIR(FYCO1) similarly suggested a higher expression level of the mutant constructs (**Figure 2B**). The elevated protein level and increased number of p62 bodies seen in cells expressing chimeric p62 constructs may indicate a less efficient turnover of these constructs by autophagy.

An important regulator of p62 bodies under stress conditions is KEAP1 that is recruited via the KIR motif (Jain et al., 2010; Komatsu et al., 2010). Since this motif is potentially affected in the chimeric constructs, we performed GST pulldown assays to test if the mutated p62 constructs are able to interact with KEAP1. In these assays, myc-tagged KEAP1 was *in vitro* translated and incubated with GST or GST tagged p62 constructs. Our data revealed that the chimeric p62 constructs were affected in their binding to KEAP1. p62-LIR(ULK1) did not interact, and for p62-LIR(FYCO1) the binding was less efficient than for WT p62 (**Figure 2E and -F**). This shows that residues N-terminal to the KIR motif can have a strong impact on the binding of p62 to KEAP1, and our attempts to replace the LIR motif in p62 without affecting the KIR motif evidently failed. The p62-LIR(FYCO1) construct did however interact with KEAP1 *in vitro*.

The binding of p62-LIR (FYCO1) to p62 was confirmed in cell transfection experiments where we co-overexpressed Myc-tagged p62 with KEAP1 fused to the mCherry-EYFP double tag. This double tag can be used as an autophagy marker since EYFP (like EGFP) is unstable in an acidic environment and the green fluorescence therefore lost when the tagged protein is taken up by a lysosome (Pankiv et al., 2007). In confocal imaging analyses, mCherry-EYFP tagged KEAP1 therefore appears as yellow in the cytoplasm and red only after uptake into a lysosome. KEAP1 is a well-known autophagy substrate, but degradation of overexpressed KEAP1 by autophagy strongly depends on p62 and more specifically by the KIR dependent binding of p62

to KEAP1(Jain et al., 2010). We therefore transfected mCherry-EYFP tagged KEAP1 in p62 knockout (KO) HeLa cells. When expressed alone it displayed a diffuse localization pattern lacking red-only puncta (**Figure 2G**). In line with previous studies (Jain et al., 2010), co-expression of p62 resulted in accumulation of KEAP1 in p62 bodies (yellow dots) and degradation of KEAP1 by autophagy (red only dots) (**Figure 2G**). Co-expression of p62-LIR(FYCO1) had a similar effect on KEAP1 as WT p62 resulting in accumulation of KEAP1 in p62 bodies (yellow dots) and degradation of KEAP1 by autophagy (red only dots). Co-expression of p62-LIR(ULK1) had no effect on the localization pattern of KEAP1, supporting the conclusion that p62-LIR(ULK1) does not interact with KEAP1 (**Figure 2G**).

Impaired starvation-induced degradation of p62 LIR chimera

To identify effects caused by the LIR substitutions on the autophagic turnover of p62, cells stably expressing different GFP-p62 constructs were observed by confocal fluorescence microscopy. Cells were treated or not with BafA1 both in full media (FM) and in starvation media (HBSS). All three constructs displayed an increase in GFP-p62 puncta in response to the treatment with BafA1, indicating lysosomal degradation (**Figure 3A**). The treatment of cells with BafA1 resulted in a very high number of p62 puncta, and we were therefore unable to count the number of p62 bodies, either manually or using the Volocity software. Instead, confocal images were analyzed by Volocity software by measuring the average GFP puncta intensity from more than 100 cells. Three independent experiments were performed with each cell line, and in each experiment, the average GFP puncta intensity in full medium without BafA1 was used for normalization. The use of Volocity software confirmed the visual observation that in FM, the treatment with BafA1 gave a strong increase in GFP-positive puncta (**Figure 3B**). This correlates with an efficient lysosomal degradation of all three GFP-p62 constructs in FM. It is however notable that GFP-p62-LIR(FYCO1) displayed less accumulation upon BafA1 treatment than GFP-p62 or GFP-p62-LIR(ULK1) (**Figure 3B**), indicating a less efficient autophagic turnover of this construct in FM.

Cells were here inspected manually (**Figure 3A**) or by the use of Volocity software (**Figure 3B**). In both cases, we observed a dramatic loss of GFP-p62 puncta indicating an efficient degradation of WT GFP-p62 upon starvation. This is in line with previous studies (Mejlvang). However, a similar starvation-induced degradation was not seen for the chimeric constructs (**Figure 3A and -B**). Instead, their levels increased, and the increase in GFP-p62 puncta was

in particular strong for the GFP-p62-LIR(ULK1) construct. This appears to indicate that the starvation induced degradation is less efficient for chimeric GFP-p62 constructs. Nevertheless, HBSS+BafA1 treated cells contained even more GFP-p62-LIR(ULK1) puncta than HBSS treated cells (**Figure 3A and –B**), indicating that GFP-p62-LIR(ULK1) is degraded in HBSS treated cells. For GFP-p62-LIR(FYCO1), there was no difference in GFP-p62 puncta between HBSS and HBSS+BafA1 treated cells (**Figure 3A and –B**), suggesting a more severe inhibition of starvation-induced degradation. Cell extracts from cells treated in the same way were also analyzed by western blot experiments. The western blot data supported the conclusions made from confocal imaging of cells (**Figure 3C**). In particular, we observed increased levels of the chimeric GFP-p62 constructs after 4h of starvation, in sharp contrast to WT GFP-p62 that was strongly reduced (**Figure 3C**).

Co-localization of chimeric p62 constructs with endogenous LC3B

The recruitment of endogenous LC3B to GFP-p62 bodies formed in stably transfected MEF cells were analyzed by immunostaining and confocal microscopy. Visual inspection of p62 bodies by confocal imaging showed that a large fraction of the p62 bodies co-localized with LC3B. However, the pattern of the co-localization differed depending on the construct expressed (**Figure 4A**). When inspecting LC3B positive GFP-p62 bodies, the LC3B staining completely covered the inspected GFP-p62 bodies (**Figure 4A**). A similar type staining pattern was seen for bodies formed by GFP-p62-LIR(FYCO1), suggesting a direct binding of GFP-p62-LIR(FYCO1) to LC3B in these structures. For the GFP-p62-LIR(ULK1) construct that does not interact with LC3B, there was very little overlap between the GFP positive bodies and LC3B. Instead, LC3B appeared to accumulate in structures that were adjacent to the GFP positive bodies (**Figure 4A**). The frequency of these structures suggests that they may have a role connected to the degradation of p62 bodies formed by the GFP-p62-LIR(ULK1) construct. The extent of co-localization between p62 bodies and LC3B puncta was measured by Volocity software (**Figure 4B**). For the GFP-p62-LIR(ULK1) construct, there was no full co-localization. Hence, instead we counted the fraction of cells that contained an adjacent LC3B positive structure (**Figure 4C**). The fraction of GFP-p62-LIR(ULK1) bodies containing an adjacent LC3B structure was very similar to the fraction of GFP-p62 or GFP-p62-LIR(FYCO1) bodies that were positive for LC3B (**Figure 4B and –C**).

Due to lack of specific antibodies working in murine cells we could not check the co-localization of p62 with other Atg8 family proteins in the MEF cells. It is therefore unknown if LC3B was replaced by a GABARAP subfamily member in cells expressing GFP-p62-LIR(ULK1). To test if GFP-p62-LIR(ULK1) could form indirect interactions with LC3B when expressed in cells, we performed GST pulldown experiments using cell lysates from cells expressing different GFP-p62 constructs. Cell lysates were in these experiments incubated with GST, GST-LC3B or GST-GABARAP, and the co-precipitation of GFP-p62 from cell lysates analyzed by western blotting. It appeared that all constructs interacted strongly with both GST-LC3B and GST-GABARAP in this assay (**Figure 4D**). This suggests that GFP-p62-LIR(ULK1) may potentially form an indirect interaction with LC3B in cells. However, it is important to keep in mind that p62 is highly polymeric and a single interaction with GST-LC3B may in this assay result in the co-precipitation of a large number of p62 molecules. This said, GFP-p62-LIR(ULK1) is clearly most efficiently co-purified with GST-GABARAP relative to the two other constructs, and we have no evidence for that LC3B is required for the degradation of GFP-p62-LIR(ULK1) by autophagy.

DISCUSSION

The purpose of this study was to test if LC3 binding is essential for the degradation of p62 by autophagy. The LIR motif of p62 has a very broad ATG8 binding specificity, and previous studies have not properly investigated if p62 can use all the different ATG8 family members for the docking of a p62 containing complex to the phagophore. In an early study by the group of Elazar, the use of chimeras of LC3B and GABARAPL2 with their N-terminal arms swapped indicated that the N-terminal arm of LC3 is more efficient in recruiting p62 to the phagophore than the N-terminal arm of GABARAPL2 (Shvets et al., 2011).

Our aim here was to test further if a binding to LC3A or –B is essential for the degradation of p62 by autophagy. Our approach was to make p62 chimera constructs that either interacted only with LC3A and –B, or interacted with all ATG8 family members except for LC3A and –B. Unfortunately, we failed to make a p62 constructed that specifically interacted with the LC3 subfamily, but we succeeded in making a p62 construct that did not interact with LC3A or –B. In the latter construct, the LIR in p62 was exchanged by the GABARAP subfamily specific LIR motif from ULK1. This construct, named p62-LIR(ULK1), was degraded by autophagy in FM.

An important question we had was if p62 replaces LC3B with another ATG8 homologue if it cannot interact with LC3B. Since p62-LIR(ULK1) was efficiently degraded by selective autophagy in FM, the answer to this question is presumably yes. We noted that the degradation of p62-LIR(ULK1) in FM was less efficient than the degradation of wt p62, but this may be because a large quanta of ATG8 molecules are needed. When p62 is not allowed to interact with LC3B, there is probably less ATG8 molecules available, and this may reduce the efficiency of the process. To test if LC3B is recruited to p62 bodies, cells expressing the chimera p62 constructs were immunostained for endogenous LC3B. As expected, WT GFP-p62 strongly co-localized with endogenous LC3B, strongly supporting the conclusion that LC3B is a main partner for p62 in selective autophagy. Endogenous LC3B was not recruited into droplets (p62 bodies) formed by GFP-p62-LIR(ULK1). We found that LC3B was on adjacent structures strongly associated with p62-LIR(ULK1) bodies, but although some minor overlap was seen, LC3B was apparently excluded from the bodies. Our belief, strongly supported in the literature, is that p62 has to bind to an ATG8 family member for the degradation by selective autophagy. Unfortunately, we have no GABARAP subfamily specific antibodies that works with murine cells. Therefore, the use of MEF cells prevented us from testing if endogenous ATG8s of the GABARAP subfamily were recruited into p62 bodies formed by GFP-p62-LIR(ULK1). Further studies are therefore required to find out if the degradation of GFP-p62-LIR(ULK1) in FM depends on the binding of p62 to a GABARAP subfamily member.

Our approach here was to replace the LIR in p62 with a LIR of different binding preference, but we chose to replace only a short region in p62 encompassing the core LIR motif and a few adjacent residues. The reason for this is that we tried to keep the KIR motif intact in the chimeric constructs, but it is probably necessary to delete a larger region in order to replace the features of the whole LIR motif. While the core motif is necessary for binding, residues adjacent to the core motif determine the binding preference. In our case when we tried to replace the native LIR motif with motifs from ULK1 or FYCO1, essential residues are most likely either located outside of the deleted region in p62, or they are not included in the inserted LIR motifs from ULK1 or FYCO1. In retrospect, the best solution would have been to delete the whole LIR-KIR region in p62 and replace it with an extending LIR region from ULK1 or FYCO1 containing all necessary elements. This would have led to a loss of KEAP1 binding in all LIR chimera constructs, but our alternative approach were we tried to preserve the KIR motif failed to do so. It turned out that a replacement of the LIR motif easily affected KEAP1 binding even if the core KIR motif was not affected. By deleting the whole LIR-KIR region, we would know

that all features associated with this region were similarly lost in all chimera p62 constructs and this would have facilitated the interpretations of the data.

A very surprising finding we had was that the chimera p62 constructs were not degraded in response to starvation, and their levels even increased. This is very different from WT GFP-p62 that was efficiently degraded in response to starvation, and all the constructs were degraded in FM. This discrepancy may reflect that another degradation pathway is used in response to starvation that in FM, and we recently reported that degradation of p62 in response to starvation is partially mediated by endosomal microautophagy (Mejlvang et al., 2018). In the current study, the GFP-p62 constructs were stably expressed in MEF cells, and this is a cell line where we have previously demonstrated that endosomal microautophagy of p62 is important in response to starvation (Mejlvang et al., 2018). Our previous study reported that starvation induced degradation of GFP-p62 in MEF cells occurs by endosomal microautophagy and is LIR dependent (Mejlvang et al., 2018). Our new data do not distinguish between macroautophagy or endosomal microautophagy of p62. It is therefore unclear which degradation pathway is inhibited in cells expressing the chimera p62 constructs. The exact mechanism of endosomal microautophagy of p62 is also unclear. The LIR motif in p62 is required, as are ATG8 family proteins (Mejlvang et al., 2018). However, the exact role for the p62-ATG8 interaction in endosomal microautophagy is not known. It is neither known how p62 is recruited to the endosome. It is tempting to speculate that p62 is recruited by ATG8 proteins that are lipidated to the endosomal membrane, and the best candidate would be LC3B since previous studies have already reported the lipidation of LC3B to endosomal structures (). We may therefore speculate that starvation induced autophagy of p62 is affected because this degradation pathway is more dependent on the p62-LC3 interaction than the macroautophagy pathway. An alternative explanation would be that another feature associated with the LIR-KIR region is essential for starvation induced p62 degradation. The chimera GFP-p62-LIR(ULK1) construct displayed no interaction with KEAP1, and the LIR-KIR region has previously also been linked to FIP200 recruitment (Eleonora Turco, 2020; Hara et al., 2008). In this study the role of FIP200 and the overlap between LIR-KIR and FIR was not studied. The reason for this is that it is known that mutation on the L341 residue of p62 inhibit the interactions with FIP200 same as LIR (Faruk Mohammad Omar, 2021). In this study we exchanged the whole region. As a result, part of the FIR sequence was missing from the chimeric constructs.

Future studies should address the degradation pathway that is affected and use more specific mutations to find out if defects in the degradation of the chimera constructs can be explained by changes in their ATG8 binding preferences.

Acknowledgements

We are thankful to the Advanced Microscopy Core Facility at the Faculty of Health Sciences, UiT-The Arctic University of Norway for assistance and use of instruments. This work was funded by grant number 249884 from the Norwegian Research Council to TJ.

References

- Alemu, E.A., T. Lamark, K.M. Torgersen, A.B. Birgisdottir, K.B. Larsen, A. Jain, H. Olsvik, A. Øvervatn, V. Kirkin, and T. Johansen. 2012. ATG8 family proteins act as scaffolds for assembly of the ULK complex: sequence requirements for LC3-interacting region (LIR) motifs. *J Biol Chem.* 287:39275-39290.
- Birgisdottir Å, B., T. Lamark, and T. Johansen. 2013. The LIR motif - crucial for selective autophagy. *J Cell Sci.* 126:3237-3247.
- Bjørkøy, G., T. Lamark, A. Brech, H. Outzen, M. Perander, A. Overvatn, H. Stenmark, and T. Johansen. 2005. p62/SQSTM1 forms protein aggregates degraded by autophagy and has a protective effect on huntingtin-induced cell death. *J Cell Biol.* 171:603-614.
- Cheng, X., Y. Wang, Y. Gong, F. Li, Y. Guo, S. Hu, J. Liu, and L. Pan. 2016. Structural basis of FYCO1 and MAP1LC3A interaction reveals a novel binding mode for Atg8-family proteins. *Autophagy.* 12:1330-1339.
- Eleonora Turco, I.F., Sascha Martens. 2020. FIP200 organizes the autophagy machinery at p62-ubiquitin condensates beyond activation of the ULK1 kinase. *BioRxiv.*
- Faruk Mohammad Omar, Y.I., Shun Kageyama, Afnan H. El-Gowily, Yu-shin Sou, Masato Koike, Nobuo Noda, Masaaki Komatsu. 2021. Droplets of amyotrophic lateral sclerosis-associated p62/SQSTM1 mutants show slower inner fluidity.
- Hara, T., A. Takamura, C. Kishi, S. Iemura, T. Natsume, J.L. Guan, and N. Mizushima. 2008. FIP200, a ULK-interacting protein, is required for autophagosome formation in mammalian cells. *J Cell Biol.* 181:497-510.
- Jain, A., T. Lamark, E. Sjøttem, K.B. Larsen, J.A. Awuh, A. Øvervatn, M. McMahon, J.D. Hayes, and T. Johansen. 2010. p62/SQSTM1 is a target gene for transcription factor NRF2 and creates a positive feedback loop by inducing antioxidant response element-driven gene transcription. *J Biol Chem.* 285:22576-22591.
- Jakobi, A.J., S.T. Huber, S.A. Mortensen, S.W. Schultz, A. Palara, T. Kuhm, B.K. Shrestha, T. Lamark, W.J.H. Hagen, M. Wilmanns, T. Johansen, A. Brech, and C. Sachse. 2020. Structural basis of p62/SQSTM1 helical filaments and their role in cellular cargo uptake. *Nat Commun.* 11:440.
- Johansen, T., and T. Lamark. 2020. Selective Autophagy: ATG8 Family Proteins, LIR Motifs and Cargo Receptors. *J Mol Biol.* 432:80-103.
- Kirkin, V., T. Lamark, T. Johansen, and I. Dikic. 2009. NBR1 co-operates with p62 in selective autophagy of ubiquitinated targets. *Autophagy.* 5:732-733.
- Komatsu, M., H. Kurokawa, S. Waguri, K. Taguchi, A. Kobayashi, Y. Ichimura, Y.S. Sou, I. Ueno, A. Sakamoto, K.I. Tong, M. Kim, Y. Nishito, S. Iemura, T. Natsume, T. Ueno, E. Kominami, H.

- Motohashi, K. Tanaka, and M. Yamamoto. 2010. The selective autophagy substrate p62 activates the stress responsive transcription factor Nrf2 through inactivation of Keap1. *Nat Cell Biol.* 12:213-223.
- Komatsu, M., S. Waguri, M. Koike, Y.-s. Sou, T. Ueno, T. Hara, N. Mizushima, J.-i. Iwata, J. Ezaki, S. Murata, J. Hamazaki, Y. Nishito, S.-i. Iemura, T. Natsume, T. Yanagawa, J. Uwayama, E. Warabi, H. Yoshida, T. Ishii, A. Kobayashi, M. Yamamoto, Z. Yue, Y. Uchiyama, E. Kominami, and K. Tanaka. 2007. Homeostatic Levels of p62 Control Cytoplasmic Inclusion Body Formation in Autophagy-Deficient Mice. *Cell.* 131:1149-1163.
- Lamark, T., M. Perander, H. Outzen, K. Kristiansen, A. Øvervatn, E. Michaelsen, G. Bjørkøy, and T. Johansen. 2003. Interaction codes within the family of mammalian Phox and Bem1p domain-containing proteins. *J Biol Chem.* 278:34568-34581.
- Maruyama, Y., Y.S. Sou, S. Kageyama, T. Takahashi, T. Ueno, K. Tanaka, M. Komatsu, and Y. Ichimura. 2014. LC3B is indispensable for selective autophagy of p62 but not basal autophagy. *Biochem Biophys Res Commun.* 446:309-315.
- Mejlvang, J., H. Olsvik, S. Svenning, J.A. Bruun, Y.P. Abudu, K.B. Larsen, A. Brech, T.E. Hansen, H. Brenne, T. Hansen, H. Stenmark, and T. Johansen. 2018. Starvation induces rapid degradation of selective autophagy receptors by endosomal microautophagy. *J Cell Biol.* 217:3640-3655.
- Nguyen, T.N., B.S. Padman, J. Usher, V. Oorschot, G. Ramm, and M. Lazarou. 2016. Atg8 family LC3/GABARAP proteins are crucial for autophagosome-lysosome fusion but not autophagosome formation during PINK1/Parkin mitophagy and starvation. *J Cell Biol.* 215:857-874.
- Olsvik, H.L., T. Lamark, K. Takagi, K.B. Larsen, G. Evjen, A. Øvervatn, T. Mizushima, and T. Johansen. 2015. FYCO1 Contains a C-terminally Extended, LC3A/B-preferring LC3-interacting Region (LIR) Motif Required for Efficient Maturation of Autophagosomes during Basal Autophagy. *J Biol Chem.* 290:29361-29374.
- Pankiv, S., E.A. Alemu, A. Brech, J.A. Bruun, T. Lamark, A. Overvatn, G. Bjørkøy, and T. Johansen. 2010. FYCO1 is a Rab7 effector that binds to LC3 and PI3P to mediate microtubule plus end-directed vesicle transport. *J Cell Biol.* 188:253-269.
- Pankiv, S., T.H. Clausen, T. Lamark, A. Brech, J.A. Bruun, H. Outzen, A. Øvervatn, G. Bjørkøy, and T. Johansen. 2007. p62/SQSTM1 binds directly to Atg8/LC3 to facilitate degradation of ubiquitinated protein aggregates by autophagy. *J Biol Chem.* 282:24131-24145.
- Popelka, H., and D.J. Klionsky. 2018. Structural basis for extremely strong binding affinity of giant ankyrins to LC3/GABARAP and its application in the inhibition of autophagy. *Autophagy.* 14:1847-1849.
- Shpilka, T., H. Weidberg, S. Pietrokovski, and Z. Elazar. 2011. Atg8: an autophagy-related ubiquitin-like protein family. *Genome Biol.* 12:226.
- Shvets, E., A. Abada, H. Weidberg, and Z. Elazar. 2011. Dissecting the involvement of LC3B and GATE-16 in p62 recruitment into autophagosomes. *Autophagy.* 7:683-688.
- Skytte Rasmussen, M., S. Mouilleron, B. Kumar Shrestha, M. Wirth, R. Lee, K. Bowitz Larsen, Y. Abudu Princely, N. O'Reilly, E. Sjøttem, S.A. Tooze, T. Lamark, and T. Johansen. 2017. ATG4B contains a C-terminal LIR motif important for binding and efficient cleavage of mammalian orthologs of yeast Atg8. *Autophagy.* 13:834-853.
- Weidberg, H., T. Shpilka, E. Shvets, and Z. Elazar. 2010. Mammalian Atg8s: one is simply not enough. *Autophagy.* 6:808-809.
- Wirth, M., W. Zhang, M. Razi, L. Nyoni, D. Joshi, N. O'Reilly, T. Johansen, S.A. Tooze, and S. Mouilleron. 2019. Molecular determinants regulating selective binding of autophagy adapters and receptors to ATG8 proteins. *Nature Communications.* 10:2055.

FIGURE LEGENDS

Figure 1. p62 LIR chimeric constructs with altered binding preference for ATG8 family proteins

- A. p62 structure cartoon showing the sequence that has been exchanged. p62 LIR was replaced with canonical LIRs from either FYCO1 or ULK1. The black color represents amino acids that belongs to p62 wt sequence. The amino acid sequence from the new LIRs is marked with red color.
- B. Myc-p62 was in vitro translated in the presence of ³⁵S methionine and tested in GST pulldown assay for binding to all 6 different Atg8s, which was fused to GST. Bound proteins were detected by autoradiography and immobilized GST fusion proteins by Coomassie brilliant blue staining.
- C. Myc-p62-LIR(ULK1) was in vitro translated in the presence of ³⁵S methionine and tested in GST pulldown assay for binding to all 6 different Atg8s, which was fused to GST. Bound proteins were detected by autoradiography and immobilized GST fusion proteins by Coomassie brilliant blue staining.
- D. Myc-p62-LIR(FYCO1) was in vitro translated in the presence of ³⁵S methionine and tested in GST pulldown assay for binding to all 6 different Atg8s, which was fused to GST. Bound proteins were detected by autoradiography and immobilized GST fusion proteins by Coomassie brilliant blue staining.
- E. Quantification of the binding efficiency between p62 variants and all six Atg8s. Data presented as mean \pm SD of the average binding efficiencies from 3 independent experiments. The statistical significance was also evaluated by the Prism GraphPad 9 software (ns- $P > 0.05$, *- $P \leq 0.05$, **- $P \geq 0.01$, ***- $0.01 \leq P \leq 0.001$ and ****- $P \leq 0.001$) by using one -way ANOVA nonparametric test or group comparison for unpaired t-test with Welch's correction for samples' comparison when SD are not equal.

Figure 2. Impaired KEAP1 binding of chimeric p62 constructs

- A. Western blot assay of MEF p62 KO cell lines reconstituted with either WT or the two LIR chimera constructs. Stable cell lines with the three indicated p62 variants were induced with doxycycline, and either left untreated or treated with the autophagy inhibitor Bafilomycin A1 for 8h. Cells were lysed in 5xSDS and the lysates were sonicated for 10sec.

- B. Confocal Fluorescence images of MEF KO cells reconstituted with either WT or the two LIR chimera constructs, and induced with doxycycline. Scale bar 10 μ m
- C. Quantification analysis of the average number of p62 bodies per cell per cell line. Each dot corresponds to the average number of p62 bodies per cell from one confocal image. The bars represent the mean \pm SD of the average number of p62 bodies. The statistical significance was also evaluated by the Prism GraphPad 9 software (ns- $P>0.05$, *- $P\leq 0.05$, **- $P\geq 0.01$, ***- $0.01\leq P\leq 0.001$ and ****- $P\leq 0.001$) by using one-way ANOVA nonparametric test or group comparison for unpaired t-test with Welch's correction for samples' comparison when SD are not equal.
- D. Quantification analysis of the average size of the p62 bodies per cell per cell line. Data were collected from 3 independent experiments. Each dot corresponds to the average p62 body size per cell one confocal image. The bars represent the mean \pm SD of the average size of p62 bodies. The statistical significance was also evaluated by the Prism GraphPad 9 software (ns- $P>0.05$, *- $P\leq 0.05$, **- $P\geq 0.01$, ***- $0.01\leq P\leq 0.001$ and ****- $P\leq 0.001$) by using one-way ANOVA nonparametric test or group comparison for unpaired t-test with Welch's correction for samples' comparison when SD are not equal.
- E. Myc-KEAP1 was in vitro translated in the presence of 35 S methionine and tested in GST pulldown assay for binding to GST-fusions of p62 WT and LIR chimera constructs. Bound proteins were detected by autoradiography and immobilized GST fusion proteins by Coomassie brilliant blue staining.
- F. Quantifications of the binding efficiency between KEAP1 and p62 WT or LIR variants. Data presented as mean binding in percent of input, with error bars showing \pm SD.
- G. Confocal fluorescence images of HeLa p62 KO cells co-transfected with mCherry-EYFP-KEAP1 and myc-p62 WT or LIR variants. Cells were fixed with 4% PFA 48h after transfection. Scale bar 10 μ m.

Figure 3. Impaired starvation-induced degradation of p62 LIR variants.

- A. Confocal fluorescence imaging of MEF p62 KO cell lines reconstituted with either WT or the two LIR chimera constructs. Cells were induced with doxycycline, and kept in either full medium or HBSS with and without Bafilomycin A1. Scale bar 10 μ m.

- B. Quantification of the relative p62 body intensities for each cell line. More than 100 cells were measured from 3 different experiments. Because of the different backgrounds in each cell line, different thresholds were applied when the counting was made by Volocity software. The bars represent the mean \pm SD of p62 body intensities relative to the FM intensity for each cell line separately. The statistical significance was evaluated by Prism GraphPad 9 software (ns- $P > 0.05$, *- $P \leq 0.05$, **- $P \geq 0.01$, ***- $0.01 \leq P \leq 0.001$ and ****- $P \leq 0.001$) by using one -way ANOVA nonparametric test or group comparison for unpaired t-test with Welch's correction for samples' comparison when SD are not equal.
- C. Western blot analysis of p62 from lysates from indicated cell lines treated or not with bafilomycin A1 and/or Hank's for 4h. Cell were lysed in 5% SDS and lysates were sonicated for 10sec. Actin was used as a loading control.

Figure 4 - Co-localization of chimeric p62 constructs with endogenous LC3B

- A. Confocal fluorescence microscopy analysis of MEF p62 KO cells reconstituted with the indicated GFP-p62 constructs. Cells were fixed with 4% PFA, permeabilized with 0,1% Triton and stained for endogenous LC3B. Scale bar 10 μ m.
- B. Quantification analysis made by Volocity software showing the percentage of p62 bodies colocalized with LC3B. Each dot corresponds to one confocal image. Each image contains a varying number of cells. More than 100 cells were counted. The bars represent the mean \pm SD from two independent experiments. The statistical significance was evaluated by Prism GraphPad 9 software (ns- $P > 0.05$, *- $P \leq 0.05$, **- $P \geq 0.01$, ***- $0.01 \leq P \leq 0.001$ and ****- $P \leq 0.001$) by using one -way ANOVA nonparametric test or group comparison for unpaired t-test with Welch's correction for samples' comparison when SD are not equal.
- C. GST pull-down from cell lysates from the indicated reconstituted GFP-p62 variant stable cell lines. Cells were lysed in RIPA buffer. The lysates were incubated for 4h together with GST, GST-LC3B or GST-GABARAP. The experiment was performed three times. Interactions were detected by p62 antibody staining and the immobilized GST beads by ponceau staining.

Figure 1

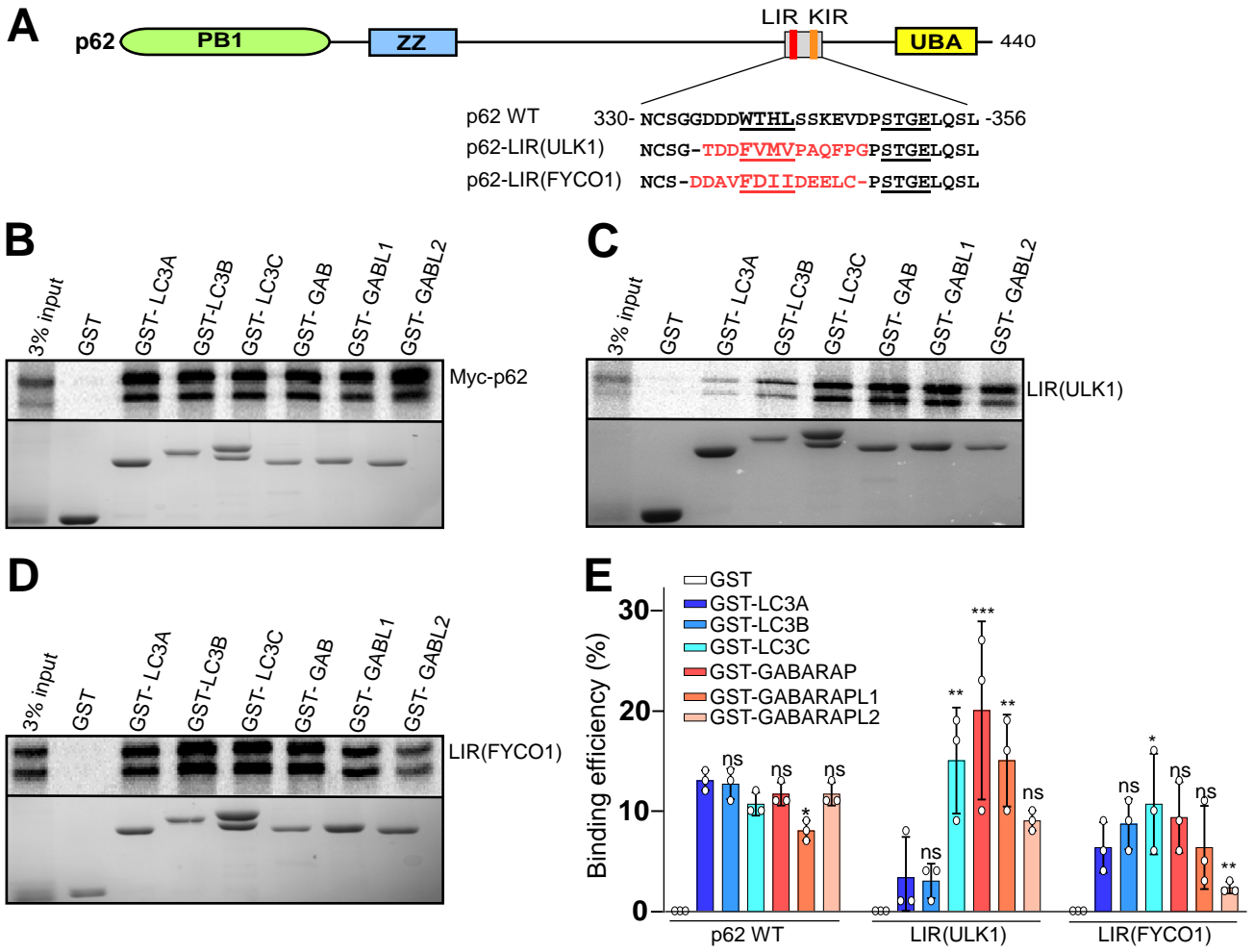


Figure 2

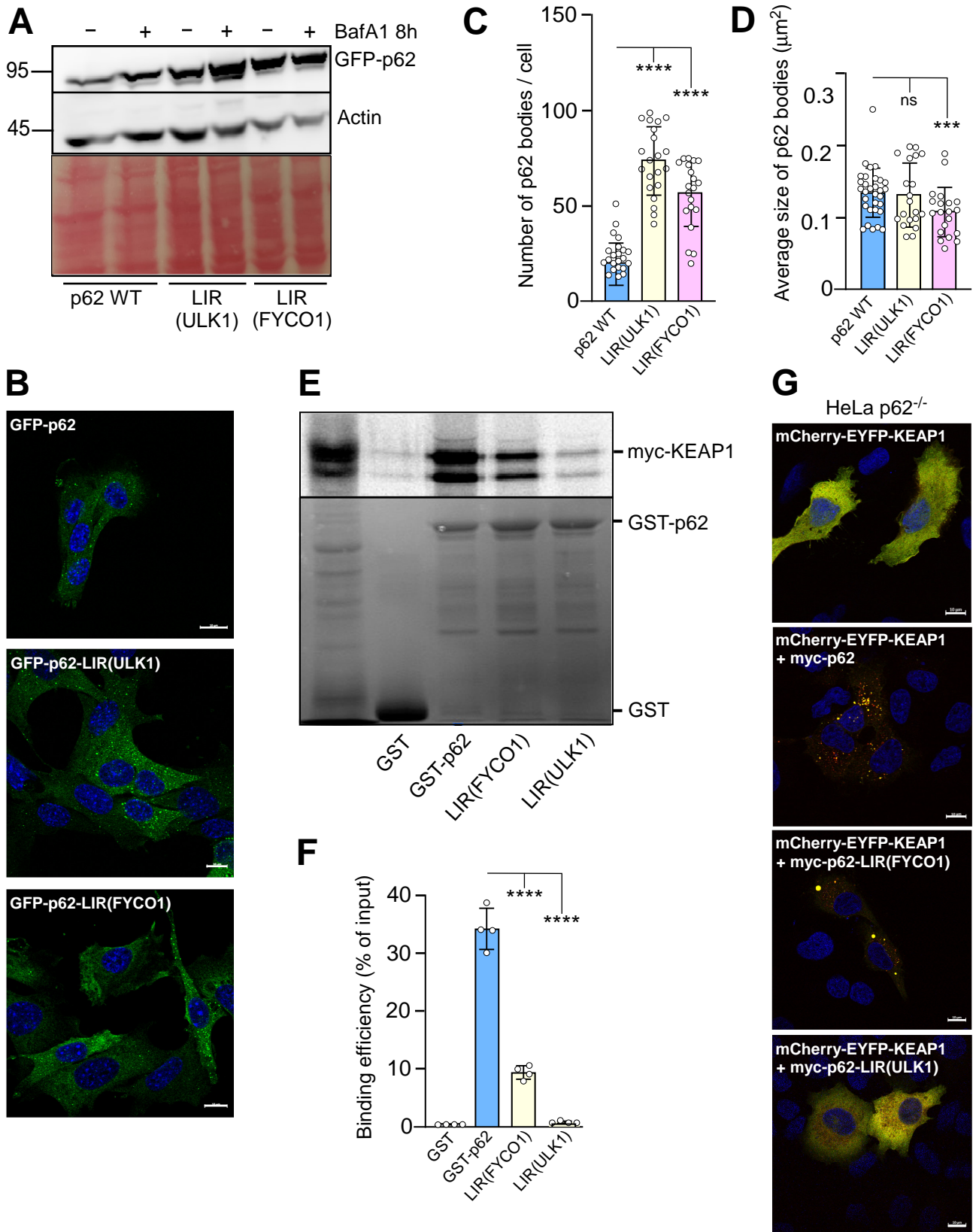


Figure 3

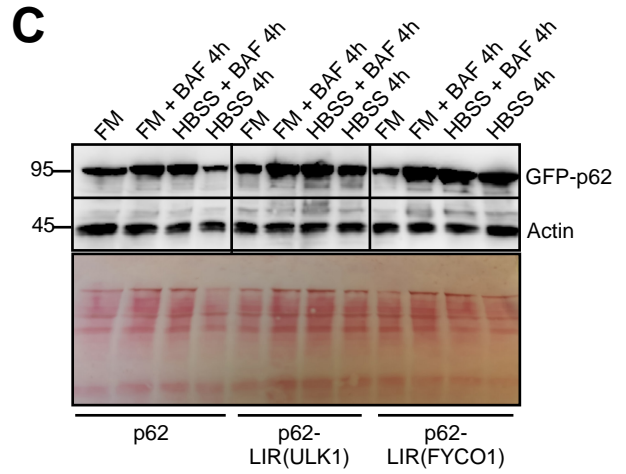
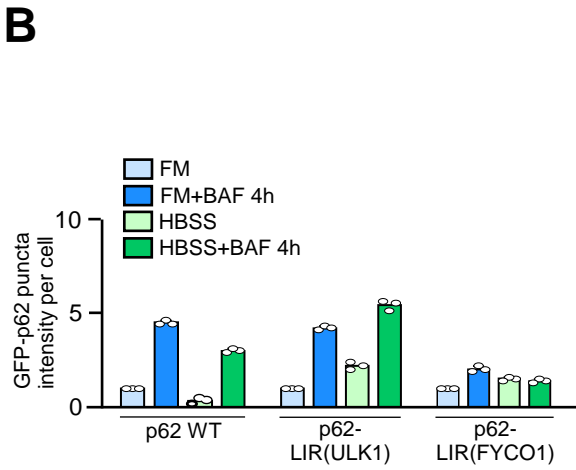
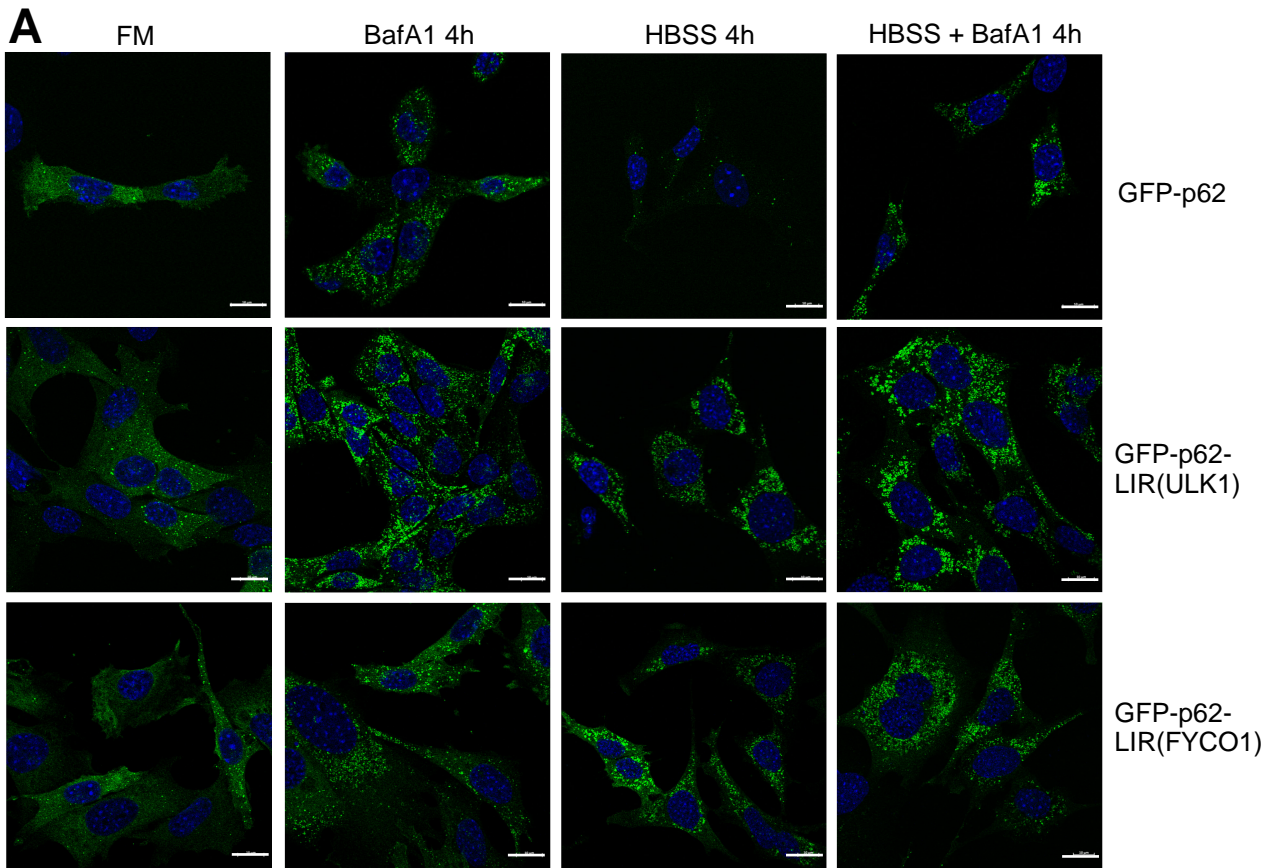
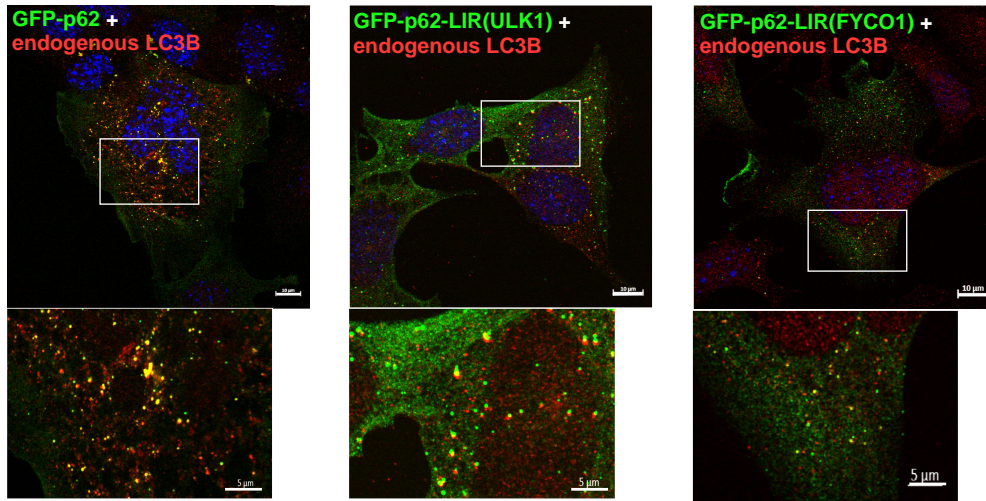
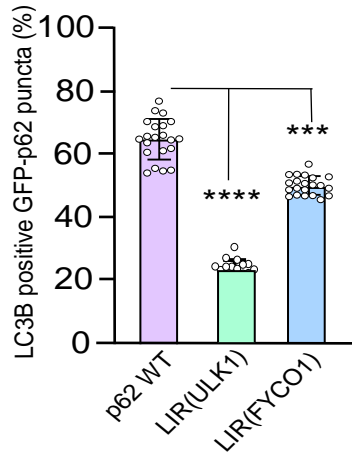


Figure 4

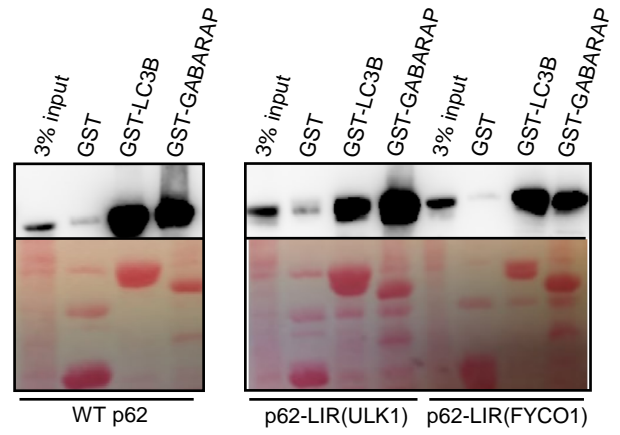
A



B



C



PAPER-III

The C-terminal Lys435 residue is required for efficient degradation of p62/SQSTM1 by autophagy

Anthimi Palara, Mireia Nager, Hallvard Lauritz Olsvik, Aud Karin Øvervatn, Gry Evjen, Kenneth Bowitz Larsen, Trond Lamark and Terje Johansen

Autophagy Research Group, Department of Medical Biology, University of Tromsø – The Arctic University of Norway, 9037 Tromsø, Norway.

Correspondence to: Trond Lamark, Email: trond.lamark@uit.no or Terje Johansen, Email: terje.johansen@uit.no

Running Title: Role of Lys residues in selective autophagy of p62

Keywords: acetylation, autophagy, post-translational modifications, p62, p62 bodies, ubiquitin

ABSTRACT

The selective autophagy receptor p62/SQSTM1 is regulated by post-translational modifications including phosphorylations, ubiquitinations and acetylations. Here, we investigated the role of lysine (K) residues in p62 for the formation of p62 bodies and autophagic turnover of p62 and a specific substrate, KEAP1. By mutating all 19 K residues to arginine residues (Rs) we found, somewhat surprisingly, that K7 is the only lysine residue in p62 that is absolutely required for formation of p62 bodies. This may be explained by the important role of K7 in PB1 domain-mediated polymerization of p62. However, lack of the 16 Ks located between K7 in the PB1 domain and K420 in the UBA domain led to irregular (conglomerate) morphology of p62 bodies. A total lack of lysines in p62 did not preclude its degradation by autophagy upon acute starvation, although this mutant could not form p62 bodies. Mutations of K420 in the UBA domain and K435 immediately C-terminal to the UBA domain affected the number of p62 bodies. The K435R mutation inhibited degradation of p62 by autophagy under basal conditions and the degradation of KEAP1 seen under starvation. The K420R mutation in the UBA domain blocks induction of p62 bodies in response to sulforaphane-induced oxidative stress. Treatment with the deacetylase inhibitor Trichostatin A (TSA) increased the size of p62 bodies, depending on K420 and K435, while acetylation mimicking mutations of K420 and K435 promote selective autophagic degradation of p62. Acetylation of the K435 residue in p62 promotes binding to ubiquitin. The phospho-mimicking S403E mutant and acetylation mimicking double mutant K420Q/K435Q both increase ubiquitin binding and autophagic turnover, but they do not act additively. Hence, phosphorylation and acetylation may not act in concert. The defective and mimicking mutants reveal a complex pattern of regulatory interactions affecting formation of p62 bodies and autophagic degradation of p62 and KEAP1.

INTRODUCTION

Macroautophagy (hereafter referred to as autophagy) is a lysosomal degradation process of cytoplasmic components which is highly conserved from yeast to mammals (Ohsumi, 2014). In this process a flat or crescent double membrane structure called the phagophore forms, expands and closes upon itself and is sealed to form the autophagosome which can then fuse with the lysosome to enable degradation and recycling of the cargo sequestered by the autophagosome. Autophagosomes can also fuse with late endosomes first to form amphisomes (Gordon and Seglen, 1988). Autophagy is connected through various ways to a large number of human diseases, as its functions are essential for cell survival, homeostasis, development and cell death. The last two decades has seen an increased interest in identifying the roles of autophagy in ageing, cancer, neurodegenerative disorders, and other pathophysiologicals (Dikic and Elazar, 2018; Levine and Kroemer, 2019; Mizushima and Levine, 2020). Autophagy, more specifically, selective autophagy is an important homeostatic process for protein and organelle quality control as aggregates of misfolded proteins as well as damaged or surplus organelles are degraded by this route (Johansen and Lamark, 2011; Kirkin and Rogov, 2019). Selective autophagy is dependent on cargo receptor or adaptor proteins which recruit the phagophore to the cargo (autophagic substrate) to be degraded (Johansen and Lamark, 2020; Kirkin and Rogov, 2019; Lamark and Johansen, 2021; Stolz et al., 2014) . The main cargo receptor in selective autophagy and the first discovered is p62/SQSTM1 (Bjørkøy et al., 2005; Pankiv et al., 2007). p62 is a scaffold protein participating in the regulation of different physiological processes in the cell, including responses to various stressors and cellular metabolism (Sánchez-Martín and Komatsu, 2018).

p62 is a polymeric protein that forms round bodies in both the cytoplasm and nucleus of mammalian cells, so called p62 bodies (Lamark et al., 2003; Pankiv et al., 2007). p62 forms flexible helical filaments both in vitro and in cells via PB1 domain polymerization (Agudo-Canalejo et al., 2021; Ciuffa et al., 2015; Jakobi et al., 2020). Recent studies have shown that p62 bodies are liquid-liquid droplets or liquid condensates which permits the interaction between proteins in a secure membrane-less environment (Sun et al., 2018; Zaffagnini et al., 2018). The formation of p62 bodies or droplets is driven by the binding of ubiquitin chains to the C-terminal UBA domain of p62 and dependent on the N-terminal PB1 domain mediated polymerization/oligomerization of p62 (Bjørkøy et al., 2005; Itakura and Mizushima, 2011; Lamark et al., 2003; Sun et al., 2018; Wilson et al., 2003; Zaffagnini et al., 2018). Depending on their size the p62 bodies or droplets can be degraded both by wholesale and by piecemeal

macroautophagy as phagophores form on the droplets by wetting (Agudo-Canalejo et al., 2021). The PB1 domain allows also interactions with NBR1 which may modulate droplet formation (Kirkin et al., 2009a; Sánchez-Martín et al., 2020). Another crucial domain in p62 for its function as an autophagy receptor is the LC3 Interaction Region (LIR) (Pankiv et al., 2007). The LIR domain endows p62 with the property to bind to the family of six ATG8 proteins. This ability is required for efficient degradation of p62 and its cargo by selective autophagy (Birgisdottir Á et al., 2013; Johansen and Lamark, 2020; Pankiv et al., 2007). In p62, the LIR motif is located immediately N-terminal to the KEAP1 interacting (KIR) motif. The KEAP1 protein is one of the known autophagic cargos, which binds to p62 and is degraded by selective autophagy (Bae et al., 2013; Jain et al., 2010; Jakobi et al., 2020; Komatsu et al., 2010; Taguchi et al., 2012). Furthermore, the main role of KEAP1 is to regulate the antioxidant response by binding the transcription factor NRF2 in the cytoplasm. As part of an ubiquitin E3 ligase complex with RBX1 and Cullin3, KEAP1 binds to NRF2 that gets ubiquitinated, and degraded by the proteasome under unstressed conditions. Upon oxidative stress, KEAP1 is modified on specific cysteine residues by oxidants and electrophiles leading to a conformational change in the E3 ligase complex inhibiting the ubiquitination of NRF2, which gets stuck on KEAP1. Newly synthesized NRF2 will then bypass KEAP1 and translocate to the nucleus to activate the expression of the antioxidant response gene repertoire regulated by NRF2 (Baird et al., 2013; Baird and Yamamoto, 2020). Findings by the group of Komatsu and our group demonstrated that p62 acts competitively with NRF2 in binding to KEAP1 and we also showed that NRF2 regulates p62 transcription creating a positive feedback loop activating antioxidant response genes at elevated levels of p62 (Jain et al., 2010; Komatsu et al., 2010). Phosphorylation of S349 in the KIR motif of p62 that binds to KEAP1 increases binding of p62 to KEAP1 (Komatsu et al., 2010).

Overlapping with the LIR and KIR motifs of p62 is a region binding to the conserved C-terminal domain of FIP200 of the ULK1 complex consisting of ULK1 (or ULK2), FIP200, ATG13 and ATG101. Hence, it is surmised that this interaction is highly relevant for the ability of p62 to recruit core autophagy components for autophagosome formation (Turco et al., 2019). Recent findings suggest that soluble selective autophagy receptors like p62, NDP52 and Optineurin recruit core components of the autophagy machinery to enable phagophore formation on the cargo they are bound to (Chang et al., 2021; Johansen and Lamark, 2020).

Formation of p62 bodies, or droplets, is regulated by the expression level, oligomerization status and ubiquitin binding activity of p62. Post-translational modifications (PTMs) including

phosphorylations, ubiquitinations and acetylations affect oligomerization and ubiquitin binding of p62. The latter is regulated by phosphorylation of S403 by TBK1 (Matsumoto et al., 2011; Pilli et al., 2012), and S407 by ULK1 (Lim et al., 2015). These phosphorylations lead to increased ubiquitin binding and larger p62 bodies. It is likely that ULK1 phosphorylation of S407 may stimulate S403 phosphorylation (Deng et al., 2020). Under stress conditions, TAK1 (TGF β activated kinase 1, also called MAP3K7) promotes phosphorylation of p62 on several sites also outside the UBA domain that leads to increased formation of p62 bodies. The p62 bodies then mediate TAK1 signaling effectively switching p62 from autophagy receptor function to signalosome function as a scaffold protein (Kehl et al., 2019).

The isolated UBA domain of p62 is able to dimerize and thereby preclude ubiquitin binding (Isogai et al., 2011; Long et al., 2010). It is not clear if the dimeric form actually is formed in cells, but several studies support the hypothesis that an important role for PTMs is to prevent UBA dimerization. Several K residues in p62 are ubiquitinated (Lee et al., 2017; Overå et al., 2019; Peng et al., 2017), and the ubiquitination of K420 by recruited KEAP1-Cullin-3 E3 ligase complexes was shown to induce p62 body formation by disrupting dimerization of the UBA domain. p62 also interacts with and gets ubiquitinated by the E2 Ub conjugating enzymes, UBE2D2 and UBE2D3 upon heat shock, proteasomal inhibition and ubiquitin overexpression (Peng et al., 2017). p62 is also ubiquitinated by the E3 ligase TRIM32, resulting in an increased formation of p62 bodies (Overå et al., 2019). There is also evidence for that acetylation of K420 and/or K435 by TIP60 similarly prevents the formation of UBA dimers and thereby increases the binding of p62 to ubiquitin (You et al., 2019).

We here investigated the role of K residues in p62. By mutating all K residues to R, we found that K7 is the only lysine residue in p62 that is needed for formation of p62 bodies. However, the isolated mutation of K420 or K435 had a strong impact on the formation of p62 bodies. In addition, we found that a mutation of all 16 K residues between the K7 residue and the UBA domain resulted in p62 bodies with a more fragmented and clustered morphology. Our conclusion is therefore that while a modification of K residues may not be required for the formation of p62 bodies, it may nevertheless regulate the efficiency of their formation and their morphology.

MATERIALS AND METHODS

Reagents

The reagents used were as follows: Bafilomycin A1, (Santa Cruz Biotech; SC-201550), Doxycycline (Sigma-Aldrich, D9891), MG132 (Sigma-Aldrich; C2211-5MG), TNT T7-coupled reticulocyte lysate system (Promega; 14610), Ponceau S (Sigma-Aldrich; P3504), buffered HBSS (Hank's Balanced Salt Solution)(Sigma-Aldrich, H9269), Penicillin/Streptomycin (Sigma-Aldrich, P4333), Metafectene Pro (BionTex, T040), fetal bovine serum (Biochrom, S0615), SuperSignal West Femto chemiluminescent kit (Thermo Scientific, 34096), Urea (Fluka, 51459), Trichostatin A (Sigma-Aldrich, T8552), sulforaphane (Sigma-Aldrich, S441-5MG), Blastidicin S HCl (Gibco, A11139-03), Coomassie Brilliant Blue R-250 Dye (Thermo Scientific, 20278), DAPI, (Thermo Scientific, 62248), Isopropyl β -d-1-thiogalactopyranoside (IPTG) (Sigma-Aldrich, I6758), ³⁵S-methionine (PerkinElmer, NEG709A500UC).

Antibodies

The following primary antibodies were used: Rabbit- anti-p62 (MBL, PM045), Guinea pig anti-p62/SQSTM1 (Progen, GP62-C), rabbit anti-KEAP1(Proteintech, 10503-2-AP), rabbit anti-actin (Sigma-Aldrich, A2066), rabbit anti-LC3B (MBL, PM036), rabbit anti-Acetylated Lysine (Cell Signaling, 9441). These secondary antibodies were employed: HRP-conjugated goat polyclonal anti rabbit antibody (BD Bioscience, 554021) and secondary goat polyclonal anti-rabbit IRDye 800LW antibody (LI-COR Biosciences, 926-32211) and donkey anti-guinea pig IRDye 680 LT antibody (LI-COR Biosciences, 926-68030).

Plasmids

Plasmid constructs were made by conventional cloning techniques and the Gateway recombination system. Point mutations were made using oligonucleotides from ThermoFisher and following PCR mutagenesis protocol using Pfu polymerase kit (Agilent Technologies, 600254-52). All constructs were verified by sequencing (BigDye, applied Biosystems). The following plasmids were previously made: pENTR-p62 (Lamark et al., 2003), pDONOR201-p62 K_{zero} (Aichem et al., 2012), pDest-EGFP-C1 (Lamark et al., 2003), pDest-mCherry-EYFP (Bhujabal et al., 2017), pDest-mCherry-EYFP-p62 (Jakobi et al., 2020), pDest-mCherry-EYFP-KEAP1 (Jakobi et al., 2020), pDest-myc (Lamark et al., 2003), pDest-myc-p62 (Lamark et al., 2003), pDest-mCherry-KEAP1 (Jain et al., 2010), pGEX-2T (Bacterial GST fusion expression

vector, Amersham Pharmacia-Biotech), pDest15-LC3A (Pankiv et al., 2007), pDest15-LC3B (Pankiv et al., 2007), pDest15-LC3C (Pankiv et al., 2007), pDest15-GABARAP (Pankiv et al., 2007), pDest15-GABARAPL1 (Pankiv et al., 2007), pDest15-GABARAPL2 (Pankiv et al., 2007), pDest15-4x Ubiquitin (Kirkin et al., 2009b) and pDest-LTR-EGFP (Skytte Rasmussen et al., 2017).

The plasmids that were made in this study are enlisted in Tables 1-3.

Table 1: Entry clones made by site-directed mutagenesis in this study.

pENTR-p62 K420R
pENTR-p62 K435R
pENTR-p62 K420R/K435R
pENTR-p62 K420Q/K435Q
pDONOR201- p62 (K/R) R7K
pDONOR201-p62 (K/R) R7K/R420K
pDONOR201-p62 (K/R) R7K/R435K
pDONOR201-p62 (K/R) R7K\R420K\R435K
pDONOR201-p62 (K/R)R7K\R420Q\R435Q
pENTR-p62 S403E
pENTR-p62 S403E\K420Q\K435Q
pENTR-p62 S403A
pENTR-p62 S403A\K420Q\K435Q
pENTR-p62 M404V

Table 2: Gateway expression clones made in this study

pDest-myc-p62 K420R	pDest-mCherry-EYFP-p62	pDest-EGFP-p62-K435R
pDest-myc-p62 K435R	pDest-mCherry-EYFP-p62 S403E	
pDest-myc-p62K _{zero}	pDest-mCherry-EYFP-p62 S403A	
pDest-myc-p62 (K\R) R7K	pDest-mCherry-EYFP-p62 K420Q\K435Q	

pDest-myc- p62 M404V	pDest-mCherry-EYFP-p62 S403E\K420Q\K435Q	
	pDest-mCherry-EYFP-p62 S403A\K420Q\K435Q	

Generation of stable cell lines A mouse embryonic fibroblast (MEF) p62 KO cell line was used as recipient for the generation of stable cell lines. Stably transfected cells were made using a retroviral vector derived from pLTR (Ichimura et al., 2008). pLRT has a tetracycline inducible expression module, and this vector was modified in our laboratory to contain an N-terminal EGFP tag and a Gateway cassette for insertion of cDNA constructs. Selected p62 constructs were inserted into this vector by gateway reactions, and GFP-p62 expression clones transfected Different pENTR and pDONOR201 constructs were combined with tag ,which is a viral mammalian transfection vector and doxycycline control inducible and carries a gateway cassette. Viral supernatant was harvested, filtered through a 0.45µM filter from HEK293 Plat-E cells. The filtered supernatant was added to the MEF p62 -/- cell, 24,48 and 72h post transfection. MEFs were split and reseeded in a medium containing 100µg/ml blastisidine S HCl (Thermo Fisher Scientific, R210-01). Induction of GFP-tagged proteins was achieved by treatment of stable cells lines with the indicated amount of doxycycline for 24h before the experiments took place.

Table 3: Gateway expression clones used for the generation of the stable cell lines

pDest-LTR-EGFP-p62	pDest-LTR-EGFP-p62 (K/R)
pDest-LTR-EGFP-p62 K420R	pDest-LTR-EGFP-p62 (K/R) R7K
pDest-LTR-EGFP-p62 K435R	pDest-LTR-EGFP-p62 (K/R) R7K/R420K
pDest-LTR-EGFP-p62 K420R/K435R	pDest-LTR-EGFP-p62 (K/R) R7K\R420K\R435K
pDest-LTR-EGFP-p62 K420Q/K435Q	pDest-LTR-EGFP-p62 (K/R) R7K\R420Q\R435Q

Mammalian cell culture

Murine embryonic fibroblast (MEF) cells knock out (KO) for p62 (Ichimura et al., 2008), and HeLa cells KO for p62 were used (Jakobi et al., 2020). Cells were cultured in Dulbecco's modified Eagle's medium (DMEM) (Sigma-Aldrich, D6046) supplemented with 10% fetal bovine serum (Biochrom, S0615) and 1% streptomycin-penicillin (Sigma-Aldrich, P4333), and 100ng/ml Blasticidin S HCl (Gibco A11139-03) and kept in the incubator at 37°C and 5% CO₂

GST- pulldown assays using in vitro translated proteins

GST-fusion proteins (ATG8s, 4xUbiquitin, PB1-NBR1) were expressed in *Escherichia coli* SoluBL21(DE3) (Genlantis #C700200) in LB medium. Protein expression was induced by addition of 0.5 mM IPTG and cells were further grown in the presence of IPTG for at least 4 hours at 37°C. Harvested cells were sonicated in lysis buffer (20 mM Tris-HCl pH 7.5, 10 mM EDTA, 5 mM EGTA, 150 mM NaCl). The lysates were mixed with glutathione-Sepharose 4 Fast Flow beads (GE Healthcare, 17513201) for 1 hour at 4°C under rotation, and the beads carrying immobilized GST fusion proteins were washed 3 times with NETN buffer (50 mM Tris pH 8.0, 150 mM NaCl, 1 mM EDTA, 0,5% NP-40) and used in GST pulldown assays with *in vitro* translated proteins. *In vitro* translation using the TNT coupled Reticulocyte Lysate System (Promega L4610) was done in the presence of radioactive ³⁵S-methionine. *In vitro* translated proteins were first incubated with empty glutathione-Sepharose 4 Fast Flow beads in NETN buffer supplemented with complete Mini EDTA-free protease inhibitor for 30 min at 4°C on a rotating wheel to avoid unspecific binding. The precleared lysates were subsequently incubated with beads loaded with immobilized GST fusion proteins for 1h at 4°C under rotation. The beads were washed 5 times with cold NETN buffer without inhibitors. After the last wash, samples were resuspended in loading buffer (100 mM Tris pH7.4, 4% SDS, 20% Glycerol, 0.2% bromophenol blue and 200 mM DTT (Sigma #D0632)) and boiled for 10 minutes. Eluted proteins were analyzed by SDS-PAGE. Gels were stained with Coomassie Brilliant Blue R-250 Dye (Thermo Fisher Scientific #20278) for the detection of GST fusion proteins. Gels were then vacuum dried for 1 hour, and the ³⁵S- labeled proteins were detected and analyzed by Fujifilm bioimaging analyzer BAS-5000 (Fujifilm).

Western blotting

Cells were lysed in 5x Laemli buffer (50mM Tris pH 7.4, 5% SDS, 10% Glycerol, 200 mM DTT (Sigma #D0632), heated for 2 minutes and sonicated for 10 sec. Protein levels were measured with BCA assay kit (Thermofisher 10741395(23225), followed by addition of bromophenol blue (0.1%) and DTT (100 mM). Samples were run on 8-10% SDS polyacrylamide gels and blotted either on PVDF membranes 0.2 μ m (Amersham, GE10600021) followed by Ponceau S staining or LI-COR nitrocellulose membranes 0.45 μ m were used for near-infrared western blots (LI-COR Biosciences, 926-31092). Blocking in both cases was with 5% nonfat milk in PBS-Tween 20 (0.1%). Membranes were incubated for one day or two at 4°C while rotation. Secondary antibody incubation was performed in room temperature for 1.5 hours in PBS-Tween 20 containing secondary antibody. Development was made by using LAS-4000 (Fujifilm) or Odyssey CLX (LI-COR).

GST-pulldown - in vivo binding to 4x ubiquitin

GST-4xUbiquitin was expressed in *E.coli* SoluBL21(DE3) (Genlantis #C700200) in LB medium. Protein expression was induced by addition of 0.5 mM IPTG and cells were incubated while shaking at 37°C for at least 4 hours. Harvested cells were sonicated in the lysis buffer (20 mM Tris-HCl pH 7.5, 10 mM EDTA, 5 mM EGTA, 150 mM NaCl). The GST-fusion proteins were purified on glutathione-Sepharose 4 Fast Flow beads by incubating on a rotator at 4°C for 1 hour, followed by washing with 1M Urea buffer (see 8M urea buffer). 1 M urea buffer was also used to store and prolong GST-fusion protein stability. Cells were seeded in 10 cm dishes one day in advance and induction of GFP-p62 protein expression in the stable expressing cells was done by adding doxycycline. Next day cells were lysed and harvested. To ensure complete extraction of aggregates formed by p62, cells were lysed in Urea buffer, 8M (50mM NaCl, 8M UREA, 0,5% Triton x100, 10mM Tris pH7.4, 5mM EDTA) or 1M (1:8 dilution in dH₂O from 8M UREA). Cell extracts were spined down and 3% of the amount was kept as input. Since 8 M urea denature proteins, extracts were diluted into 1 M urea before adding to the beads and the binding allowed to occur overnight at 4°C, while rotating. The next day microcentrifuge tubes were centrifuged at 7000xG for 3 minutes. Beads were transferred to 2ml autoclaved tubes and washed 2 times with 1M urea buffer and 3 times with RIPA buffer. Then as the western blot, adding 20 μ l of bromophenol blue (0.1%) and DTT (100 mM) and boil for 10 minutes. Samples were run on 10% SDS polyacrylamide gels and blotted on Hybond nitrocellulose membranes followed by Ponceau S staining. Blocking was done with 5% nonfat milk in PBS-Tween 20(0.1%). Membranes were incubated for one day at 4°C with rotation. Secondary

antibody incubation was performed in room temperature for 1.5 hours in PBS-Tween 20 containing secondary antibody. Development was done using LAS-4000 (Fujifilm).

Important notification, cell lines with diffused background will be sensitive to 8M Urea buffer, so the process was repeated both in 8M Urea buffer, where only the strong binding can be seen and in 1M urea buffer, which is milder buffer and more interactions are preserved.

Transient Transfection

Cells were seeded and induced with doxycycline. Cells were transfected with TransIt LT1/Metafectene PRO (Nordic Biosite 319-T040-5.0). DNA concentration was adjusted depending on the ability of the specific p62 variants ability to form dots. Media was changed after 12hrs to normal full media containing doxycycline. Cells were fixed with 4% formaldehyde 48 hours after transfection.

Immunofluorescence

Cells were placed on glass coverslips (VWR #6310150) and induced one day in advance with doxycycline. After treatment, when it was needed, cells were fixed in 4% formaldehyde (PFA) for 15 minutes at room temperature and then permeabilized with 0.1% Triton X-100 in PBS at room temperature for 5 minutes. Samples were blocked with 3% goat serum diluted in PBS for 1 hour in room temperature. Samples were stained with primary antibody, which was diluted in 1% goat serum containing PBS for 1-2 hours in room temperature. Alexa Fluor secondary antibodies were used for 1 hour in room temperature. There were three washes with PBS between each staining with antibodies. Last 10 minutes before the end of the staining with the secondary antibody 1 μ g/ml DAPI was added to the samples. At the end samples were washed 4 times in PBS and one time with pure water before they were mounted in 10 μ l of Mowiol and placed on a glass microscope slide.

Light microscopy

Fixed cells were imaged on a Zeiss Axio Observer Z.1 microscope, fitted with a LSM800 scanner for confocal microscopy (Carl Zeiss microscopy). Images were captured with a 63x NA1.4 oil immersion lens for coverslips. Optimal settings were determined using the Best signal setup in the Zen blue software.

Quantification of data and statistical analysis

Confocal imaging data were quantified using Volocity software (Quorum Technologies). Data in all figures are presented as mean +/- Standard deviation (SD) from minimum 3 biological independent experiments, unless otherwise stated. Dot plots were made in PRISM (Graphpad) and the statistical significance was also evaluated by the same software (ns $P > 0.05$, * $P \leq 0.05$, ** ≤ 0.01 , *** $0.01 \leq P \leq 0.001$, **** $P \leq 0.001$) by using one-way ANOVA nonparametric test or group comparison for unpaired t-test with Welch's correction for groups comparison when SDs are not equals.

RESULTS

Mutation of K420 and K435 affects the number of p62 bodies

The formation of p62 bodies or droplets is dependent on PB1 domain polymerization (Jakobi et al., 2020; Lamark et al., 2003; Wilson et al., 2003) and ubiquitin binding by the UBA domain of p62 (Sun et al., 2018; Zaffagnini et al., 2018). Ubiquitination of p62 is known to regulate both ubiquitin binding by the UBA domain of p62 (Lee et al., 2017; Peng et al., 2017; You et al., 2019), and polymerization of the PB1 domain (Pan et al., 2016). There are 19 K residues in p62 (**Figure 1A**). To improve our understanding of the role some of these K residues may have for the function of p62, we initially made a series of mutant constructs of p62 where K420 and/or K435 in the UBA domain were replaced by Arg (R) residues (K420R, K435R and K420R/K435R), all the 19 Ks were replaced with Rs named p62(K/R), and one where all Ks except for K7 were replaced, p62(K/R)R7K. In this latter mutant we also mutated back R420 to K and both R420 and R435 to K. The K to R mutations efficiently block ubiquitylation and acetylation on K residues. To investigate the overall effect of these mutations on the formation of p62 bodies, we reconstituted p62 knockout (KO) MEF cells with GFP-p62, GFP-p62 K420R, GFP-p62 K435R, GFP-p62 K420R/K435R, GFP-p62(K/R), GFP-p62(K/R)R7K, GFP-p62(K/R)R7K/R420K and GFP-p62(K/R)R7K/R420K/R435K (**Figure 1B** and **-C**). We were unable to make stable cells expressing the GFP-p62(K/R)R7K/R435K mutant construct. The LTR-EGFP retroviral vector was used for creation of stable cell lines, and expression of GFP-p62 constructs was induced with doxycycline. When analyzed under normal growth conditions in full medium GFP-p62 (WT) displayed the characteristic localization pattern including a diffuse cytoplasmic fraction and the presence of round p62 bodies (**Figure 1B**). The UBA domain contains only one Lys residue, K420, but K435 is located immediately C-terminal to

the UBA domain and affects ubiquitin binding (You et al., 2019). A mutation of either of these two residues had a strong effect on p62 body formation (**Figure 1B**). A mutation of K420 (K420R) increased the formation of p62 bodies, while a mutation of K435 (K435R) reduced the formation of p62 bodies. The K435R mutation appeared to be dominant since mutation of both residues gave a similar phenotype as the mutation of only the K435 residue (**Figure 1E, -F and -G**). Correlating with our manual observations (**Figure 1E**), computer based image analyses confirmed a strongly increased number of p62 bodies in cells expressing GFP-p62 K420R, while cells expressing GFP-p62 K435R or GFP-p62 K420R/K435R had a lower number of p62 bodies than WT GFP-p62 (**Figure 1G**). The computer-based analyses also revealed that p62 bodies formed by GFP-p62 K420R/K435R were smaller than p62 bodies formed by other constructs analyzed (**Figure 1F**).

Lys7 is the only Lys residue in p62 that is indispensable for formation of p62 bodies

A diffuse localization pattern without p62 bodies was observed for GFP-p62(K/R) (**Figure 1C**). This is as expected since the PB1 domain mediated-polymerization of p62 required for formation of p62 bodies (droplets) is compromised by mutating the K7 residue in the PB1 domain (Lamark et al., 2003). In contrast, GFP-p62(K/R)R7K, where K7 is added back, displayed a punctuated localization pattern resembling that of WT p62 (**Figure 1C**). However, the p62 bodies formed by GFP-p62(K/R)R7K had a more irregular shape than those formed by WT p62 and the diffuse cytoplasmic fraction was strongly reduced in cells expressing GFP-p62(K/R)R7K (**Figure 1D**). The irregular shape seems to be a result of an increased ability to form tight assemblies or conglomerates of droplets of similar size. Our conclusion is therefore that except for K7, no other K residues in p62 are required for the formation of p62 bodies. However, their loss affects the morphology of p62 bodies.

The K7R mutation inhibits the interaction between p62 and NBR1

The K7R mutation reduces strongly PB1 domain-mediated the self-interaction of p62, but potentially also affects heterodimeric PB1 interactions of p62 with other PB1 interaction partners like NBR1. NBR1 is recruited to p62 bodies, depending on the p62-NBR1 PB1 interaction and facilitates both formation and degradation of p62 bodies (Kirkin et al., 2009b). To test if the interaction of p62 with NBR1 is affected by the K7R mutation, GST pull-down

experiments were performed. In these experiments, the isolated PB1 domain of NBR1 fused to GST was expressed in *E. coli*, and then tested for binding to in vitro translated WT p62, p62(K/R) and p62(K/R)R7K. All the three p62 constructs interacted with the PB1 domain of NBR1, but p62(K/R)R7K bound more efficiently to NBR1 than p62(K/R) (**Figure S1A**). This correlates with a reduced binding efficiency caused by the K7R mutation. Since NBR1 facilitates p62 body formation, the failure of the GFP-p62(K/R) construct to accumulate in p62 bodies may partially rely on inefficient recruitment of NBR1. Unless recruited to p62 bodies, NBR1 is rapidly degraded by autophagy (Kirkin et al., 2009a). This may explain why we observed a very low level of endogenous NBR1 in cells expressing GFP-p62(K/R), when compared to cells expressing p62 constructs forming p62 bodies (**Figure S1B**).

Lack of the 16 Lys residues between K7 and K420 leads to irregular (conglomerate) morphology of p62 bodies

After confirming that p62 bodies were formed by the GFP-p62(K/R)R7K construct carrying 18 different K to R mutations, we performed in vitro GST pulldown experiments to test if the exchange of Ks to Rs had any impact on other important functional elements in p62 such as the LIR motif and the UBA domain. We first tested the binding of in vitro translated WT p62 or p62(K/R) to human ATG8 family proteins fused to GST, and the binding was similar for the two p62 constructs (**Figure S1C**). There are two Ks, K313 and K344, which are located before and after the p62 LIR motif. Apparently, these two mutations did not interfere with the p62-ATG8 interaction. Next, we checked the *in vitro* binding efficiency of WT p62, p62(K/R)R7K and p62 M404V (p62 mutant which is unable to bind Ubiquitin REF to 4x Ubiquitin fused to GST). This experiment revealed no detectable difference in binding to ubiquitin between WT p62 and p62(K/R)R7K (**Figure S1D**). Hence, the K to R mutations (including K420R and K435R in the UBA domain) has no large structural effect on the ability of p62 to interact with ubiquitin in vitro. In addition, our data with the p62(K/R)R7K construct demonstrates that a modification of K residues in p62 is not required for the binding of p62 to ubiquitin in vitro. This does not exclude an important regulatory role of post-translational modifications in regulating the strength of the interaction, but ubiquitin binding may occur without them.

When we added back the K420 and both K420 and K435 in the (K/R)R7K constructs we observed an increased ability to form droplets with K420 added back that was reduced when also K435 was added back (**Figure 1C, -E and -G**). Since the irregular morphology were seen

with GFP-p62(K/R) R7K, GFP-p62(K/R) R7K/R420K and GFP-p62(K/R) R7K/R420K/R435K (**Figure 1C -E**) it is probably caused by the loss of the 16 K residues between K7 and the UBA domain. We were unable to stably express GFP-p62(K/R) R7K/R435K in cells. Transient transfections gave very few transfected cells in p62 KO MEF cells, but this construct similarly gave irregular p62 bodies (**Figure S1E**). It is beyond the scope of this study to identify the specific mutation(s) responsible for the irregular morphology of p62 bodies, but further studies should look at this.

When making the GFP-p62 expressing cell lines, we observed that the proliferation rate varied depending on the expressed p62 construct. We therefore measured the proliferation rates in different cell lines under basal conditions starting with 5000 cells. (**Figure S1F**). The lowest proliferation rates were observed for GFP-p62(K/R) and GFP-p62(K/R)R7K/R420K/R435K. The lack of the 16 residues between K7 and K420 and giving a diffuse localization...give growth problems. These two K/R mutant constructs display diffuse localization and inhibited totally or partially in droplet formation and display diffuse localization.

p62 with a K435R mutation is not degraded by autophagy under basal conditions

Confocal imaging was used to investigate the ability of the GFP-p62 mutant constructs to be degraded by selective autophagy under basal conditions. Cells were treated or not with BafA1 for 4 hours, in order to inhibit lysosomal degradation. The area occupied by GFP puncta was measured using Volocity software, and autophagy was measured as an increase in the intensity of GFP puncta in cells treated with BafA1 relative to the untreated control. Because of the variety of phenotypes observed for the different GFP-p62 constructs, it was impossible to apply the same threshold in the Volocity software. Using the same protocol to analyze partly diffuse and strongly aggregated mutants of p62 gave invalid results either caused by the inclusion of diffuse p62 mistaken as GFP puncta, or by the exclusion of weaker GFP puncta mistaken as diffuse protein. The solution was to group the diffuse and the aggregated constructs and to apply a different threshold for each of these GFP-p62 groups. The most efficient accumulation upon BafA1 treatment was seen for WT GFP-p62 (**Figure 2A and -B**). Measured as relative increase in GFP puncta intensity, much less accumulation was seen for the GFP-p62 K420R construct than for WT p62 (**Figure 2B**). However, the GFP-p62 K420R construct has a strongly elevated basal level of p62 bodies (**Figure 2A**). On the other hand, GFP-p62 K435R has a mainly diffuse localization pattern with relatively few p62 bodies under basal conditions, and treatment with

BafA1 did not increase its accumulation in GFP puncta (**Figure 2A and -B**). This implies that the K435R mutation impedes both the formation of p62 bodies and inhibits degradation of p62 by autophagy in full medium conditions. The K435R mutation is also present in the similarly diffuse GFP-p62 K420R/K435R construct, but this construct showed some accumulation in GFP puncta upon BafA1 treatment (**Figure 2A and -B**). The increased ability of the K420R mutation to positively affect formation of p62 bodies clearly counteracts the K435R mutation resulting in a turnover by autophagy under basal conditions.

Western blot analyses verified the expression of the correct size proteins in the stable cell lines for GFP-62, GFP-p62 K420R, GFP-p62 K435R and GFP-p62 K420R/K435R.

Interestingly, all the constructs with the 16 internal Ks mutated to Rs were degraded by autophagy under basal conditions, measured as an increase in GFP puncta intensity upon the treatment of cells with BafA1 (**Figure 3A and -B**). It is notable that also the GFP-p62(K/R)R7K/R420K construct accumulated more GFP puncta upon BafA1 treatment since this construct contains the K435R mutation inhibiting autophagy of p62 K435R (**Figure 2B**). However, GFP-p62 K435R displays a highly diffuse localization pattern, while GFP-p62(K/R)R7K/R420K displays a highly aggregated localization pattern. The strong tendency of GFP-p62(K/R)R7K/R420K to accumulate in irregular p62 bodies may potentially explain the degradation of this construct by autophagy.

We verified the expression and correct size of the different GFP-p62 constructs by western blot analyses, after induction of protein expression with Dox (**Figure 3C**). Accumulation upon BafA1 treatment is seen for all constructs. To enable solubilization of the most aggregated p62 constructs, the cells were solubilized in 5% SDS containing buffer and the cell lysates were sonicated for 10 seconds. Still, we cannot be certain that all the p62 protein was solubilized. We regard the analyses of GFP puncta intensity as more reliable than protein levels determined from western blot analyses (see Discussion).

Lys residues in p62 are not essential for degradation of p62 in response to starvation

Starvation induced autophagy was measured using the same approach as for the study of basal autophagy. Cells were starved in the presence or absence of BafA1, and autophagy during starvation was measured as the difference in GFP puncta intensity between BafA1 treated and untreated cells. Our data showed an efficient degradation of all the tested GFP-p62 constructs

in response to starvation (**Figures 2A, -2B, -3A and 3B**). As a supplement to the confocal imaging based protocol used above to measure degradation of different GFP-p62 constructs by autophagy, the autophagic degradation of different GFP-p62 constructs was also analyzed by quantitative western blot experiments using near-infrared fluorescence detection with anti-p62 antibodies. The western blot data confirmed that the GFP-p62 K435R construct is not degraded by basal autophagy under basal conditions (**Figure 4A and -B**). There was no increase in the level of GFP-p62 K435R in cell extracts from cells grown in full medium (FM) and treated with BafA1. All other constructs displayed an increased p62 level in FM upon BafA1 treatment, indicating efficient basal autophagy. The western blot experiments also confirmed that all the GFP-p62 constructs were efficiently degraded by autophagy in response to starvation (**Figure 4A and -B**). This conclusion was based on a reduced GFP-p62 level in HBSS treated cells (compared to FM), and a higher level in HBSS+BafA1 treated cells than in HBSS treated cells.

KEAP1 is degraded by autophagy in response to starvation

The NRF2 regulator KEAP1 is recruited to p62 bodies via an interaction with the KIR motif in p62 (Jain et al., 2010; Komatsu et al., 2010). The functional interplay between p62 and KEAP1 is complex. On one hand, KEAP1 is degraded by p62 dependent selective autophagy to facilitate NRF2 activation. On the other hand, KEAP1 is in a complex with the E3 ligase Cullin 3, and a recruitment of KEAP1 to p62 bodies induces ubiquitination of K residues in p62. Transient transfection of mCherry-tagged KEAP1 confirmed that KEAP1 is consistently recruited to p62 bodies formed by the different GFP-p62 constructs (**Figure S1G**). This was also expected, since the KIR motif is not directly affected by mutations of K residues in p62. Since KEAP1 is present in p62 bodies and since autophagy of KEAP1 depends on p62 mediated selective autophagy, we therefore measured the level of endogenous KEAP1 in our western blot experiments. Under basal conditions (FM), there was no BafA1 induced increase indicating autophagic degradation of KEAP1 in cells expressing WT GFP-p62 (**Figure 4A and -C**). However, basal autophagy of KEAP1 appeared to occur in cells accumulating p62 bodies with a more irregular morphology than those formed by WT p62, i. e. GFP-p62(K/R)R7K, GFP-p62(K/R)R7K/R420K, and GFP-p62(K/R)R7K/R420K/R435K. All these cell lines displayed an elevated level of KEAP1 in FM+BafA1 treated cells, as compared to untreated cells (**Figure 4A and -C**). In HBSS treated cells, endogenous KEAP1 was degraded in all the GFP-p62 expressing cell lines, as shown by a strongly reduced protein level upon the treatment with HBSS (**Figure 4C**). In most of the cell lines, the level of KEAP1 was partially rescued by the

addition of BafA1, suggested an involvement of p62-dependent selective autophagy. The exception was for the GFP-p62 K435R construct, where we only observed a weak increase in the level of KEAP1 in cells treated with HBSS+BafA1 (**Figure 4C**). It is therefore unclear if this construct is able to mediate starvation-induced autophagy of KEAP1. In general, the levels of endogenous KEAP1 appeared to correlate with the expression levels seen for the different GFP-p62 constructs. The degradation seen for KEAP1 in response to starvation is interesting, and our data suggest a role for the K435 residue in this selective autophagy process.

Trichostatin A (TSA) treatment increases the size of p62 bodies, depending on K420 and K435 in the UBA domain

Trichostatin A (TSA) is an established global de-acetylation inhibitor. TSA treatment allows the proteins to retain acetylation, and by preventing de-acetylation, the use of TSA mimics acetylation. Our aim was to use TSA to measure how acetylation of Ks in p62 affected p62 bodies. TSA is a universal inhibitor affecting all the proteins inside the cell, and effects on p62 bodies can also be due to the acetylation of other proteins recruited to the p62 bodies. Cells were treated for 12 hours with TSA (100 ng/ml). Twelve hours were used to allow sufficient time for the drug to work while avoiding cell death occurring upon longer treatment. The GFP-p62 K420R/K435R expressing cell line did not tolerate the treatment with TSA and was therefore excluded from the TSA experiments. Acetylation of K residues was detected by immunostaining of cells using anti-AcK antibodies. The main targets of the TSA treatment are the nuclear histones. Increased AcK staining in the nucleus in response to TSA treatment worked as a positive control for that the treatment is working, as shown for GFP-p62 expressing cells in **Figure 5A**. Western blot of extract of GFP-p62 expressing cells after 12h with TSA treatment showed that acetylation of histones were strongly increased (**Figure 5B**).

TSA treatment for 12 hours of cells expressing WT p62 gave a slight increase in the number of p62 bodies, both in FM and in FM+BafA1 treated cells (**Figure 5C and -D**), but a more pronounced effect was a strong increase in the average size of p62 bodies (**Figure 5C and -E**). An important question is whether the increased number and size of p62 bodies is a direct effect of acetylation of p62? This is plausible since acetylation of K420 and K435 is shown to facilitate p62 body formation (You et al., 2019). A strong TSA-induced increase in GFP-p62 puncta size was observed in cells expressing GFP-p62(K/R)R7K/R420K or GFP-p62(K/R)R7K/R420K/R435K, suggesting that the add-back of K420 and/or K435 is sufficient

to rescue the TSA effect. A slight increase in puncta size was also observed for GFP-p62 constructs carrying a K420R mutation or a K435R mutation (**Figure 5E**). Our data therefore suggest that acetylation of K420 and/or K435 in cells treated with TSA results in an increased size of p62 bodies, and the strongest increase was seen for WT GFP-p62 and GFP-p62(K/R)R7K/R420K/R435K, the two constructs containing both K240 and K435 regulating dimerization and ubiquitin binding of the UBA domain.

TSA treatment had a very interesting effect on the number of p62 bodies formed by GFP-p62 K420R in FM. This construct displayed a highly aggregated phenotype resulting in an elevated number of p62 bodies (**Figure 2A and -5C**). In cells treated with TSA, the number of GFP bodies formed by this construct in FM was dramatically reduced (**Figure 5C and -D**). It is not known why the K420R mutant construct accumulates more in p62 bodies than WT p62, but we speculate that the effect of TSA may be to exchange ubiquitin modifications on critical K residues like K435 with acetylation.

The K420R mutation in the UBA domain blocks induction of p62 bodies in response to sulforaphane-induced oxidative stress

Sulforaphane (SFN), a natural compound found in cruciferous vegetables and broccoli sprouts, is used to induce mild oxidative stress in the cells. SFN activates NRF2 signaling by inhibiting KEAP1-Cullin3 mediated proteasomal degradation of NRF2 (Lee et al., 2021; Lee and Hu, 2020). SFN also induces the formation of p62 bodies (Sha et al., 2018). The mechanism for how SFN induces p62 body formation is not known, and it is neither known if KEAP1 is recruited to p62 bodies in SFN treated cells. If recruited to p62 bodies, KEAP1 is shown to induce the ubiquitination of K420 in the UBA domain of p62 (Lee et al., 2017).

To investigate the effect of SFN, cells expressing different GFP-p62 constructs were treated or not with 20 μ M SFN for two hours (**Figure 6A**). The number and size of p62 bodies was then determined. The addition of SFN to cells expressing WT GFP-p62 strongly increased the number of p62 bodies (**Figure 6B**), and the p62 bodies formed also had a larger size (**Figure 6C**). For all the tested GFP-p62 constructs, SFN increased the size of the p62 bodies (**Figure 6C**), but an increase in their number depended on the presence of K420 in the UBA domain (**Figure 6B**). A reduction was seen for GFP-p62 K420R while an increased number was seen for GFP-p62 K435R. This is consistent with the conclusion that K420 is essential for the induction of p62 bodies by SFN. The SFN response (increased number of p62 bodies) was not

rescued by an add-back of K420 to p62(K/R)R7K (GFP-p62(K/R)R7K/R420K), but adding back both K420 and K435 (GFP-p62(K/R)R7K/R420K/R435K) partially rescued the SFN response (**Figure 6B**). In conclusion, the SFN induced increase in the number of p62 bodies depends on K420 in the UBA domain and may be most efficient if also K435 is present.

Acetylation mimicking mutations of K420 and K435 promote selective autophagic degradation of p62

No amino acid substitution can mimic ubiquitination, but for p62 K to Q mutation has been shown to mimic acetylation of K420 and K435 in the UBA domain (You et al., 2019). We therefore made two different GFP-p62 constructs containing the K420Q/K435Q double mutation (named 2KQ); GFP-p62 2KQ and GFP-p62(K/R)R7K/2KQ. These constructs were stably expressed in p62 KO MEFs and p62 bodies analyzed by confocal imaging and compared to p62 bodies formed in cells expressing WT GFP-p62 (**Figure 7A**). In FM, the 2KQ mutation gave a clearly reduced number of p62 bodies (**Figure 7B**), but the average size of p62 bodies was not significantly changed in cells expressing 2KQ mutated constructs (**Figure 7C**). Another important observation was that the two cell lines expressing the 2KQ mutated constructs lacked a diffuse fraction of p62 (**Figure 7A**). Substitution of Ks with Qs in the UBA domain did not affect the colocalization with LC3B in the cells (**Figure 8A and -B**). We also analyzed the fluorescence intensity of GFP-p62 puncta in cells treated or not with BafA1 and/or HBSS (**Figure 8C and -D**). Both in FM and HBSS treated cells, BafA1 gave a strong increase in GFP puncta intensity in cells expressing the 2KQ mutant construct. Taken together with clearly reduced number of p62 bodies, and lack of diffuse fraction, this clearly suggests an efficient degradation of the 2KQ construct by autophagy.

Ubiquitination of K420 is required for the response of p62 to SFN treatment

While treatment of cells expressing WT p62 with TSA for 12h or SFN for 2h increased both the number and size of p62 bodies, these treatments had much less or no effect in cells expressing GFP-p62 2KQ construct (**Figure 7B and -C**). There was only a slight increase in the number of p62 bodies in cells treated with TSA for GFP-p62 2KQ while the p62(K/R)K7/R420Q/R435Q even showed a decrease (**Figure 7B**). These two mutants did not respond to treatment with SFN. Hence, the 2KQ mutation blocks the effects seen on p62 bodies

for WT p62 upon treatment with TSA or SFN. This observation alone shows that acetylation of K residues in the UBA domain is not the modification that leads to the SFN response. Taken together with the results for the K420R and K435R mutants (**Figure 6 A-C**), we conclude that ubiquitination of K420 in the UBA domain is likely required for the response to the SFN treatment.

Acetylation of the K435 residue in p62 promotes binding to ubiquitin

In order to look more into how ubiquitin binding by the UBA domain was affected by the mutation of Lys residues we performed GST pulldown assays with bead-bound recombinant GST-4xUbiquitin (4 ubiquitin covalently attached in a linear manner) using cell lysates prepared in 1M urea buffer. While the K420R mutant bound better than WT to linear ubiquitin fused to GST, K435R, on the other hand, was unable to bind (**Figure 9B**). The double mutant K420R/K435R did not bind to ubiquitin, while the add back mutant p62(K/R)R7K/R420K/R435K did bind as did the 2KQ mutant and the p62(K/R)R7K/R420Q/R435Q add back mutant. This clearly shows that the K435R mutation is incompatible with binding to ubiquitin in cells and that acetylation of K435 promotes binding to ubiquitin. In these experiments the highly aggregated (K/R)R7K mutant and the add back mutant p62(K/R)R7K/R420K mutants were not properly solubilized in the urea buffer and we could not properly assess their binding efficiency

To look at the ubiquitin interaction in cells by immunostaining we transiently expressed myc-p62 WT, K420R, K435R and (K/R)R7K mutants and stained for p62 and endogenous ubiquitin (**Figure 9C**). There was significantly less ubiquitin colocalized with the K435R mutant than the other constructs while the K420R and the (K/R)R7K mutants showed more colocalization (**Figure 9E and -D**). Taken together, our results clearly confirm the important role of K435 in ubiquitin binding.

Phospho-mimicking S403E and acetylation mimicking 2KQ mutants both increase ubiquitin binding and autophagic turnover, but they do not act additively

Phosphorylation of p62 at serine 403 (S403) has been reported to increase the affinity between UBA and polyubiquitin and to regulate autophagic clearance of p62 bodies (Matsumoto et al.,

2011). Acetylation of K420 and K435 has been shown to increase ubiquitin binding and autophagic turnover of p62 bodies (You et al., 2019). Our results here corroborate these findings. To study the combined effect of phosphorylation mimicking and acetylation mimicking mutants on autophagic turnover of p62 we made mCherry-GFP tandem tag constructs, and analyzed confocal images of transiently transfected p62 KO HeLa cells expressing mCherry-GFP-p62 WT, 2KQ, S403E, S403A, S403E/2KQ and S403A/2KQ constructs (**Figure 10A-E**). The S403E substitution mimics the effect of phosphorylation of S403 while S403A is inhibiting this phosphorylation. The 2KQ had the highest number of red dots and also the largest fraction of red only dots and the smallest yellow dots (**Figure 10B, -D and -E**). This confirms the rapid autophagic turnover of this construct. The S403E phosphor-mimicking mutant displayed increased number of red dots in comparison to WT, but it also had more and larger yellow dots than WT. Hence, the fraction of red only dots was similar to WT. and DT-p62 WT (FIG 14E). The non-phosphorylatable S403A mutant had the lowest number and also the lowest fraction of red only dots of all constructs tested underscoring the importance of S403. Perhaps surprisingly, combining the S403E and 2KQ mutations in one construct did not increase the autophagic turnover. This is likely because the S403E mutation favors formation of p62 bodies and this counteracts the rapid degradation that the 2KQ mutations induce. It would then be expected that the S403A/2KQ mutant would perhaps be degraded more effectively. However, this seems not to be the case based on the tandem tag data. This could indicate that dynamics of phosphorylation/dephosphorylation could be required on S403 or that the Ala substitution has a negative effect on ubiquitin binding by the UBA domain.

Taken together, the results suggest that S403 is acting dominantly over the 2KQ by increasing formation of p62 bodies. Both acetylation (2KQ) and phosphorylation (S403E) increase the binding efficiency of p62 to ubiquitin. The acetylation on K420 and particularly K435 promotes the autophagic turnover of p62.

DISCUSSION

Previous studies indicate that post-translational modifications of K residues in p62 has a strong impact both on the formation of p62 bodies and on their degradation by selective autophagy (Lee et al., 2017; Pan et al., 2016; Svenning et al., 2011; You et al., 2019; Zhang et al., 2019). In particular, there is strong evidence for that the phosphorylation of the S403 or S407 residues in the UBA domain, or the acetylation or ubiquitination of the two K residues located in the

UBA domain of p62 (K420) or in its C-terminal extension (K435) are essential regulatory events (Braak et al., 2011; Kageyama et al., 2021; Lee et al., 2017; Matsumoto et al., 2011; Peng et al., 2017; You et al., 2019). The purpose of these modifications is believed to be to regulate the interaction of p62 with ubiquitin and/or the droplet dynamics of p62 bodies. We here made a series of p62 mutants with selected K residues mutated into R residues, and their behavior was investigated in stably transfected cells depleted for endogenous p62. In line with previous studies, we found that a mutation of either of the K420 and K435 residues affected p62 body formation even under basal growth conditions. The K420R mutation gave more p62 bodies, while the K435R mutation reduced the number of p62 bodies.

A major challenge in using an approach based on the expression of mutant p62 constructs is that the K residues in the UBA domain can be modified either by acetylation or ubiquitination. The acetylation of K residues in the UBA domain has previously been successfully studied by the expression of acetylation mimicking K to Q mutations (You et al., 2019), and we used this approach in this study as well. However, it is not possible to mimic ubiquitination in a similar way. Therefore, a direct comparison of p62 constructs that were either “acetylated” or “ubiquitinated” was not possible. Another level of complexity comes from the fact that ubiquitin binding by the UBA domain in p62 is also strongly regulated by phosphorylation of the S403 and S407 residues (Deng et al., 2011; Kageyama et al., 2021; Matsumoto et al., 2011). Although we included p62 constructs with a mutated S403 residue, these mutants were only included in a limited set of experiments. To fully understand the role of PTMs in regulating the UBA domain, it will be important to investigate the interplay between phosphorylation events and modifications on the K residues, and our study generally fails to explain this crosstalk beyond what is already known. Nevertheless, our data indicated that phosphorylation and acetylation of the UBA domain has no additive effects, suggesting that these types of modifications may be alternative mechanisms that can be used independently for the activation of the UBA domain in p62.

Previous studies suggest an important role for the ubiquitination of the K420 residue in regulating p62 body formation (Lee et al., 2017; Peng et al., 2017). The main conclusion in these studies is that the ubiquitination of K420 inhibits dimerization of the UBA domain, and that ubiquitination of K420 is therefore required for efficient ubiquitin binding and formation of p62 bodies. We instead observed that K420R mutants accumulate in very large p62 bodies under basal conditions, and this indicates that a modification of K420 is not required for p62 body formation. However, our data support the conclusion that this ubiquitination of K420 may

be essential for the increased formation of p62 bodies in response to oxidative stress induced by sulphoraphane. In this case, the K420 residue appears to be more important than the K435 residue for the induction of p62 body formation. This correlates with the proposed model where KEAP1 together with co-recruited Cullin3 is responsible for the ubiquitination of K420 resulting in an inhibition of p62 dimer formation and increased ubiquitin binding (Lee et al., 2017). What remains to be shown is that sulphoraphane increases the interaction of KEAP1 with p62, and that KEAP1 and/or Cullin3 are needed for the formation of p62 bodies in response to Sulphoraphane treatment. Our data indicates that KEAP1 is constitutively associated with p62 bodies, but a binding of endogenous KEAP1 to p62 depends on a phosphorylation of the KIR motif in p62. Sulphoraphane strongly induces the formation of p62 bodies, and this suggests a mechanism where KEAP1 is involved. However, several other ubiquitin modifying enzymes are implicated in the regulation of p62 , and how the UBA domain is regulated by PTMs in response to oxidative stress is fully understood.

The acetylation of K420 and K435 is previously associated with an increased degradation of p62 bodies (You et al., 2019), and our data from cells expressing the K420Q/K435Q mutated p62 construct fully agree with this. We even found that the K435R construct was not degraded by autophagy under basal conditions. Degradation of KEAP1 was also impaired in cells expressing the K435R mutated p62 construct. However, the K420R/K435R construct was efficiently degraded by autophagy under the same conditions. The interpretation of our data is therefore difficult. and somehow the negative effect of the K435R mutation appears to be rescued by an additional loss of the K420 residue. p62-K435R and p62-K420R/K435R displayed a similar expression in cells characterized by a low number of p62 bodies and a more diffuse localization pattern than wt p62.

Another factor that may explain some of the confusions in our data is that the formation of p62 bodies is not required for the degradation p62 by autophagy. p62 is degraded via different autophagy pathways. In particular the degradation of diffuse pools of p62 is less understood and may involve both macroautophagy and endosomal microautophagy pathways (Mejlvang et al., 2018). The accumulation of clusters of p62 puncta in response to the treatment of cells with the autophagy inhibitor bafilomycin A1 (BafA1) indicates efficient degradation by selective autophagy, but the use of BafA1 does not distinguish between the degradation of p62 bodies and degradation of the diffuse pool of p62. Related to this study, this caused problems since constructs that are not easily degraded as bodies may be degraded as diffuse fractions and there

is a risk that we have overlooked important effects on the degradation of p62 bodies because of this.

Our data showed that a p62 construct with all K residues mutated into R residues was efficiently degraded by autophagy. This means that a post-translational modification of K residues in p62 is not needed for the degradation of p62 by autophagy. In addition, the degradation is evidently not inhibited by the K7R mutation. We showed previously that a complete block in PB1-mediated self-interaction caused by the R21A/R22A mutation prevented autophagy of p62 (Jakobi et al., 2020). The lack of effect on autophagy by the K7R mutation may reflect that this mutation does not block the self-interaction completely.

Another surprising observation we had was that K7 was the only K residue that was required for the formation of p62 bodies. However, the morphology of the p62 bodies may be affected by the presence or absence of specific K residues. There are 19 K residues in p62, and an interesting observation we had was that a deletion of all the 16 K residues between the essential K7 residue and the UBA domain gave p62 bodies with a conglomerated phenotype. These structures appeared very different from the rounded morphology typical for droplets normally formed by p62. The irregular phenotype likely reflects that “normal” p62 bodies depends on the ubiquitination of K residues N-terminal to the UBA domain. Since our main focus was on the UBA domain, we did not continue to identify the exact K residues that were responsible for the irregular phenotype. We neither performed confocal live cell imaging or correlative EM studies to investigate their dynamics or morphology. The conglomerated phenotype did not seem to affect their degradation by autophagy. The defect these mutant constructs may have may therefore be restricted to the formation of the p62 bodies, and not in their degradation. Of note, a similar conglomerated phenotype was previously observed for the p62 Δ 123-319 deletion construct (Jakobi et al., 2020), a construct lacking several of the internal K residues.

Acknowledgements

We are grateful to Masaaki Komatsu for the generous gift of p62 KO MEFs cells and the pLTR retroviral tetracycline-inducible expression vector. We thank the Advanced Microscopy Core Facility at the Faculty of Health Sciences, UiT-The Arctic University of Norway for assistance

and use of instruments. This work was funded by grant number 249884 from the Norwegian Research Council to TJ.

REFERENCES

- Agudo-Canalejo, J., S.W. Schultz, H. Chino, S.M. Migliano, C. Saito, I. Koyama-Honda, H. Stenmark, A. Brech, A.I. May, N. Mizushima, and R.L. Knorr. 2021. Wetting regulates autophagy of phase-separated compartments and the cytosol. *Nature*. 591:142-146.
- Aichem, A., B. Kalveram, V. Spinnenhirn, K. Kluge, N. Catone, T. Johansen, and M. Groettrup. 2012. The proteomic analysis of endogenous FAT10 substrates identifies p62/SQSTM1 as a substrate of FAT10ylation. *J Cell Sci*. 125:4576-4585.
- Bae, S.H., S.H. Sung, S.Y. Oh, J.M. Lim, S.K. Lee, Y.N. Park, H.E. Lee, D. Kang, and S.G. Rhee. 2013. Sestrins activate Nrf2 by promoting p62-dependent autophagic degradation of Keap1 and prevent oxidative liver damage. *Cell Metab*. 17:73-84.
- Baird, L., D. Llères, S. Swift, and A.T. Dinkova-Kostova. 2013. Regulatory flexibility in the Nrf2-mediated stress response is conferred by conformational cycling of the Keap1-Nrf2 protein complex. *Proc Natl Acad Sci U S A*. 110:15259-15264.
- Baird, L., and M. Yamamoto. 2020. The Molecular Mechanisms Regulating the KEAP1-NRF2 Pathway. *Mol Cell Biol*. 40.
- Bhujabal, Z., B. Birgisdóttir Á, E. Sjøttem, H.B. Brenne, A. Øvervatn, S. Habisov, V. Kirkin, T. Lamark, and T. Johansen. 2017. FKBP8 recruits LC3A to mediate Parkin-independent mitophagy. *EMBO Rep*. 18:947-961.
- Birgisdóttir Á, B., T. Lamark, and T. Johansen. 2013. The LIR motif - crucial for selective autophagy. *J Cell Sci*. 126:3237-3247.
- Bjørkøy, G., T. Lamark, A. Brech, H. Outzen, M. Perander, A. Overvatn, H. Stenmark, and T. Johansen. 2005. p62/SQSTM1 forms protein aggregates degraded by autophagy and has a protective effect on huntingtin-induced cell death. *J Cell Biol*. 171:603-614.
- Braak, H., D.R. Thal, and K. Del Tredici. 2011. Nerve cells immunoreactive for p62 in select hypothalamic and brainstem nuclei of controls and Parkinson's disease cases. *J Neural Transm (Vienna)*. 118:809-819.
- Chang, C., L.E. Jensen, and J.H. Hurley. 2021. Autophagosome biogenesis comes out of the black box. *Nat Cell Biol*. 23:450-456.
- Ciuffa, R., T. Lamark, A.K. Tarafder, A. Guesdon, S. Rybina, W.J. Hagen, T. Johansen, and C. Sachse. 2015. The selective autophagy receptor p62 forms a flexible filamentous helical scaffold. *Cell Rep*. 11:748-758.
- Deng, H.X., W. Chen, S.T. Hong, K.M. Boycott, G.H. Gorrie, N. Siddique, Y. Yang, F. Fecto, Y. Shi, H. Zhai, H. Jiang, M. Hirano, E. Rampersaud, G.H. Jansen, S. Donkervoort, E.H. Bigio, B.R. Brooks, K. Ajroud, R.L. Sufit, J.L. Haines, E. Mugnaini, M.A. Pericak-Vance, and T. Siddique. 2011. Mutations in UBQLN2 cause dominant X-linked juvenile and adult-onset ALS and ALS/dementia. *Nature*. 477:211-215.
- Deng, Z., J. Lim, Q. Wang, K. Purtell, S. Wu, G.M. Palomo, H. Tan, G. Manfredi, Y. Zhao, J. Peng, B. Hu, S. Chen, and Z. Yue. 2020. ALS-FTLD-linked mutations of SQSTM1/p62 disrupt selective autophagy and NFE2L2/NRF2 anti-oxidative stress pathway. *Autophagy*. 16:917-931.
- Dikic, I., and Z. Elazar. 2018. Mechanism and medical implications of mammalian autophagy. *Nat Rev Mol Cell Biol*. 19:349-364.
- Gordon, P.B., and P.O. Seglen. 1988. Prelysosomal convergence of autophagic and endocytic pathways. *Biochem Biophys Res Commun*. 151:40-47.

- Ichimura, Y., T. Kumanomidou, Y.S. Sou, T. Mizushima, J. Ezaki, T. Ueno, E. Kominami, T. Yamane, K. Tanaka, and M. Komatsu. 2008. Structural basis for sorting mechanism of p62 in selective autophagy. *J Biol Chem.* 283:22847-22857.
- Isogai, S., D. Morimoto, K. Arita, S. Unzai, T. Tenno, J. Hasegawa, Y.S. Sou, M. Komatsu, K. Tanaka, M. Shirakawa, and H. Tochio. 2011. Crystal structure of the ubiquitin-associated (UBA) domain of p62 and its interaction with ubiquitin. *J Biol Chem.* 286:31864-31874.
- Itakura, E., and N. Mizushima. 2011. p62 Targeting to the autophagosome formation site requires self-oligomerization but not LC3 binding. *J Cell Biol.* 192:17-27.
- Jain, A., T. Lamark, E. Sjøttem, K.B. Larsen, J.A. Awuh, A. Øvervatn, M. McMahon, J.D. Hayes, and T. Johansen. 2010. p62/SQSTM1 is a target gene for transcription factor NRF2 and creates a positive feedback loop by inducing antioxidant response element-driven gene transcription. *J Biol Chem.* 285:22576-22591.
- Jakobi, A.J., S.T. Huber, S.A. Mortensen, S.W. Schultz, A. Palara, T. Kuhm, B.K. Shrestha, T. Lamark, W.J.H. Hagen, M. Wilmanns, T. Johansen, A. Brech, and C. Sachse. 2020. Structural basis of p62/SQSTM1 helical filaments and their role in cellular cargo uptake. *Nat Commun.* 11:440.
- Johansen, T., and T. Lamark. 2011. Selective autophagy mediated by autophagic adapter proteins. *Autophagy.* 7:279-296.
- Johansen, T., and T. Lamark. 2020. Selective Autophagy: ATG8 Family Proteins, LIR Motifs and Cargo Receptors. *J Mol Biol.* 432:80-103.
- Kageyama, S., S.R. Gudmundsson, Y.S. Sou, Y. Ichimura, N. Tamura, S. Kazuno, T. Ueno, Y. Miura, D. Noshiro, M. Abe, T. Mizushima, N. Miura, S. Okuda, H. Motohashi, J.A. Lee, K. Sakimura, T. Ohe, N.N. Noda, S. Waguri, E.L. Eskelinen, and M. Komatsu. 2021. p62/SQSTM1-droplet serves as a platform for autophagosome formation and anti-oxidative stress response. *Nat Commun.* 12:16.
- Kehl, S.R., B.A. Soos, B. Saha, S.W. Choi, A.W. Herren, T. Johansen, and M.A. Mandell. 2019. TAK1 converts Sequestosome 1/p62 from an autophagy receptor to a signaling platform. *EMBO Rep.* 20:e46238.
- Kirkin, V., T. Lamark, T. Johansen, and I. Dikic. 2009a. NBR1 co-operates with p62 in selective autophagy of ubiquitinated targets. *Autophagy.* 5:732-733.
- Kirkin, V., T. Lamark, Y.S. Sou, G. Bjørkøy, J.L. Nunn, J.A. Bruun, E. Shvets, D.G. McEwan, T.H. Clausen, P. Wild, I. Bilusic, J.P. Theurillat, A. Øvervatn, T. Ishii, Z. Elazar, M. Komatsu, I. Dikic, and T. Johansen. 2009b. A role for NBR1 in autophagosomal degradation of ubiquitinated substrates. *Mol Cell.* 33:505-516.
- Kirkin, V., and V.V. Rogov. 2019. A Diversity of Selective Autophagy Receptors Determines the Specificity of the Autophagy Pathway. *Mol Cell.* 76:268-285.
- Komatsu, M., H. Kurokawa, S. Waguri, K. Taguchi, A. Kobayashi, Y. Ichimura, Y.S. Sou, I. Ueno, A. Sakamoto, K.I. Tong, M. Kim, Y. Nishito, S. Iemura, T. Natsume, T. Ueno, E. Kominami, H. Motohashi, K. Tanaka, and M. Yamamoto. 2010. The selective autophagy substrate p62 activates the stress responsive transcription factor Nrf2 through inactivation of Keap1. *Nat Cell Biol.* 12:213-223.
- Lamark, T., and T. Johansen. 2021. Mechanisms of Selective Autophagy. *Annu Rev Cell Dev Biol.*
- Lamark, T., M. Perander, H. Outzen, K. Kristiansen, A. Øvervatn, E. Michaelsen, G. Bjørkøy, and T. Johansen. 2003. Interaction codes within the family of mammalian Phox and Bem1p domain-containing proteins. *J Biol Chem.* 278:34568-34581.
- Lee, D.Y., M.Y. Song, and E.H. Kim. 2021. Role of Oxidative Stress and Nrf2/KEAP1 Signaling in Colorectal Cancer: Mechanisms and Therapeutic Perspectives with Phytochemicals. *Antioxidants (Basel).* 10.
- Lee, S., and L. Hu. 2020. Nrf2 activation through the inhibition of Keap1-Nrf2 protein-protein interaction. *Med Chem Res.* 29:846-867.
- Lee, Y., T.F. Chou, S.K. Pittman, A.L. Keith, B. Razani, and C.C. Wehl. 2017. Keap1/Cullin3 Modulates p62/SQSTM1 Activity via UBA Domain Ubiquitination. *Cell Rep.* 19:188-202.

- Levine, B., and G. Kroemer. 2019. Biological Functions of Autophagy Genes: A Disease Perspective. *Cell*. 176:11-42.
- Lim, J., M.L. Lachenmayer, S. Wu, W. Liu, M. Kundu, R. Wang, M. Komatsu, Y.J. Oh, Y. Zhao, and Z. Yue. 2015. Proteotoxic Stress Induces Phosphorylation of p62/SQSTM1 by ULK1 to Regulate Selective Autophagic Clearance of Protein Aggregates. *PLOS Genetics*. 11:e1004987.
- Long, J., T.P. Garner, M.J. Pandya, C.J. Craven, P. Chen, B. Shaw, M.P. Williamson, R. Layfield, and M.S. Searle. 2010. Dimerisation of the UBA domain of p62 inhibits ubiquitin binding and regulates NF-kappaB signalling. *J Mol Biol*. 396:178-194.
- Matsumoto, G., K. Wada, M. Okuno, M. Kurosawa, and N. Nukina. 2011. Serine 403 phosphorylation of p62/SQSTM1 regulates selective autophagic clearance of ubiquitinated proteins. *Mol Cell*. 44:279-289.
- Mejlvang, J., H. Olsvik, S. Svenning, J.A. Bruun, Y.P. Abudu, K.B. Larsen, A. Brech, T.E. Hansen, H. Brenne, T. Hansen, H. Stenmark, and T. Johansen. 2018. Starvation induces rapid degradation of selective autophagy receptors by endosomal microautophagy. *J Cell Biol*. 217:3640-3655.
- Mizushima, N., and B. Levine. 2020. Autophagy in Human Diseases. *N Engl J Med*. 383:1564-1576.
- Ohsumi, Y. 2014. Historical landmarks of autophagy research. *Cell Res*. 24:9-23.
- Overå, K.S., J. Garcia-Garcia, Z. Bhujabal, A. Jain, A. Øvervatn, K.B. Larsen, V. Deretic, T. Johansen, T. Lamark, and E. Sjøttem. 2019. TRIM32, but not its muscular dystrophy-associated mutant, positively regulates and is targeted to autophagic degradation by p62/SQSTM1. *J Cell Sci*. 132.
- Pan, J.A., Y. Sun, Y.P. Jiang, A.J. Bott, N. Jaber, Z. Dou, B. Yang, J.S. Chen, J.M. Catanzaro, C. Du, W.X. Ding, M.T. Diaz-Meco, J. Moscat, K. Ozato, R.Z. Lin, and W.X. Zong. 2016. TRIM21 Ubiquitylates SQSTM1/p62 and Suppresses Protein Sequestration to Regulate Redox Homeostasis. *Mol Cell*. 61:720-733.
- Pankiv, S., T.H. Clausen, T. Lamark, A. Brech, J.A. Bruun, H. Outzen, A. Øvervatn, G. Bjørkøy, and T. Johansen. 2007. p62/SQSTM1 binds directly to Atg8/LC3 to facilitate degradation of ubiquitinated protein aggregates by autophagy. *J Biol Chem*. 282:24131-24145.
- Peng, H., J. Yang, G. Li, Q. You, W. Han, T. Li, D. Gao, X. Xie, B.H. Lee, J. Du, J. Hou, T. Zhang, H. Rao, Y. Huang, Q. Li, R. Zeng, L. Hui, H. Wang, Q. Xia, X. Zhang, Y. He, M. Komatsu, I. Dikic, D. Finley, and R. Hu. 2017. Ubiquitylation of p62/sequestosome1 activates its autophagy receptor function and controls selective autophagy upon ubiquitin stress. *Cell Res*. 27:657-674.
- Pilli, M., J. Arko-Mensah, M. Ponpuak, E. Roberts, S. Master, M.A. Mandell, N. Dupont, W. Ornatowski, S. Jiang, S.B. Bradfute, J.A. Bruun, T.E. Hansen, T. Johansen, and V. Deretic. 2012. TBK-1 promotes autophagy-mediated antimicrobial defense by controlling autophagosome maturation. *Immunity*. 37:223-234.
- Sánchez-Martín, P., and M. Komatsu. 2018. p62/SQSTM1 - steering the cell through health and disease. *J Cell Sci*. 131.
- Sánchez-Martín, P., Y.S. Sou, S. Kageyama, M. Koike, S. Waguri, and M. Komatsu. 2020. NBR1-mediated p62-liquid droplets enhance the Keap1-Nrf2 system. *EMBO Rep*. 21:e48902.
- Sha, Z., H.M. Schnell, K. Ruoff, and A. Goldberg. 2018. Rapid induction of p62 and GABARAP1 upon proteasome inhibition promotes survival before autophagy activation. *J Cell Biol*. 217:1757-1776.
- Skytte Rasmussen, M., S. Mouilleron, B. Kumar Shrestha, M. Wirth, R. Lee, K. Bowitz Larsen, Y. Abudu Princely, N. O'Reilly, E. Sjøttem, S.A. Tooze, T. Lamark, and T. Johansen. 2017. ATG4B contains a C-terminal LIR motif important for binding and efficient cleavage of mammalian orthologs of yeast Atg8. *Autophagy*. 13:834-853.
- Stolz, A., A. Ernst, and I. Dikic. 2014. Cargo recognition and trafficking in selective autophagy. *Nat Cell Biol*. 16:495-501.
- Sun, D., R. Wu, J. Zheng, P. Li, and L. Yu. 2018. Polyubiquitin chain-induced p62 phase separation drives autophagic cargo segregation. *Cell Res*. 28:405-415.

- Svenning, S., T. Lamark, K. Krause, and T. Johansen. 2011. Plant NBR1 is a selective autophagy substrate and a functional hybrid of the mammalian autophagic adapters NBR1 and p62/SQSTM1. *Autophagy*. 7:993-1010.
- Taguchi, K., N. Fujikawa, M. Komatsu, T. Ishii, M. Unno, T. Akaike, H. Motohashi, and M. Yamamoto. 2012. Keap1 degradation by autophagy for the maintenance of redox homeostasis. *Proc Natl Acad Sci U S A*. 109:13561-13566.
- Turco, E., M. Witt, C. Abert, T. Bock-Bierbaum, M.-Y. Su, R. Trapannone, M. Sztacho, A. Danieli, X. Shi, G. Zaffagnini, A. Gamper, M. Schuschnig, D. Fracchiolla, D. Bernklau, J. Romanov, M. Hartl, J.H. Hurley, O. Daumke, and S. Martens. 2019. FIP200 Claw Domain Binding to p62 Promotes Autophagosome Formation at Ubiquitin Condensates. *Molecular Cell*. 74:330-346.e311.
- Wilson, M.I., D.J. Gill, O. Perisic, M.T. Quinn, and R.L. Williams. 2003. PB1 domain-mediated heterodimerization in NADPH oxidase and signaling complexes of atypical protein kinase C with Par6 and p62. *Mol Cell*. 12:39-50.
- You, Z., W.X. Jiang, L.Y. Qin, Z. Gong, W. Wan, J. Li, Y. Wang, H. Zhang, C. Peng, T. Zhou, C. Tang, and W. Liu. 2019. Requirement for p62 acetylation in the aggregation of ubiquitylated proteins under nutrient stress. *Nat Commun*. 10:5792.
- Zaffagnini, G., A. Savova, A. Danieli, J. Romanov, S. Tremel, M. Ebner, T. Peterbauer, M. Sztacho, R. Trapannone, A.K. Tarafder, C. Sachse, and S. Martens. 2018. p62 filaments capture and present ubiquitinated cargos for autophagy. *Embo j*. 37.
- Zhang, Y., S.R. Mun, J.F. Linares, C.G. Towers, A. Thorburn, M.T. Diaz-Meco, Y.T. Kwon, and T.G. Kutateladze. 2019. Mechanistic insight into the regulation of SQSTM1/p62. *Autophagy*. 15:735-737.

FIGURE LEGENDS

Figure 1. **Mutation of K420 and K435 affects the number of p62 bodies.** (A) p62 structure cartoon with all the 20 Lysines (K) listed on the p62 sequence. (B) Confocal fluorescence microscopy of MEF p62 KO cells stably reconstituted with the indicated doxycycline induced GFP-p62 constructs. Scale bars 10 μm . (C) Confocal fluorescence microscopy of MEF p62 KO cells stably reconstituted with the indicated doxycycline induced GFP-p62 constructs. (K/R) indicates a mutation of all 20 K residues in p62 to Arginines (R). Scale bars 10 μm . (D) Confocal microscopy image of GFP-p62(K/R)R7K, visualizing the irregular and conglomerated morphology of p62 bodies formed by (K/R) constructs. Scale bars 10 or 2 μm . (E) Qualitative analysis of GFP-p62 based on the manual observation of stable cell lines. Black dots represent the relative ability of different GFP-p62 constructs to form p62 bodies. R indicates a rounded morphology typical for WT p62 bodies. IR indicates a conglomerated morphology as shown in D. The amount of diffusely localized protein is indicated as high (D), some (d; as wt) or absent (-). (F) Quantitative analysis measuring the average size of the GFP-p62 bodies using Volocity software. Each dot corresponds to the average size of p62 bodies in a single confocal image. Confocal images were collected from three independent experiments, and for each condition more than 100 cells were analyzed. The bars represent the mean \pm SD of the average size of p62 bodies. The statistical significance was also evaluated by the Prism GraphPad 9 software (ns- $P>0.05$, *- $P\leq 0.05$, **- $P\geq 0.01$, ***- $0.01\leq P\leq 0.001$ and ****- $P\leq 0.001$) by using one-way ANOVA nonparametric test or group comparison for unpaired t-test with Welch's correction for samples' comparison when SD are not equal. (G) Quantitative analysis measuring the average number of GFP-p62 bodies per cell using Volocity software. Each dot corresponds to the average number of p62 bodies per cell in a single confocal image. Confocal images were collected from three independent experiments, and for each condition, more than 100 cells were analyzed. The bars represent the mean \pm SD of the average number of p62 bodies. The statistical significance was also evaluated by the Prism GraphPad 9 software (ns- $P>0.05$, *- $P\leq 0.05$, **- $P\geq 0.01$, ***- $0.01\leq P\leq 0.001$ and ****- $P\leq 0.001$) by using one-way ANOVA nonparametric test or group comparison for unpaired t-test with Welch's correction for samples' comparison when SD are not equal.

Figure 2. **p62 with a K435R mutation is not degraded by autophagy under basal conditions.** (A) Confocal fluorescence microscopy of MEF p62 KO cells reconstituted with the

indicated GFP-p62 constructs. Cells were treated as indicated (4 hours) with BafA1 and/or HBSS. Scale bars 10 μ m. **(B)** Quantitative analysis of A, measuring the relative effect of BafA1 and/or HBSS on the accumulation of GFP-p62 in puncta. For each condition, the GFP intensity in puncta were measured in more than 100 cells using Volocity software. Because of the different levels of diffuse protein between cell lines, different thresholds were applied. The bars represent the mean GFP puncta intensity per cell, relative to FM. **(C)** Western blot experiment showing expression of the indicated GFP-p62 constructs in stable cell lines after induction with doxycycline and treatment or not with BafA1 (4 hours). Cells were lysed in 5% SDS and lysates were sonicated for 10sec. GFP-p62 in cell lysates were detected by immunoblotting with anti-GFP antibodies using the Odyssey-CLX (LI-COR) system. Actin and total protein (Ponceau staining) were used as loading control.

Figure 3. Lys residues in p62 are not essential for the degradation of p62 in response to starvation. **(A)** Confocal fluorescence microscopy of MEF p62 KO cells reconstituted with the indicated GFP-p62(K/R) constructs and treated as indicated (4 hours) with BafA1 and/or HBSS. Scale bars 10 μ m. **(B)** Quantitative analysis of A, measuring the relative effect of BafA1 and/or HBSS on the accumulation of GFP-p62 in puncta. For each condition, the GFP intensity in puncta were measured in more than 100 cells using Volocity software. Because of the different levels of diffuse protein between cell lines, different thresholds were applied. The bars represent the mean GFP puncta intensity per cell, relative to FM. **(C)** Western blot experiment showing expression of the indicated GFP-p62(K/R) constructs in stable cell lines after induction with doxycycline and treatment or not with BafA1 (4 hours). GFP-p62(K/R) constructs in cell lysates were detected by immunoblotting with anti-GFP antibodies.

Figure 4. KEAP1 is degraded by autophagy in response to starvation. **(A)** Western blot analyses of GFP-p62 (red) and endogenous KEAP1 (green) in lysates from MEF p62 KO cells reconstituted with the indicated GFP-p62 constructs, and treated or not with BafA1 and/or HBSS. The experiments were performed using the Odyssey-CLX system, immunoblotting with anti-GFP and anti-KEAP1 antibodies, and total protein (Ponceau staining) as loading control. **(B)** Quantification of relative GFP-p62 level in western blot experiments shown in A. For each GFP-p62 construct, the levels in treated cells were normalized to the level in FM. The dots represent single western blot experiments. The bars represent the mean \pm SD of band intensities

relative to the total protein loading control. The statistical significance was evaluated by the Prism GraphPad 9 software (ns- $P>0.05$, *- $P\leq 0.05$, **- $P\geq 0.01$, ***- $0.01\leq P\leq 0.001$ and ****- $P\leq 0.001$) by using one -way ANOVA nonparametric test or group comparison for unpaired t-test with Welch's correction for samples' comparison when SD are not equal. **(C)** Quantification of relative endogenous KEAP1 level in western blot experiments shown in A. For each cell line, the levels of KEAP1 in treated cells were normalized to the level in FM. The dots represent single western blot experiments. The bars represent the mean \pm SD of band intensities relative to the total protein loading control. The statistical significance was also evaluated by the Prism GraphPad 9 software (ns- $P>0.05$, *- $P\leq 0.05$, **- $P\geq 0.01$, ****- $0.01\leq P\leq 0.001$ and ***- $P\leq 0.001$) by using one -way ANOVA nonparametric test or group comparison for unpaired t-test with Welch's correction for samples' comparison when SD are not equal. **(D)** Western blot analyses of endogenous KEAP1 (green) in lysates from MEF p62 KO cells treated or not with BafA1 and/or HBSS.

Figure 5. Trichostatin A (TSA) treatment increases the size of p62 bodies, depending on K420 and K435 in the UBA domain. **(A)** Control experiment indicating efficient TSA induced acetylation in MEF p62 KO cells reconstituted with wt GFP-p62. Cells were treated or not with TSA for 12 hours. Cells were fixed, and acetylation was visualized by immunoblotting using anti-Acetylated-Lysin antibodies. Scale bars 10 μ m. **(B)** Western blot experiment using cell lysates from MEF p62 KO cells reconstituted with wt GFP-p62, and treated with TSA as in A. The experiments were performed using the Odyssey-CLX system. Acetylated histones was detected by immunoblotting with anti-Acetylated-Lysin antibodies. Actin was used as loading control. **(C)** Confocal fluorescence microscopy analysis of MEF p62 KO cells reconstituted with the indicated GFP-p62 constructs and treated or not with TSA for 12h. Scale bars 10 μ m. **(D)** Quantification of the average number of GFP-p62 bodies per cell in the experiment in C. Each dot corresponds to the average number of p62 bodies per cell in a single confocal image. Confocal images were collected from three independent experiments, and for each condition, more than 100 cells were analyzed. The bars represent the mean \pm SD of the number of p62 bodies per cell. The statistical significance was also evaluated by the Prism GraphPad 9 software (ns- $P>0.05$, *- $P\leq 0.05$, **- $P\geq 0.01$, ***- $0.01\leq P\leq 0.001$ and ****- $P\leq 0.001$) by using one -way ANOVA nonparametric test or group comparison for unpaired t-test with Welch's correction for samples' comparison when SD are not equal. **(E)** Quantification of average size of GFP-p62 bodies in cells analyzed in C, using Volocity software. Each dot corresponds to the

average size of p62 bodies in a single confocal image. Confocal images were collected from three independent experiments, and for each condition more than 100 cells were analyzed. The bars represent the mean \pm SD of the average size of p62 bodies per cell. The statistical significance was also evaluated by the Prism GraphPad 9 software (ns- $P>0.05$, *- $P\leq 0.05$, **- $P\geq 0.01$, ***- $0.01\leq P\leq 0.001$ and ****- $P\leq 0.001$) by using one -way ANOVA nonparametric test or group comparison for unpaired t-test with Welch's correction for samples' comparison when SD are not equal.

Figure 6. The K420R mutation in the UBA domain blocks induction of p62 bodies in response to sulphoraphane-induced oxidative stress. (A) Confocal fluorescence microscopy analysis of MEF p62 KO cells reconstituted with the indicated GFP-p62 constructs, and treated or not with sulphoraphane (SFN) for 2h. Scale bar 10 μ m. (B) Quantification of the average number of GFP-p62 bodies per cell in the experiment in A. Each dot corresponds to the average number of p62 bodies per cell in a single confocal image. Confocal images were collected from three independent experiments, and for each condition, more than 100 cells were analyzed. The bars represent the mean \pm SD of the number of p62 bodies per cell. The statistical significance was also evaluated by the Prism GraphPad 9 software (ns- $P>0.05$, *- $P\leq 0.05$, **- $P\geq 0.01$, ***- $0.01\leq P\leq 0.001$ and ****- $P\leq 0.001$) by using one -way ANOVA nonparametric test or group comparison for unpaired t-test with Welch's correction for samples' comparison when SD are not equal. (C) Quantification of average size of GFP-p62 bodies in cells analyzed in A, using Volocity software. Each dot corresponds to the average size of p62 bodies in a single confocal image. Confocal images were collected from three independent experiments, and for each condition more than 100 cells were analyzed. The bars represent the mean \pm SD of the average size of p62 bodies per cell. The statistical significance was also evaluated by the Prism GraphPad 9 software (ns- $P>0.05$, *- $P\leq 0.05$, **- $P\geq 0.01$, ***- $0.01\leq P\leq 0.001$ and ****- $P\leq 0.001$) by using one -way ANOVA nonparametric test or group comparison for unpaired t-test with Welch's correction for samples' comparison when SD are not equal.

Figure 7. Ubiquitination of K420 is required for the induction of p62 bodies in response to SFN treatment. (A) Confocal fluorescence microscopy analysis of MEF p62 KO cells reconstituted with acetylation mimicking mutants of GFP-p62, and treated or not as indicated with TSA or SFN. Scale bars 10 μ m. (B) Quantification of the average number of GFP-p62

bodies per cell in the experiment in A. Each dot corresponds to the average number of p62 bodies per cell in a single confocal image. Confocal images were collected from three independent experiments, and for each condition, more than 100 cells were analyzed. The bars represent the mean \pm SD of the number of p62 bodies per cell. The statistical significance was also evaluated by the Prism GraphPad 9 software (ns- $P > 0.05$, *- $P \leq 0.05$, **- $P \geq 0.01$, ***- $0.01 \leq P \leq 0.001$ and ****- $P \leq 0.001$) by using one -way ANOVA nonparametric test or group comparison for unpaired t-test with Welch's correction for samples' comparison when SD are not equal. (C) Quantification of average size of GFP-p62 bodies in cells analyzed in A, using Volocity software. Each dot corresponds to the average size of p62 bodies in a single confocal image. Confocal images were collected from three independent experiments, and for each condition more than 100 cells were analyzed. The bars represent the mean \pm SD of the average size of p62 bodies per cell. The statistical significance was also evaluated by the Prism GraphPad 9 software (ns- $P > 0.05$, *- $P \leq 0.05$, **- $P \geq 0.01$, ***- $0.01 \leq P \leq 0.001$ and ****- $P \leq 0.001$) by using one -way ANOVA nonparametric test or group comparison for unpaired t-test with Welch's correction for samples' comparison when SD are not equal.

Figure 8. Acetylation mimicking mutations of K420 and K435 promote selective autophagic degradation of p62. (A) Co-localization of acetylation-mimicking mutants of GFP-p62 with endogenous LC3B. MEF p62 KO cells reconstituted with the indicated GFP-p62 constructs were fixed with 4% PFA, permeabilized with 0,1% Triton and stained for endogenous LC3B. Scale bars 10 μ m. (B) Quantification of the co-localization of LC3B in GFP-p62 bodies in the experiment in A. Each dot corresponds to the average co-localization in a single confocal image. Confocal images were collected from two independent experiments, and for each cell line, more than 100 cells were analyzed. The bars represent the mean \pm SD of % colocalization with LC3B. The statistical significance was also evaluated by the Prism GraphPad 9 software (ns- $P > 0.05$, *- $P \leq 0.05$, **- $P \geq 0.01$, ***- $0.01 \leq P \leq 0.001$ and ****- $P \leq 0.001$) by using one -way ANOVA nonparametric test or group comparison for unpaired t-test with Welch's correction for samples' comparison when SD are not equal. (C) Confocal fluorescence microscopy of MEF p62 KO cells reconstituted with the indicated GFP-p62(K/R) constructs and treated as indicated with BafA1 and/or HBSS. Scale bars 10 μ m. (D) Quantitative analysis of the experiment in C, measuring the relative effect of BafA1 and/or HBSS on the accumulation of GFP-p62 in puncta. For each condition, the GFP intensity in puncta were measured in more than 100 cells from three separate experiments using Volocity software.

Because of the different levels of diffuse protein between cell lines, different thresholds were applied. The bars represent the mean GFP puncta intensity per cell, relative to FM. The bars represent the mean \pm SD of p62 bodies intensities relative to the FM p62 bodies intensities for each cell line separately. The statistical significance was also evaluated by the Prism GraphPad 9 software (ns- $P > 0.05$, *- $P \leq 0.05$, **- $P \geq 0.01$, ***- $0.01 \leq P \leq 0.001$ and ****- $P \leq 0.001$) by using one -way ANOVA nonparametric test or group comparison for unpaired t-test with Welch's correction for samples' comparison when SD are not equal.

Figure 9. The K435 residue is important for the binding of p62 to ubiquitin. (A) p62 structure cartoon indicating post-translational modified sites in the UBA domain. (B) GST pull-down assays using lysates of MEF p62 KO cells reconstituted with the indicated GFP-p62 constructs and immobilized GST-4xUbiquitin (4xUb). The GST-4xUb contains 1-4 linear ubiquitin moieties fused to GST. Cells were lysed in 1M UREA buffer. The highly aggregated GFP-p62(K/R)R7K and GFP-p62(K/R)R7K/R420K constructs were not solubilized in the urea buffer and are therefore absent in the lysates (input). The depicted experiment was performed only once, but additional experiments were performed with less cell lines to confirm the observations. GFP-p62 constructs in the lysates or co-precipitates were detected by immunoblotting using anti-p62 antibodies. Immobilized GST and GST-4xUb were visualized by Ponceau staining. (C) Co-localization of myc-tagged p62 bodies with Ubiquitin. HeLa cells were transiently transfected with the indicated myc-p62 constructs. 48 hours after the transfection, cells were immunostained for endogenous ubiquitin using FK2 antibodies. Scale bars 10 μ m. (D) Quantification of the co-localization of p62 bodies with endogenous Ubiquitin in C, using Volocity software. Each dot corresponds to the average co-localization in a single confocal image. Confocal images were collected from 2 independent experiments, and for each cell line, more than 100 cells were analyzed. The bars represent the mean \pm SD % of colocalization between p62 indicated variant and ubiquitin. The statistical significance was also evaluated by the Prism GraphPad 9 software (ns- $P > 0.05$, *- $P \leq 0.05$, **- $P \geq 0.01$, ****- $0.01 \leq P \leq 0.001$ and ***- $P \leq 0.001$) by using one -way ANOVA nonparametric test or group comparison for unpaired t-test with Welch's correction for samples' comparison when SD are not equal.

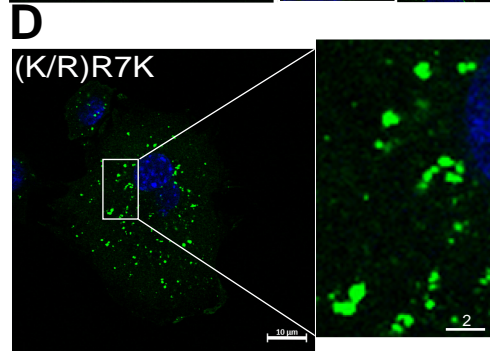
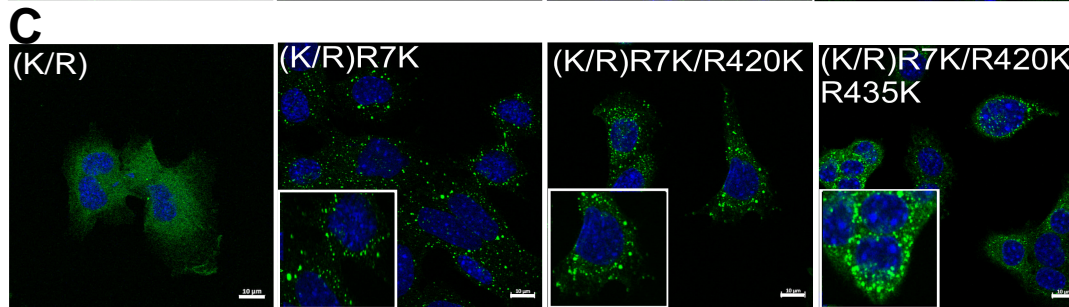
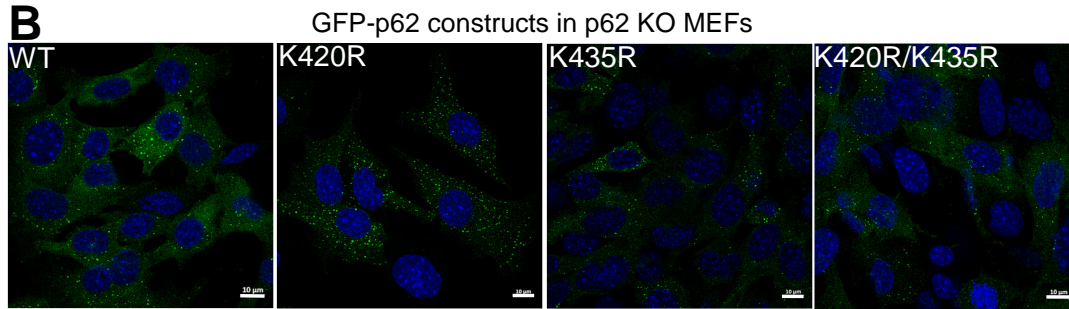
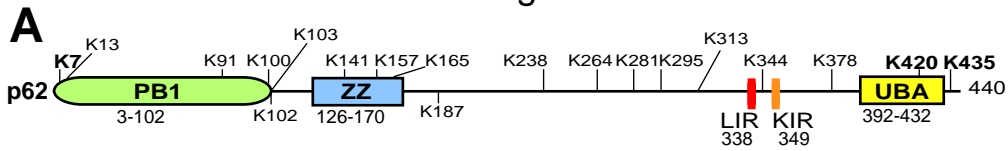
Figure 10. **Phospho-mimicking S403E and acetylation mimicking 2KQ mutants both increase autophagic turnover, but they do not act additively.** (A) Confocal fluorescence microscopy of HeLa cells transiently transfected with the indicated mCherry-EYFP tagged p62 constructs. 48h after transfection, cells were fixed with 4% PFA and analyzed by confocal microscopy. Scale bars 10 μ m. (B) Quantitative analysis measuring the average number of red-only puncta per cell, based on a manual counting of red-only puncta in >50 cells from two independent transfection experiments for each transfected p62 construct. The bars represent the mean \pm SD of the number of red puncta per cell for each cell line separately. The statistical significance was also evaluated by the Prism GraphPad 9 software (ns- $P>0.05$, *- $P\leq 0.05$, **- $P\geq 0.01$, ***- $0.01\leq P\leq 0.001$ and ****- $P\leq 0.001$) by using one -way ANOVA nonparametric test or group comparison for unpaired t-test with Welch's correction for samples' comparison when SD are not equal. (C) Quantitative analysis measuring the average number of yellow puncta per cell, based on a manual counting of yellow puncta in >50 cells from two independent transfection experiments for each transfected p62 construct. The bars represent the mean \pm SD of the number of yellow puncta per cell for each cell line separately. The statistical significance was also evaluated by the Prism GraphPad 9 software (ns- $P>0.05$, *- $P\leq 0.05$, **- $P\geq 0.01$, ***- $0.01\leq P\leq 0.001$ and ****- $P\leq 0.001$) by using one -way ANOVA nonparametric test or group comparison for unpaired t-test with Welch's correction for samples' comparison when SD are not equal. (D) Graphical representation of the relative fraction of red only p62 bodies per cell line. Statistical analysis was made by prism GraphPad 9. (E) Qualitative analysis of cell lines transiently transfected with the indicated mCherry-EYFP tagged p62 constructs. Black dots represent the relative ability of different constructs to form p62 bodies (yellow) when they are transiently transfected. The level of diffuse protein is indicated as d (present) or – (absent).

Supplementary Figure Legend

Figure S1. **A lack of K residues does not affect the in vitro interactions of p62 with ATG8 family proteins or Ubiquitin.** (A) A lack of K residues in p62 does not interfere with the *in vitro* interaction of p62 with NBR1. Myc-p62, myc-p62(K\R) or myc-p62(K\R)R7K were *in vitro* translated in the presence of [³⁵S]-methionine and tested in GST pulldown assays for binding to the PB1 domain of NBR1 fused to GST and immobilized on beads. Myc-p62 constructs were detected by autoradiography and immobilized GST or GST fusions by CBB. (B) Western blot analysis of cell lysates prepared from MEF p62 KO cells stably reconstituted with the indicated GFP-p62 constructs. Cells were lysed in 1% SDS, and the levels of GFP-

p62, endogenous NBR1 and endogenous KEAP1 analyzed by immunoblotting using anti-p62, anti-NBR1 and anti-KEAP1 antibodies, respectively. Harvesting of cells with 1% SDS cannot dissolve the p62 condensates made by this cell line. **(C)** A lack of K residues in p62 does not interfere with the *in vitro* interaction of p62 with ATG8 family proteins. Myc-p62 or myc-p62(K\R)R7K were *in vitro* translated in the presence of S³⁵ methionine and tested in GST pulldown assays for binding to the indicated ATG8 family proteins fused to GST and immobilized on beads. Myc-p62 constructs were detected by autoradiography and immobilized GST or GST fusion proteins by Coomassie brilliant blue staining (CBB). **(D)** A lack of K residues in p62 does not interfere with the *in vitro* interaction of p62 with Ubiquitin. Myc-p62, myc-p62(K\R)R7K or myc-p62 M404V (negative control unable to bind to Ubiquitin) were *in vitro* translated in the presence of S³⁵ methionine and tested in GST pulldown assay for binding to all GST-tagged 4xUb. 4x- Ubiquitin, which was fused into GST. Myc-p62 constructs were detected by autoradiography and immobilized GST or GST-4xUb by CBB. **(E)** Confocal images from MEF p62 KO cells transiently transfected with GFP-p62 or GFP-p62(K\R)R7K\R435K. Scale bars 10µm. **(F)** Proliferation assays of MEF p62 KO cells stably reconstituted with the indicated GFP-p62 constructs were made in Incucyte. 5000 cells were seeded for each MEF p62 KO reconstituted cell line, and cell proliferation was measured for three days. **(G)** Confocal fluorescence imaging from MEF p62 KO cell lines reconstituted with GFP-p62 variants, as indicated, and transiently transfected with mCherry-KEAP1. Scale bars 10µm.

Figure 1



E

GFP-p62 construct	Ability to form p62 bodies	p62 body morphology	Diffuse fluorescence
WT	●●	R	d
K420R	●●●●	R	—
K435R	●	R	D
K420R/K435R	●	R	D
(K/R)	—	—	D
(K/R)R7K	●●●	IR	—
(K/R)R7K/R420K	●●●●	IR	—
(K/R)R7K/R420K/R435K	●●	IR	d

r = regular shape, ir = irregular shape, d = weak diffuse fluorescence, D = strong diffuse fluorescence

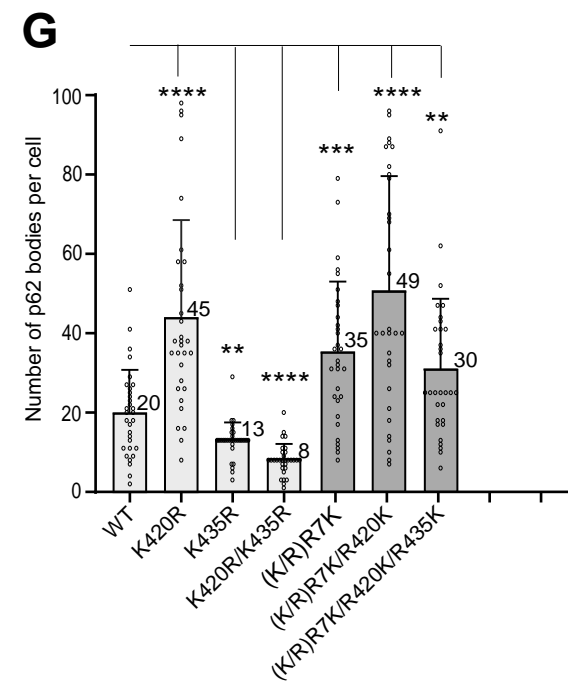
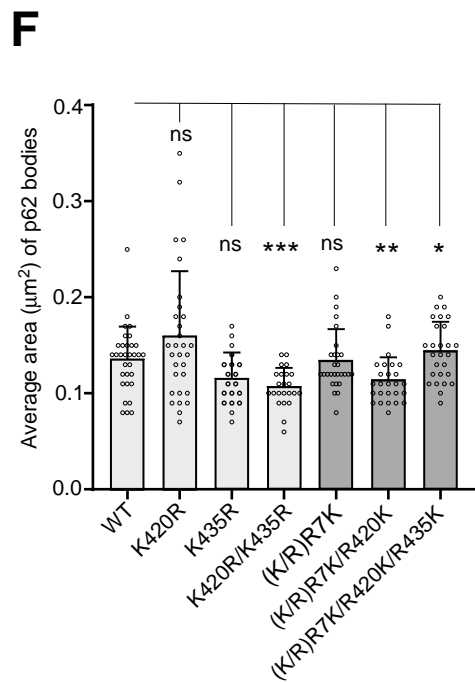
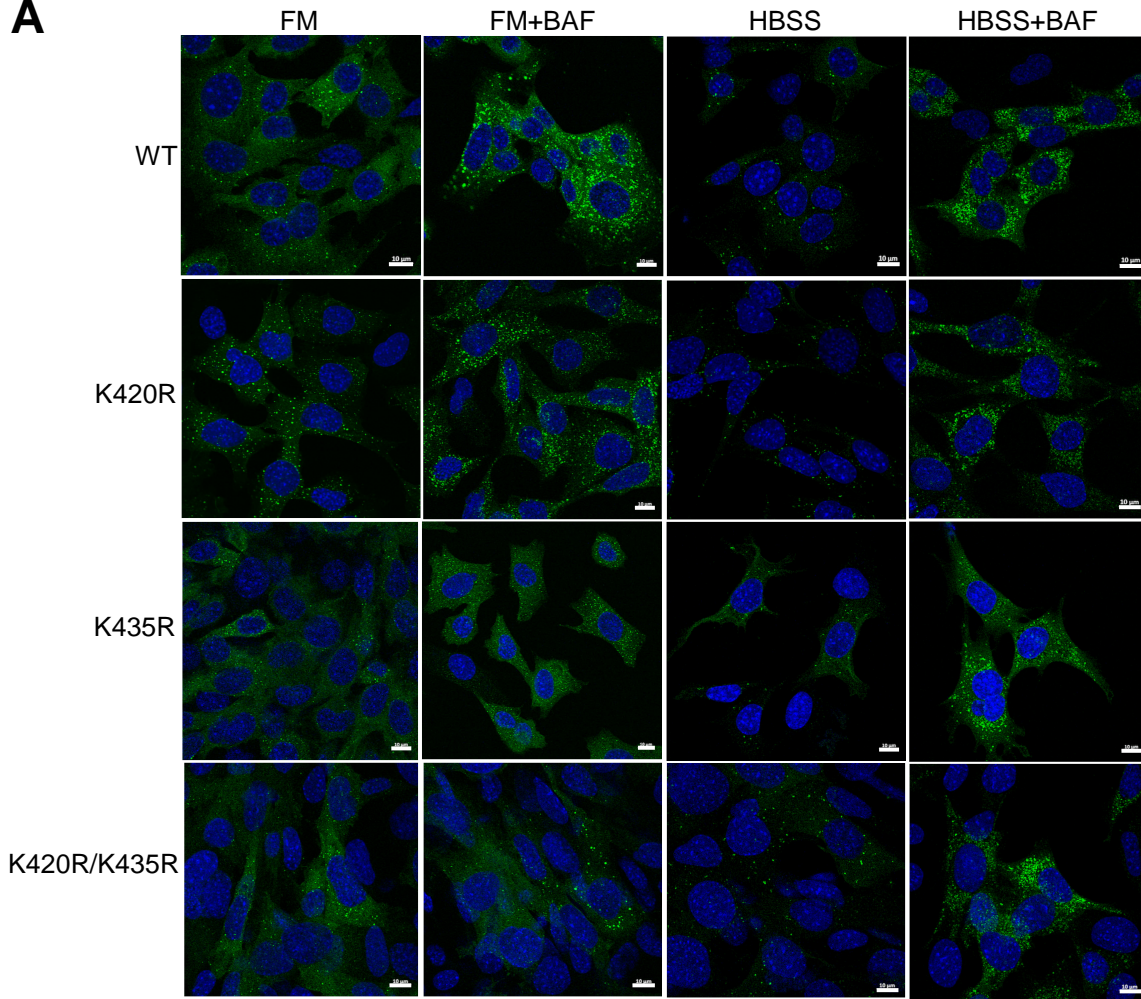
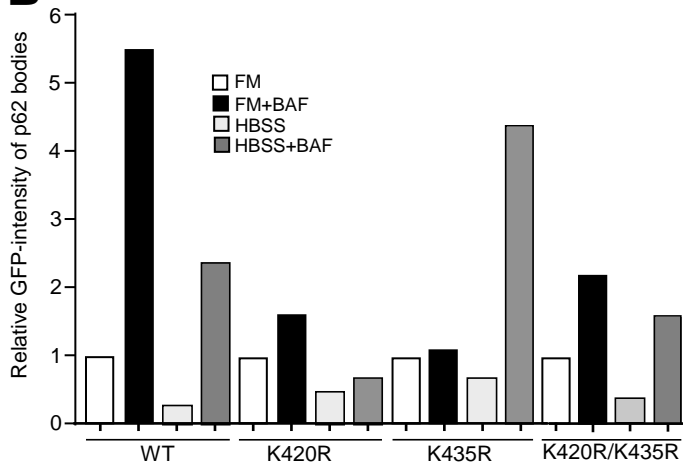


Figure 2

A



B



C

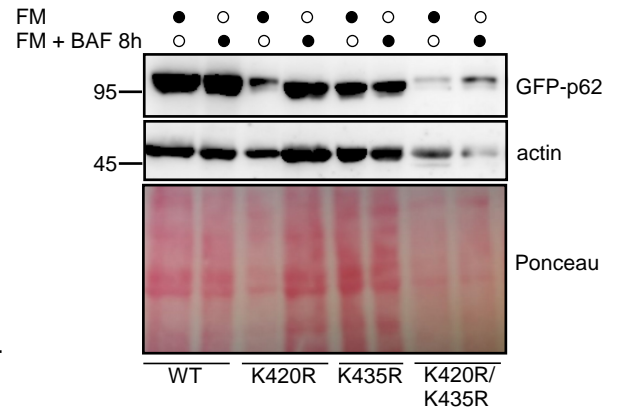
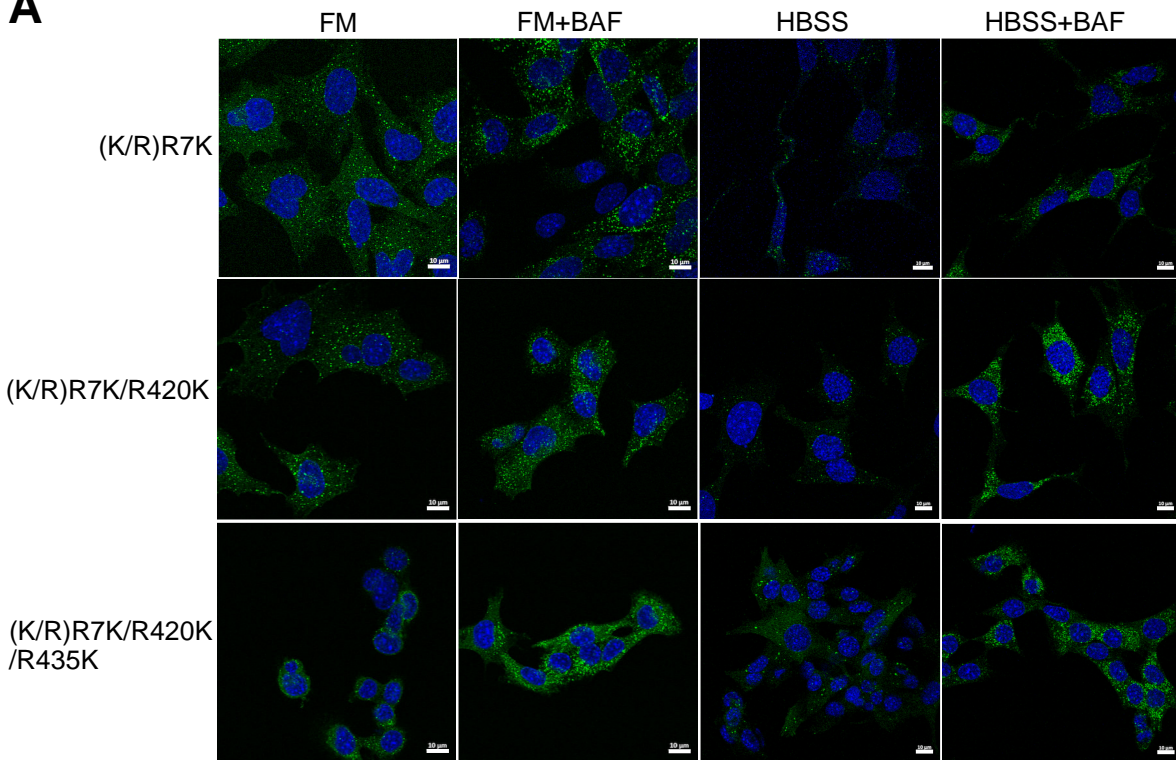
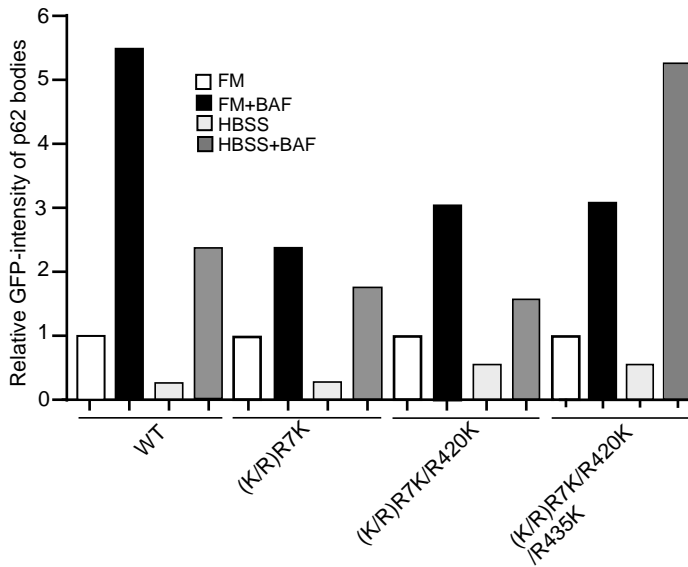


Figure 3

A



B



C

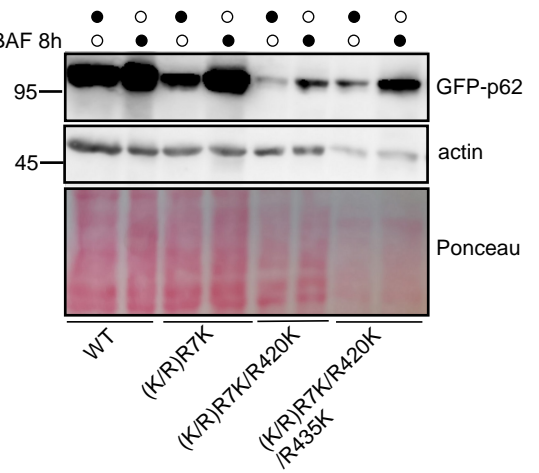


Figure 4

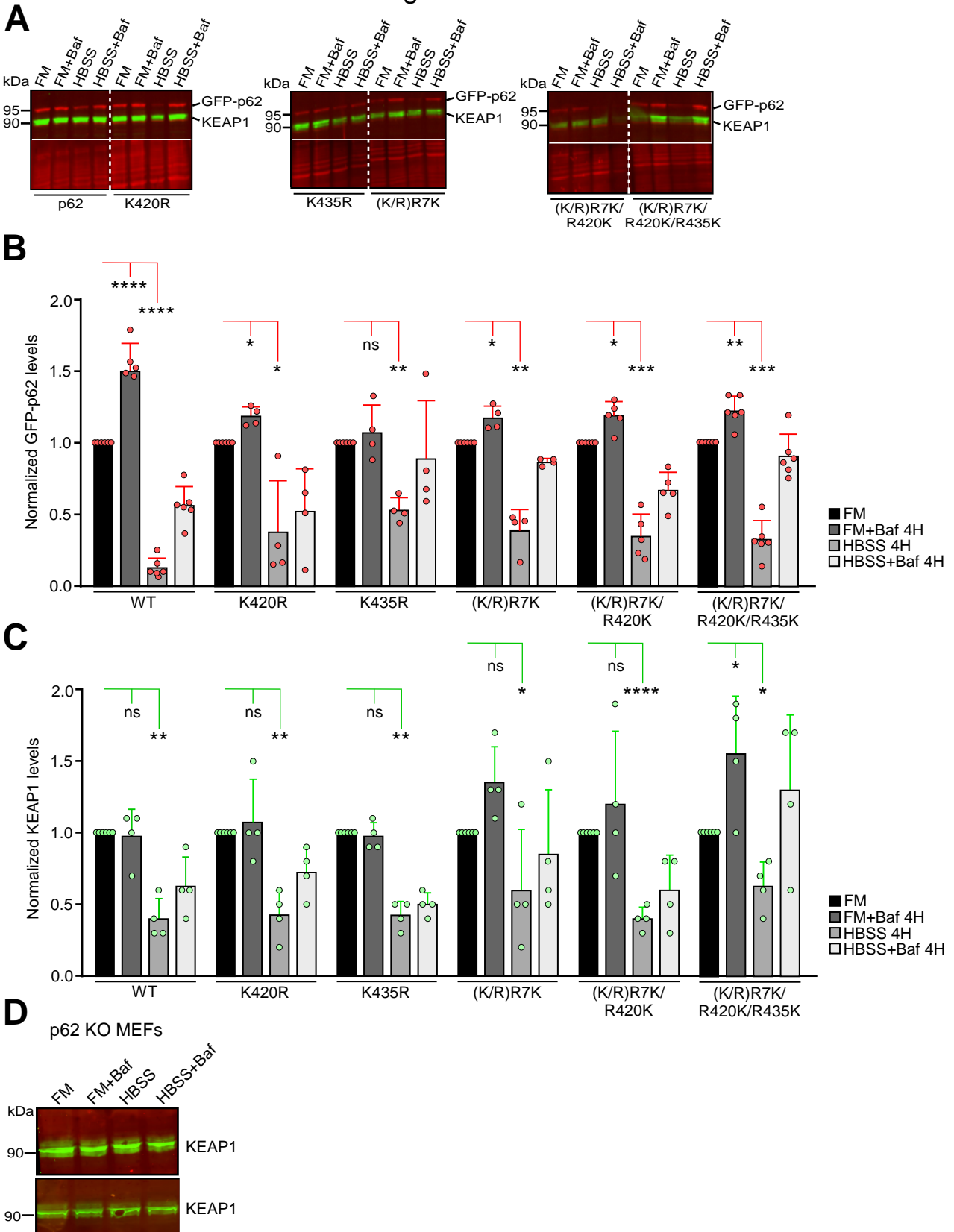


Figure 5

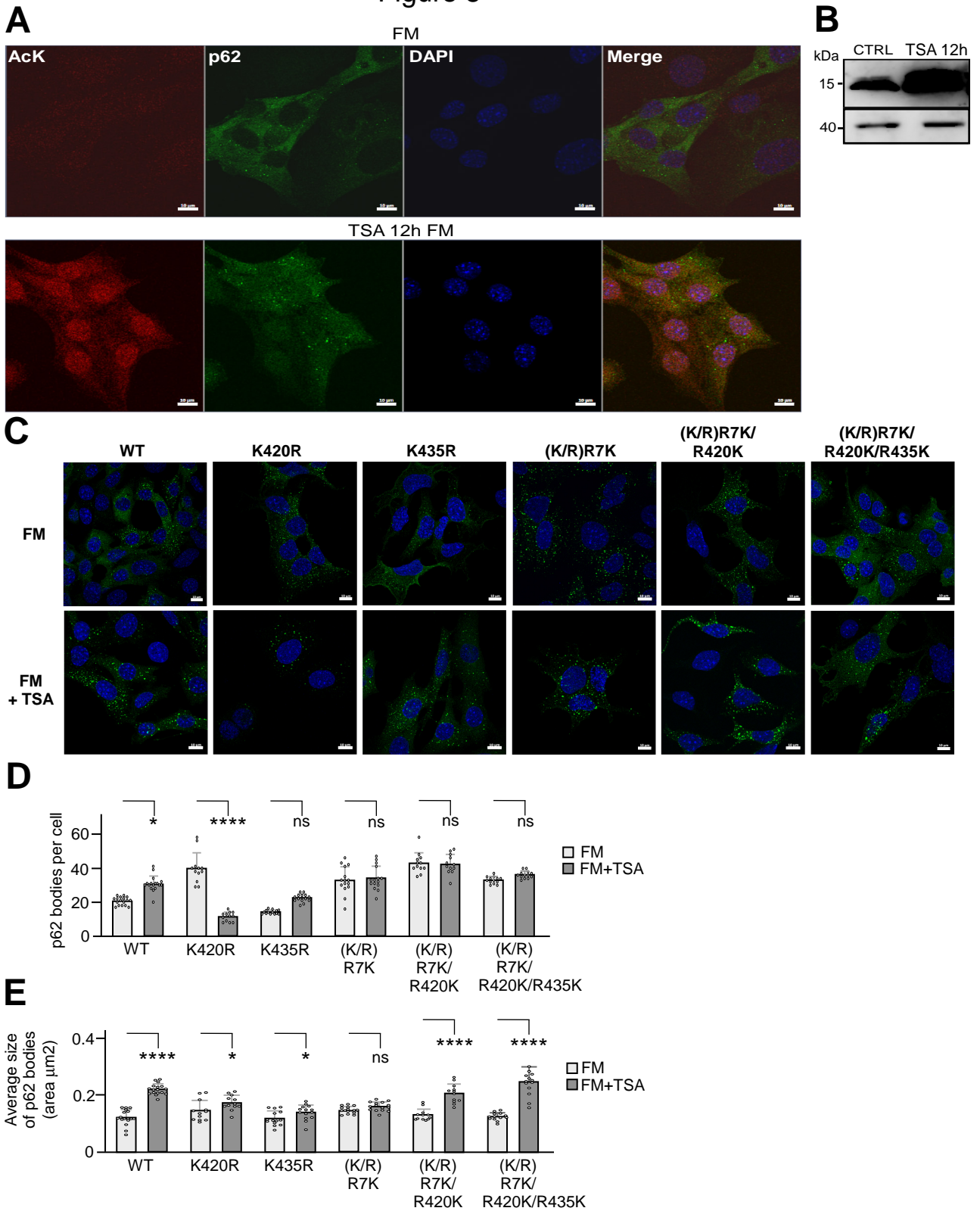
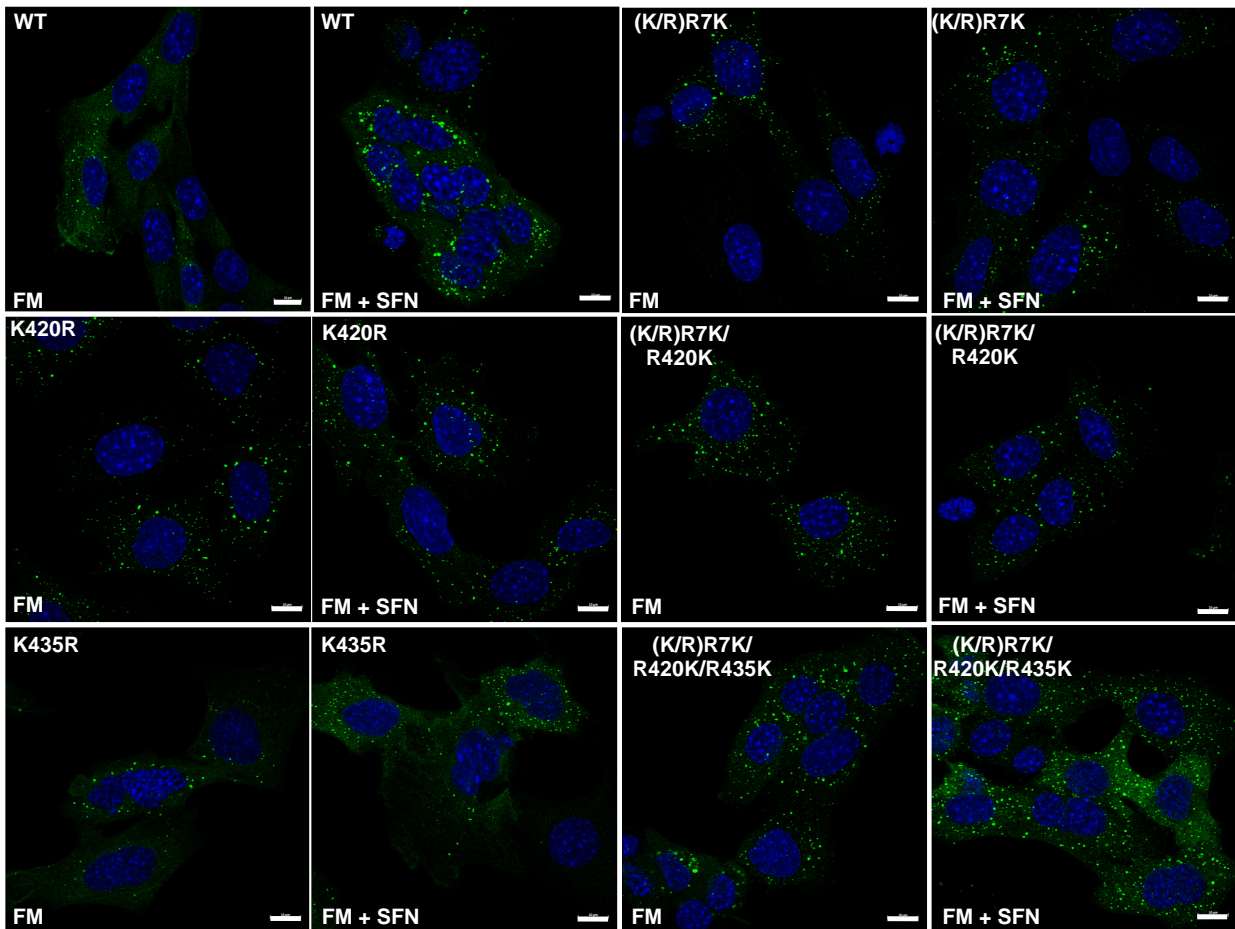
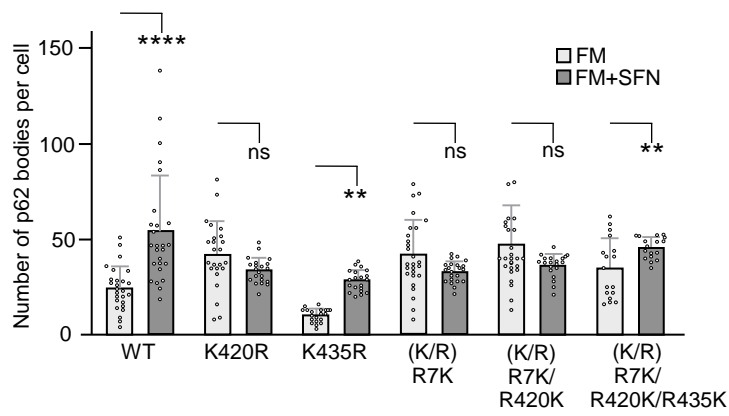


Figure 6

A



B



C

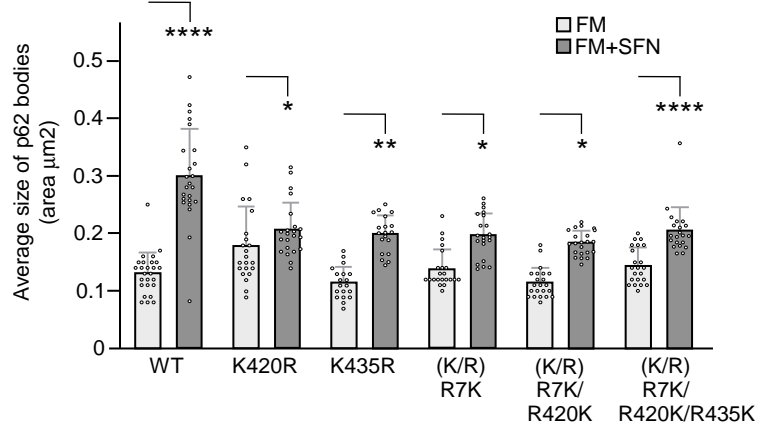
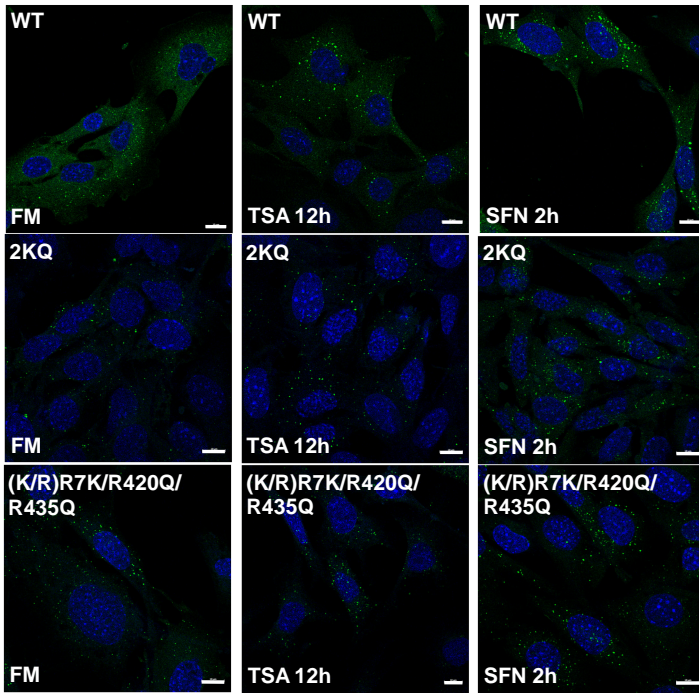
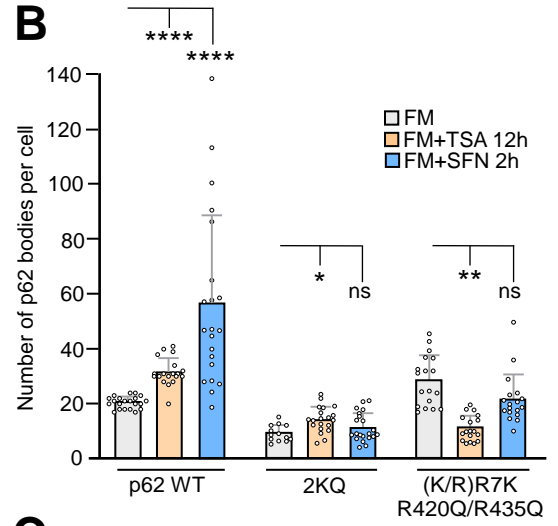


Figure 7

A



B



C

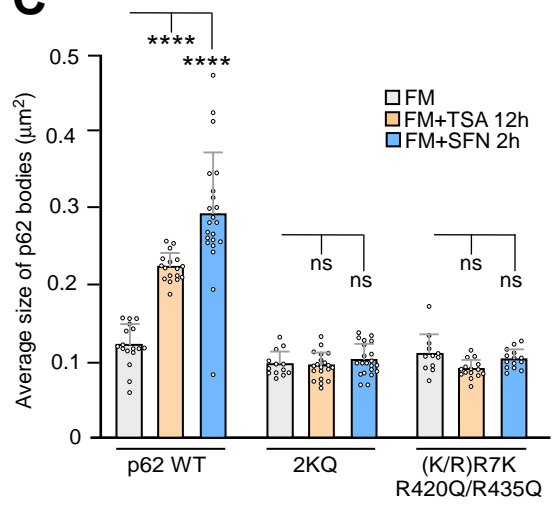


Figure 8

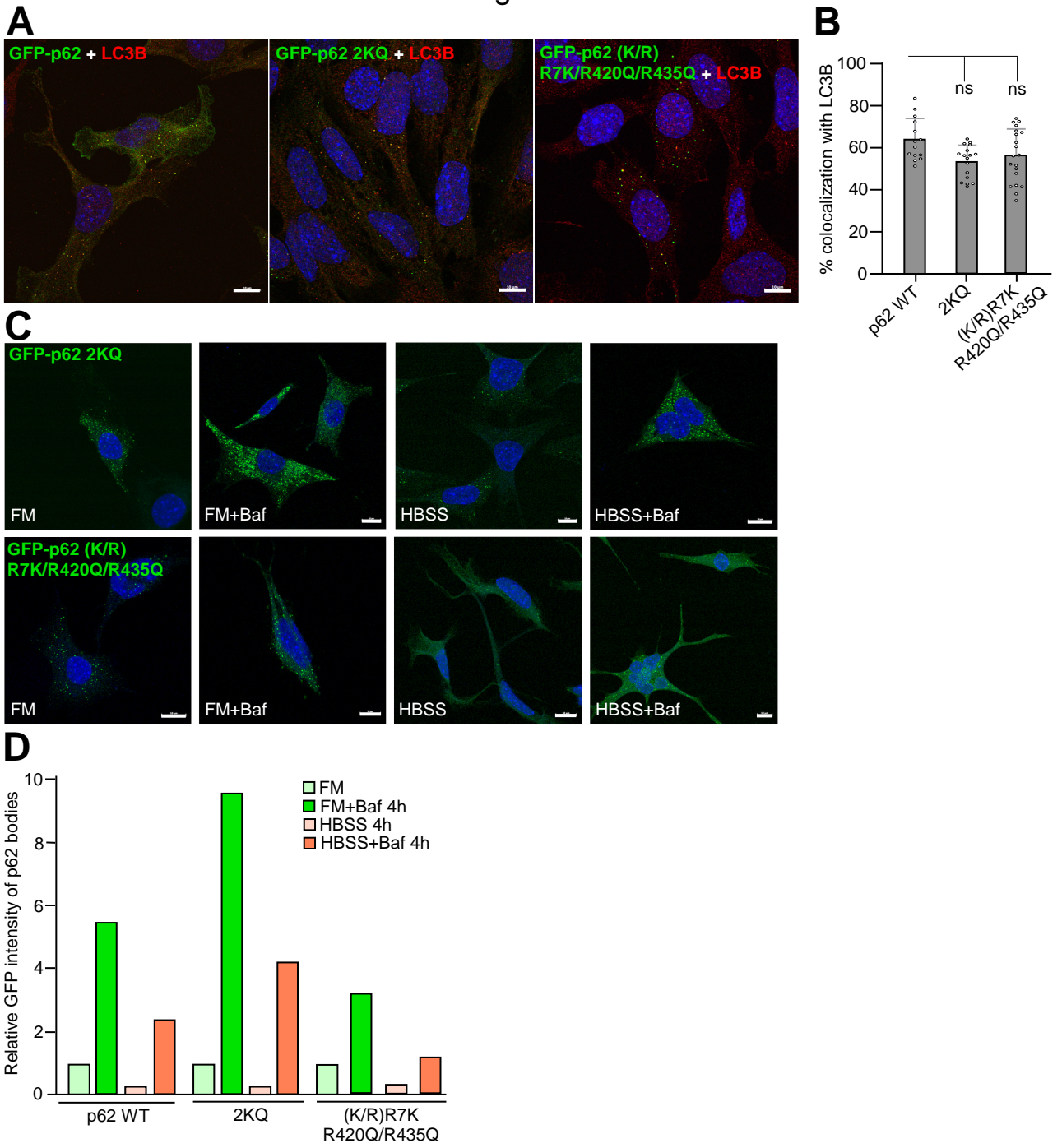


Figure 9

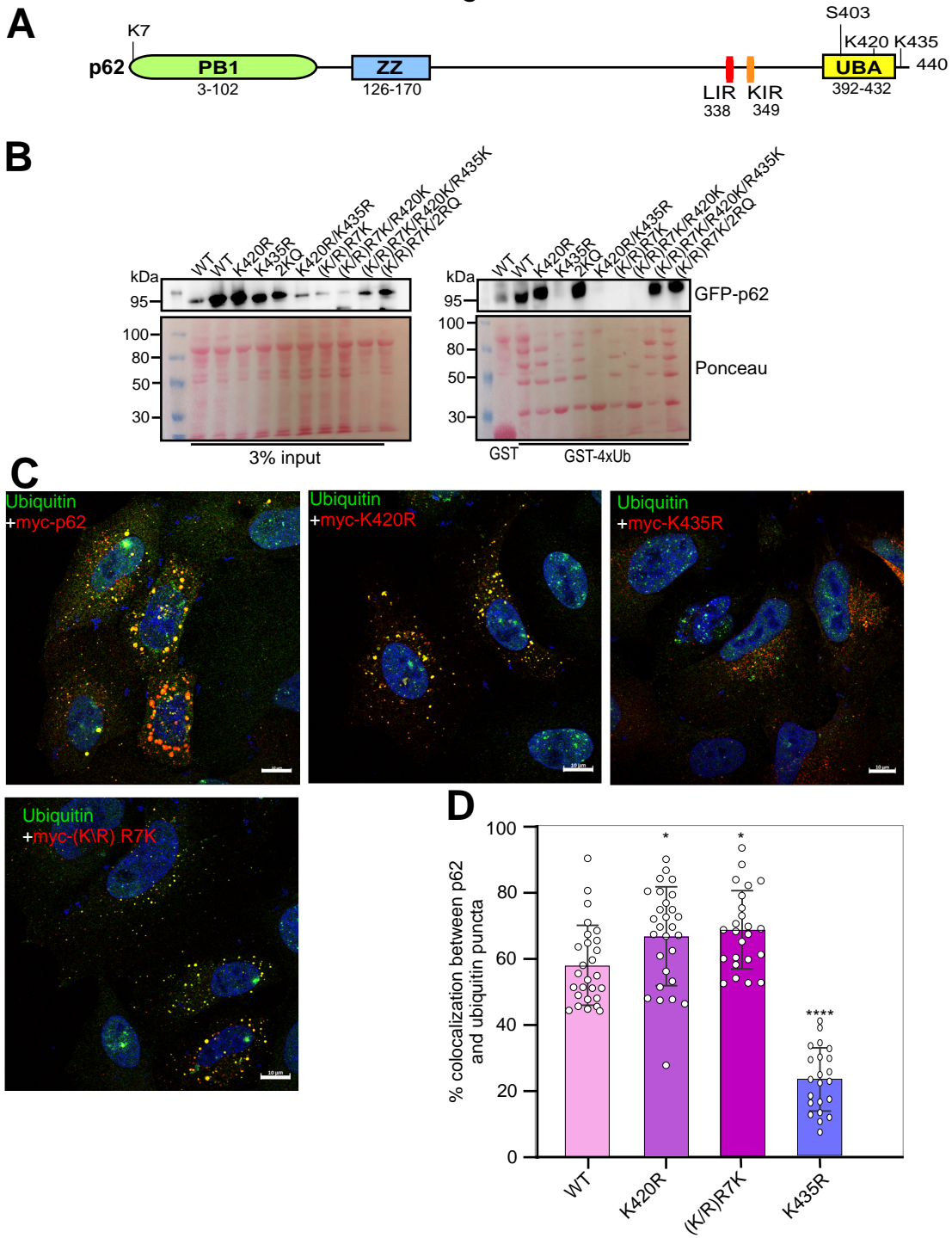
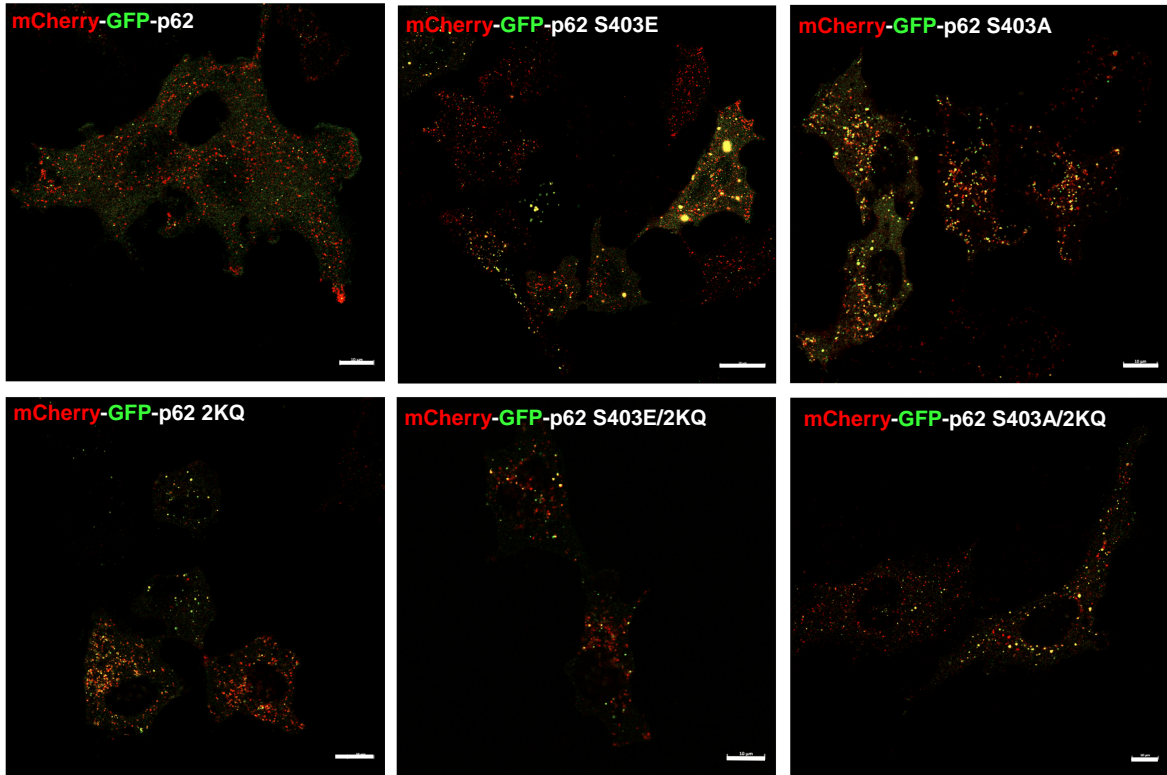
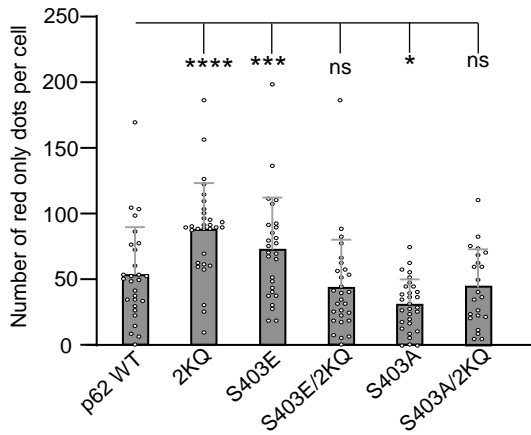


Figure 10

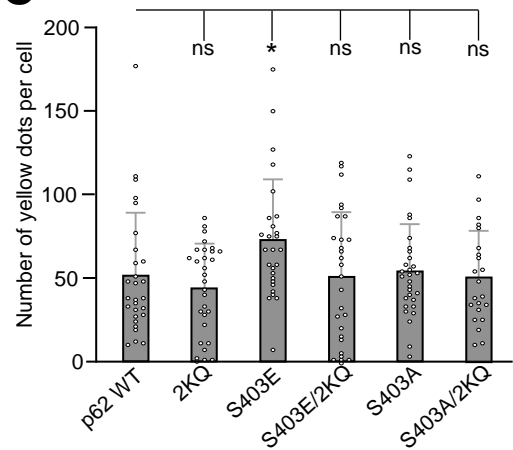
A



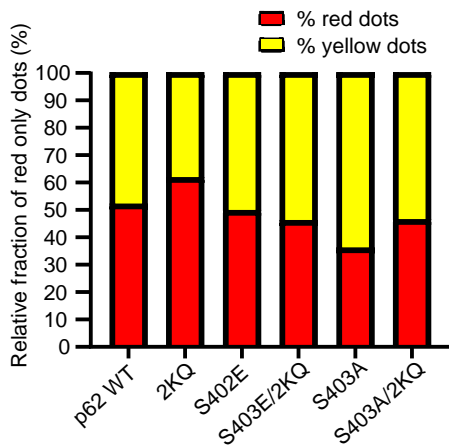
B



C



D



E

Construct name	Size of yellow dots	Level of diffuse fluorescence
WT	● ●	d
2KQ	●	-
S403E	● ● ● ●	d
S403E/2KQ	● ●	-
S403A	● ● ●	d
S403A/2KQ	● ●	-

Supplemental Figure S1

